UNDERSTANDING SIZE-DEPENDENT STRUCTURE AND PROPERTIES OF SPINEL IRON OXIDE NANOCRYSTALS UNDER 10 NM DIAMETER

by

SUSAN RUDD COOPER

A DISSERTATION

Presented to the Department of Chemistry and Biochemistry
and the Graduate School of the University of Oregon
in partial fulfillment of the requirements
for the degree of
Doctor of Philosophy

December 2018

DISSERTATION APPROVAL PAGE

Student: Susan Rudd Cooper

Title: Understanding Size-Dependent Structure and Properties of Spinel Iron Oxide Nanocrystals Under 10 nm Diameter

This dissertation has been accepted and approved in partial fulfillment of the requirements for the Doctor of Philosophy degree in the Department of Chemistry and Biochemistry by:

Victoria DeRose	Chairperson
James Hutchison	Advisor
Darren Johnson	Advisor
Catherine Page	Core Member
Benjamín Alemán	Institutional Representative

and

Janet Woodruff-Borden	Vice Provost and Dean of the Graduate School

Original approval signatures are on file with the University of Oregon Graduate School.

Degree awarded December 2018

DISSERTATION ABSTRACT

Susan Rudd Cooper

Doctor of Philosophy

Department of Chemistry and Biochemistry

December 2018

Title: Understanding Size-Dependent Structure and Properties of Spinel Iron Oxide Nanocrystals Under 10 nm Diameter

Iron oxide nanoparticles (NPs) are promising materials for use in many applications, including new cancer treatments and in cleaning water, because they exhibit size-dependent magnetic and absorptive properties. NP properties are caused by structural attributes of the NPs, like surface disorder and cation vacancies. However, NP synthetic methods also impact structure, therefore properties, of NPs. Furthermore, the synthetic method is often changed in order to change the core diameter of NPs. Determining if properties are caused by the dimensions of the NP is impossible if there are also structural features present in the NP caused by the synthetic method, like grain boundaries or polycrystalline shells. In Chapter II of this dissertation, we show a new continuous growth synthesis of spinel iron oxide where the diameter of NPs is changed by the amount of precursor added to the reaction, meaning the only structural feature changing between the NPs is size. Continuous growth, therefore, can be used to probe the impact that size has on NP structure and properties. We report that saturation magnetization of NPs produced from continuous growth is size-dependent and higher in magnitude than NPs of the same core diameter made by other syntheses. In chapter III of this dissertation we determine nanoscale structure by Pair Distribution Function (PDF)

analysis of Total X-ray Scattering data of NPs isolated from the reaction with core diameters between 3-10 nm. In Chapter IV of this dissertation we monitored the growth of NPs *in situ* with Total X-ray Scattering to gain insight on the structures of NPs while forming. *In situ* measurements of Total X-ray Scattering data gave insights into how precursor oxidation state influences the structures formed during formation of NPs, with more oxidized precursor giving a more oxidized product and a reduced precursor yielding a more reduced product even though the NPs formed by either method are indistinguishable by *ex situ* analysis.

This dissertation includes previously published and unpublished co-authored material.

CURRICULUM VITAE

NAME OF AUTHOR: Susan Rudd Cooper

GRADUATE AND UNDERGRADUATE SCHOOLS ATTENDED:

University of Oregon, Eugene
California Polytechnic State University San Luis Obispo

DEGREES AWARDED:

Doctor of Philosophy, Chemistry, 2018, University of Oregon
Bachelor of Science, Chemistry, 2008, California Polytechnic State University San Luis Obispo

AREAS OF SPECIAL INTEREST:

Synthesis of Nanocrystals
Metal Oxide Nanocrystals
Total X-ray Scattering
Pair Distribution Function Analysis

PROFESSIONAL EXPERIENCE:

Graduate Research Fellow, Hutchison and Johnson Lab, University of Oregon 2013-2015, 2018

NSF Research Fellow, Hutchison and Johnson Lab, University of Oregon 2015 - 2018

Teaching Assistant, General Chemistry Lab, University of Oregon 2013-2014

Bio Architecture Lab Inc., Berkeley, California Research Associate, Analytical Lead, 2010-2013

Creek Environmental Laboratories Inc., San Luis Obispo, California Metals and Wet Chemistry Analyst, 2009-2010

TestAmerica Laboratories Inc., Shelton, Connecticut Gas Chromatography Analyst 1, 2008-2009

GRANTS, AWARDS, AND HONORS:

Graduate Research Fellowship Program Awardee, National Science Foundation
2015 – 2018

ARCS scholar, University of Oregon, Department of Chemistry and Biochemistry
2015 - 2018

PUBLICATIONS:

1. **Cooper, S.R.**; Plummer; L.K.; Cosby, A.G.; Lenox, P; Dhagat, P; Hutchison, J.E. Insights into the Magnetic Properties of Sub-10 nm Iron Oxide Nanocrystals through the Use of a Continuous Growth Synthesis. *Chem. Mater.* **2018**, *30*, 6053-6062

2. **Cooper, S. R.;** Nell, B. P.; and Tyler, D. R. Fluxional Behavior of cis-$Fe(DMeOPrPE)_2(H)_2$ (DMeOPrPE = 1,2-[bis(dimethoxypropyl)phosphino]ethane); Implications for the Pressure Swing Purification of Natural Gas *J Inorg Organometc Polym* **2017**, *27*, 57-62.

3. Enquist-Newman, M.; Faust, A. M. E.; Bravo, D. D.; Santos, C. N. S.; Raisner, R. M.; Hanel, A.; Sarvabhowman, P.; Le, C.; Regitsky, D. D.; **Cooper, S. R.;** et al. Efficient Ethanol Production from Brown Macroalgae Sugars by a Synthetic Yeast Platform. *Nature* **2014**, *505*, 239–243.

4. Wargacki, A. J.; Leonard, E.; Win, M. N.; Regitsky, D. D.; Santos, C. N. S.; Kim, P. B.; **Cooper, S. R.;** Raisner, R. M.; Herman, A.; Sivitz, A. B.; et al. An Engineered Microbial Platform for Direct Biofuel Production from Brown Macroalgae. *Science* **2012**, *335*, 308–313.

ACKNOWLEDGMENTS

I would like to acknowledge both of my advisors, Dr. Jim Hutchison and Dr. Darren Johnson. Both of my advisors were wonderful to work with and changed the way I approach problems scientifically and how I lead. I am very grateful to have had the experience of being advised by Jim and Darren.

I would also like to thank my committee members. I feel lucky to have had both Dr. Victoria DeRose and Dr. Catherine Page on my committee who were not just committee members but mentors. I would also like to thank Dr. Benjamín Alemán for being my institutional committee member.

In addition to working at the University of Oregon, I also collaborated with Dr. Kirsten Jensen at the University of Copenhagen. I learned how to analyze Total X-ray Scattering Data with Pair Distribution Function Analysis from Kirsten. She is co-author on Chapter III and Chapter IV of this dissertation and I spent 6 months of my graduate work in her lab in Copenhagen. This dissertation would not have been as successful without her guidance using Total X-ray Scattering.

I would like to thank the Center for Advanced Materials Characterization (CAMCOR) at UO, Josh Razink for acquiring HRTEM, Dr. Erik Hadland and Dr. Sam Young for assistance with XRD and SAXS measurements, Dr. Jan Ilavsky for creating and making available IRENA Macros for SAXS modeling and Andy Ungerer at Oregon State University for assistance with ICP-OES acquisition. This work was supported through the National Science Foundation Graduate Research Fellowship Program under Grant No. 1309047. I would like to thank ARCS for funding support from 2015-2018. The ARCS foundation also is a wonderful organization that provides not only financial

support but builds relationships with the scholars for which I am really grateful. I would also like to thank the University of Oregon for funding support.

I was also a member of two labs and worked with numerous talented scientists. I would like to thank Kenyon Plummer for being a wonderful co-author and a great person to work with. I would like to thank Dr. Sam Young and Meredith Sharps for assisting me in running beamline experiments. Chapter IV of this thesis would not have been possible without their hard work during *in situ* measurements. Alexia Cosby and Randal Candler were two undergraduates who worked with me during my graduate career. I can't wait to see what they do in the future. I would like to thank my office mates Meredith Sharps, Sean Fontenot and Jordan Levine for being great co-workers and for their support over the last few years. I would like to thank those that graduated before me, especially Dr. Anna Oliveri, Dr. Maisha Kamunde-Devonish, Dr. Blake Tresca, Dr. Kara Nell, Dr. Beverly Smith, Dr. Ed Elliot, Dr. Brandi Baldock, Dr. Adam Jansons and Dr. Sam Young for their help as mentors and friends. I would also like to thank current members of both labs: Jaclyn Kellon, Kenyon Plummer, Tawney Knecht, Aurora Ginzburg, Brantly Fulton, Brandon Crockett, Meredith Sharps, Jordan Levine, Lizzie Cochran, Lisa Eytel, Hazel Fargher, Ngoc-Minh Phan, Trevor Shear, Thais De Faria and Jeremy Bard.

One of the best things about the University of Oregon is the great community that exists in the chemistry department. I would like to especially thank Dr. Lisa Enman and Dr. Andrea Loes for being wonderful over the last five years. I could not have done this without these two amazing women. I would also like to thank Dr. Annie Greenaway, Dr. Michaela Burke, Dr. Matt Kast, Dr. Conerd Frederickson, Dr. Loni Kringle and Huiying Ji for their wonderful friendship.

I would also like to thank my parents, Cathryn Cooper and Darrel Ray Cooper, and my grandparents, Karen Rudd and Bob Rudd, for their support. My best friend from high school, Melissa Drummonds, is one of the best people on earth and I am so thankful for her friendship and support. I would also like to thank Gina Marie Jensen for being the best honorary aunt I could ask for and for always providing unconditional support.

TABLE OF CONTENTS

Chapter Page

Chapter Page

Chapter Page

Chapter Page

LIST OF FIGURES

Figure Page

Figure Page

Figure Page

Figure Page

Figure Page

Figure Page

Figure Page

LIST OF TABLES

Table Page

Table Page

CHAPTER I

SIZE-DEPENDENT STRUCTURE AND REACTIVITY OF NANOCRYSTALS UNDER 10 NANOMETERS IN DIAMETER

Portions of this chapter will be published in the forthcoming publication co-authored with my advisors James E. Hutchison and Darren W. Johnson. I am the primary contributor to the writing of this introduction.

Introduction

Nanoscience is of great interest because there are size-dependent properties of materials that we would like to harness for use in applications.[1–4] Nanoscale properties are caused by nanoparticle (NP) structural attributes that include: structure[5–10] (phase and defects), composition[11,12] (core and surface material) or morphology[7,13] (size, dispersity and shape). NPs that show enhanced properties will change health,[14–16] energy,[17,18] and environmental[19,20] fields. For example, superparamagnetic iron oxide NPs with size-dependent magnetization can be used to detect or treat diseases.[13] Complex chalcogenides like Cu_2ZnSnS_4 (CZTS) can make more efficient solar cells from earth abundant elements with tunable optoelectronic properties. [11,17,21–23] TiO_2 can photo-catalytically clean water of organic contaminants[24] while iron oxide can adsorb harmful metal contaminants[5,25] in water. However, different studies of NPs reported to have the same structure, composition and morphology do not report the same properties.

Synthetic conditions can be changed to control NP structural attributes like size,[26] surface chemistry[27,28] or shape[29–31]. For example, in order to change the size of NPs, the temperature,[26,32–36] reactant ratios,[37–43] pH,[44] heating rate,[45] precursor concentration [7,8,34,46–50] and time[36,43,50,51] of the reaction can all be changed. However, size is not the only attribute impacted with changes in these synthetic parameters. For example, temperature changes the presence of strain producing defects like stacking faults[52] and interruptions in the lattice of NPs, such as, grain boundaries.[8,52–54] Therefore, conclusions about how NP structural attributes impact the properties of NPs cannot be made if the synthesis causes inadvertent changes to multiple structural attributes. When NPs are made from complex materials that have either metals that have multiple oxidation states or multiple metal cations, it becomes even more complicated to isolate NP structural attributes to determine their effect on properties. For example, involvement of lower oxidation states in iron oxide NP synthesis introduces antiphase boundaries in the core of the NP as a result of wüstite formation. [7,8,55] In the synthesis of CZTS, the involvement of multiple metal cation precursors causes the nucleation of multiple materials at the same time, seriously limiting production of complex metal chalcogenides.[6,17,56] Without stronger understanding of the reaction mechanisms, nanoscientists have relied heavily on trial and error to enhance properties through synthesis.[57] However, this approach is an inefficient way to find new NP synthesis techniques, thus we need to develop design principles that consider the specific chemistries of different systems.

This review will cover what steps are needed by the field in order to obtain synthetic design principles to control NP properties and increase reproducibility in NP syntheses. First, current and emerging nucleation and growth theories will be discussed.

Next, the reactivity of synthetic systems will be covered. Specifically, we consider how NP formation is affected by reaction type, precursor, and NP structure. We will also discuss the effects that NP structural attributes (size, ligand and phase) have on properties. Currently, it is difficult to determine how structure relates to properties due to inadvertent NP characteristics caused by synthetic conditions. Finally, we will discuss how advances in synthetic methods and characterization methods will allow chemists to understand design principles.

Classical Design Principles

Nucleation and growth

Classical nucleation and growth[58,59] theory is most commonly used to describe the formation of NPs due to its universal applicability to NP systems. In the classical theory, nucleation occurs when a critical radius of material is reached.[58,59] The critical radius is the minimum size of NP that will survive in solution without dissolving, or when the volume free energy term of the material becomes larger in magnitude than the surface free energy term of the material. [58,59] Smaller NPs have a higher chemical potential and therefore dissolve more readily than larger NPs. [58,59] The critical size depends upon temperature, supersaturation and the surface free energy[58,59] but not on the individual chemistry of the materials being formed.

After nucleation, the NP growth is often explained by diffusion-limited growth described by Fick's first law of diffusion.[59] However, the reaction can be limited either by the diffusion of monomer to the surface of the NP or by the reaction of monomer with the NP surface.[33,58] One of the critical assumptions in the classical growth theory is that

the reaction constant is independent of the material chemistry because it is solely a precipitation reaction; however, this assumption will not be valid in the reported cases where size influences reactivity.[59] It will also not be valid if there are multiple reactions that can occur on the surface and not solely a precipitation of material. Other assumptions are that the NPs are spherical and that there is one interfacial energy for the entire NP. [59] However, size-dependent structure is expected to impact the growth of NPs.[5] For example, small NPs have increased catalytic behavior caused by surface structure.[60] Thus, classical growth theory is over simplified and is inadequate to assist in developing design principles for the formation of NPs.

Other nucleation and growth theories

One nucleation model where the precursor and nucleation interactions matter, and affect growth, is the Finke-Watzky model. [58,59,61] The Finke-Watzky model is a two-step mechanism that involves slow and continuous nucleation, followed by an auto catalytic reaction-controlled growth.[61] In the nucleation step, monomer A is converted into the product B (A->B).[61] After nucleation is complete the monomer reacts with the product to form B (A +B -> 2B).[61] Nucleation occurs slowly until enough of B is formed to autocatalytically form B from A.[61] The Finke-Watzky model was used to explain the occurrence of auto-catalytic growth behavior in the formation of metal clusters.[61] While the Finke-Watzky model addresses the situation where NPs and precursor have an effect on each other during the reaction, it still does not incorporate specific chemical pathways for different compositions.

Another nucleation category is the non-Classical nucleation model[62] which describes the formation of NPs through heterogeneous growth. These have thermodynamically stable structures during the formation of materials that are intermediates to larger NPs.[62] These stable structures either have lower surface energy or lower volume energy than larger NPs causing a local minima for stable structures before the formation of larger NPs.[63,64] Examples include: amorphous nuclei that undergo crystallization to form NPs, aggregation of nuclei to form larger NPs, oriented attachment (when two NPs become one NP along the same crystallographic direction) or heterogeneous nucleation (the nucleation of a substance onto another material).[62] All of these models are general and do not provide information regarding the specific chemistry.

Toward New Design Principles

New approaches are being used to determine the synthetic mechanisms of NP formation, but, there is still a gap in knowledge of how reaction parameters impact NP growth. The first reason for the gap in knowledge is that most synthetic methods do not allow for the systematic testing of different synthetic conditions. For example, a common approach to controlling the size of NPs is to change the temperature of the reaction.[26] Changing the temperature of the reaction, however, also changes the mechanism of the reaction and will impact other structural features, like internal core structure.[8,55] The internal core structure that deviates from bulk crystallographic structure is hard to detect by traditional structural characterization techniques which rely on long range repeating crystallographic units.[65] The wide range of values of properties reported for NPs with the

same structure made by different methods suggests that structural defects are common, but remain undetected, in most NP samples.[7]

There are a variety of characterization techniques that are capable of elucidating nanoscale structure including High Resolution Transmission Electron Microscopy (HR-TEM) and Total X-ray Scattering techniques. HR-TEM can be used to directly observe structural defects including stacking faults[52] and antiphase boundaries[8]. Strain mapping of HR-TEM has also been used to elucidate areas of high strain in NPs, for example stacking faults, that are not as apparent in the data.[54] Advanced characterization techniques that probe nanoscale structure like Pair Distribution Function analysis (PDF) of Total X-ray Scattering have allowed for the determination of nanoscale structure of precursors and NP products.[66–69] PDF analysis takes into account Bragg scattering that gives information on global structure and diffuse scattering, providing information on local structure.[65,70] By using Total X-ray Scattering to probe local structure *in situ*, information about the nanoscale structure can be gained during the reaction.[67,68]

By studying many different systems *in situ*, new information on the mechanism of formation can be elucidated.[69] Precursors for instance can have a variety of different structures including monomer metal complexes, clusters or polymers.[69] The precursor structure can influence the mechanism of the reaction. For example, SnO_2 NPs were made with a Sn precursor that took the structure of an aquo-monomer metal complex.[67] Sn aquo-monomers then condense to form small, multi-Sn bridged clusters that aggregate to form final NPs.[67] However, in the synthesis of ZrO_2 NPs, NPs are formed through decomposition of a polymeric Zr precursor.[69] In the synthesis of InP NPs, monodisperse cluster species are formed as intermediates. [63,71,72] In each of these cases, the differences

in the speciation of precursor depends upon the oxidation of precursor, the solvent and the ligand shell. In order to determine design principles for the formation of monodisperse NPs, *in situ* studies of materials under a variety of synthetic conditions is necessary.

Common Reaction Types in Solution Synthesis of NPs

Different types of solution phase reactions can be used in order to form NPs. Here the focus will be on the formation of NPs in solution because more control over size, structure and surface chemistry can be achieved than in solid state reactions.[73] The most cost-effective and straightforward method of making NPs in solution is through hydrolysis reactions like hydrothermal or co-precipitation syntheses. Hydrolysis, however, leads to NPs with large dispersities and a high number of NP defects.[10,39,44,74] One of the most promising advances in the synthesis of NPs involves thermal decomposition of a metal precursor in non-aqueous media.[26] NPs produced by this method are monodisperse, but they can be plagued by internal NP defects that are hard to detect.[8,55] The final type of reaction that will be discussed is continuous growth of NPs, a new synthetic technique that allows for slow controlled growth by adding the precursor slowly at a low reaction temperature.[75,76]

Formation of NPs occurs very fast during hydrolysis, reducing the selectivity for what products are formed in the reaction.[73] Reduced selectivity leads to polydisperse NPs with a variety of shapes and sizes.[39,44] Hydrolysis has been shown to produce polycrystalline shells on the surface of NPs.[10] Therefore, size-dependent studies of NPs formed by hydrolysis reactions will be prone to defects that are not representative of their

size but are caused by the synthetic parameters.[10,39,42,44,74] Even though hydrolysis reactions are easy to perform, NPs made by hydrolysis lead to conflicting results of properties attributed to NP structural attributes due to their high number of NP defects.[7]

Non-aqueous methods for NP synthesis use the tool box of organic chemical reactions to form NPs, enabling slower and more controlled reactions than hydrolysis reactions.[73,77] NPs produced by non-aqueous methods have uniform size and have increased crystallinity compared to hydrolysis reactions.[73] Another benefit is the presence of ligands on the surface of the NPs that enable them to be soluble in organic solvents.[73] Common precursors for metal oxide NPs include metal halides and carboxylates.[26,40,41] Some of the organic reactions that lead to metal oxide bond formation are alkyl halide elimination, ether elimination, ester elimination and thermal decomposition.[73]

Thermal decomposition is the most common method for making NPs through non-aqueous methods and has resulted in increased control of NP size and shape with narrow dispersities.[26,46,78] However, thermal decomposition of a precursor produces a wide variety of intermediates including radical reactions CO_2, H_2, CO, alkenes, esters and ketones.[79] The increased reactivity of radicals leads to lower selectivity in NP formation and produces a undesirable intermediates and products.[80] Thermal decomposition reactions have been shown to impart defects in the internal structure of NPs like stacking faults[52] and grain boundaries.[8,52–54] The presence of strain producing defects have been shown to negatively impact material properties.[7]

Continuous growth of NPs uses ester elimination to form metal oxide NPs. The reaction promoting NP growth is a single controlled catalytic esterification reaction, with no radical reactions because the reaction temperature is below thermal decomposition of

the precursor. [7,47,76,81] The products of catalytic esterification are ester, water and NPs, a much more selective reaction compared to thermal decomposition.[75] Continuous growth allows for living growth on the surface of NPs where more precursor can be added to the reaction to increase the size of the NPs.[76] By slowly adding precursor to the NPs the growth is slow and controlled. [76] Continuous growth also allows for systematic variation of NP parameters like temperature and precursor. The continuous growth method can be used for a variety of metal oxides by slowly injecting a metal oleate precursor into oleic acid.[47,75,81]

In chapter two of this dissertation, the continuous growth method has been used to produce NPs of spinel iron oxide with core diameters from 3-10 nm.[7] When comparing the magnetic properties of spinel iron oxide, superior magnetic properties were observed for NPs made by the continuous growth method compared to NPs made by thermal decomposition.[7] The use a controlled reaction mechanism, is hypothesized to be the cause of increased magnetic properties due to fewer NP defects.

Properties Impacted by Unintended NP Structural Attributes

Unfortunately, the literature is full of reports on the properties of nanomaterials that are caused or impacted by unintended NP structural attributes introduced during synthesis due to a lack of selectivity.[7,26,27,32,41,42,45] The issue is that in order to change the attribute of interest, like size[32] or ligand shell[27], other NP structural attributes also change. The fact that multiple features are changing at the same time makes determining the size-dependent, as well as surface structure-dependent, properties of NPs impossible. The data

become even more confusing when there are multiple oxidation states available or multiple metal cations are incorporated into the lattice.

Size-dependent properties impacted by unintended NP structural attributes

Elucidation of size-dependent magnetic properties of spinel iron oxide has been difficult due to unintended NP structural attributes caused by NP defects.[7] Size-dependent magnetic properties are reported to be caused by a thin non-magnetic layer on the surface of the NP that is between 0.35-1 nm thick.[74,82–84] It has been posited that the non-magnetic layer is caused by an interruption of the magnetic lattice at the surface of the NPs.[8,85] When the surface to volume ratio is high, the non-magnetic layer at the surface starts to constitute a large percentage of the NP volume. The surface is not the only place that an interruption in the magnetic lattice could occur, with interruptions also occurring at phase boundaries, stacking faults or other structural defects.[8] Spinel iron oxide has been shown to form wüstite under reducing conditions, which lowers the magnetic properties even when the NPs are oxidized after the synthesis.[8] NPs made by a variety of methods report values of saturation magnetization from 17-81 emu/g for 5 nm core diameter NPs.[7] The presence of defects in spinel iron oxide caused by synthetic methods has hindered the ability to attribute properties to size-dependence. In chapter two of this dissertation we show that NPs made by a continuous growth method have very thin non-contributing magnetic layers of 0.2 nm or less and have superior magnetic properties.[7]

The structure of the NPs as they form can also impact the reactivity in addition to the precursor and solvent. Size-dependent structural features like vacancies,[86,87] NP crystallinity,[9] lattice strain,[88] and surface strain[89] can impact the reactivity of NPs.

Nanoscale structure has impacts on both the properties of NPs as well as the growth.[5,68] The impact of the NP surface is often not considered in NP formation, as in classical growth theory, but it is a changing variable throughout the synthesis that likely makes a large impact.

In chapter three of this dissertation, the size-dependent structure of spinel iron oxide NPs is determined by PDF analysis of Total X-ray Scattering. Spinel iron oxide NPs have been shown to have size-dependent occupancy on tetrahedrally coordinated cation sites.[31,90–94] These vacant sites are more reactive which makes them particularly adsorbent sites for arsenate on the surface of spinel iron oxide NPs. Increased reactivity is expected to impact the growth of NPs since these vacant cation sites should also be especially reactive for iron monomers as well.[5] In chapter three, we also show size-dependent growth of NPs. Larger NPs grow slower than smaller NPs in the presence of the same amount of precursor. We conclude that the size-dependent structure of spherical spinel iron oxide NPs impacts the rate of growth of spinel iron oxide.

Properties dependent on surface chemistry impacted by unintended NP structural attributes

It is of great interest to determine how the ligands impact the properties of NPs. However, multiple parameters are changed in order to change the ligands, which results in contradictory reports in the literature.[27,41] For spinel iron oxide, Roca *et al.* reported no spin canting at the NP surface due to the presence of oleic acid compared to NPs that were ligand free.[27] The NPs were extremely different, however, with the NPs with oleic acid made by thermal decomposition in organic solvent and NPs that were ligand free

were made by co-precipitation. [27] Other investigators showed that oleic acid promotes an appreciable amount of spin canting at the surface.[41] In another example, ZnS crystallinity was linked to the NP ligand shell but the mechanism of formation for NPs made with different ligands were different from each other.[12] Without a better understanding of the co-dependence of synthesis, structure and properties, even with many studies to investigate the effects of a specific structural feature, little can be concluded.

Properties dependent on precursor impacted by unintended NP structural attributes

Precursor ligands, precursor metal cation identity and precursor oxidation state can be used to tune reactions to form NPs. For example, Hard-Soft Acid-Base Theory can be used to predict reactivity of NP precursor.[95] The reaction can be controlled by using a precursor salt that is weakly coordinated to promote fast nucleation and ligands that bind tightly to promote slow growth.[95] By tuning precursor reactivity more control can be achieved over the NPs formed.

In a recently reported synthetic method for metal chalcogenides the authors were able to tune the reactivity of the reaction to make NPs of different sizes and compositions.[96] This approach takes advantage of trends in both precursor ligands and cation metal identity.[96] Different metal oleates were reacted with substituted thioureas in order to form metal chalcogenides of varying composition.[96] Principles of physical organic chemistry were used in order to design reactants that would have the appropriate reaction rates to form NPs with narrow dispersities and uniform morphology.[96] Depending on the reactivity of the metal oleates (Pb > Cd > Zn reactivity) thioureas can be used to complement the metal reactivity.[96] Thioureas with electron withdrawing

substituents, with fewer substituents and with increased steric bulk exhibited increased reaction rates.[96] The control seen by changing the reactivity of ligands and cations illustrates how much the reaction medium can impact the final product formed.

One of the greatest synthetic challenges in materials chemistry is the ability to control the structure of complex nanomaterials that are composed of multiple metal cations.[56] For example, CZTS NPs are a promising material for solution processed solar cells but the synthesis of CZTS is plagued by poor quality materials with a multitude of defects including phase segregation, disorder and vacancies.[56] One predominant issue with the synthesis of CZTS is that the metal precursors used to make CZTS nucleate and decompose at different rates and temperatures.[21,97] Lack of understanding on the nanoscale structure and synthesis of CZTS has caused uncertainty regarding the materials properties when reduced to the nanometer size range.[21] For instance, optical properties of CZTS have been shown to be size-dependent, however, thorough investigation of other structural features like Cu and Zn disorder and Sn vacancies was not performed, although they are known to impact optical properties as well.[6,21] In order to exploit the properties and promise of complex materials there needs to be greater control and understanding of the reactivity of reaction components.

In chapter four of this dissertation, continuous growth and *in situ* PDF were used to determine precursor impact on NP formation. By using continuous growth, the reactions could be kept constant except for the precursor. The two precursors tested were Fe (II) and Fe (III) oleate. It was found that Fe (III) oleate was a much better esterification catalyst than Fe (II) oleate, producing three times more ester over 32 minutes. Analysis of *in situ* PDF data revealed that the growth mechanism between the

two precursors also varied. Fe (II) oleate formed as a mixture of wüstite and spinel iron oxide while Fe (III) oleate formed as the spinel structure. Understanding that the reactivity of the two precursors is different allows for insight into the structures formed in spinel iron oxide NPs beyond the continuous growth synthesis.

Insight in chapter four of this dissertation is gained in the behavior of other synthetic methods under reducing conditions. The low reactivity of Fe (II) oleate to esterify likely leads to a greater amount of radical reactions in the formation of spinel iron oxide in reducing conditions at high temperature, causing defects that impact the properties of NPs. By using general synthetic methods with advanced characterization techniques, the complexity of NP formation can be appreciated and incorporated into rational design of NPs.

Outlook

While there is currently much confusion about how NP structural attributes relate to the properties due to the presence of unintended structural features, new synthetic methods and characterization techniques are allowing for increased insight. The main challenge in synthesis of NPs is the lack of reproducibility and the effects of intermediates that introduce undesirable impurities or structural defects in synthetic techniques. In order to increase reproducibility, an understanding of how synthetic parameters impact nucleation and growth is needed. With greater understanding of the reactions occurring in NP formation, a rational design of NPs will be possible.

New synthetic techniques that are more general and selective, like continuous growth, paired with Total X-ray Scattering techniques, will allow for understanding of how synthetic parameters effect products. The importance of precursor oxidation state in

the formation of spinel iron oxide has been determined by *in situ* analysis of Total X-ray Scattering data collected during continuous growth. In order to design NP syntheses, more work on how systematic changes of parameters impacts NP formation will be needed. The work reported in this dissertation is the first in, hopefully, a large number of studies that probe reaction parameters systematically using continuous growth, like reaction type, precursor (precursor oxidation state, precursor cation identity, precursor ligand), NP nanoscale structure and temperature in order to understand the production of nanomaterials.

Overview of Dissertation

Chapter two of this dissertation is titled *Insights into the Magnetic Properties of Sub-10 nm Iron Oxide Nanocrystals through the Use of a Continuous Growth Synthesis* and has been previously published in Chemistry of Materials.[7] Chapter two details the synthesis of spinel iron oxide NCs between 3-10 nm in diameter and the magnetic properties of the NCs. This work was co-authored by Susan R. Cooper, L. Kenyon Plummer, Alexia G. Cosby, Philip Lenox, Albrecht Jander, Pallavi Dhagat, and James E. Hutchison. I am a co-first author on this co-authored material. Kenyon Plummer and I performed the experiments and analyzed the data in this work. Kenyon and I also wrote the manuscript in collaboration with James Hutchison. Alexia G. Cosby made many nanoparticles and characterized them for this work. The magnetization curves were collected by Philip Lenox, Albrecht Jander and Pallavi Dhagat at Oregon State University. Kenyon and I were involved closely in the analysis of the magnetization curves.

Chapter three of this dissertation is titled *Size-Dependent Structural Features and Enhanced Reactivity of Sub-10 nm Iron Oxide Nanocrystals.* Chapter three details the structural analysis of spinel iron oxide NCs made by the method in chapter two, by Pair Distribution Function analysis of Total X-ray Scattering data. This work was co-authored by Susan R. Cooper, Randall Candler, Alexia G. Cosby, Darren W. Johnson, Kirsten M. Ø. Jensen and James E. Hutchison. I am a first author on this co-authored material. I was the lead in this project and coordinated making all samples with my two undergraduates, Randall Candler and Alexia G. Cosby. I collected Total X-ray Scattering data at Argonne National lab Advanced Photon Source with Kirsten M. Ø. Jensen and analyzed the data with her advisement. I wrote the manuscript with Darren W. Johnson, Kirsten M. Ø. Jensen and James E. Hutchison.

The title of chapter four of this dissertation is *In situ study total scattering study of the formation of iron oxide nanoparticles*. Chapter four details the *in situ* analysis of Total X-ray Scattering data by Pair Distribution Function Analysis of spinel iron oxide NCs made by continuous growth. This work is co-authored by Susan R. Cooper, Kenyon L. Plummer, Samantha L. Young, Meredith C. Sharps, Alexia G. Cosby, Randall Candler, Darren W. Johnson, James E. Hutchison and Kirsten M. Ø. Jensen. I am a first author on this co-authored material. I was the lead in this project and coordinated making samples for *ex situ* analysis with my co-author Kenyon L. Plummer and my two undergraduates, Randall Candler and Alexia G. Cosby. I collected total X-ray scattering data at Argonne National lab Advanced Photon Source with Kirsten M. Ø. Jensen, Samantha L. Young and Meredith C. Sharps. I wrote the material with Kenyon L.

Plummer, Meredith C. Sharps, Darren W. Johnson, Kirsten M. Ø. Jensen and James E. Hutchison.

Chapter 5 of this dissertation will be a conclusion and detail future directions for the work in this dissertation. This is co-authored with my advisors, Darren W. Johnson, James E. Hutchison, who advised the writing of this material.

CHAPTER II

INSIGHTS INTO THE MAGNETIC PROPERTIES OF SUB-10 NM IRON OXIDE NANOCRYSTALS THROUGH THE USE OF A CONTINUOUS GROWTH SYNTHESIS

This chapter was published previously in the following citation:

Cooper, S. R.; Plummer, L. K.; Cosby, A. G.; Lenox, P.; Jander, A.; Dhagat, P.; Hutchison, J. E. Insights into the Magnetic Properties of Sub-10 Nm Iron Oxide Nanocrystals through the Use of a Continuous Growth Synthesis. *Chem. Mater.* **2018**, *30*, 6053–6062.

Introduction

The size-dependent magnetic properties of nanocrystals (NCs) such as iron oxide have been widely studied and harnessed for use in technologically important applications.[1–5] Changes in the magnetic properties occur most frequently in samples below 20 nm, where superparamagnetic behavior emerges.[6] For NC systems in general, Auffan *et al*. stated that NC properties are more likely to deviate from bulk when core diameters drop below 15 nm.[7] At the smallest sizes, it has been suggested that the properties of iron oxide NCs are strongly influenced by variations in the local structure of the surface and core in the form of vacancies, structural phase differences, and atomic disorder, in addition to effects solely induced by NC diameter.[8–10] For example, the

magnetic properties of iron oxide are influenced by the phase (the spinel phases (magnetite and maghemite) and more reduced forms[11–14]) and surface structure (defects, vacancies, and disorder),[9,15–20] as well as the size[21–24] and shape[25–28] of the core. Each of these structural features needs to be individually, and independently, tuned to attain optimal performance in applications. For instance, magnetic hyperthermia treatment requires NCs with uniform sizes (narrow dispersity) within the range of 10-20 nm that have high saturation magnetization (M_S) and high anisotropy.[29,30] For ideal T1 MRI contrast agents, small NCs (<3 nm) with a large number of unpaired spins and a small magnetic moment are needed.[23] NCs for water purification must be small to have a large increase in surface area to adsorb contaminants as well as having a sufficient magnetic moment for separations.[9,31] In cases where a high saturation magnetization is required, each atomic layer of material added to the NC must contribute as many aligned spins as possible.

The influence of structure on the magnetic properties of iron oxide NCs has been investigated in the past but there are wide disparities in the values of saturation magnetization (M_S) reported for different NCs in the sub-10 nm size range. For example, M_S values reported for 5 nm spinel iron oxide NCs range from 17 Am^2/kg [15] to 82 Am^2/kg[32] indicating that diameter is not the only structural feature influencing the values of M_S for spinel iron oxide NCs. It has been suggested that ligand shell,[16,17] surface roughness,[18] phase (maghemite, magnetite, and wüstite),[24,33,10,34,35] and core structural disorder[12,33,36–38] can also influence the M_S values. The use of different synthetic methods to access samples with different core sizes further complicates the interpretation of size-

dependent M_S data because different reaction conditions influence the atomic-level core and surface structure in addition to core size.

Most studies conclude that M_S values for small NCs are lower than the bulk values and decrease with size,[15,16,18,21,23,26,34,39–44] although there are some reports that suggest bulk values for NCs as small as 5 nm.[17,32,45] The loss of magnetically interacting neighboring atoms, often referred to as broken exchange bonds, at the surface of the material is widely thought to cause the spins at the surface to misalign with the core and no longer contribute to the magnetization of the material.[15,46,47] When the NCs are small, the large surface-to-volume ratio causes these canted spins to be a larger percentage of spins in the NC and therefore reduces the M_S. For example, the first layer of Fe-O-Fe (~ 0.3 nm thick) of a 10 nm NCs is 17% of the NCs volume, whereas the same shell thickness would comprise nearly 40% of the volume in a 4 nm NC. The reported values of the thickness of the magnetically disordered layer vary widely in the literature from more than a nanometer thick,[15,47] to some reports suggesting no surface layer at all.[17] Taken together, these large disparities in values of M_S and differences in the thickness of a magnetically disordered layer, for NCs of same size, suggest that the differences may be due to differences in core or surface structure induced by different synthetic methods.

Reaction conditions have been shown to have significant influence over the magnetic properties for spinel iron oxide NCs. For example, surfactants and ligands can change the ligand shell and therefore the surface structure.[16–18] Roca *et al.* observed M_S close to bulk values for 6.4 nm diameter NCs with very small canting angles measured by Mössbauer, an effect that they attributed to the oleic acid ligand shell.[17] However, other studies have shown significant decreases in M_S values for NCs containing oleic acid

ligands.[10,21,23,41,42] Reaction solvent can also affect the properties of the NCs. For example, the formation of a reduced wüstite phase that may occur during high temperature syntheses[11,42,48,49] can be mitigated by synthesizing[37] NCs in dibenzyl ether. The use of an oxidizing atmosphere during NC formation can influence the reaction products by producing spinel instead of a reduced phase.[33] Syntheses conducted at low temperatures, below the thermal decomposition temperature of the precursor, typically report the highest values of M_S for NCs that show size-dependence below 10 nm diameter, suggesting that low-temperature synthetic conditions may lead to high quality NCs.[16,40] It has been suggested that thermal decomposition reactions produce radical species[10,49–52] that exhibit less selective reactivity. Despite the numerous reports on the magnetic properties of iron oxide NCs, it is difficult to draw conclusions regarding the size-dependence because many reports have very few NCs below 10 nm in diameter to compare.

To understand the influence of NC size on magnetic properties, we need access to a series of sub-10 nm NCs with incremental sizes. We reasoned that a lower temperature, continuous growth synthesis could provide a more selective reaction pathway to produce NCs with sub-nm size increments, employing the same reaction conditions for each size in the series. A lower temperature synthesis would reduce or eliminate the production of highly reactive intermediates and minimize the risk of introducing strain-producing defects. Strain-producing defects include grain boundaries, antiphase boundaries, twin planes and stacking faults. Further, the use of a single, defined reaction pathway will be more likely to result in controlled and uniform NC growth. Given the strong dependence

of properties on reaction conditions,[17,18,33,37] each NC in the series should be made under the same synthetic conditions (additives, solvent, atmosphere and temperature).

Herein we report the M_S and magnetic size of a series of spinel iron oxide NCs produced via a continuous growth method that provides access to small (core diameter <10 nm) NCs with specifically defined diameters. A new, lower temperature (230°C) method, involving a selective catalytic esterification mechanism, allowed for continuous growth and the production of closely sized increments all synthesized under the same reaction conditions.[53,54] By simply varying the amount of precursor added, the size can be controlled to within a single atomic layer, producing a series of eight distinct size populations evenly distributed between 4 and 10 nm in diameter. Structural characterization suggests that the NCs possess the spinel structure with high maghemite content. The M_S values for the members of this series show a clear size-dependent trend. Further, the M_S values are higher than comparably sized NCs produced by other synthesis methods, suggesting that the continuous growth process introduces fewer strain-producing defects, increasing the effective magnetic size of the NCs.

Results and Discussion

Synthesis and characterization of NCs

To target the NCs needed for this study, we employed a continuous growth method that our group has established for the synthesis of metal oxides in which a metal oleate precursor is slowly dripped into hot oleyl alcohol.[53,54] We observed previously that the metal center catalyzes the esterification of the oleate with oleyl alcohol at relatively low temperatures developing metal hydroxyl species *in situ* that then condense to form

NCs.[53] Given the success of this approach for producing single crystal NCs with controlled composition and structure with near atomic-layer precision in indium oxide,[54,55] we anticipated that it would work well to produce the series of iron oxide NCs needed for this study. We found that as we added iron oleate precursor slowly to the reaction flask containing hot oleyl alcohol, NCs grow continuously and maintain narrow size dispersion. Since the size is varied by the addition of precursor into the reaction vessel, the temperature, solvent and ligand shell are constant for all synthesized sizes. Addition of precursor also allows for a layer of metal oxide to be added at a time, allowing the synthesis of any diameter NC desired.

Iron oxide NCs were synthesized by adding an iron oleate precursor at a slow injection rate (0.17 ml/min) into oleyl alcohol at 230°C under a constant flow (120 mL/min) of nitrogen. In order to ensure that there was always an excess of oleyl alcohol in the flask, more oleyl alcohol was added to the reaction after every 1 mmol of iron oleate. NCs were sampled for analysis at intervals throughout each synthetic trial by removing aliquots of the reaction mixture and allowing the samples to cool rapidly to room temperature. The sizes of the isolated samples were determined by small angle x-ray scattering (SAXS), as seen in Figure 1. Transmission electron microscopy (TEM) was used to determine the morphology of the NCs of a select number of samples (Figure 2A-D). High resolution TEM (HRTEM) was used to determine the crystallinity and confirm low defect concentration in the NCs as seen in Figure 2E-H. The structure of the NCs was analyzed by powder x-ray diffraction (XRD) and Rietveld refinement as seen in Figure 3A and Figure S4-S6. The percentage of the magnetite and maghemite phases of

the spinel structure in the NCs was determined by near-IR optical absorbance,[56] as seen in Figure 3B.

Over the course of the synthesis, SAXS analysis showed that the NCs grew as more iron precursor was added to the reaction (shown in Figure 1 and Figures S1 and S2). The size of the NCs can be tuned from about 4 to 10 nm by varying the amount of precursor added to the reaction. During the addition of precursor, the dispersities remained low (below 15%) for all but the smallest sample size (Figure 1A and Table S1). The NC core volume (or molecular mass) exhibited linear growth with respect to the amount of iron precursor added to the reaction flask (Figure 1B), suggesting a living growth mechanism.[57] Linear growth enables predictable and reproducible NC diameters from synthesis to synthesis. Reproducibility was verified by completing three separate syntheses which all gave similar NC sizes and dispersities (Figure S1). Variation in final size and growth rate is a result of different number of nuclei being formed during the nucleation event (see discussion in SI following Figure S1). In our synthesis size is controlled by the precursor added to the reaction rather than the nucleation event alone (as is the case with one-pot heat up methods) enabling isolation of samples from 4-10 nm from each batch even if nucleation step is different.

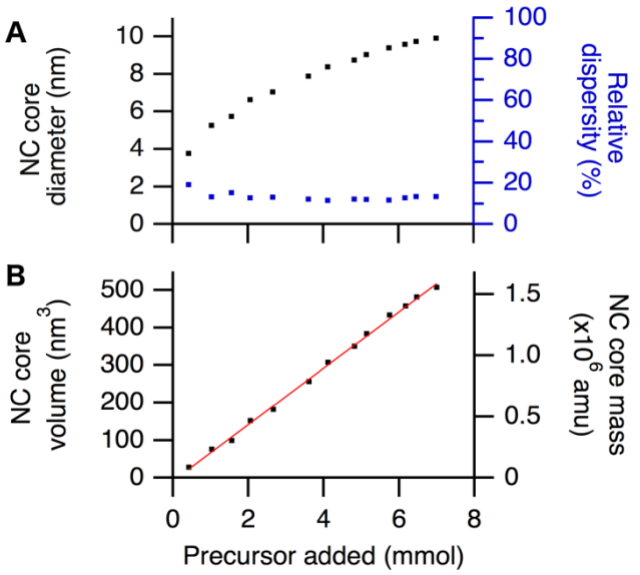

Figure 1. Size analysis of NCs by SAXS throughout a slow injection reaction showing NC diameter (A), and volume and mass of the NC core (B) plotted as a function of precursor added to the solution. Linear regression analysis of volume vs. precursor resulted in a linear relationship (R^2=0.998). In repeated SAXS measurements, the standard deviation of the mean size is less than 0.7 Å.

TEM images (Figure 2A-D) were analyzed to determine the morphology of the NCs. Figure 2 shows a spherical morphology over this size range for all NCs throughout the synthesis. We examined samples across the size range with HRTEM to determine the crystallinity of the NCs throughout their growth. The HRTEM images show lattice fringes that extend through the entirety of the NC, suggesting NCs are single crystal (Figure 2E-H). Fast Fourier Transform (FFT) was performed on HRTEM images to further confirm that NCs are single crystalline. Indexed FFT patterns are included in Figure S3.

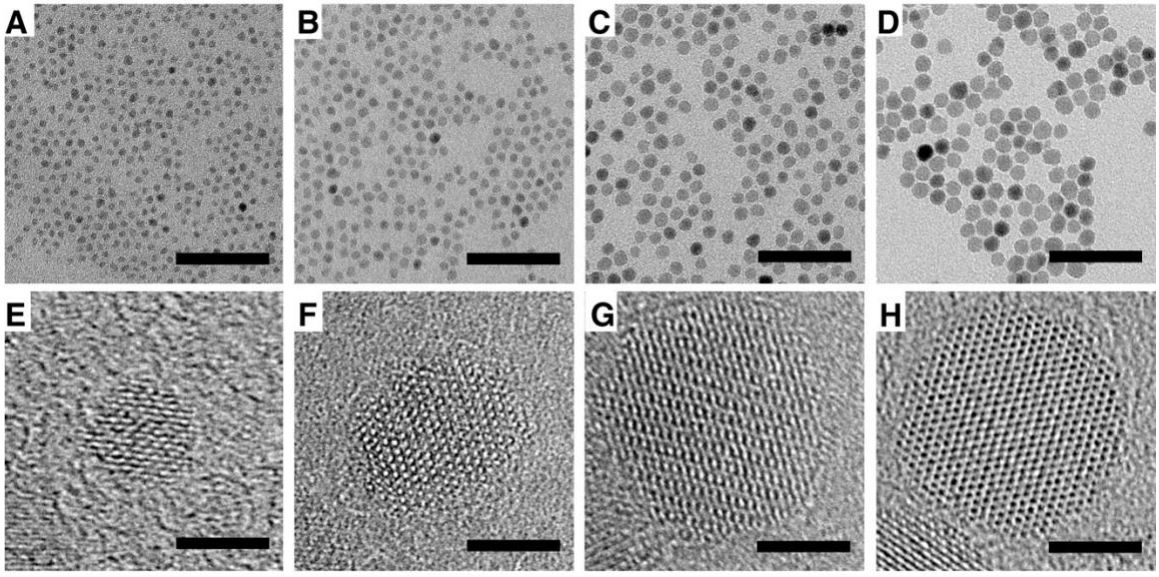

Figure 2. TEM and HRTEM micrographs demonstrating morphology and crystallinity of NCs with sizes (determined by SAXS) of 3.9 +/- 0.6 nm (A, E), 5.1 +/- 0.7 nm (B, F), 6.6 +/- 0.6 nm (C, G), and 8.0 +/- 0.8 nm (D, H). Scale bars are 50 nm for top row and 3 nm for bottom row.

XRD patterns for three representative NC samples across the synthesized size range (Figure 3A) were analyzed by Rietveld analysis (Table S2-S4 and Figure S4-S6) to determine the phase of the NCs. Figure 3A shows the spinel crystal structure of iron oxide is present and are free of peaks associated with the wüstite phase. The Rietveld analysis fits and refined parameters are included in the supporting information.

Spinel iron oxide may contain two phases; maghemite (ɣ-Fe_2O_3) and magnetite (Fe_3O_4) where the difference in the two phases is the oxidation state of iron in the structure.[58–60] Magnetite contains both Fe^{2+} and Fe^{3+} cations whereas maghemite contains only Fe^{3+} and has some vacancies in sites where Fe^{2+} occurs in the octahedrally coordinated sites of the magnetite phase.[59] The maghemite and magnetite phases of the spinel iron oxide structure are hard to elucidate with XRD because there are only subtle differences between the patterns for the two phases and these become less pronounced

from the broadening of the peaks in the small NC sizes.[10] We employed near-IR optical absorbance spectroscopy (Figure 3B) to determine the percentage of magnetite and maghemite in each NC sample. For samples containing magnetite, there is a strong absorbance from 800-2000 nm due to the charge transfer from Fe^{2+} to Fe^{3+} that can be used to quantify the amount of magnetite in spinel iron oxide NCs.[56] Spectra were normalized at 400 nm where an isosbestic point for magnetite and maghemite occurs. Using a theoretical absorbance cross section for 10 nm magnetite NCs calculated by Tang *et al.*,[56] a percentage of magnetite is determined from the ratio of the absorbance at 1450 nm to that expected of pure magnetite (0.39 units as scaled in Figure 3B). The percentage of magnetite in the NCs increases from 2% to 26% as the core size increases from 3.9 nm to 8 nm (Table S5).

Magnetic properties

Access to this unique series of well-defined NCs all produced by the same synthesis, affords an opportunity for in-depth investigations regarding the size-dependence of the magnetic properties. Magnetization curves were acquired at room temperature for eight different samples (Figure S8) with core sizes ranging from 3.9 to 8 nm using a vibrating sample magnetometer (VSM). Samples were dispersed in KBr and pressed into pellets for analysis. The amount of iron oxide in each pellet was quantified using inductively coupled plasma optical emission spectroscopy (ICP-OES). The magnetic response of a pure KBr pellet was subtracted from the magnetization curve obtained for each pellet.

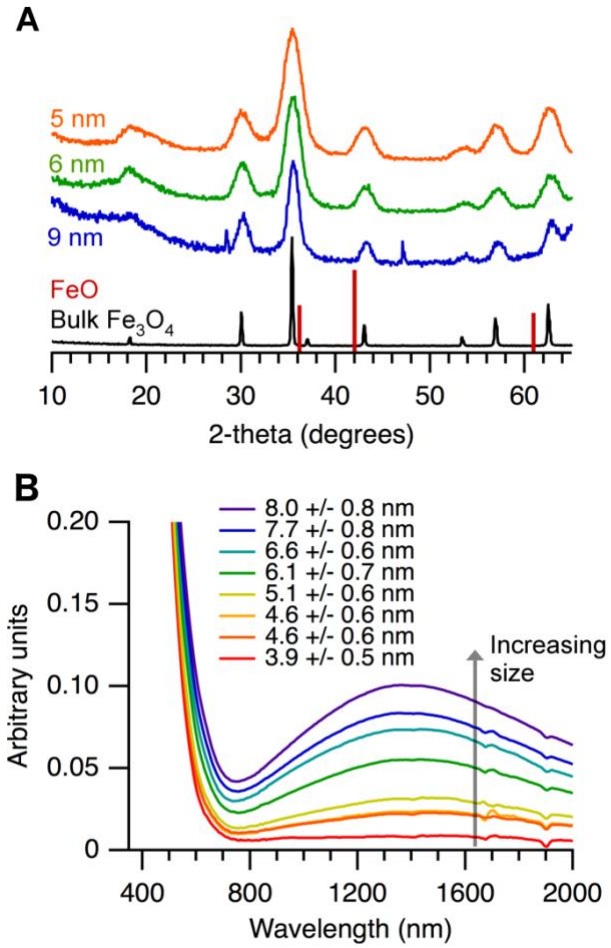

Figure 3. Structure and phase analysis of NCs throughout a slow injection reaction. Powder XRD patterns (A) of several sizes showing a narrowing of peaks as the NCs increase in size. The peaks at 28˚ and 47˚ in the blue pattern (9 nm sample) are due to the substrate. A pattern of bulk magnetite (black) and calculated wüstite (red lines) are shown at bottom of the stack for reference. Normalized optical absorbance spectra (B) of NC solutions were acquired to determine the maghemite/magnetite content. Larger NCs have greater absorption centered at 1450 nm demonstrating greater magnetite content.

M_S was determined for each sample by fitting the magnetization curves to the Langevin equation (eqn. 1).[33,61]

$$m(B) = V_{ICP} M_S \left[coth\left(\frac{mB}{k_B T}\right) - \frac{k_B T}{mB} \right], \qquad (1)$$

In equation 1, $m(B)$ is the moment of the sample measured by VSM at an applied field, B; V_{ICP} is the total volume of iron oxide in the sample determined from ICP-OES

measurements; M_S is the saturation magnetization of the iron oxide in the sample; and m is the moment of a single NC. The measured magnetization curves were normalized to the M_S values provided by the fit so that the curves could be readily compared to one another. The individual magnetization curves and the fits to the Langevin equation can be found in Figure S7.

The normalized magnetization curves are shown in Figure 4. Each curve passes through the origin: there is no remnant magnetization at zero field and no hysteresis for any of the samples. The curves suggest that all the NCs exhibit superparamagnetic behavior because they completely demagnetize in the absence of a magnetic field at room temperature. By inspection, it is also clear that the NCs exhibit size-dependent magnetic behavior. The smaller NCs have smaller magnetic moments than the larger NCs and require greater fields to maintain magnetization against thermally-induced demagnetization. As a result, the magnetic susceptibility (slope of curves through zero field) for smaller NCs is lower than for larger NCs.[61]

The M_S values for the NCs trend with size across the series (Figure 5, Table S5), with larger NCs having a larger M_S and smaller NCs having a reduced M_S as might be expected based upon literature reports.[21,23,43] The value measured for 8.0 nm NCs was 78 Am^2/kg, decreasing to 55 Am^2/kg for NCs with a diameter of 3.9 nm. These values are somewhat smaller, but comparable, to the range of values expected for bulk maghemite (60-80 Am^2/kg).[62]

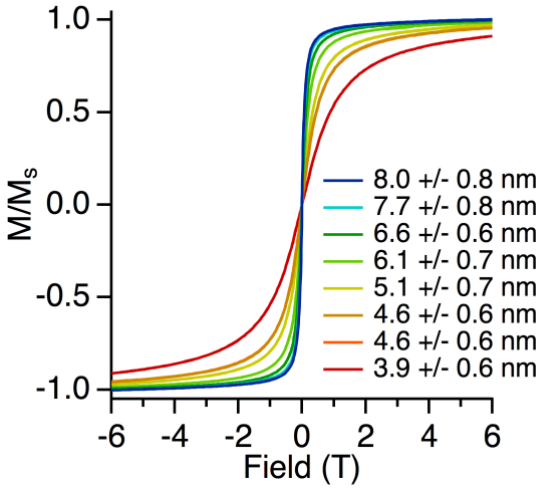

Figure 4. Normalized magnetization as a function of applied field for the eight distinct NC samples between 4-8 nm in diameter.

Figure 5 displays the M_S values obtained in this study and compares them to those from five published studies[16,21,45,41,40] that are the most comparable to our series of NCs (a more complete collection is included in Figure S9). As can be seen in the figure, our values are amongst the highest reported in the literature for NCs in this size range and show size-dependent values across this size series. Each of these studies examines iron oxide NCs with sizes under 10 nm and wherein the size dispersions of each sample are below 20% and are reported to be all spinel structure. All but one of the previously reported studies (Demortière *et al.*[21]) used the same reaction temperature, solvent, and ligands to synthesize each size in their size series. The M_S values vary by more than 100% between reports with a 4 nm NC having a reported M_S between 37 and 83 Am^2/kg (from Demortiere *et al.*[21] and Castellanos-Rubio *et al.*[45], respectively). Since the size is the same for these materials there must be other variables leading to the differences in M_S.

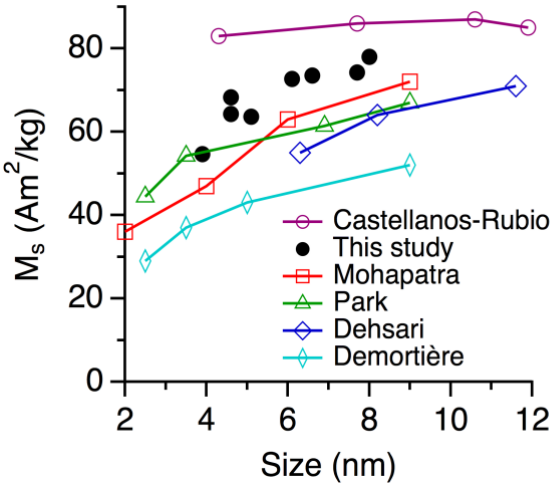

Figure 5. *Ms* plotted as a function of NC diameter up to 10 nm for this study (black circles) and other studies that examined at least three samples under ten nanometers in size with narrow size dispersion. Studies compared are from Castellanos-Rubio *et al.* (purple circles), Mohapatra *et al.*[16] (Red squares), Park *et al.* (green triangles), Dehsari *et al.* (blue diamonds), and Demortière *et al.*[21] (light blue, narrow diamonds). For a representative sample the standard deviation in the method for this measurement was 1.2 Am^2/kg—the error bars are much smaller than the size of the marker used in the graph for each sample.

The syntheses described above can be grouped into three categories: high temperature syntheses in the presence of an oxidizing agent (air or dibenzyl ether), high temperature syntheses in the presence of esterification reagents (oleic acid and amine or alcohol) and low temperature syntheses (230˚C and under). The lowest values for size-dependent *Ms* in Figure 5 were synthesized by thermal decomposition of an iron oleate precursor in air (Demortère *et al.*[21]). Even though these magnetic data were collected at 5K (which yields higher *Ms* values than those collected at 300K) they were still among the lowest values. The next highest *Ms* values shown in the figure are for NCs synthesized by a high temperature reaction of an iron precursor in the presence of dibenzyl ether and esterification reagents, for example oleic acid, oleylamine and 1,2 hexadecandiol (Dehsari *et al.*[41]). Even higher *Ms* values were obtained for NCs

synthesized at much lower temperatures: for example at 200°C (Mohapatra *et al.*[16]) and 95°C (Park *et al.*[40]). Castellanos-Rubio *et al.*[45] reported near bulk M_S values but also showed no size dependence, in contrast to 13 other studies (Figure S9) in the same size range. The major difference in their study[45] was the use of an Fe^0 precursor that often produces iron NCs,[63,64] but carried out in the presence of dibenzyl ether. Their results[45] also contrast with Dehsari *et al.*[41] who used dibenzyl ether as a solvent, as well, but with an Fe^{3+} precursor, producing NCs that have values well below the bulk M_S values. Our own results that show higher M_S values compared to most literature examples were produced using esterification reactions and lower reaction temperatures.

The trend in the size-dependent M_S values shown in Figure 5 suggests that differences in reaction conditions might be the cause of the variations in properties of the resulting NCs. Given that the NCs represented here have comparable sizes, similarly narrow size distributions, and uniform morphologies, the differences in magnetic properties are likely the result of different amounts of strain-producing defects in the NC cores. Strain-producing defects within the NC structure are known to decrease the effective M_S,[12,33,37,65,66] and each of the three categories of synthetic conditions discussed above are expected to influence the number of strain-producing defects in the cores of the NCs to different degrees. Synthesizing NCs in the presence of oxygen[33] or dibenzyl ether[37] prevents the formation of reduced iron oxide that result in strain-producing defects even after oxidation to the spinel structure.[12] The use of starting materials that can potentially undergo esterification and amidification[53,67–70] can facilitate metal oxide formation through defined reaction pathways that prevent the formation of highly reactive species generated in radical reactions (i.e. thermal decomposition) thereby,

reducing the number of strain-producing defects. The reactions carried out at lower temperatures, which showed the best magnetic properties in prior studies,[16,40] may produce the fewest strain-producing defects because the approach avoids the highly reactive intermediates and reduced forms of iron oxide produced during thermal decomposition.

Our synthesis likely results in reduced numbers of strain-producing defects because it employs a defined esterification mechanism and is performed at a lower temperature. Furthermore, it involves slow injection of precursor that likely slows NC growth rate compared to the rapid growth found in methods where all precursor is added at once. Rapid growth may trap strain-producing defects within the crystal while relatively slow growth during slow injection may limit the number of strain-producing defects.

The larger values of M_S found in our NCs prompted us to further analyze the volume of each NC that contributes to the magnetization by determining the effective magnetic size for the NCs in each sample. The magnetic size can by derived from the Langevin equation and is the portion of the core material within the NC that has an M_S of the bulk material.[26,30,54,55,61] To obtain the magnetic size, we set $m = M_D * \frac{\pi}{6} {D_C}^3$ in Equation 1 where M_D is the saturation magnetization of bulk maghemite (76 Am^2/kg or 372 kA/m) and the term $\frac{\pi}{6} {D_c}^3$ is the volume of the magnetically active core where D_c is the diameter. We chose to use the bulk saturation magnetization value of maghemite because our NIR studies showed that the NCs are primarily maghemite. We assumed a lognormal distribution of magnetic diameter.[61] Figure S10 illustrates the trend obtained

if we calculate an M_D based upon the percentage of each phase measured by near-IR for each NC size. Additional details are provided in the Materials and Methods section.

The magnetic sizes determined by fitting are compared to the physical size measured by SAXS analysis in Figure 6. The magnetic sizes are nearly identical to the physical sizes, which implies that nearly all of the core material contributes fully to the magnetic properties of the NC, leading to the higher values of M_S compared to the literature examples. If we assume that most of the inactive material resides at the surface,[46] our results suggest that there is only a very thin non-magnetic shell. Across the series, there are no significant differences in the thickness of the shell. The slight trend toward larger magnetic sizes at larger physical sizes may be due to small increases in magnetite content at the larger sizes.

The larger magnetically active volume in our NCs suggests that these NCs possess a very thin non-magnetic surface layer and have few strain-producing defects. Our evaluation suggests that the disordered layer is less than 0.2 nm thick which would restrict the magnetic disorder to the iron atoms at the surface of the particle. Reductions in M_S from bulk values reported within the NC literature are typically attributed to a magnetically disordered surface layer, and the reported magnetically disordered shell thicknesses is between 0.35-1.0 nm thick.[15,18,21,47,71] The fact that the magnetic size is nearly the physical size within our series suggests that these larger thicknesses may be due to strain-producing defects within the NCs as opposed to larger disordered surface layers. A close examination of our NCs by HRTEM shows single crystal spherical NCs with few NCs exhibiting strain-producing defects. Thus, it seems likely that the increased M_S values are the result of the fewer strain-producing defects introduced because of the

condensation-based reaction mechanism, slower growth rate and lower temperature offered by the slow injection synthesis.

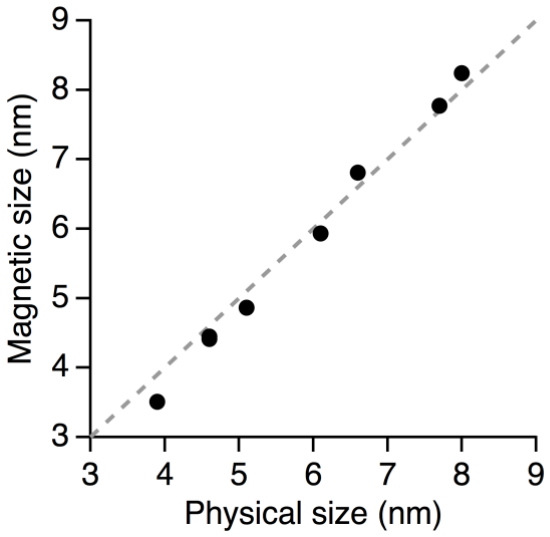

Figure 6. The effective magnetic size from Langevin function fit plotted as a function of physical size determined by SAXS where the gray dashed line is y=x.

Comparison of our synthetic method to alternatives reported in the literature offers new insight into how to design syntheses that will produce NCs that are defect free for the study of properties and structure in NCs less than 10 nm in diameter. The attributes of our synthesis ensure the size and size induced structure are what is being studied, not artifacts introduced as a result of variations in synthetic methods. Lower-temperature and slow growth through a single defined growth mechanism, are likely responsible for the high degree of crystallinity and enhanced magnetic properties of these NCs. Such a mechanism contrasts with thermal decomposition methods that produce NCs that are known to produce a number of byproducts.[49–52] Thermal decomposition reactions produce a variety of organic radicals that have a multitude of competing and accessible reaction pathways resulting in a large number of different products including H_2, CO,

CO_2, alkenes, ketones, and esters.[49,50,72] It might be expected that there would be an increased incidence of strain-producing defects in NCs produced by lower selectivity shown in thermal decomposition pathways. In fact, the other size series in this size range that have M_S values approaching ours and size dependence produced NCs at low temperatures[16,40] where radical mechanisms are not likely involved. Based upon these findings taken together, it seems that a reasonable strategy to produce defect-free NCs is to identify and use synthetic methods that avoid radicals or other highly reactive species, have slower growth rates and keep a low temperature. In this way, it may be possible to more effectively tune and tailor the properties of nanomaterials.

Conclusions

A series of sub-10 nm spinel iron oxide NCs, produced using a continuous growth method, were used to study fundamental questions relating nanoscale structure to size-dependent magnetic properties. This series of NCs is ideal for these studies because size is the only physical characteristic that varies during this continuous growth synthesis. The NCs show a decrease in M_S with a decrease in the diameter of the NCs as has been shown in other studies; however, these NCs have higher M_S values than NCs produced in the same size range by other methods. The magnetic size was approximately the same size as measured by SAXS and TEM indicating a much thinner magnetically dead layer than was previously thought to be present on NCs. This analysis changes our understanding of the nanoscale structure and properties of spinel iron oxide NCs by demonstrating that the magnetically dead layer can, in fact, be much thinner than previously reported and maintain size-dependent magnetic properties across the range. We believe that the high crystallinity, and thus enhanced magnetism, of the NCs measured in this study is due to

the attributes of the slow injection synthesis (condensation reaction pathway, slow growth, and relatively low synthesis temperature). Our results further imply that relatively low temperature syntheses may be a strategy to avoid strain-producing defects.

Magnetic and adsorptive properties of small iron oxide NCs have long been of interest to environmental, health, and physics communities, but synthetic approaches to adequately study structure-property relationships have not existed. This slow injection synthesis method is a facile way to produce high quality NCs that can be used by physics, biology, and environmental science fields in order to probe and exploit promising size-dependent properties. For instance, Mössbauer studies using these high quality NCs could be done to examine the origins of these size-dependent magnetic properties. We expect that continuous NC growth will be a useful, transferable strategy to produce other NCs to examine the influence of size on the properties of those materials.

Materials and Methods

Materials

Iron (II) acetate (99.99%), technical grade oleic acid (90%) from Sigma Aldrich was used to make the iron oleate precursor. Magnetite powder from Aldrich (99.99% trace metals basis) used for bulk magnetite XRD trace. Technical grade oleyl alcohol (85%) from Alfa Aesar was used as the solvent in the synthesis of spinel iron oxide NCs.

Synthesis

To make the precursor, 6 mmol of iron (II) acetate (1.04 g) is stirred in a 20 mL vial with a septum with 12 ml of oleic acid under a flow of N_2 heated in an oil bath to 150°C for 1 hour. The oleyl alcohol (12.5 mL) is heated in a 100 mL three neck flask to 230°C under a flow of N_2 of 120 mL/min. The three-neck flask has three septa: one that

delivers N_2 through a needle, one holds a larger gauge needle to allow water to escape and the third holds a thermocouple that is connected to a heating controller with a heating mantle. The liquid is magnetically stirred vigorously with a stir bar. One mmol of the precursor is added to the oleyl alcohol at an addition rate of 10 mL/hr with the use of a syringe pump and a 10 mL luer lock plastic syringe with a stainless steel 20-gauge needle. After addition of 2 ml of precursor, 3 ml of oleyl alcohol is added to the reaction. This process is repeated until 6 mmol of iron oleate is added to the reaction. The oleyl alcohol and NC solution is heated at 230°C for an additional 20 minutes after all precursor is added. The reaction is cooled under a flow of N_2 and then was put into a 50 mL centrifuge tube and washed with ethanol in order to precipitate the NCs. The samples are washed with acetone and centrifuged at 7000 rpm for 20 min. The NCs are then dispersed in toluene and centrifuged once at 3500 rpm for 5 min to remove any remaining insoluble material.

To study the growth of the NCs, a 1 mL gas tight syringe with a 20-gauge stainless steel needle was used to remove 0.3 mL of reaction solution at various points in the addition. The sample was then put into a 15 mL centrifuge tube and allowed to cool to room temperature. These samples were also washed in the same way by centrifugation in acetone and were dispersed finally in toluene and centrifuged.

Physical characterization

Transmission electron microscopy images were taken with an FEI Tecnai G2 Spirit microscope. 400 mesh copper TEM grids (Ted Pella) were prepared by dip-coating in dilute solutions of NCs. High resolution TEM was acquired with FEI's Titan 80-300

kV microscope. Diameter was determined from particle area in TEM images using FIJI[73] software to corroborate the NC size with SAXS.

Small angle x-ray scattering patterns (SAXS) were acquired using the SAXSess mc^2 from Anton Paar with work up of SAXS data by Irena software package to determine NC core size, dispersity and volume fraction.[74] Modeling was done using a Gaussian distribution with a spherical form factor and a dilute system structure factor. For samples that were magnetically characterized, a lognormal distribution was used in modeling so that the physical and magnetic sizes could be compared directly. A background was refined in order to account for fluorescence of iron. X-ray diffraction patterns were procured with a Rigaku SmartLab diffractometer using Cu Kα radiation and a diffracted beam monochromator to eliminate background iron fluorescence. Near-IR measurements were performed on dilute (~1 mg/mL) dispersions of NCs in toluene in 3 mm path length quartz cuvette using PerkinElmer Lambda-1050 UV/Vis/NIR spectrophotometer.

Magnetic characterization

The magnetic properties of the NCs were measured by room temperature vibrating sample magnetometry (VSM) using the Physical Property Measurement System by Quantum Design, Inc. The magnetic moment was calibrated using a 1 mm diameter Yttrium Iron Garnet Sphere with a mass of 0.0028 mg and a certified magnetization of 27.6 Am^2/kg at 0.5 T magnetic field (standard reference material 2853 from National Institute of Standards and Technology). Solid pellets consisting of the NCs in KBr, a non-magnetic binder, were prepared for the measurements as follows: The NC dispersion (in toluene) was sonicated for 5 minutes and pipetted into a measured quantity of KBr powder. The fluid and KBr binder were mixed by mortar and pestle for 30 minutes in

atmosphere while the toluene solvent was allowed to evaporate. The dry powder mixture was then pressed into pellets. The resulting pellets had a concentration of magnetic NCs of about 0.3% by volume. The actual amounts of iron oxide in pellets were determined after magnetic measurements by ICP-OES.

For iron quantification using ICP-OES, KBr pellets containing magnetically characterized NCs were dissolved in 2 mL concentrated HNO_3 (JTBaker Ultrex ® II ultrapure reagent) over a 48-hour period. Samples were diluted to 2% HNO_3 with nanopure water for analysis. For the calibration curve, ten iron solutions between 100 ppm and 0.01 ppm were prepared from a 1000 ppm Fe standard (ICCA) in 2% HNO_3 matrix. ICP-OES measurements were acquired using a Thermo Scientific X-Series II CCT.

To fit the VSM measurements, the magnetic diameters in the sample were assumed to have a lognormal distribution with a probability density function,

$$P(D_C) = \frac{1}{D_C}\frac{1}{\sigma\sqrt{2\pi}}exp\left(\frac{(\ln D_C - \mu)^2}{2\sigma^2}\right) \qquad (2)$$

having parameters μ and σ. Equations (1) (i.e. the Langevin equation) and (2) were fit by nonlinear regression to the VSM data, with the free parameters M_S, μ, and σ determined independently for each pellet sample. The effective magnetic size of the NC, or the mean magnetic core diameter, $\langle D_C \rangle$, is determined from the parameters of the lognormal distribution according to $\langle D_C \rangle = \exp\left(\mu + \frac{\sigma^2}{2}\right)$.

Bridge to Chapter III

In Chapter II of this dissertation, we established that nanocrystals made by the continuous growth method have increased magnetic properties compared to nanoparticles made by other synthetic methods. Increased magnetic properties indicates that NCs made by continuous growth have fewer defects. In order to learn more about the structure of these materials, we will use Pair Distribution Function analysis of Total X-ray Scattering to probe the nanoscale structure of NCs made by continuous growth over the same size range. From PDF analysis we will elucidate any trends in structure, like occupancy of iron cation sites, of NCs which do not seem to contain structure cause solely by the synthetic method.

CHAPTER III

SIZE-DEPENDENT STRUCTURAL FEATURES AND ENHANCED REACTIVITY OF SUB-10 NM IRON OXIDE NANOCRYSTALS

Portions of this chapter will be published in the forthcoming publication co-authored with Susan R. Cooper, Randall Candler, Alexia G. Cosby, Darren W. Johnson, Kirsten M. Ø. Jensen and James E. Hutchison. I was the lead in this project and coordinated making all samples with my two undergraduates Randall Candler and Alexia G. Cosby. I collected total X-ray scattering data at Argonne National lab Advanced Photon Source with Kirsten M. Ø. Jensen and analyzed the data with her advisement. I wrote the material with input from Darren W. Johnson, Kirsten M. Ø. Jensen and James E. Hutchison.

Introduction

An idealized view of inorganic nanocrystals (NCs) is that they are miniature versions of bulk structures, but with significantly higher surface-to-volume ratios.[1–3] In the case of iron oxide, at the larger end of the nanoscale (>20 nm), this is a reasonable description because the surface, the outer Fe-O-Fe shell, is only 9% of the volume of the NC. However, at the lower end of the nanoscale the surface atoms make up a much larger fraction of the NC volume, for example 40% of the atoms are exposed on the surface of a 4 nm diameter NC.[1] Furthermore, those surface atoms are under-coordinated and thus, more likely to adopt different structural motifs than that of the bulk

material.[1,3] Such structural changes are expected to have profound effects on the NC properties and reactivity, influencing, for example, the magnetic properties or the adsorption of other metals at surface sites.[4–6] We report findings counter to the conventional viewpoint that NCs are merely miniatures of bulk materials with the use of Pair Distribution Function analysis of Total X-ray Scattering data (PDF) to uncover the atomic-level structural changes that influence properties and reactivity for small (core diameter < 10 nm) spinel iron oxide NCs.

Spinel-structured iron oxide NCs adopt either of two different phases, magnetite[7] (Fe_3O_4) or maghemite[8] (γ-Fe_2O_3), depending on the iron oxidation state of the metal cations in the NC. The structure of magnetite contains Fe^{+2} and Fe^{+3} while all iron in maghemite is comprised of only Fe^{3+}.[9] Both structures contain tetrahedrally and octahedrally coordinated iron, as illustrated in Figure 1, which shows the tetragonal spinel structure $P4_32_12$.[8] Charge balance in the maghemite phase is obtained by the occurrence of vacancies on octahedral sites in the spinel structure (purple cations). It has been widely reported that small NCs are predominantly maghemite, whereas large NCs are predominantly magnetite.[10–15] Few reports describe the extent of oxidation for a series of samples under 10 nm, and the values obtained vary widely for NCs that have similar sizes.[10,12,16] For example, in one study, 9 nm NCs have been reported to be 60%[10] magnetite but in a different study, 10 nm NCs were determined to have 15%[12] magnetite. The ratio of magnetite to maghemite in spinel iron oxide NCs is important because it impacts the magnetic properties, like saturation magnetization[16–21] and the presence of a Verwey transition[22,23], as well as the conductivity of the material.[9–11,24–27]

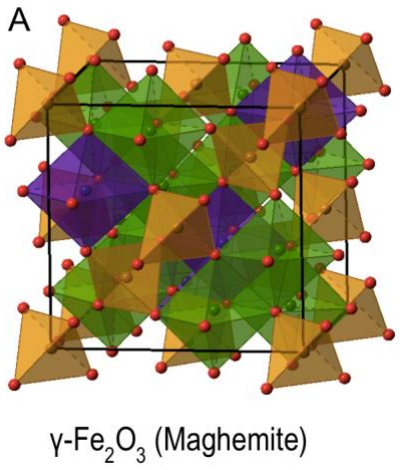

Figure 1. Unit cell of a *P4₃2₁2* spinel iron oxide crystal structure. The octahedrally coordinated cations are green and purple while the tetrahedrally coordinated cations are in gold. The purple octahedrally coordinated iron cations are the sites that are vacant in the maghemite structure.

For spinel NCs below 10 nm in diameter, it has also been reported that there are decreased occupancy at the tetrahedrally coordinated (Td) iron sites. However, few studies have been done to investigate the structure of NCs under 10 nm diameter and the presence of Td cation vacancies. Six nm diameter NCs synthesized using a co-precipitation method were found to have lower occupancy on Td iron sites on the surface of the NCs.[5] In addition, an *in situ* study of hydrothermally synthesized spinel iron oxide NCs reported lower occupancy at the Td iron sites in NCs below 6 nm in diameter.[28] They attributed the vacancies at Td iron sites to the mechanism of formation as opposed to a size-dependent feature.[28] With the small number of reports of size-dependent Td cation occupancy, it is still unknown if lower occupancy on Td iron sites persists across all small sized iron oxide NCs or only in NCs produced by aqueous syntheses known to have strain-producing defects[13,29–31] (like polycrystalline surfaces) and non-uniform morphology.

Relatively small changes in the surface chemistry of NCs can have significant influence on NC properties and may strongly influence reactivity.[5,32,33] For example, gold NCs are known to have higher catalytic activity per surface area caused by changes in surface structure.[32] Yet, determining structure in nanomaterials is difficult because the inherent lack of long-range order in the atomic structure which hinders the determination of structure from conventional techniques like powder X-ray diffraction (XRD).[34] In XRD, information in the Bragg scattering is lost due to broadening of the Bragg peaks from the short-range order of NCs.[34,35] PDF analyzes both diffuse scattering, caused by local structure, and Bragg scattering, caused by global structure.[34,35] PDF allows for the refinement of detailed structural information, including occupancy of cation sites and atomic positions.[28] However, to make conclusions on a size-dependent structural features, it must be clear that the structure is not caused by the reaction conditions.

In addition to the analytical challenges of determining atomic scale structure in NCs, the lack of methods to synthesize nanomaterials with atomic-level control of structure has limited detailed investigations.[6,36] Most synthetic methods require one to change the reaction conditions, including temperature,[10,16,18] additives[16,19,21,37–40] and solvent,[10,40–43] in order to control NC size. These variables can introduce other structural changes in addition to controlling size. [6,19,29,42,44–56] Some reaction conditions can introduce strain-producing defects such as antiphase boundaries, grain boundaries, twin planes or stacking faults.[29,44–46] A synthesis recently developed in our laboratory makes it possible to synthesize small (below 10 nm) iron oxide NCs with sub-nanometer size control through a non-aqueous continuous growth mechanism with almost no strain-producing defects.[6,43,57] The NCs are produced under the same reaction conditions with

the only difference between each NC size being the amount of added precursor to change the resulting NC diameter. Fewer strain-producing defects occur in NCs made by continuous growth due to the low temperature synthesis, enabled through a selective catalytic esterification mechanism instead of an unselective radical or hydrolysis reaction.[6]

Here, we report nanoscale structural characterization determined through PDF for uniform iron oxide NCs with 17 distinct sizes between 3-10 nm. All the samples were found to adopt the spinel structure but contained varying amounts of magnetite and maghemite. The smaller the NC core diameter, the lower the occupancy on Td cation sites showing that decreased occupancy on Td iron sites in spinel iron oxide is ubiquitous for spherical NCs below 10 nm core diameter. The presence of these sites may explain the increased reactivity for NCs below 10 nm during the NC growth process.

Results and discussion

NC synthesis and characterization

. There are two attributes of our synthetic method that allow us to address unanswered questions regarding nanoscale structure and size-dependent reactivity. The first attribute is that the NCs are of high quality because our continuous growth synthetic method makes NCs that have been shown to have almost no strain-producing defects and increased magnetic properties.[6] The second attribute is that the size of the NCs can be changed by the dropwise addition of precursor allowing for incremental, sub-nm increases in NC core diameter allowing for analysis of how size-dependent structure and properties change from 3-10nm.[6,43] It has been previously shown that the continuous growth through catalytic esterification of NCs is enabled by a reactive surface, however,

it is still unknown what role the surface chemistry plays in the formation of NCs and how the size-dependent structure affects reactivity.[43] By using PDF, a technique ideal for studying nanoscale structure[34], we will gain insight into the size-dependent structure and how these structural changes impact reactivity of small NCs.

For the NCs used to probe NC structure from 3-10 nm, the size and size distribution were determined by small angle X-ray scattering (SAXS) on a selection of the NCs over the size range (Table B1). SAXS scattering curves are shown in Figure 2. The SAXS curves were modeled using a Gaussian distribution function, a spherical form factor and a non-interacting dilute system structure factor.[58] The size dispersity of the NCs was all below 20% for each NC (Table B1). In order to study size-dependent structure, dispersities below 20% in NC populations are required. If the NC populations have larger dispersities NC structure and properties cannot be attributed to a particular core diameter. TEM was used to verify that the morphology of the NCs was spherical for all sizes (Figure 3 and Figure B1). TEM size analysis of four NCs (Table B1) corroborates the SAXS data.

XRD can be used for bulk materials to obtain quantitative structural information by refining the data to a known structural model.[7,8,59] As discussed above, the difference between maghemite and magnetite is the occurrence of vacancies on the octahedrally coordinated iron sites in the structure.[7,8] In bulk materials, these vacancies are known to order, forming a spinel superstructure.[60] The degree of ordering on the octahedrally coordinated sites has been described in several space groups including cubic *Fd-3m*[7] and $P4_33_2$[61] as well as tetragonal $P4_32_12$[8] and $P4_12_12$[60] (Figure B2).[59] Using XRD,

superstructure can be seen for the various amounts of ordering that can occur of octahedrally coordinated cation vacancies in the lattice (Figure B2-B3).

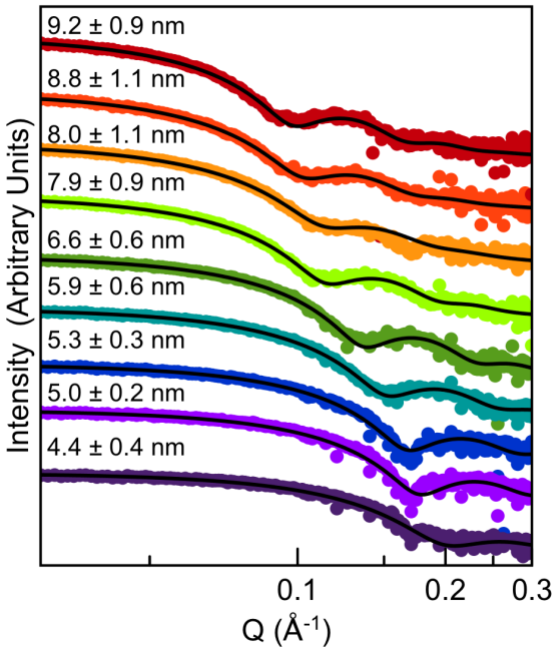

Figure 2. SAXS patterns (colored dots) and calculated models (black lines) for samples analyzed by SAXS to determine NC diameter and dispersities. SAXS patterns are shown for eight different sizes with the largest NCs on top and smallest NCs on the bottom.

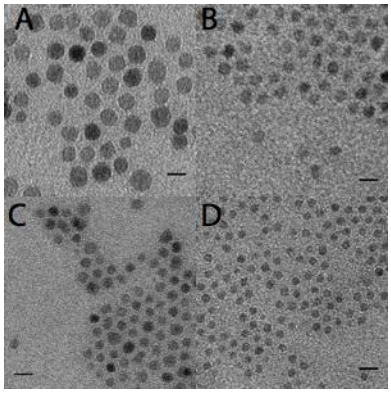

Figure 3. Shows the TEMs used to determine spherical morphology of four representative NCs of different sizes. A) 9.6 nm, B) 6.1 nm, C) 5.2 nm and D) 3.8 nm. Scale bar on TEM is 10 nm.

For our small samples, the nano-size Bragg peak broadening causes small superstructure peaks to broaden into the baseline making it hard to refine vacancies (Figure B4-B6).[27] Rietveld refinement of XRD data for NCs in this study is described best using a simple magnetite structure (*Fd-3m*)[7] (Figure B4-B6 and Table B2-B5). However, we expect some amount of maghemite to be present in these samples.[6] In order to understand the atomic arrangement and the occupancy of cations throughout the lattice a technique that not only measures global structure from Bragg scattering but also incorporates local structure from diffuse scattering is needed.

PDF analysis has recently emerged as a method to probe the atomic arrangement in nanoscale structures by obtaining information about materials that are amorphous or nanoscale, which therefore do not have well defined global structure..[29,34,35] In order to obtain a wide variety of different sizes of NCs, aliquots were removed from the reaction mixture during precursor addition. All NCs were measured in their reaction solution due to the small amount of solid that could be collected from the aliquots (especially in the smallest NCs). In addition, measuring NCs in solution minimized any variations that could occur from washing and drying the NCs.[16] NCs were very dilute, 20-120 mM for the smallest and largest NC respectively. Therefore, most of the signal from Total X-ray Scattering data was due to the solvent, a mixture of oleyl alcohol and oleic acid (Figure B7). However, after background subtraction, PDFs used for determining nanoscale structural information can be obtained in these dilute NCs (Figure 4B).

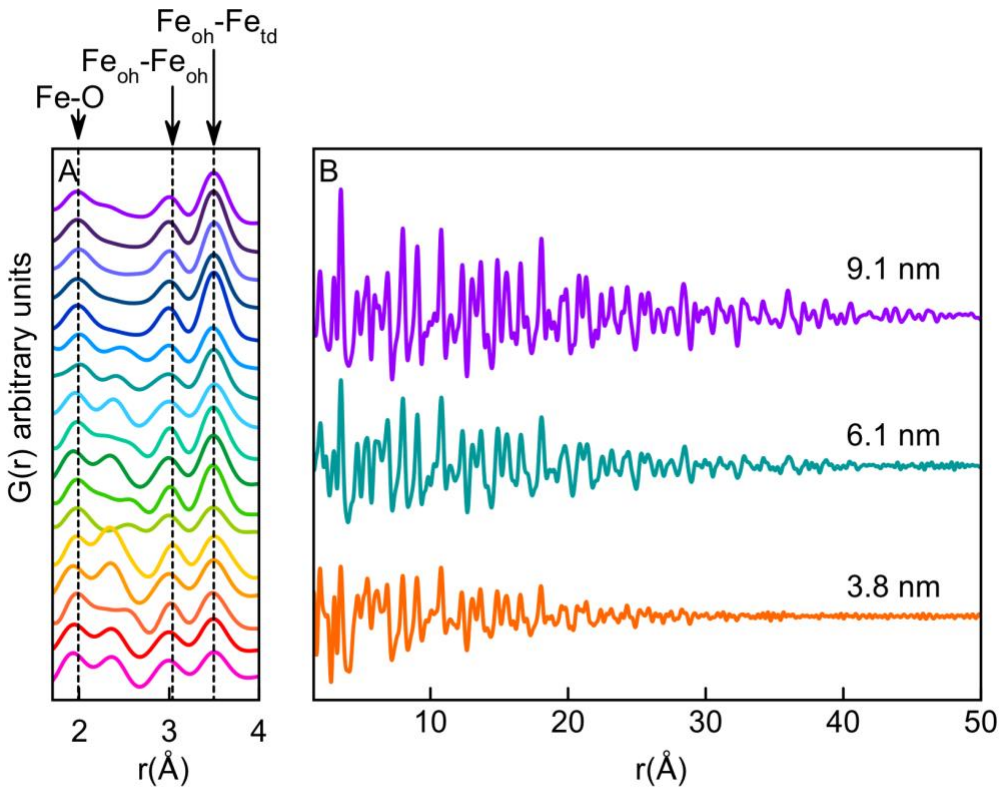

Figure 4. Local and long-range order of generated PDFs from Total X-ray Scattering data. A) Displays local r-range, from 1.4-4 Å in PDFs obtained from 17 different samples ranging from 3-10 nm in diameter. The 2.9 nm NC is at the bottom (pink) and 9.1 nm NC is at the top (violet). B) Shows the extended r-range of three selected PDFs of different sizes from 2.7-60 Å.

Once PDFs were calculated from Total X-ray Scattering data we can assign atom pairs present in spinel iron oxide.[7] The short-range order (1.4–4 Å) of each of the PDFs can be seen in Figure 4A, with dashed lines highlighting the evolution of three atom pairs. The peak at 2Å originates from the Fe-O distances found in both octahedra [FeO_6] and tetrahedra [FeO_4] in the spinel structure. The two other significant peaks can be assigned to Fe-Fe correlations. The peak at 3Å arises mainly due to the first distance between octahedrally coordinated iron sites (Fe_{oct}-Fe_{oct}) whereas the peak at 3.5Å is at the first distance between octahedrally and tetrahedrally coordinated iron sites (Fe_{oct}-Fe_{tet}).

The primary finding from Fig. 4A is that the intensity of the Fe_{oct}-Fe_{tet} peak increases as NCs get larger. Such an increase could be the result of an increase in the occupancy of Td iron sites in the NCs as diameter increases. Figure 4B contains the full range PDF (1.5 to 60Å) of NCs of three sizes: 3.8, 6.1 and 9.1 nm. As NCs get larger (from bottom to top) we can see longer range structural coherence (atom pairs at higher *r* values) confirming larger NC size.

In order to obtain structural information for the NCs, structural parameters including the unit cell size, atomic positions, and cation occupancy were refined (full list of refined parameters using each structural model is included in Table B6 – B18). Refinement of parameters occurs by fitting the PDF to a known structural model, in our case spinel iron oxide. Since spinel iron oxide NCs are a mixture of two phases, magnetite and maghemite, there are four different structural models, *Fd-3m*,[7] $P4_33_2$,[61] $P4_32_12$[8] and $P4_12_12$,[60] that can be used for spinel iron oxide. The difference between these four models is the amount of ordering of octahedrally coordinated vacancies throughout the unit cell. *Fd-3m* and $P4_33_2$ spinel structures are both cubic but *Fd-3m* has octahedrally coordinated (Oh) cation vacancies that are averaged over the whole structure while $P4_33_2$ has ordered Oh cation vacancies.[7,61] $P4_32_12$ and $P4_12_12$ both have tetragonal unit cells and ordered Oh cation vacancies, however $P4_12_12$ has a tripling of the c-axis of the unit cell.[8,60] To determine which of the four spinel structural models described these NCs best, we can compare the agreement factor (R_W) for refinements performed with each structural model (Figure B8, B18-D and B21-D). The lower the R_W value the better the refinement agrees with the data. By comparing the R_W values for NCs from

refinements using different models we can determine which is describing the data the best.

Refinements using the maghemite structure in spacegroup[8] $P4_32_12$ had the lowest R_W values, of 0.13 and 0.44 for the smallest and largest NCs respectively, that refined physically reasonable parameters. *Fd-3m* refined the highest R_W values, 0.24 and 0.48 for the smallest NCs and largest NCs respectively (Table B12-Figure B18-B20), $P4_33_2$ was in the middle of *Fd-3m* and $P4_32_12$ with refined R_W values of 0.16 and 0.46 for the smallest and largest NCs respectively (Table B15-Figure B21-B23). The model in the spacegroup $P4_12_12$ has the lowest R_W values, 0.08 and 0.32 for the smallest NCs and largest NCs respectively (Table B18-Figure B24-B26), however $P4_12_12$ has 71 parameters that are refined vs. 25 parameters that are refined for the $P4_32_12$ structure. The slight improvement in fit quality for $P4_12_12$ compared to $P4_32_12$ is likely the result of using more refinement parameters as opposed to producing a better model. As can be seen in Figure B27 the largest NC refined using $P4_12_12$ refines 1.36 Å as the smallest bond length. We are likely over refining the data since non-physical bonds are being expressed that are much lower than previously reported for spinel iron oxide (smallest bonds refined prior are 1.64 Å [60]). Bond lengths when using $P4_32_12$ remain physical (Figure B9-B13). We will rely on the $P4_32_12$ model to extract quantitative structural data including size of the crystallites, unit cell parameters, and cation vacancies. Fits for these refinements are seen in Figure 5. A full list of parameters that were refined as well as starting values are included in the Table B6-B9 and Figure B17.

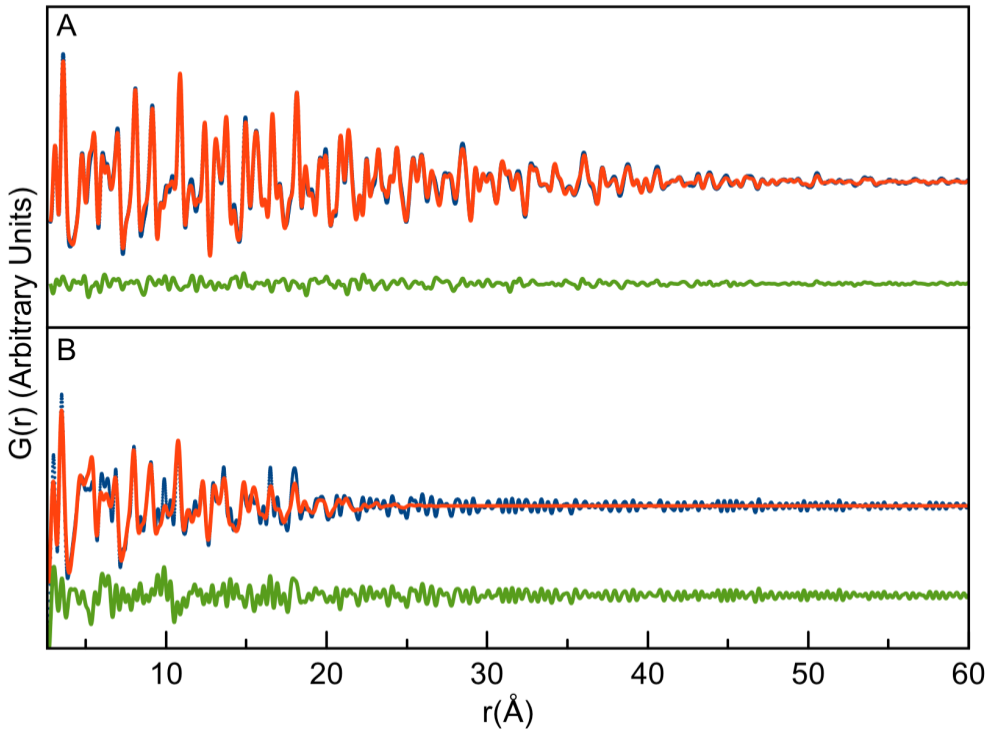

Figure 5. Fits of PDF data to space group $P4_32_12$ A) for the 9.6 nm NC (size by PDF) and B) for the 2.9 nm NC (size by PDF). In both plots the blue dots are the data, the red line is the model and the green line is the difference curve.

The NC sizes refined by PDF agree well with the size refined from SAXS across the size series (Figure 6). The line in Figure 6 is a guide to the eye if both measurements were to give the same value (x=y). Agreement between the two methods indicates the NCs are single crystalline. We reported previously, NCs synthesized by the slow injection method are single crystalline by high-resolution TEM.[6]

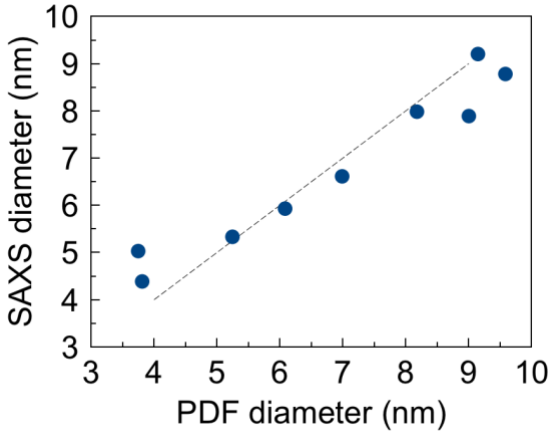

Figure 6. SAXS diameter versus refined PDF diameter refined using space group $P4_32_12$. The dotted line is a guide to the eye and has equation x=y.

Oxidation of spinel iron oxide NCs

It is possible from the refinement of PDF to determine the percentage magnetite in the NCs, a difficult parameter to determine in nanoscale materials. In the Greaves model,[8] the occupancy on the Fe(4) position in $P4_32_12$ structural model is the site representing ordered vacancies. The Fe (4) position has an occupancy of 0.33 in spinel iron oxide that is pure maghemite and an occupancy of 1.0 in spinel iron oxide that is pure magnetite. NCs show size-dependence in their magnetite content with larger NCs having more magnetite content and smaller NCs having more maghemite content. NCs that were synthesized days before measurement, or fresh NCs (purple dots in 7A), have percent magnetite values from 10-45% magnetite for NCs from 4 – 6 nm diameter. NCs synthesized at least 3 weeks before measurement, or aged NCs (green dots in Figure 7), have a trend from 0-40% magnetite for 3-10 nm NCs respectively. Furthermore, fresh NCs have higher magnetite values than aged NCs, indicating that oxidation of the NCs continues at ambient conditions over time.

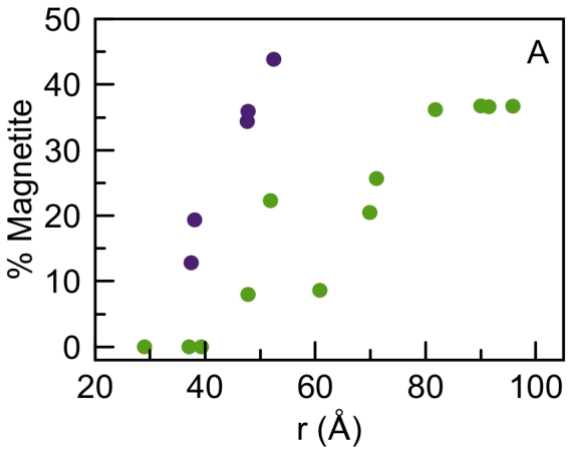

Figure 7. A) Refined percent magnetite versus NC diameter refined using space group $P4_32_12$. Green dots represent NCs that were synthesized from 4 months to 3 weeks before measurements were taken. Purple dots represent NCs that were synthesized 5 days before measurements were taken.

Decreased magnetite content of aged NCs, suggest that oxidation of spinel iron oxide will equilibrate over time to a final magnetite content for a given diameter. It is well established that the surface of spinel iron oxide NCs is the most oxidized due to increased cation mobility due to tensile stress at the surface.[15,62,63] Conversely the core of the NC is more reduced due to compressive stresses in the core. Assuming all the magnetite is located at the core of the NC, we can use the percent magnetite of the NCs to calculate the magnetite volume.[16,18,29] The remaining volume of the NC is attributed to the thickness of the oxidized layer on the surface. The oxidized volume at the surface of the NCs is 1.4 ± 0.3 nm thick across the size series. This estimation does assume that the two phases are separate but in reality, a gradient composition is likely. Our data suggests that once a distance between 1-2 nm into the NC is oxidized, the composition of the NC remains constant as long as intentional oxidation is not applied (for example heating NCs

in an oxidizing atmosphere). Comparing previously reported magnetite content of iron oxide NCs made by continuous growth measured by near-IR[26] with aged NCs gives the same percent magnetite for a given NC diameter (Figure B13).[6] These two distinct trends in magnetite content for fresh and aged NCs show that over time NCs oxidize but reach a constant extent of oxidation around 3 weeks in ambient conditions in non-polar solvent.

There are large disparities for values of percent magnetite for the same diameter NCs reported in the literature (Figure B14 – Figure B16). However, we have shown that with continuous growth, the same NC diameter has the same magnetite content for aged NCs. One reason for the discrepancy in values across studies is that NCs in the literature will have undergone different amounts of oxidation depending on their treatment, storage and time since synthesis. It is also possible that NCs made by different methods would have different final magnetite content values. Factors that may affect the oxidation of the NCs are initial precursor oxidation state, atmosphere of the synthesis, addition of benzyl alcohol or other oxidants, ligands and the content of dissolved oxygen in the solvents used for washing and storage.[42,44]

Size-dependent structure: Td iron sites

It is important to understand the Td cation vacancies in small NCs as this could impact their reactivity and adsorptive properties. The Td cation occupancy can also be determined by refining the occupancy of the Fe (1) position in the Greaves model.[8] As NC diameter decreases there is a lower occupancy on the Td iron sites (Figure 8) meaning that the lattice contains more vacancies on Td cation sites when smaller. Full

occupancy of tetrahedrally coordinated cation sites appears to be reached around a NC core diameter of 10 nm.

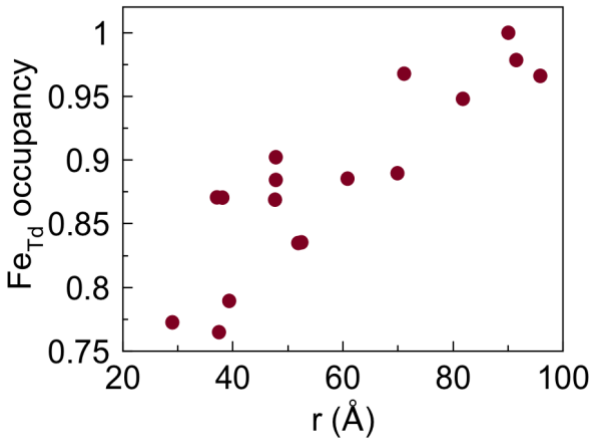

Figure 8. Tetrahedrally coordinated iron site occupancy versus NC diameter refined using space group *P4₃2₁2*.

Vacancies at Td cation sites are not an artifact of defect prone synthetic methods but present in spinel iron oxide spherical NCs below 10 nm. Prior reports of Td vacancies, occured in NCs produced by hydrothermal[28] or aqueous co-precipitation[5] methods. These aqueous methods are known to produce NCs with increased occurrences of strain-producing defects and large dispersities.[13,29–31,39] The continuous growth method produces NCs with almost no strain-producing defects.[6] Td cation vacancies are ubiquitous for spinel iron oxide NCs below 10 nm over a variety of synthetic methods.

Size-Dependent Reactivity

When monitoring the progression of the slow injection synthesis by SAXS we can see a change in reaction rate during the addition of precursor (Figure 9A and B28 – B29). As we add iron precursor to the reaction we see a reaction rate that shows continuous, linear growth at the beginning of addition. As can be seen in Figure 9A, after 3 mmol of

iron (II) oleate has been added to the reaction the growth rate slows significantly. The growth rate is still linear, but the reaction rate is slower even though precursor is being added through the entire reaction at the same injection rate.

A change in growth rate is unexpected because the surface area of the NCs is increasing and precursor concentration is increasing. When a population of NCs are growing with no increase in number of NCs (no new nucleation) the surface area of the system increases (Figure 9B). Therefore, there should be an increase in the available surface to react with precursor. In addition, precursor is being injected slowly over the course of the reaction. The concentration of available precursor should increase if added precursor is not leading to growth and no new nucleation occurs. The dispersities of the NCs remain low after the change in reaction rate indicating a second nucleation event is not occurring. Something else that must be changing when the reaction rate slows while addition of new precursor continues.

In the classical theory describing diffusion-limited growth, faster growth of smaller NCs is explained as a mass transport effect.[64] After a critical radius is reached, smaller NCs use less material to grow so there is a thinner depletion layer from the NC surface to bulk concentration. If instead of diffusion-limited growth, the growth process is reaction-limited, there is no size-dependence of growth rate. The continuous growth reaction is not diffusion limited after the change in growth rate because precursor is being continually added to the reaction. Therefore, NCs made by continuous growth are not described by classical growth theory which assumes that the rate constant is not affected by the NC size. The assumption that rate constant does not change with size is not a reasonable assumption if the structure of the material changes at small sizes.

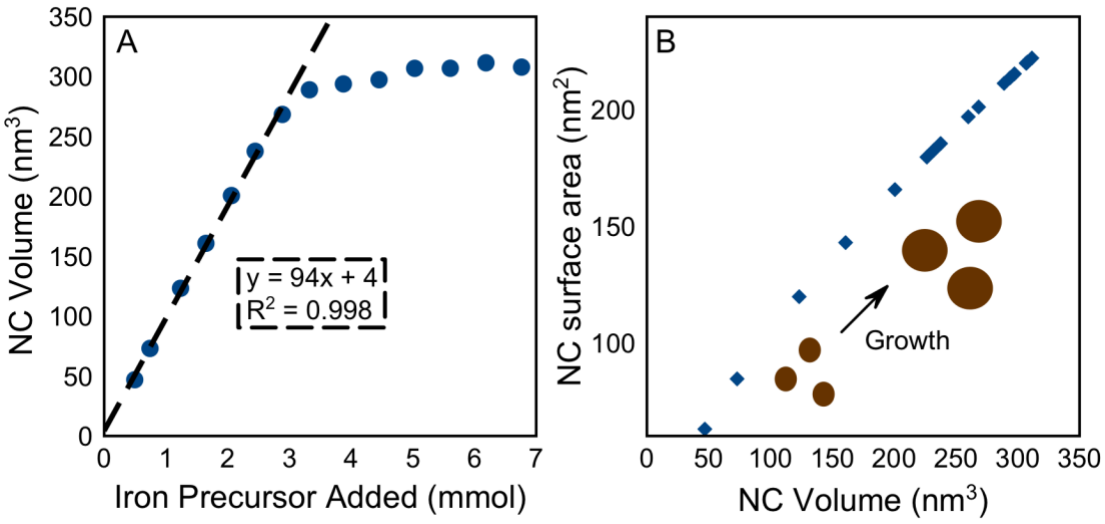

Figure 9. Data of NC volume versus iron precursor added to the reaction and the corresponding increase in surface area with increasing NC volume. A) Volume of NCs measured by *ex situ* SAXS during the addition of precursor. The linear equation for the initial reaction rate is included in the dashed box. Linear equations are included for both reaction rates. B) NC surface area for NCs of increasing volume (blue diamonds). The brown circles represent the relative increase in size and surface area of a single population of NCs.

As spinel iron oxide NCs get larger, the structure of the NC changes by containing fewer Td vacancies. Td vacancies are known to be especially reactive sites on the NC surface enabling increased adsorption of arseite.[5] Increased adsorption of arsenic on Td cation sites is because arsenite mimics a Td iron cation.[5] Therefore, vacant Td cation sites are likely to also be more reactive for iron precursor in addition to arsenite.

Increases in reactivity at the surface of NCs caused by changes in the nanoscale structure at small sizes, underpins how understanding nanoscale structure can gain insight into the formation mechanisms and properties of NCs. When using an esterification mechanism of spinel iron oxide NCs, a size-dependent increase in reactivity caused by size-dependent structure impacts NC growth. Td cation vacancies have been shown to be

ubiquitous in NCs of spinel iron oxide below 10 nm made by different synthetic methods implying that surface structure could impact the formation of NCs by other synthetic methods as well. Classical nucleation and growth theory still may be appropriate for NC systems that do not rely on esterification for NC formation. However, if it is known that a material has size-dependent structural changes, size-dependent growth may impact NC formation mechanisms.

Conclusions

We have shown that using PDF analysis with NCs that are synthetically ideal to study size-dependent structure and properties can yield enhanced understanding. We have determined the nanoscale size-dependent structure in a series of 17 NCs from 3-10 nm. The percentage of magnetite in the NCs was size-dependent with smaller NCs being more maghemite in phase. NCs showed a constant extent of oxidation in aged NCs which corresponded to the volume of a 1.2-1.6 nm oxidized shell at the surface of the NCs. Td cation vacancies in spherical NCs below 10 nm in diameter appear to be ubiquitous regardless of synthetic method. Increased Td cation vacancies in the NCs increases the reactivity of the surface of the NCs which impacts the mechanism of growth.

The structure of materials is known to impact properties but due to lack of analytical tools to study NCs the link between structure and properties has not been thoroughly investigated. PDF is a powerful tool for the determination of nanoscale structure and the use of PDF to study the structure of other systems will enrich the understanding of nanoscale structure across different materials. The use of PDF will allow for the NC community to rationally design the synthesis of NCs by gaining understanding of how structure impacts reactivity of different materials at different sizes.

For spinel iron oxide, *in situ* structural studies will elucidate the size-dependent phase variation and nanoscale structure of NCs upon synthesis and give incite as how to further control the final NC structure. Further studies of how these nanoscale structural features relate to properties of these materials will be important to the magnetic, biomedical, environmental and materials scientist communities.

Increased reactivity seen here for small NC sizes will give insight on growth mechanisms of NCs. Classical growth theory is currently used to explain NC mechanisms, but classical growth is likely an oversimplified model to explain reactions in NC formation. Size-dependent reactivity of NCs seen in this work challenges one of the main assumptions made in classical growth theory which is that the reaction constant is not affected by the size of the NCs. The knowledge of size dependent reactivity will help design syntheses to make smaller NCs which are known to be most likely to have size-dependent properties.[1] In addition, control of Td cation vacancies could lead to better adsorbents for toxic metals other than arsenic found to adsorb on iron oxide NCs, including chromium[65], lead[66] and selenium[67], to be target analytes. [66,67]

Materials and Methods

Synthesis

The iron oleate precursor is synthesized with a ratio of 1 mmol of iron (II) acetate (Sigma Aldrich, > 99.99% trace metals basis) for every 2 ml oleic acid (Sigma Aldrich, technical grade 90%) and is heated for 1 hour at 150°C. The slow injection synthesis involves adding this 0.5M iron oleate precursor at 10 ml/hr to a flask of 12.5 ml oleyl alcohol at 230°C. The size of the NC can be controlled by the amount of precursor added to the flask as reported previously.[6,43] NCs can be made from 4-11 nm by adding between

0.3 to 6 mmol of precursor. After every 2 ml of 0.5 M precursor added to the reaction flask 3 ml of oleyl alcohol is added to replenish the esterified starting material. After all precursor is added the NC solution is heated for an additional 20 min at the reaction temperature. In order to isolate NCs of different sizes for PDF analysis NCs are removed from the synthesis with a 20-gauge syringe needle at different mmol added and cooled rapidly by being placed in vials on ice to expedite cooling.

The NC background is a mixture of oleyl alcohol, oleic acid and oleyl oleate. We used a background of dilute oleic acid in oleyl alcohol at concentrations between 0.24 – 1.0 M of oleic acid and did not add any oleyl oleate assuming it would scatter similarly to combinations of oleic acid and oleyl alcohol. These concentrations of backgrounds are the concentration of oleic acid if no esterification occurred in NCs made with 0.3-6 mmol of added iron oleate precursor in the reaction mixture. The dilute nature of these NCs required that each NC be carefully background subtracted. The background is a mixture of oleic acid and oleyl alcohol at concentrations between 0.3-0.8 M.

PDF Characterization

All total scattering measurements were taken at the Advanced Photon Source at Argonne National Lab in Chicago, Il at the 11-ID-B beamline. The energy of the x-rays was 58.66 kev with a wavelength of 0.2114 Å. Samples were exposed for 2 seconds for 150, 450 or 900 exposures. An autosampler was used to measure up to 28 samples pre-prepared in capillaries at a time. Samples were integrated using Fit2D[68]. The PDFs were then generated using xPDFsuite.[25-27] Diffpy-CMI was used to model the data using each of the crystal structures: *Fd-3m*,[7] $P4_33_2$,[61] $P4_32_12$[8] and $P4_12_12$[60].[69] The scale, low

temperature vibrational correlation, and atomic coordinates were refined from 2.7 to 20 Å. The unit cell parameters, crystallite size, atomic occupancies were refined from 2.7 to 60 Å. For each of these crystal structures the iron thermal parameters were determined for the largest NC and all other NCs had the thermal parameters fixed to this value. A select few NCs were also analyzed with $P4_12_12$. The thermal parameters were set to 0.5, a value similar to all other crystal structures in this model.

The solvent wave described by Zobel *et al.* due to NC surface ordering of solvent was also included in the structural model.[70] The larger NCs do not show any residual curve which we believe to be due to the increasing insolubility of the NCs as they get larger coating the sides of the capillary tubes prior to analysis. Further information on the refinements of this sign wave due to solvent restructuring can be found in the supplementary information.

SAXS Characterization

SAXS patterns were acquired using the lab-scale SAXSess mc^2 from Anton Paar. The system used a Cu Kα X-ray tube in order to generate X-rays (λ=0.154 nm). The system was equipped with a CCD detector (charge coupled device) from Roper Scientific. Data was averaged from 50 frames that were acquired between 1-25s. Data was reduced with SAXSquant involving a background and dark subtraction. Data was analyzed by the Irena software package (version 2.62) in the Igor software (version 6.37) to determine NC core size and dispersities. To model the data a size distribution model was implemented with a Gaussian distribution. The structure factor was a dilute system and a spherical form factor was used to model all of the data. The iron oxide contrast was

calculated to be 1.235 *$10^{23}$$cm^{-4}$. The size, dispersity and volume fraction of the NCs were modeled using modelling II in the Irena software package to be used with Igorpro. [21] A dilute structure factor and a spherical form factor with a Gaussian distribution was used in the SAXS model. In order to account for the fluorescence of iron we also refined the background.

TEM Characterization

TEM grids (Ted Pella, 400 mesh copper) were drop-casting dilute solutions of NCs. Images were taken with an FEI Tecnai G2 Spirit microscope to determine NC morphology and corroborate size with PDF and SAXS. Images were processed with FIJI[71] software to determine diameter and dispersity.

Bridge to Chapter Four

In Chapter III of this dissertation, we established that small nanocrystals (NCs) (below 6 nm) have a lower occupancy of tetrahedrally coordinated cations compared to large NCs. We also reported in Chapter III, that the lower occupancy of tetrahedrally coordinated cations results in increased reactivity of the NC surface. In Chapter IV of this dissertation, we will acquire in situ data of a continuous growth synthesis of spinel iron oxide. From this study we will determine not just the structure of the final NC products but also the structures that form during the reaction. Both precursor oxidation state and temperature will be varied to see how the formation mechanism is impacted by these synthetic conditions.

CHAPTER IV

IN SITU TOTAL X-RAY SCATTERING STUDY OF THE FORMATION OF IRON OXIDE NANOPARTICLES

Portions of the following chapter will appear in the upcoming publication co-authored by Susan R. Cooper, L. Kenyon Plummer, Samantha L. Young, Meredith C. Sharps, Alexia G. Cosby, Randall Candler, Darren W. Johnson, James E. Hutchison and Kirsten M. Ø. Jensen. I was the lead in this project and coordinated design of the *in situ* synthetic set up and analyzed all data. *Ex situ* samples were made by Kenyon L. Plummer, Alexia G. Cosby and Randall Candler. I collected total X-ray scattering data at the Argonne National lab Advanced Photon Source with Kirsten M. Ø. Jensen, Samantha L. Young and Meredith C. Sharps. I was the primary author of this manuscript with input from Kenyon L. Plummer, Meredith C. Sharps, Darren W. Johnson, Kirsten M. Ø. Jensen and James E. Hutchison.

Introduction

Nanoparticles (NPs) exhibit properties differing from bulk caused by structure (phase and defects), composition (core and surface material) and morphology (size, dispersity and shape) and are useful in a variety of applications if materials can be designed with different NP attributes.[1–3] Often multiple attributes need to be tuned in order to be appropriate for specific uses. For example, one application of interest for iron

oxide NPs is removal of contaminates from water, which would take advantage of enhanced adsorption of toxic materials at small NP sizes.[4] This application also requires strong magnetic properties, which normally decrease with core diameter, for removal of NPs with a magnetic field.[5] In order to design NPs with specific attributes there needs to be an understanding of reactivity in a NP synthesis and how reactivity influences the final NP product. However, most NP attributes are tuned by relying solely on empirical evidence, not knowledge of NP mechanisms.[6,7] Using trial and error to determine how NPs attributes can be harnessed, while effective in some cases, is inefficient and often leads to conflicting results because of the hard to detect structural differences resulting from competing reaction pathways.[8–14] More selective synthetic techniques that allow for greater control over each synthetic condition, paired with advanced characterization techniques, will allow for mechanistic understanding of different reaction pathways and enable design of specific NP features. In this work we will use a continuous growth synthesis[8] coupled with *in situ* total scattering measurements in order to determine how precursor oxidation state and temperature impact the size, phase and defects (local structure) of NPs.

Synthesis conditions can be changed in order to control NP composition and structure; however, most changes impact multiple NP attributes. The synthesis conditions that are used to control NP structural attributes are the temperature of the reaction,[10,15] ratio of additives,[16–22] heating rate,[23] precursor concentration,[8,11,24–29] solvent[12,15,25,30] and time[22,29,31,32]. The reaction temperature as well as solvent are commonly used to control the core diameter of NPs.[10,15] However, in addition to controlling the NP size, the reaction temperature can also influence the mechanism of growth resulting in changes in

the phase and defect composition. [8,9,11,13,14] Changing the solvent can also affect shape, defects and surface composition.[8,9,11–14,17,33–42] The fact that changes in synthesis conditions influence a host of structural features at the same time makes it difficult to disentagle which NP attributes ultimately lead to different properties when different synthesis conditions are used. More selective syntheses, where different synthetic conditions can be manipulated independently, are needed to determine the interrelationship of synthesis conditions, NP structure and NP properties.

From *ex situ* studies we can get an idea of how NP properties or structure change by studying the end products of reactions, but we gain no information about how reaction mechanisms influence properties and local defects that impact NP properties. For example, different iron precursors with different oxidation states (Fe(0)[43], Fe (II)[8,16–18,44], Fe (III) [10,12,15,20,23,24,45,46]) have been used to make NPs that are all reported to have the same structure; spinel iron oxide (Figure 1). However, it has been shown that the presence of a wüstite phase (Figure 1) within a spinel NP decreases magnetic properties even after that phase is oxidized to a spinel phase. [11–13,47–61] In order to design NPs with different local structures there must be an understanding of the reactivity during synthesis, including the generation of transient species, that impacts the material structure even if those structures and defects are difficult to detect in the final product.

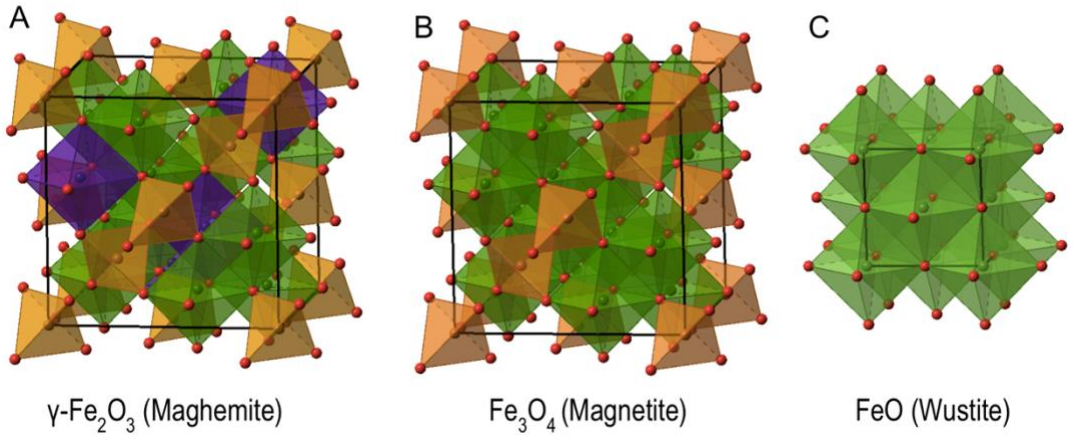

Figure 1. The polyhedral structure of materials that can form in a synthesis of spinel iron oxide including A) maghemite, B) magnetite and C) wüstite.[54,62–67] The red spheres are oxygen atoms, the green spheres are octahedrally coordinated iron cations and the gold spheres are tetrahedrally coordinated iron cations. Purple spheres are iron cations that are vacant in a maghemite structure and occupied in a magnetite structure. Around the iron cations (yellow and gold spheres), polyhedra of the same color represent the coordination environment.

In situ studies are needed that probe nanoscale structure of the materials being formed during NP formation and growth to complement *ex situ* studies of products of the synthesis. Prior studies suggest that the most important determiner of NP properties are defects or local structure within NPs that are typically different than those occurring in bulk materials.[4,8,11] Rather than relying on determinations of size[68] or global Bragg structure,[69] techniques that give insight into the local structure are needed. Pair Distribution Function Analysis (PDF) of Total Scattering Data analyzes both global and local structure by incorporating the diffuse as well as the Bragg scattering.[70–72] PDF has been shown to provide new insight into nanoscale structure of polymorphic clusters[73], size-dependent defects[74] and precursor structure.[75–77]

The use of *in situ* PDF has allowed for the understanding of both nucleation and growth of clusters and nanoparticles, offering new insights into precursor structure and

reaction mechanisms. For example, in the case of tin and zirconium, different precursor structures have been elucidated for different compositions, ranging from a single Sn aquo – complex[75] to amorphous polymers in $ZrO(NO_3)_2$ $6H_2O$[77]. For these Sn and Zr precursors, there are two different mechanisms of nucleation and growth. In the formation of SnO_2 there are first small clusters of a few bridged Sn aquo-complexes followed by aggregation of small units to make SnO_2 NPs.[75] Water content and temperature greatly impacted the speciation of the reaction mixture, therefore changing the mechanism of formation.[75] In the formation of ZrO_2 on the other hand, the polymeric Zr precursor decomposes and produces an amorphous phase before crystallization to form NPs. [77] The reaction solvent was shown to control which phase was formed, with a tetragonal phase formed in methanol and a monoclinic phase favored in a water-acetate mixture.[77] *In situ* PDF has both enabled great insight on the impact of synthetic conditions and also shown the diversity of reactions occurring in different NP systems.[36]

The formation of Fe_2O_3[74] has also been studied by *in situ* PDF providing insight into NP formation using a hydrothermal synthesis method. PDF analysis showed that the iron citrate precursor was a dimer of octahedrally coordinated iron cations. During the early stages of growth, spinel iron oxide containing only octahedrally coordinated iron cations was produced. As the reaction progressed, tetrahedrally coordinated cations were incorporated into the structure. A lower occupancy of tetrahedrally coordinated cations persisted in the NPs until they reached a core diameter of 6 nm. Analogous studies have not been reported for spinel iron oxide synthesis in organic solvents. Given the reported advantages[8,15,24] for controlling NP structure and morphology in these syntheses, it is important to understand how precursor oxidation state and structure, as well as the

reaction temperature, impact the formation of NPs in organic reaction media. Such studies will further elucidate how the chemistry of iron impacts the formation of NPs and permits greater control of structure and properties through synthesis.

Here we report a systematic *in situ* examination of the effect precursor oxidation state and temperature have on the intermediates and products formed during spinel iron oxide NP synthesis. We use PDF analysis of *in situ* total x-ray scattering data to monitor a continuous growth process. This process allows us to examine the growth process while keeping all other reaction conditions (temperature, concentration, solvent) constant. We show here that the precursor oxidation state impacts the structures formed throughout the reaction. We also show that multiple synthetic conditions affect the reactivity in the continuous growth method including the NP surface reactivity as well as the precursor reactivity.

Results and Discussion

There are a multitude of studies on iron oxide NPs, however the understanding of how different synthetic conditions ultimately affect NP properties remains unclear. A property of iron oxide NPs that illustrates this disconnect between synthesis and properties is the saturation magnetization (*Ms)*. For example, *Ms* reported for NPs of 5 nm core diameter range from 17-81 Am^2/kg.[8] NPs with the same ligand shell and core diameter have been attributed to have both higher[78] and lower[17] *Ms* values. Spinel iron oxide NPs with cubic morphology have been reported to have equal[42], higher[41] and lower [34] values of *Ms* than spherical particles. Probing the formation of NPs *in situ* by changing

conditions systematically will help elucidate the structural transformations that are leading to contradictory reports.

Precursor oxidation state and its effect on the growth of spinel iron oxide

One reason for variability in properties of spinel iron oxide is that multiple available oxidation states increase the complexity of the mechanisms of formation for NPs. The effect of precursor oxidation state on reaction products is still not well understood. The use of an Fe (II) rich oleate in our published synthetic method produces NPs from 3-10 nm diameter to form of spinel iron oxide.[8,79] The magnetic properties of NPs made by continuous growth showed superior magnetic properties compared to other spinel NPs because nearly the entire volume of the NPs contributes to the magnetic properties. The enhanced properties of these NPs were hypothesized to be due to the mechanism of formation by metal catalyzed esterification as opposed to thermal decomposition which enables radical reactions. When the synthesis of spinel iron oxide is carried out with an Fe (II) rich precursor growth of the NPs is linearly related to precursor addition during the initial stages of the reaction, but decreases over time as shown in Figure 2. Because oxidation state of the precursor is expected to have an impact on NP formation, we performed the synthesis keeping all conditions the same except substituting in a Fe (III) rich precursor.

There is a difference in growth behavior when using Fe (III) rich oleate as opposed to Fe (II) rich oleate. In Fe (III) rich oleate there is no change in the growth rate for up to 25 mmol of precursor added (Figure1, C1). The decrease in growth rate when using an Fe (II) rich oleate has been attributed to a slower reactivity of larger NPs due to

differences in surface structure of small spinel iron oxide vs larger spinel iron oxide. However, NP size must not be the only factor in the change in growth because the growth of large NPs does not seem to be effected when Fe (III) rich oleate is used. Gaining information from *ex situ* studies between products made by the two different precursors could help us elucidate what differences there are in the formation mechanism of materials.

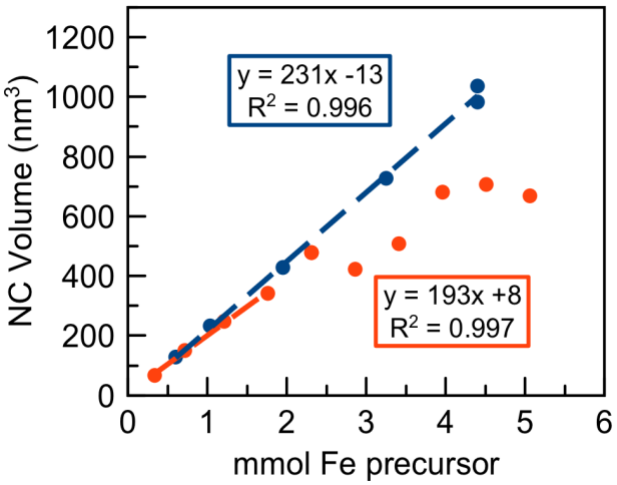

Figure 2. The growth behavior using two different precursors with different oxidation states. The NC volume for the same amount of mmol added to the reaction when using Fe (II) rich oleate (red) or a mixture of Fe (III) rich oleate (blue). Equations are from linear fits to the linear portion of the data.

NPs made by Fe (II) rich oleate and Fe (III) rich oleate are indistinguishable by *ex situ* analysis of SAXS, XRD, TEM and Hi-Res TEM until the change in growth rate by (Figure 3). NPs made with both precursors are similar in size before the change in growth rate by SAXS (Figure 2 -3), have nearly spherical morphology (Figure 3), have a spinel structure (Figure C2) and are single crystalline (Figure C2). Analysis of the NPs produced by the two different precursors do not indicate what causes the change in growth rate in NPs made by Fe (II) rich oleate. To understand the different growth

behavior when using different oxidation states of iron we must examine the reactivity between Fe (II) rich oleate and Fe (III) rich oleate.

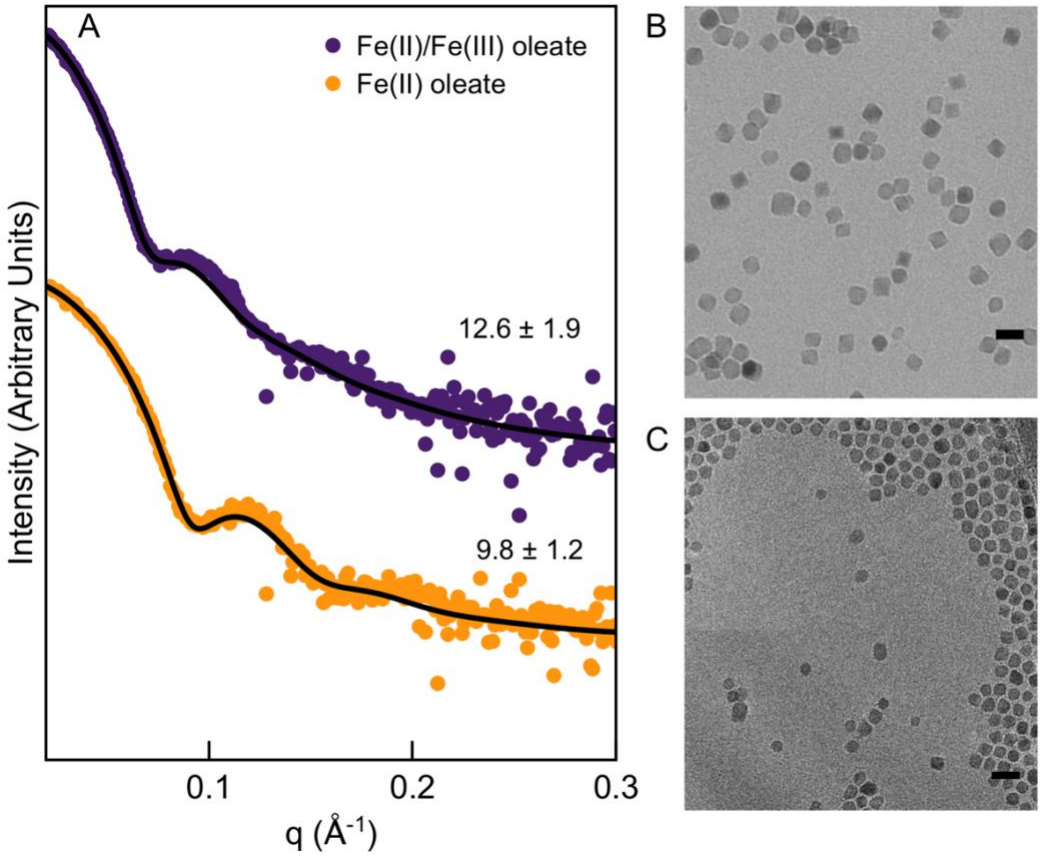

Figure 3. Analysis of sample size and morphology for 4.4 mmol added of Fe (III) rich precursor and 4.25 mmol of Fe (II) rich precursor A) SAXS of samples made using Fe (II)/Fe (III) oleate (purple) and Fe (II) oleate (orange). B) TEM of NPs made with Fe (II)/Fe (III) oleate at 230°C from 4.25 mmol and C) TEM of samples made Fe (II) oleate at 230°C with 3 mmol added.

Reactivity of Fe (II) rich oleate and Fe (III) rich oleate

For other metal oxides, the continuous growth synthesis method has been shown to involve esterification of the metal carboxylate precursors. The differences in reactivity for Fe (II) rich oleate compared to Fe (III) rich oleate might be due to differences in their activity toward esterification and/or thermal decomposition. First, we tested the thermal

decomposition temperature of both Fe (II) rich oleate and Fe (III) rich oleate using thermal gravimetric analysis (TGA). Thermal decomposition happens after 230°C for both precursors as can be seen by looking at decomposition profiles (Figure C3). In the absence of thermal decomposition, esterification is likely the main reaction that produces NPs. We used NMR to measure the amount of ester produced over time of both Fe (II) rich and Fe (III) rich oleate (Figure C4-C5, Table C2-C3). The Fe (III) rich oleate forms over three times as much ester as Fe (II) rich oleate over 32 minutes (Figure 4).

If esterification is the only pathway below 230°C but Fe (II) rich oleate is not a good esterification catalyst, Fe (II) rich oleate will be reluctant to react. Fe (II) rich oleate will be even slower to react with large NPs because, as is shown in Chapter 3 of this dissertation, NP reactivity decreases with increasing core diameter. This suggests that the change in growth rate for larger particles when using Fe (II) rich oleate as the precursor is due to decreased reactivity of Fe (II) rich oleate and decreased reactivity of large NPs.

In situ setup to probe continuous growth of spinel iron oxide

In order to detect the intermediates formed during the continuous growth reaction that leads to different growth behavior when using Fe (II) rich oleate compared to Fe (III) rich oleate, *in situ* methods are required. *In situ* PDF will be used to monitor the continuous growth synthesis using precursors of Fe (II) rich oleate and Fe (III) rich oleate while keeping all other reaction conditions the same. A photo and diagram of the *in situ* setup is included in Figure C6. Briefly, we will slowly inject either precursor into the reaction flask. Reaction solution will then be removed from the reaction flask by a pump and flow through a detection cell to be measured by Total X-ray Scattering. Finally, the

reaction liquid will be returned to the reaction flask. The removal and return of reaction solution are occurring at seven times the rate that precursor is being added to the reaction. NPs produced from the reaction setup have slightly larger dispersities but otherwise are not affected appreciably (Figure 5).

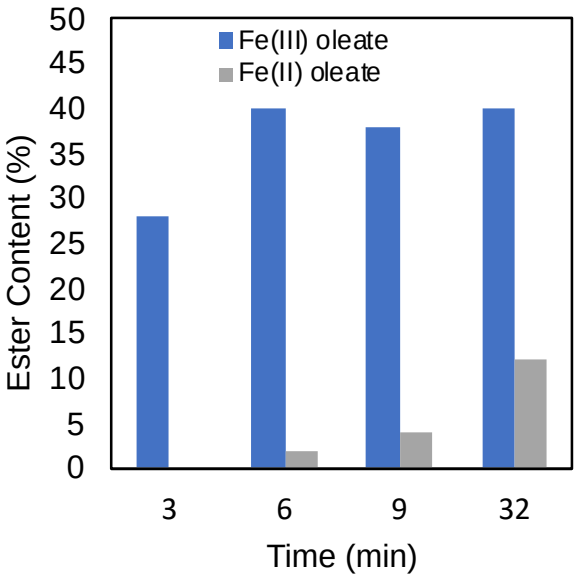

Figure 4. Percentage of ester formed during a continuous growth reaction at 150°C using Fe (II) rich and Fe (III) rich oleate compared to all organic material in the reaction determined by NMR.

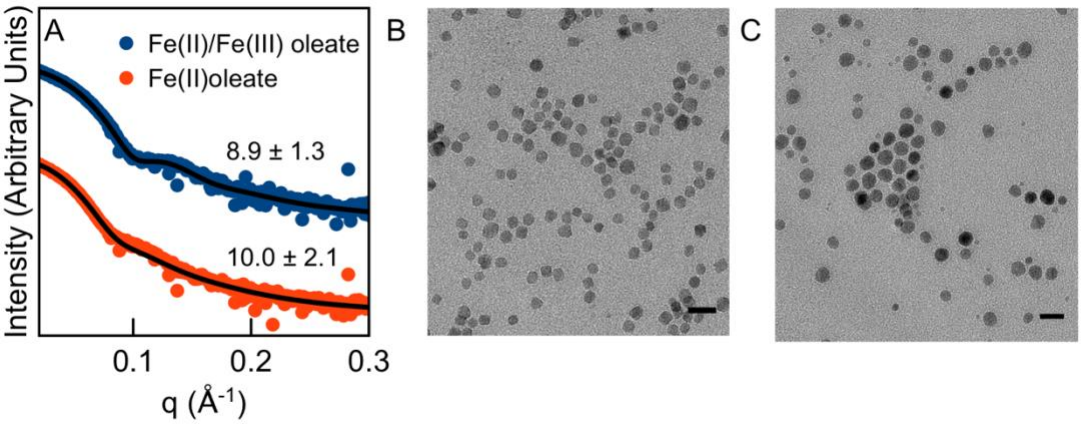

Figure 5. A) SAXS of the endpoint of NPs made at the beamline while collecting *in situ* data using Fe (III) rich oleate (red) and Fe (II) rich oleate (blue). B) TEM of NPs at the end of the reaction produced using Fe (II)/Fe (III) oleate. C) TEM of NPs at the end of the reaction produced using Fe (II) oleate.

In situ reaction of Fe (III) rich oleate precursor analyzed by Total X-ray Scattering and PDF analysis

After PDFs are generated from Total X-ray Scattering data, a model that describes the PDFs must be chosen in order to refine structural features. A spinel model taking the space group $P4_32_12$, used in chapter three of this dissertation, was used to analyze *in situ* Total X-ray Scattering data of a continuous growth synthesis using Fe (III) rich oleate precursor.[66] Fits of *in situ* data can be seen in Figure 6A-B (Figure C7-C15) using the $P4_32_12$ structural model. The $P4_32_12$ structural model describes the features of the PDF and the R_W for NCs is 0.2 or below for samples throughout the reaction (Figure C7). Details of the refinement are included in the supplementary information (Table C4-C7). Using the Fe (III) rich oleate precursor, iron oxide NPs grow as spinel throughout the reaction.

Using the spinel phase, the core diameter can be refined using Diffpy-CMI[80] in order to monitor growth of NPs in the data. The first sample with detectable NPs was collected 26 minutes into the reaction (0.8 mmol of precursor added). The earlier time points were too dilute for structural determination because the signal to noise was too small to distinguish peaks in the PDF accurately. The first sample fits a spinel iron oxide model and reveals an NP core diameter of 5.1 nm (Figure C8). The core diameter increases as more precursor is added to a final size of 6.5 nm (Figure C8). The growth stops after the final amount of precursor is added at around 110 minutes and the structural features do not change after precursor stops adding point (Figure C8).

In addition to size the nanoscale structure including octahedral and tetrahedral cation vacancies and the unit cell volume can be refined (Figure 6). The magnetite content of the spinel NPs is 80% for small NPs and 60% for large NPs (Figure 6C). Low

tetrahedrally coordinated cation (Td) site occupancy is observed in small NPs (Figure 6D). The size dependent Td occupancy seen *in situ* with Fe (III) rich oleate is comparable to Td occupancy for *ex situ* samples synthesized with Fe (II) rich oleate in chapter three of this dissertation (Figure C15). The cell volume decreases with increasing core diameter correlating with the magnetite content in the NPs. A larger cell volume is seen with larger magnetite content (Figure C9). If we add Fe (III) rich oleate we obtain Fe (III) rich spinel iron oxide while retaining size-dependent iron Td site occupancy. Analysis of the NPs made for in situ characterization by lab scale XRD and synchrotron PDF confirm the spinel structure of the NPs (Figure C16, Table C8-C9).

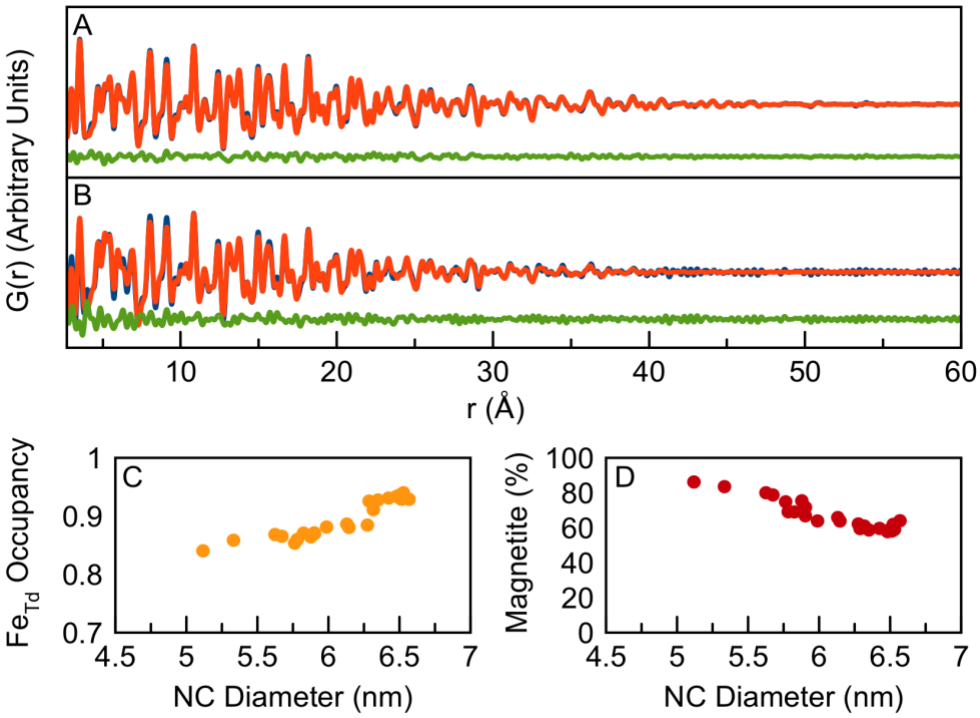

Figure 6. A) Fits for the last and B) first sample analyzed in the Fe (III) rich oleate mixed precursor and structural features over the size range analyzed *in situ*. C) tetrahedrally coordinated cation occupancy and D) the percentage of magnetite compared to the core diameter of the samples.

In situ reaction of Fe (II) rich oleate precursor analyzed by total x-ray scattering and PDF analysis

The *in situ* Total X-ray Scattering data from an Fe (II) rich oleate precursor could not be described by the same spinel structural model (Figure C17) that described the *in situ* data from continuous growth using a Fe (III) rich oleate precursor (Figure C18-C19).[66,67] Reports of spinel iron oxide NPs made in reducing conditions have been shown to contain a wüstite[11,12] phase, thus a wüstite model was used next to fit the NPs. However, structural models of wüstite[81] and cluster defect containing wüsitite[65] (Figure C17) did not adequately describe the data either (Figure C20-C22). Visually the PDFs look as if there are both peaks that are common in wüstite as well as common in spinel (Table C10-C11). Models that represent both phases were used to refine the data.

There are two structural models that can be used to describe a two-phase system of spinel iron oxide (Figure C17). The first is a superimposed structure of both spinel and wüstite which can modulate from completely wüstite to completely spinel.[54] The second is a separate two-phase fit with both wüstite and spinel.[67,81] The first structural model would describe the data best if the system was a homogenous structure of the two phases and the second structural model would fit the data best if the system were a core-shell structure.[67,81] Which model fit best is determined both by the R_W as well as the size of the final NP, which we know from *ex situ* analysis by SAXS and TEM is 10 nm (Figure 5). When comparing the fits between the homogeneous structure (Figure C23-24) and the core-shell model (Figure 7, C25-C28) the core shell model describes the NP structure much better.

Using a dual phase spinel and wüstite structural model, refinement of *in situ* Total X-ray Scattering data of NPs made with Fe (II) oleate precursor could be performed to determine the percentage of each phase in the NPs (Figure 7, Figure C25-C28, Table C12-C15). The percentage of wüstite decreases as NPs increase in core diameter. NPs still appear to be growing after the addition stops (Figure C26). The overall NP diameter can be calculated from the wüstite core size and the fraction of wüstite in the NP. Core diameter increases from 3.5 nm to 6 nm over the course of the reaction. This is a smaller final size than determined by SAXS which we hypothesize is because of either larger dispersities in the NPs or under estimation from our core-shell model. The reaction is carried out in an N_2 atmosphere with a reduced precursor, but oxidation of NPs increases as reaction time increases.

Oxidation of the NPs during the reaction is likely occurring due to three different pathways including oxidation of the precursor, oxidation of the NPs or changes in reactivity as NPs grow. The first route of oxidation is oxidation of the precursor. Since precursor is added at the same addition rate throughout the reaction this should not increase appreciably during the reaction. The second route of oxidation is oxidation of the NPs. The third route is that low reactivity of Fe (II) and large NPs leads to less Fe (II) incorporation into the structure as NPs grow.

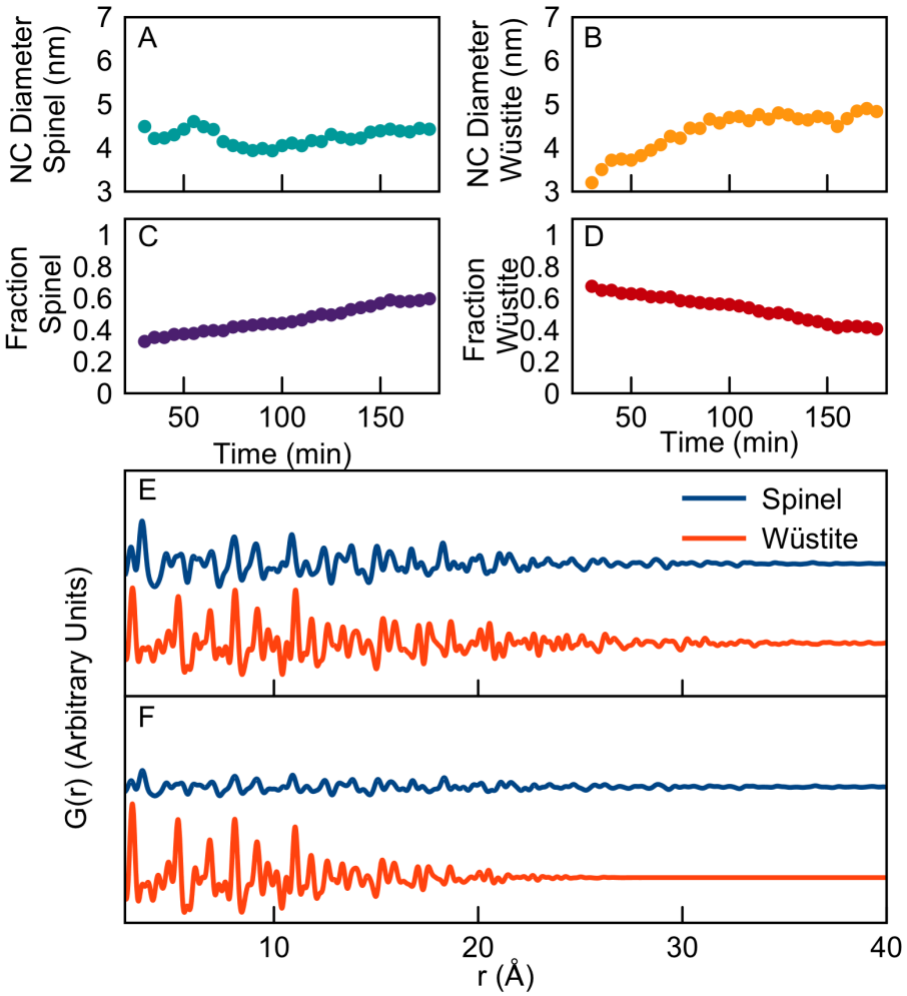

Figure 7. Refinement results for the amount of the two phases wüstite and spinel in NPs over the course of the reaction. Diameter refined for A) spinel and B) wüstite, the fraction of each phase of C) spinel and D) wüstite and the fit contribution for the sample at E) 175 min and F) 20 min in the reaction process. E) Fits of the final (top) and F) earliest (bottom) samples using a mixed model with simple spinel and wüstite phases.

The structure of ex situ products of NPs made with Fe (II) rich oleate after NPs were synthesized and stored at room temperature

The products produced from Fe (II) rich oleate precursor were analyzed weeks after synthesis by labscale XRD as well as PDF of total scattering data (Figure C29, Table C16-C19). Both techniques allowed for refinement of the NPs with spinel phases but showed contamination of NPs with residual wüstite phase. From prior data, completely oxidized NPs made from Fe (II) rich oleate with no detectable wüstite can be

obtained below 8 nm core diameter. Large NPs (above 8 nm) made with Fe (II) rich oleate contain some residual wüstite.

Precursor structure and oxidation state of Fe (II) rich oleate and Fe (III) rich oleate

Fe (III) rich oleate and Fe (II) rich oleate form NPs through very different growth mechanisms. Oxidation state has been shown in previous studies to have an impact on the speciation of the materials (Figure C30). For example, the crystal structure of Fe (II) acetate[82] is known to have a polymeric structure while Fe (III) acetylacetonate is known to form a trimer species.[83,84] There is a Fe (II) trimer known that takes a triangular ring structure [85] different from known Fe (III) and a mixed valence trimers (Figure C30).[83,84] The structure of the precursor could also be similar to a known cluster structure[86–89] or a cluster structure containing tetrahedrally coordinated iron, like the sought after keggin.[67,89,90]

Determining the structure of iron containing precursors with long chain organic ligands is not trivial. Common techniques to determine the structure of inorganic coordination compounds are not available for Fe (II) rich oleate or Fe (III) rich oleate. NMR cannot be used to determine the structure of the precursor because of paramagnetic iron in the structure which broadens NMR signals. The long chain organic ligands do not allow for crystallization of the material, so single crystal diffraction can also not be done to determine the structure. PDF analysis of Total X-ray Scattering data is a powerful technique to determine the oxidation state and structure of these metal oleate precursors.

To determine the relative oxidation state of the two precursors, Total X-ray scattering was taken of both Fe (II) rich oleate and Fe (III) rich oleate as synthesized under ambient conditions. The Fe-O bond length is shorter for Fe (III) iron cations and longer for Fe (II) iron cations. As can be seen in Figure 8, the Fe-O bond length (approximately 2.0 Å) is the shorter for Fe (III) rich oleate and the longer for the Fe (II) rich oleate as expected. Neither Fe (II) rich oleate or Fe (III) rich oleate have pure oxidation states. The two precursors do have different oxidation states with Fe (II) rich oleate being more reduced and Fe (III) rich oleate being more oxidized.

PDFs of Fe (II) rich oleate and Fe (III) rich oleate were fit with the six structural models in Figure C30. We hypothesized that the structure of Fe (II) rich oleate would resemble the structure of Fe (II) acetate and the structure of Fe (III) rich oleate would resemble the structure of Fe (III) acetylacetonate. We also thought it was possible that the precursor would adopt a known mixed valence trimer structure similar to the structure of Fe (III) acetylacetonate. A mixed valence trimer oleate was also synthesized and analyzed by Total X-ray Scattering data to see how mixed valence trimer oleate[83,84] compared to Fe (II) rich and Fe (III) rich oleate. PDFs of both Fe (II) rich oleate and Fe (III) rich oleate fit best to a mixed valence trimer structural model as well (Figure 8, C31). PDF of the mixed valence trimer oleate was described best to the mixed valence trimer structure[83,84] (Figure C32). The Fe (II) rich oleate may have some polymer content which cannot be detected in PDF data because the polymer would not exhibit long range order. The oxidation state of Fe (II) rich oleate and Fe (III) rich oleate is different but the structure of the two precursors is very similar.

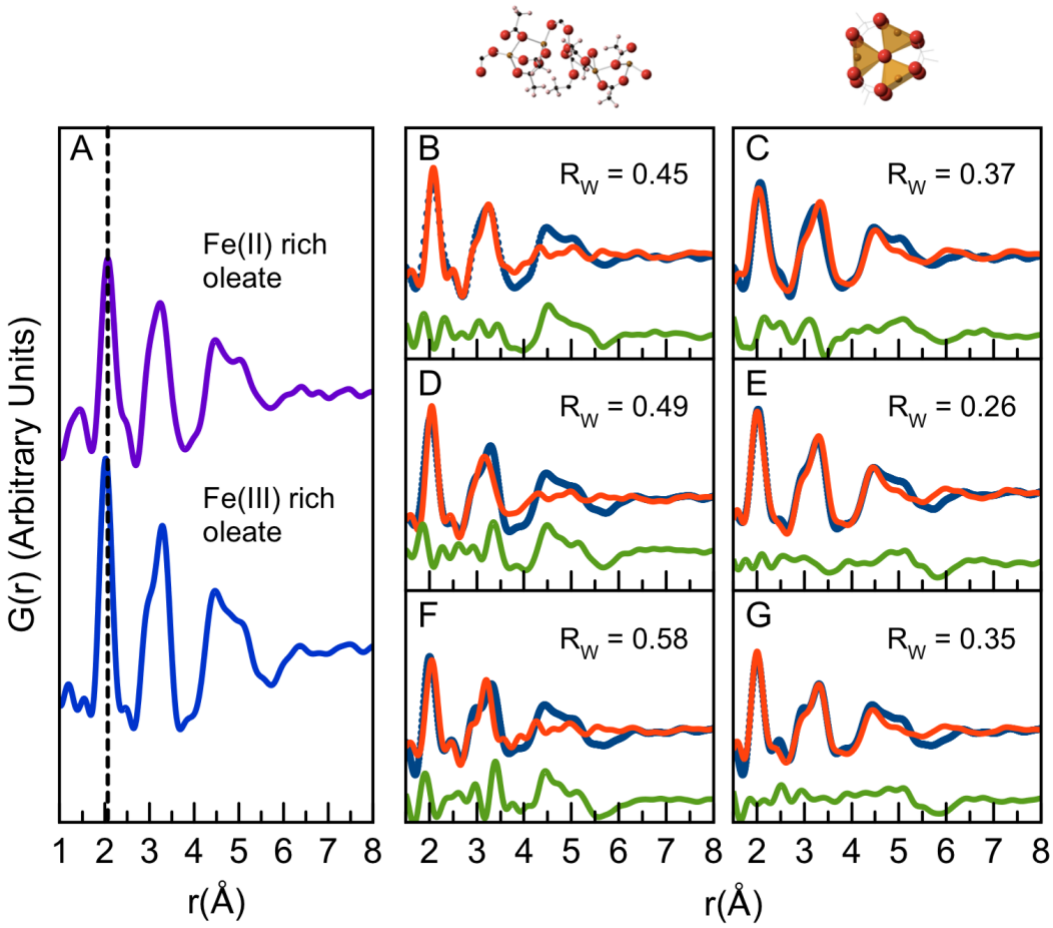

Figure 8. The fits of Fe (II) rich oleate and Fe (III) rich oleate and Fe (III) oleate with both Fe (II) acetate structure and Fe (II)/Fe (III) mixed valence iron trimer.

Synthesis of spinel iron oxide using Fe (II) oleate at reduced temperatures (230°C and 180°C) characterized by in situ using PDF

In addition to the composition of the precursor, reaction temperature is one of the most important reaction conditions that is known to influence NP formation mechanisms and the size of the NPs formed. Prior *ex situ* work produced smaller sizes at lower temperatures for the same amount of precursor added to the reaction flask with NPs as small as 2 nm in core diameter able to be isolated. Size of NPs made at 230°C and 180°C with the *in situ* set up can be seen in Figure 9. NPs that are formed at 180°C *in situ* had a significantly smaller final size with the same amount of precursor of 4.6 nm core

diameter as opposed to a 10 nm core diameter produced at 230°C. *Ex situ* studies also revealed interesting growth behavior at 180 °C where no growth was observed in aliquots from the synthesis until addition had stopped and NPs were annealed (Figure C33-C34). We wanted to probe NP reactions *in situ* in order to elucidate how temperature is affecting the reaction mechanism.

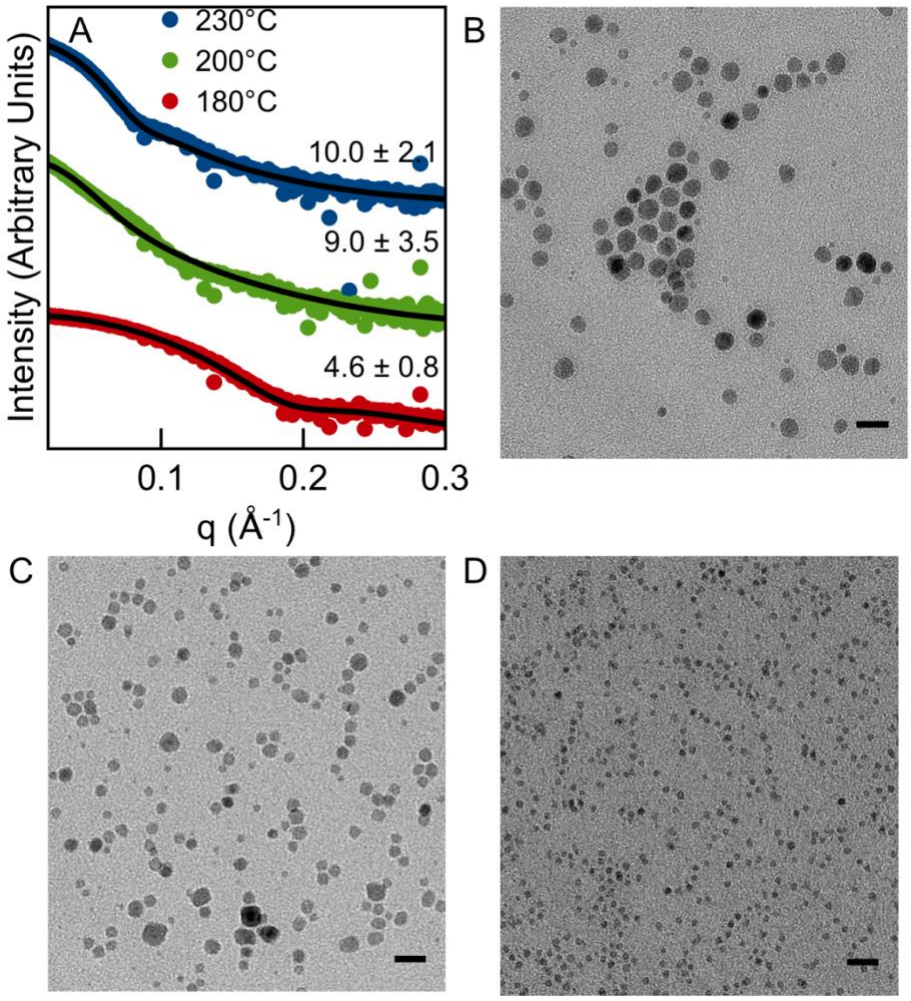

Figure 9. Comparison of the sizes and morphology of iron oxide NPs made at different temperatures as products of the *in situ* synthesis. A) SAXS patterns and sizes and dispersities of NPs made with Fe (II) oleate at 230°C (blue), 200°C (green) and 180°C (red). B) TEM of NPs made at 230°C with Fe (II) rich oleate. C) TEM of NPs made at 200°C with Fe (II) rich oleate. D) TEM of NPs made at 180°C with Fe (II) rich oleate. Scale bar is 20 nm

Comparison of in situ Synthesis of NCs at 180°C, and 230°C

Total X-ray Scattering data was collected for NPs made by continuous growth with Fe (II) oleate precursor at 180°C. The dual phase fit used in the refinement of *in situ* data for NPs made by continuous growth with a Fe (III) oleate precursor at 230°C. Data collected at 180 °C were refined from 4.2 Å to 60 Å (as opposed to 2.7 Å) because of the large amount of unreacted precursor that was persistent throughout the reaction. Fe (II) rich oleate peaks are less prominent at r values higher than 4.2 Å. R_W values from refinements were from 0.3 to 0.2. Data was refined from 70 minutes into the reaction due to the dilute and small materials at earlier time points.

Refinement of in situ data of NPs produced with Fe (II) rich oleate at 180°C had less wüstite content than NPs made at 230°C. In Figure 10 we see the contribution of both spinel and wüstite phases for fits at different time points including the earliest time points (Figure 10A, 10B), time points after injection of precursor stops (Figure 10 C, 10D) and the last data point collected *in situ* (Figure 10E, 10F). Samples produced at 230°C have a larger wüstite content while samples produced at 180°C have a larger spinel content. The NPs produced at 180°C data showed increased growth after addition of precursor stopped, similar behavior seen in ex situ samples produced by continuous growth at 180°C (Figure C35-C40). Fits of the 180°C *in situ* data did not fit well with either a pure spinel or pure wusitite phase (Figure C42-C45). Determination of phase after aging in air is shown in Figure C41 and fits with a spinel model. Data is included in Appendix C for data collected at 200C as well (Figure C46-C55). By performing the reaction at lower temperature, the oxidation state of the NPs was affected.

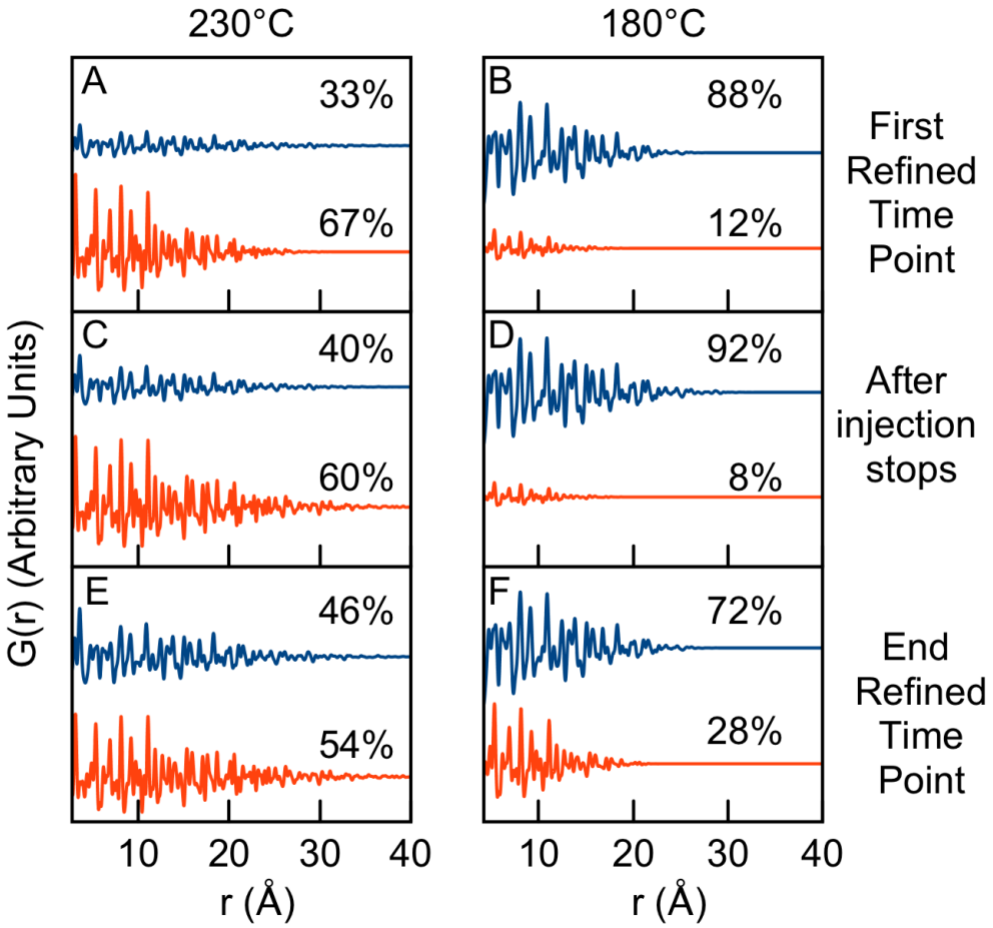

Figure 10. Component fits for three different timepoints in the reaction with temperature 230°C and 180°C using Fe (II) rich iron oleate. Blue is the spinel portion of the fit and red is the wüstite portion of the fit. The first refined timepoint for each temperature A) 230°C and B)180°C is in the top row. The acquisition after all precursor had been added C) 230°C and D) 180°C. The end point for E) 230°C and F) 180°C.

The *in situ* data of NP formation using Fe (II) rich oleate precursor at 180°C can help to elucidate what is the most likely oxidation pathway during the synthesis of NPs. The first option is that the precursor is oxidized during the reaction. The second option is that as NPs are oxidized after they are formed. Neither of these first two options are likely because the rate of oxidation should not increase with decreasing temperature. The third option is that at 180°C the rate of esterification of Fe (II) slows significantly compared to 230°C and less Fe (II) is incorporated into the NPs. Also, there was

unreacted precursor in the continuous growth synthesis at 180°C as described above, further suggesting that Fe (II) is not incorporating into the NPs. The main oxidation pathway of NPs is therefore that Fe (II) is not as reactive, therefore, Fe (II) is not incorporated at lower temperatures or into larger NPs which are less reactive.

Conclusions

In situ investigations of iron oxide NP synthesis by PDF analysis reveals precursor oxidation state and reaction temperature significantly influence the mechanisms of NP formation. The Fe (III) rich oleate precursor is a more reactive esterification catalyst than Fe (II) rich oleate, leading to more rapid and efficient incorporation of Fe (III) during synthesis. Fe (III) rich oleate results in Fe (III) rich NPs that are mainly magnetite in phase. The phase of NPs made with Fe (III) rich oleate show size dependent tetrahedrally coordinated occupancy to NPs measured *ex situ* made with Fe (II) rich oleate. Fe (II) rich oleate precursor results in more Fe (II) rich NPs which contain both spinel and wüstite phases. NPs made with Fe (II) rich oleate will oxidize to spinel after cooling to room temperature in air, but large NPs will contain some residual wüstite phase. The precursor structure is most similar to a mixed valence iron trimer for both Fe (II) rich oleate and Fe (III) rich oleate. NPs made at lower temperature with Fe (II) rich oleate form smaller sized NPs that are higher in spinel content as synthesized than NPs made at a higher temperature. The reactivity of Fe (II) rich oleate is lower than Fe (III) rich oleate which can be used to control the mechanism of spinel iron oxide NPs.

To control reactivity in a NP reaction of spinel iron oxide, oxidation state can be used to control the reaction products. Changing the oxidation state of the precursor changes the structures formed *in situ*. If a more reduced precursor is used a more reduced phase is formed during the reaction, in this case wüstite. NPs formed containing a reduced phase may lead to residual wüstite in NPs or changes in local atomic structure which is hard to detect. Iron oxide NCs made under reducing reaction conditions have been reported to have antiphase boundaries in the NPs that lower the saturation magnetization of the materials.[11] However, NPs made with Fe (II) rich oleate that form as wüstite and convert to spinel show some of the highest saturation magnetization values in the literature for NPs of the same size.[8] We hypothesize that thermal decomposition of an Fe (II) precursor under N_2 will react mainly through radical reactions since the esterification rate of Fe (II) is so slow. The formation of wüstite is not necessarily the main reason NPs formed under reducing conditions have defects but rather that thermal decomposition of Fe (II) precursors promotes radical reactions. By controlling the oxidation state of the materials during formation the phase and reaction rate can be tuned.

Knowledge of reactivity of precursor of different oxidation states can assist in the design of other materials which contain multiple oxidation states or multiple metal cations. Tuning the reactivity using both oxidation state and temperature could help to design NPs with dopants, multiple cations like ferrites and complex chalcogenides like Cu_2ZnSnS_4. Synthetic conditions of oxidation state and temperature can be used to control the speed of the reaction which could impact both the size and phase. Using the results of this study, unintended synthetic influence on the attributes of NPs that are of

interest to probe like size can be removed. Determining the reactivity of the precursor could help design NPs to obtain smaller NPs and to control the growth.

Materials and Methods

Fe (II) oleate synthesis

For the precursor synthesis, iron (II) acetate (99.99%) and oleic acid (90%, technical grade) were acquired from Sigma-Aldrich. Oleyl alcohol (85%, technical grade) was acquired from Alfa Aesar and used as the solvent in each synthesis.
Iron (II) acetate (521.8 mg, 3 mmol) was placed into a 20 mL vial fitted with a rubber septum along with 6 mL of oleic acid. The mixture was stirred under a constant flow of N_2 and heated to 150°C in an oil bath for 1 hour. Once cool, the precursor was transferred to a 10 mL BD Luer Lock plastic syringe and fitted with a custom length 16 G needle.

Fe (III) oleate synthesis

Iron (III) acetylacetonate (≥99.9%) was procured from Sigma Aldrich. Technical grade oleic acid (90%) was procured from Alfa Aesar. Iron oleate precursor was prepared by mixing a ratio of 1 mmol iron (III) acetylacetonate to 2 mL oleic acid in a 190˚C oil bath for two hours under air flow (about 200 mL/min).

Fe (III) rich oleate is made by a mixture that was made with Fe (II)/Fe (III) oleate in the ratio that would be in magnetite phase of iron oxide. Due to the Fe (II) rich oleate having some Fe (III) content this will not be a perfect ratio but will have more Fe (III) than Fe (II) and we will call this Fe (III) rich oleate.

Esterification determination with Fe (II) oleate and Fe (III) oleate

12.5 mL Oleyl alcohol (technical grade 80-85%, Alfa Aesar) was heated while stirring to 150˚C under nitrogen flow of ~250 mL/min. Two milliliters of iron precursor was injected into the oleyl alcohol at a rate of 0.17 mL/min. Aliquots (~0.3 mL) were removed using a glass syringe at various times during injection which took about 12 minutes. The reaction solution was held at 150˚ for another 20 minutes following the end of the precursor injection. During this period another three aliquots were removed. Nanoparticles were removed from aliquots by precipitating with about 8 mL acetone per aliquot and centrifuging at 7500 rpm for 10 minutes. Supernatant was collected by decanting, leaving behind brown solid. Acetone evaporated using a rotary evaporator leaving behind oil, which was analyzed by NMR.

TGA of precursor

Thermogravimetric analysis (TGA) was carried out with TA Instruments Q500. A drop of precursor oil (approximately 15 to 20 mg) was pipetted onto a tared aluminum pan resting on a platinum hanging pan. Mass was measured while heating from room temperature to 600˚C at a rate of 5˚C per minute. During the experiment, nitrogen was flowed through furnace at a rate of 60 mL/minute and through the balance chamber at a rate of 40 mL/min.

In situ synthetic set up and PDF data collection

Oleyl alcohol (12.5 mL) was placed in a 50 mL three-neck round bottom flask fitted with two rubber and one silicone septa. One rubber septum was used to deliver N_2

and acted as the inlet for the reaction mixture, the second, central rubber septum held a thermocouple attached to a heating mantle and heating controller, and the third silicone septum held the outlet for the reaction mixture as well as a larger gauge needle that acted as an escape outlet for gas and water. The liquid in the flask was placed under a constant N_2 flow, set to the desired temperature (180°C, 200°C, or 230°C), and magnetically stirred at a rate of 125 rpm.

A 16 G stainless steel needle acting as the outlet for reaction fluid was submerged fully in the oleyl alcohol. This needle was attached to a two-inch piece of silicone tubing through Luer Lock fittings. The silicone tubing was fitted with tension providers and placed around a Thomas brand Variable Flow Mini-Pump to pull reaction liquid from the flask. On the other side of the silicone tubing, a 30-centimeter length of stainless-steel tubing extended towards the beam and attached to around 6 cm of 3 mm scored glass NMR tubes secured in a custom-made cell with graphite ferrules, where PDF measurement took place. An elbow fitting extended from the other end of the cell and attached to a second, 45-centimeter length of stainless-steel tubing that returned back to the reaction flask, allowing reaction mixture to re-enter the flask. The peristaltic pump was placed on a setting of seven to ensure a constant flow of reaction fluid out of the flask.

The syringe containing the iron (II) precursor was placed onto a KD Scientific 200 syringe pump and the needle placed such that the precursor could drip cleanly into the flask. The syringe pump was set to have a 10-minute pause before the reaction began to enable securing of the hutch, movement of the detector, and the start of measurements. The contents of the precursor were then dripped into the reaction flask at an addition rate

of 2 mL/h. Each reaction ran for three hours with acquisitions every 10 seconds for the first 10 minutes, 1 minute for the next 60 minutes and 5 minutes for 100 minutes. Upon reaction completion, the product mixture was transferred to a 50 mL centrifuge tube. Each sample was washed with acetone and centrifuged at 7000 rpm for 20 minutes before being dispersed in toluene. The NCs were centrifuged once more for 5 min at 3500 rpm to remove any insoluble material.

The tubing was purged of reaction mixture and cleaned with hexanes until the hexanes ran clear. Two mL of oleyl alcohol was run through the tubing before each new experiment. The silicone tubing was replaced with fresh tubing prior to every experiment while the glass NMR tubes were used for multiple reaction.

PDF data analysis

Data was acquired at beamline 11-ID-B at Argonne National Lab's Advanced Photon Source. Instrumental resolution was refined using a CeO_2 standard. Q_{Broad} was set to 0.01 and Q_{Damp} was set to 0.04 for refinements. Samples were integrated using Fit2D[91] and PDFs were integrated then generated using xPDFsuite.[25-27] Data was analyzed using Diffpy-CMI.[80] Specific structural refinement details are included in Appendix C of this dissertation.

SAXS analysis

Small-angle X-ray scattering (SAXS) patterns were acquired for each synthesis using an Anton Paar SAXSess mc^2 instrument. NC core size, dispersity, and volume fraction were determined through modelling in the Irena software package[92] using a

Gaussian distribution equipped with a spherical form factor and a dilute system structure factor. The background was refined to account for iron fluorescence.

TEM analysis

Transmission electron microscopy grids (Ted Pella, 400 mesh copper) were prepared by drop-casting dilute solutions of the synthesized nanocrystals. Microscopy images were acquired on a FEI Technai G2 Spirit instrument and analyzed using FIJI software to determine diameter and area information. TEM data were used to corroborate size data from SAXS analysis. Determination of size and dispersity were done using FIJI[93] software.

XRD analysis

To prepare samples for XRD, approximately 30 mg nanocrystals were drop-cast onto (111) terminated silicon wafer with native oxide that was about 2 x 2 cm in size. A Rigaku SmartLab diffractometer with Cu Kα radiation and Bragg-Brentano geometry was used to collect XRD data. Additionally, a diffracted beam monochromator was installed to eliminate background from iron fluorescence. Patterns were collected from 10 to 70˚ 2-theta with a step size of 0.05˚ with scan lengths being from 5 to 8 hours. Data was refined using Rietveld refinement using FullProf software.[94]

Bridge to Chapter V

Chapter V of this dissertation includes both concluding statements and future directions. The impact this work has beyond the synthesis of iron oxide is also discussed.

CHAPTER V

PROSPECTS OF NANOCRYSTALS MADE BY PRECISE SYNTHETIC METHODS AND INCREASED INSIGHT ON NANOSCALE STRUCTURE

This Chapter was written with my advisors Darren W. Johnson and James E. Hutchison. I am a first author on this co-authored conclusion and future directions.

Concluding Remarks

Nanotechnology is expected to transform how we treat cancer, how we clean the environment from toxic materials and how we power our cities.[1–3] A major barrier, however, to the development of new applications for nanoparticles (NPs) is a lack of synthetic control of NP structural attributes like structure (phase, defects), composition (core and shell) and morphology (size, dispersity and shape).[4] Huge advances have been gained in the last 100 years in organic chemistry, where molecules can be made with impeccable specificity. NP synthesis is about 100 years behind organic synthesis, therefore materials can be made with similar composition and shape but with little understanding of defect and local structure in the materials.[5] Defect and local structure in NPs, however, is the cause of NP properties that differ from bulk.[6–8] The field is also hindered by the characterization techniques available to study structural attributes of NPs.[9] Traditional characterization techniques rely on global structure, like Bragg scattering, and do not provide information on local structure.[9] New synthetic techniques with great control over NP structural attributes are needed with the use of

characterization techniques that probe local structure to build structure property relationships of NPs.

A new synthetic method to make NPs, the continuous growth method, makes high quality metal oxide nanocrystals (NCs) with great control of size. The continuous growth method makes NCs that can be used to understand properties and structure of NCs below 10 nm in core diameter, because, the size of NCs can be changed simply by the amount of metal precursor added to the reaction flask. Continuous growth also allows for the probing of individual reaction conditions because it is facile to change one condition, like the precursor oxidation state or temperature of the reaction, while keeping every other condition the same. In addition, NCs made by continuous growth are lower in defects because NCs form through a controlled reaction pathway, a metal catalyzed esterification reaction.[4,10] Other synthetic methods to make NPs in organic solvent form NPs through thermal decomposition, which produces many intermediate products and leads to defects in the core of the NPs that are not caused by reduction in core diameter.[11,12] In this dissertation we probed spinel iron oxide properties and nanoscale structure of NCs using the continuous growth method.

In Chapter II of this dissertation, the continuous growth synthesis enabled new understanding on the size-dependent saturation magnetization of spinel iron oxide NCs from 4-10 nm. Saturation magnetization of NCs made by continuous growth were found to be size-dependent and of larger magnitude than values measured for materials of the same core diameter made by other synthetic methods. Magnetic sizes of the NCs determined by fitting magnetization curves to the Langevin function are nearly identical to the physical sizes determined by Small Angle X-ray Scattering (SAXS), suggesting

low levels of strain-producing defects and a very thin non-magnetic surface layer on the NCs. A thin non-magnetic surface layer is contrary to prior studies that report non-magnetic shells between 0.35 and 1.0 nm thick, a significant percentage of the volume of a sub-10 nm NP.[4,13,14] NPs made by other synthetic methods, like aqueous co-precipitation methods or thermal decomposition, have defects in the NP core that lead to changes in properties.[12,15–18]

In Chapter III of this dissertation, Pair Distribution Function Analysis (PDF) of Total X-ray Scattering Data were acquired and then refined to extract quantitative structural information including size and presence of cation vacancies in spinel iron oxide NCs made by continuous growth. PDF is a characterization technique that can probe the nanoscale structure. There is a decrease in the tetrahedrally coordinated cation occupancy in smaller core diameters showing that this is a ubiquitous structural feature for spherical spinel iron oxide NCs below 10 nm. We also observe a trend in the increased reactivity in smaller NCs compared to larger NCs. The increased reactivity of NCs with small core diameter impacts growth.

Finally, in Chapter IV of this dissertation, *in situ* Total X-ray Scattering data collected during a continuous growth synthesis was used to investigate the impact that precursor oxidation state has on the mechanism of NP formation. It was determined that by using a more reduced precursor, a more reduced reaction product formed. In this study, starting with Fe (II) rich precursor resulted in wüstite formation, which contains only Fe (II). We also found the reactivity of Fe (II) is slower compared to Fe (III). Slower reactivity of Fe (II) and slower reactivity on the surface of NPs with larger core diameter leads to a change in growth rate for NPs over around 6 nm in diameter.

This dissertation determined design principles that can lead to higher quality iron oxide NCs. Slow controlled growth is needed to form NPs that are low in defect concentration. NPs made with fast reaction methods, like hydrolysis or thermal decomposition, yield products that have defects that impact the properties of the material. Many of these defects are not detected by characterization methods commonly used to characterize NPs, therefore, it is the wide range of values reported for the properties of same material and core diameter which indicate defects are present. Understanding the reaction mechanisms in the formation of NPs and how reaction conditions impact the structures formed is of great importance. For example, NPs report reduced magnetic properties when wüstite is formed during the reaction. By forming NCs by continuous growth, increased magnetic properties are observed even though wüstite is formed during the reaction. We hypothesize that NPs made at temperatures above thermal decomposition and with Fe (II) precursor will be more likely to react through radical mechanisms because Fe (II) is not good at catalyzing esterification. NPs can be designed by understanding what synthetic conditions impact their structure.

Future directions

In the synthesis of iron oxide NPs, the impact of a variety of other synthetic conditions still needs to be investigated, like the impact of additives, solvent and ligand shell. Determining the impact that both ligand shell and NP shape have on properties is of particular interest.[19–22] While some studies have been done to produce NPs of different ligand shells and shapes, the methods to make NPs in these studies are methods that

impart defects. [19–22] What impact both ligand shell and shape actually have on the properties of NPs still needs to be determined.

PDF analysis of *in situ* Total X-ray Scattering data will enable even greater insight into the structures formed during NP reactions. By gaining insight on a variety of conditions and a variety of materials, synthetic strategies for a wide library of materials will be determined. Currently the syntheses that have been tested by *in situ* PDF are limited. Most syntheses are aqueous methods, which already known to be prone to defects and large dispersities. As more data is gathered for systems that produce high quality NPs, the structure of NPs will be controlled with greater specificity.

Continuous growth is a general synthetic method that can be used to make a wide variety of metal oxide NCs as well as core-shell and doped metal oxides.[23–25] Specifically, there are some materials that have been difficult to make by continuous growth. These include TiO_2 and SnO_2. Both of these materials are complex because it is easy to obtain multiple oxidation states of both Ti and Sn. For example, on initial investigation of SnO_2, it was found that small SnO_2 NCs would form, but then the material would gel over the course of a few hours and would no longer be soluble in any solvents. What we have learned about how oxidation state impacts the growth of NCs can inform a strategy to synthesize other materials using continuous growth. In this case, for SnO_2 we would like to ensure that the oxidation state remains Sn(IV) throughout the reaction. By monitoring the atmosphere (incorporating some oxygen) and the oxidation state of the precursor, we can start to change reaction parameters based on hypothesis and not trial and error.

We expect that not only metal oxide can be impacted with this work but also other materials like metal chalcogenides. Complex metal chalcogenide NPs, like Cu_2ZnSnS_4, are hindered for use as photoadsorbers because of poor material quality.[26,27] The work presented in this dissertation gives insight into what synthetic methods are most likely to make high quality NPs; synthetic conditions should be lower than the thermal decomposition temperature of the precursor, performed in organic solvents, contain reactants that will promote controlled reactions and tune size by solely adding more precursor. Choosing methods that are more likely to form high quality parent metal chalcogenides, like Cu_xS, and studying how they form by *in situ* PDF will enable the synthesis of a large library of metal chalcogenides.[28,29]

APPENDIX A

SUPPLEMENTARY INFORMATION FOR CHAPTER II: INSIGHTS INTO THE MAGNETIC PROPERTIES OF SUB-10 NM IRON OXIDE NANOCRYSTALS THROUGH THE USE OF A CONTINUOUS GROWTH SYNTHESIS

Table A1. NC diameter and dispersity determined by SAXS of NC samples shown in Figure 1A.

NC diameter and dispersity (nm)
3.8 +/- 0.7
5.3 +/- 0.6
5.9 +/- 0.7
6.7 +/- 0.7
7.2 +/- 0.6
8.0 +/- 0.7
8.5 +/- 0.8
8.8 +/- 0.9
9.1 +/- 1.0
9.4 +/- 1.0
9.6 +/- 1.1
9.8 +/- 1.2
10.0 +/- 1.2

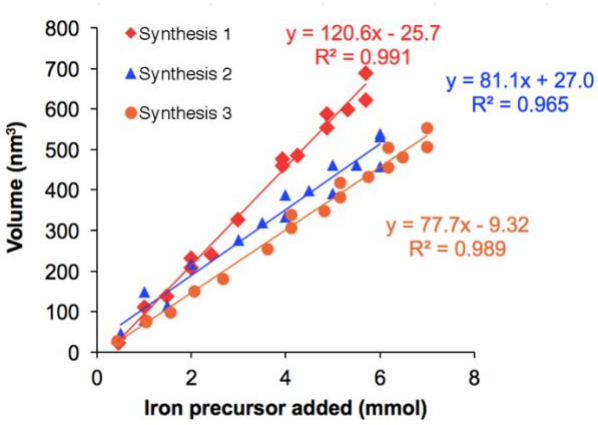

Figure A1. Growth of nanocrystals as a function of amount of precursor added for three different syntheses. Nanocrystal size is displayed in volume calculated from SAXS diameter.

Discussion of Figure A1

Variation in growth rate is a result of different number of nuclei being formed during the nucleation event. If fewer nuclei form, then each growing particle attains more of the subsequent precursor and grows larger than if more nuclei were formed. The number of nuclei formed depends on the nucleation rate and the period of time over which nucleation occurs. Nucleation is highly sensitive to reaction conditions such as temperature, surface free energy, and supersaturation.[1] There may also be variation in the nucleation period since precursor is added dropwise and the exact volume of the drops in the initial stage of the synthesis could be slightly different from synthesis to synthesis. Nonetheless, the utility of continuous injection syntheses is that the particle size is not determined by the nucleation event alone but by the amount of precursor added to the reaction flask.

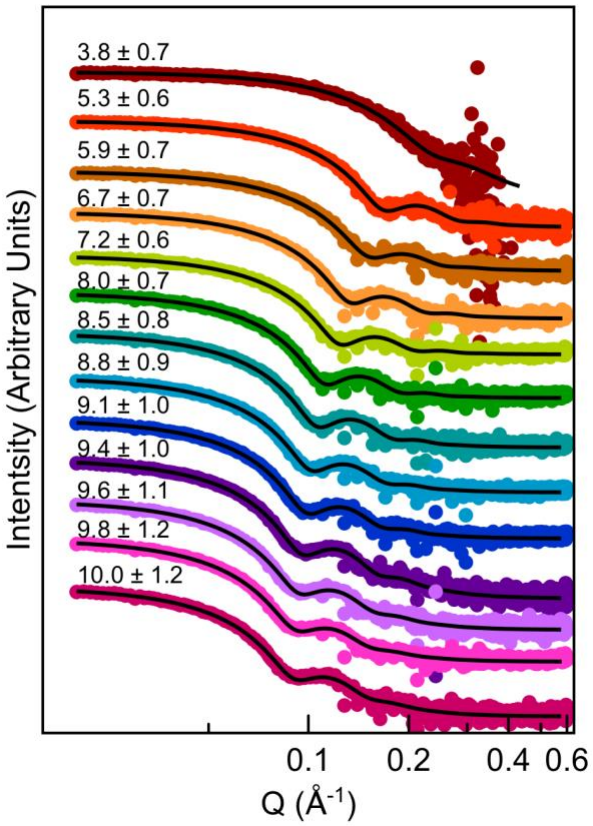

Figure A2. SAXS patterns are shown for a growth curve with sizes from 4-10 nm. The SAXS patterns are stacked from largest (top) to smallest (bottom). Black lines over each SAXS pattern is the fit used to determine size and dispersity of the NCs.

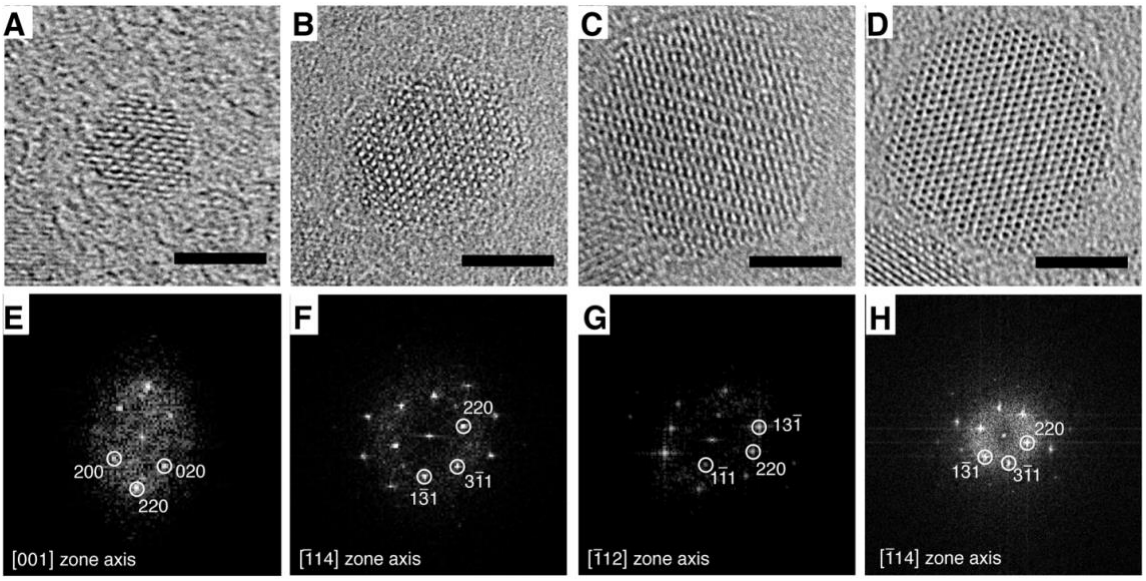

Figure A3. Indexing of HRTEM single particle electron diffraction. HRTEM of four different NC sizes (A-D) with corresponding indexed FFT patterns (E-H) directly below. NCs have sizes (determined by SAXS) of 3.9 +/- 0.6 nm (A, E), 5.1 +/- 0.7 nm (B, F), 6.6 +/- 0.6 nm (C, G), and 8.0 +/- 0.8 nm (D, H).

Discussion of Figure A3:
Indexed FFT patterns are included in Figure A3 to confirm that the particles produced are single crystalline.

Rietveld Analysis of Powder Diffraction Data

Rietveld refinement was performed using the Fullprof suite[2] on acquired Powder XRD data in order to verify the phase. A magnetite crystal structure with spacegroup *Fd-3m* was used to perform the refinement.[3] A standard of crystalline magnetite was refined to determine the instrumental broadening. The background was refined using a 12-term Chebyshev polynomial. For the magnetite phase, the scale factor was refined along with the unit cell parameter, the IG peak shape parameter and the instrumental displacement. B values of Fe and O fixed at 1 Å-2 have been used recently in detailed analysis of iron oxide nanocrystals.[4] Further, changing the B value from 0.5 Å-2 to 2.0 Å-2 for both Fe and O did not change the refined values for the unit cell parameter or the IG size parameter. The refinements and results are given in Figure A2-S4 and Table A2-S4.

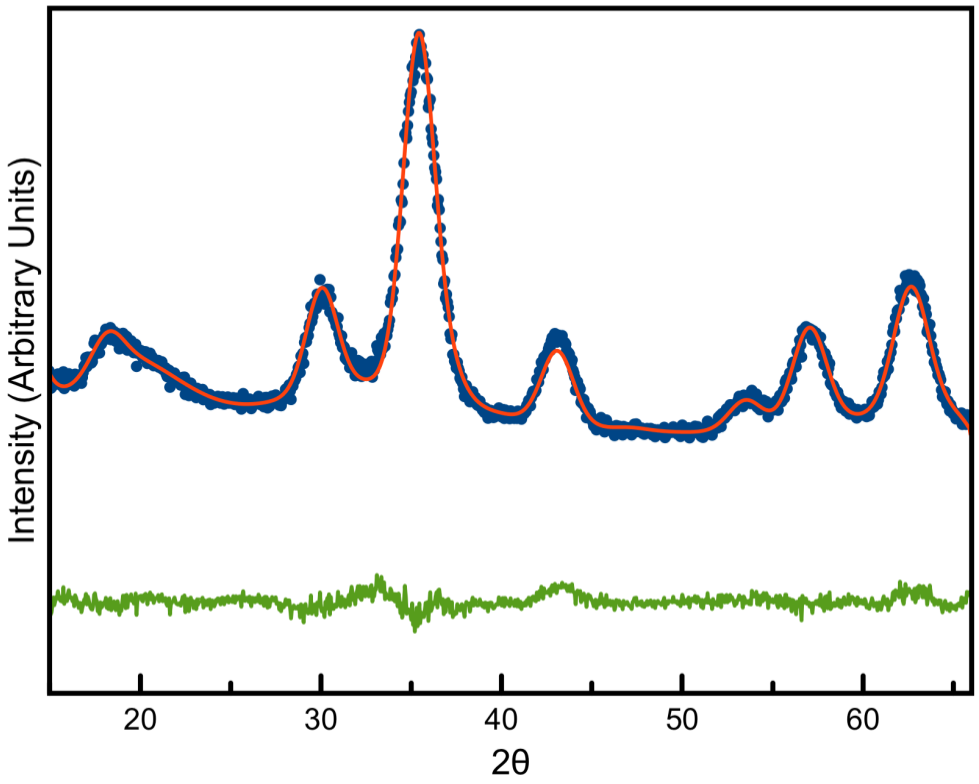

Figure A4. Powder XRD pattern (blue dots) of the 5 nm (measured by SAXS) NC sample, fit using Rietveld refinement (red line) to verify the spinel iron oxide phase and crystallite size. The difference between the data and the model is shown by the green line.

Table A2. Refined parameters using Rietveld refinement of the 5 nm NC sample (measured by SAXS). Spacegroup *Fd-3m.*

Bragg R-factor	3.8 %
R-factor	3.6 %
A	8.372 Å
Instrument Displacement	-0.15
IG	3.60
Crystallite diameter	4.4 nm

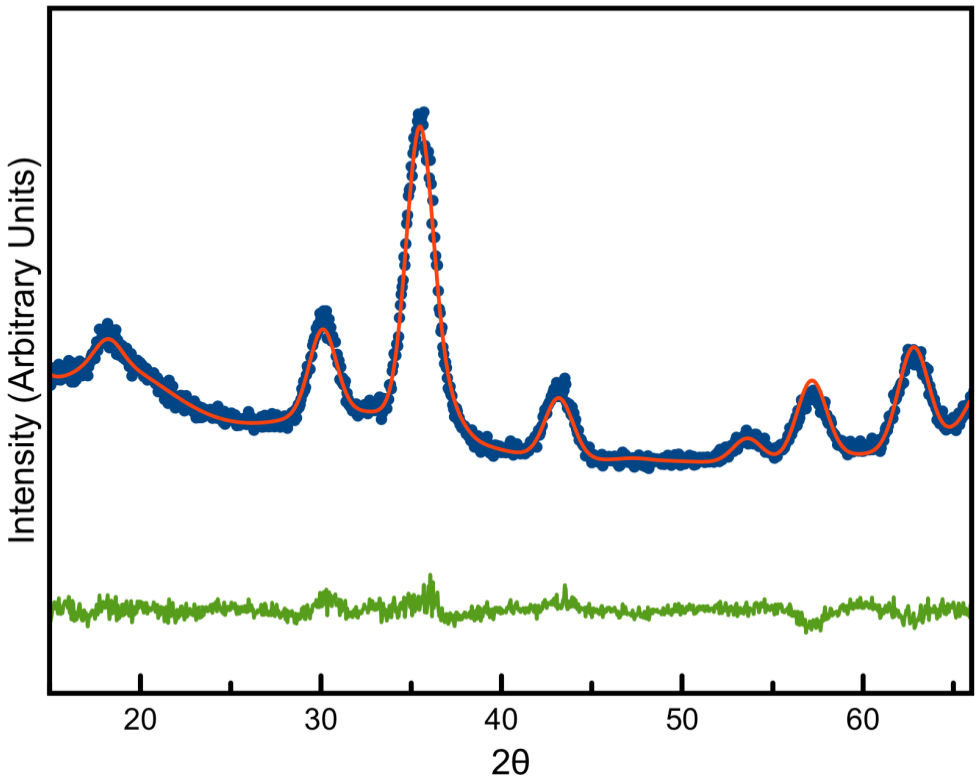

Figure A5. Powder XRD pattern (blue dots) of a 6 nm NC sample (measured by SAXS), fit using Rietveld refinement (red line) to verify the spinel iron oxide phase and crystallite size. The difference between the data and the model is shown by the green line.

Table A3. Refined parameters using Rietveld refinement of a 6 nm NC sample (measured by SAXS). Spacegroup *Fd-3m*.

Bragg R-factor	5.9%
R-factor	5.7%
A	8.353 Å
Instrument Displacement	-0.17
IG	2.73
Crystallite diameter	5.0 nm

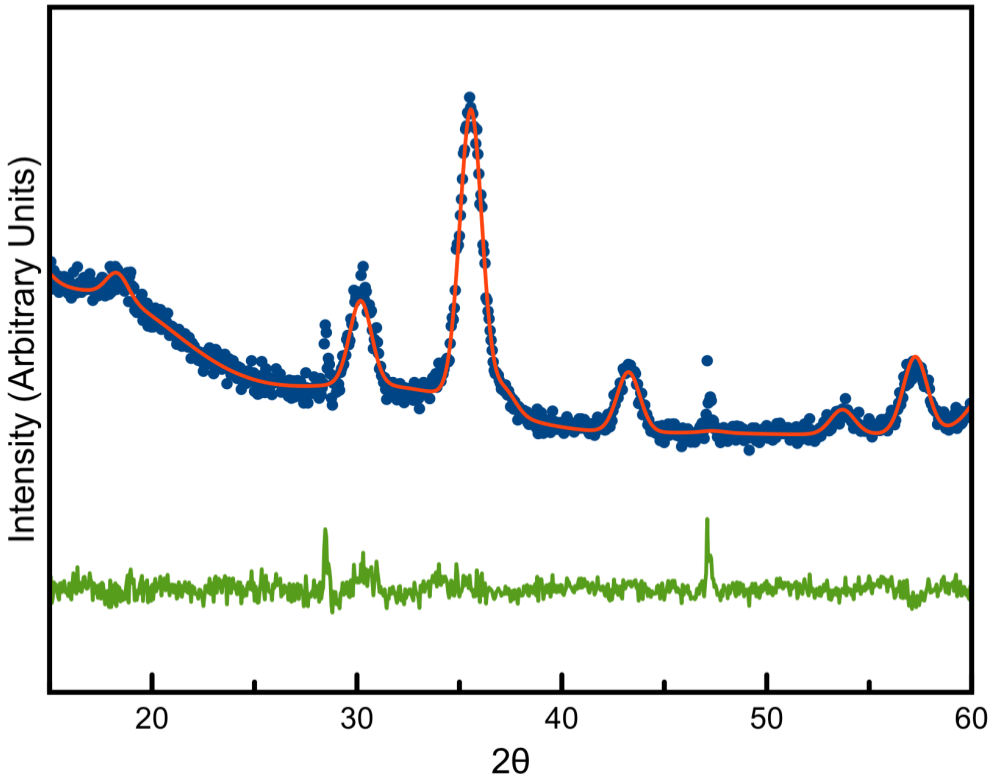

Figure A6. Powder XRD pattern (blue dots) of a 9 nm NC sample (measured by SAXS), fit using Rietveld refinement (red line) to verify the spinel iron oxide phase and crystallite size. The difference between the data and the model is shown by the green line. Peaks at 28° and 47° are from the Si wafer used as a substrate.

Table A4. Refined parameters using Rietveld refinement of a 9 nm NC sample (measured by SAXS). Spacegroup *Fd-3m.*

Bragg R-factor	4.9 %
R-factor	4.0 %
A	8.346 Å
Instrument Displacement	-0.12
IG	1.38
Crystallite diameter	7.1 nm

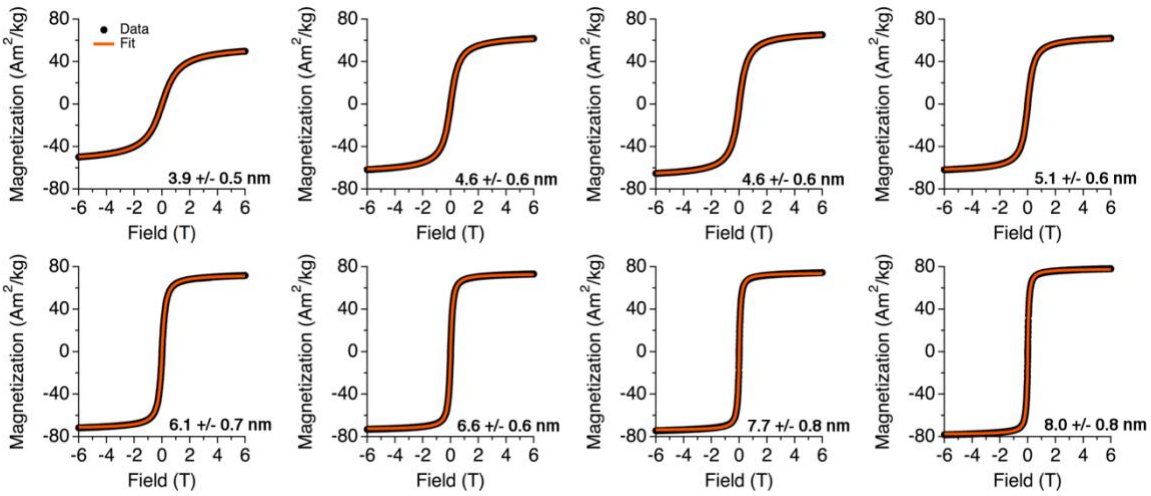

Figure A7. Room temperature magnetization curves of a size series of nanocrystals. Measured data are black while fits to Langevin equation are orange.

Table A5: Physical diameter and standard deviation of size distribution as determined by SAXS, magnetic diameter and standard deviation of distribution as determined by fitting Langevin equation to magnetization curves, percent maghemite as determined by optical absorbance, and the saturation magnetization also determined by fits to magnetization curve.

Physical size (nm)	Magnetic size (nm)	% γ-Fe_2O_3	Saturation Magnetization (Am^2/kg)
3.9 +/- 0.6	3.5 +/- 0.5	98	54.6 +/- 1.0
4.6 +/- 0.7	4.4 +/- 0.7	94	64.3 +/- 1.1
4.6 +/- 0.7	4.4 +/- 0.8	95	68.3 +/- 1.2
5.1 +/- 0.7	4.8 +/- 0.8	92	63.7 +/- 1.1
6.1 +/- 0.8	5.9 +/- 1.1	86	72.7 +/- 1.3
6.6 +/- 0.7	6.7 +/- 1.0	81	73.5 +/- 1.3
7.7 +/- 0.9	7.6 +/- 1.4	79	74.2 +/- 1.3
8.0 +/- 0.9	8.0 +/- 1.6	74	78.0 +/- 1.4

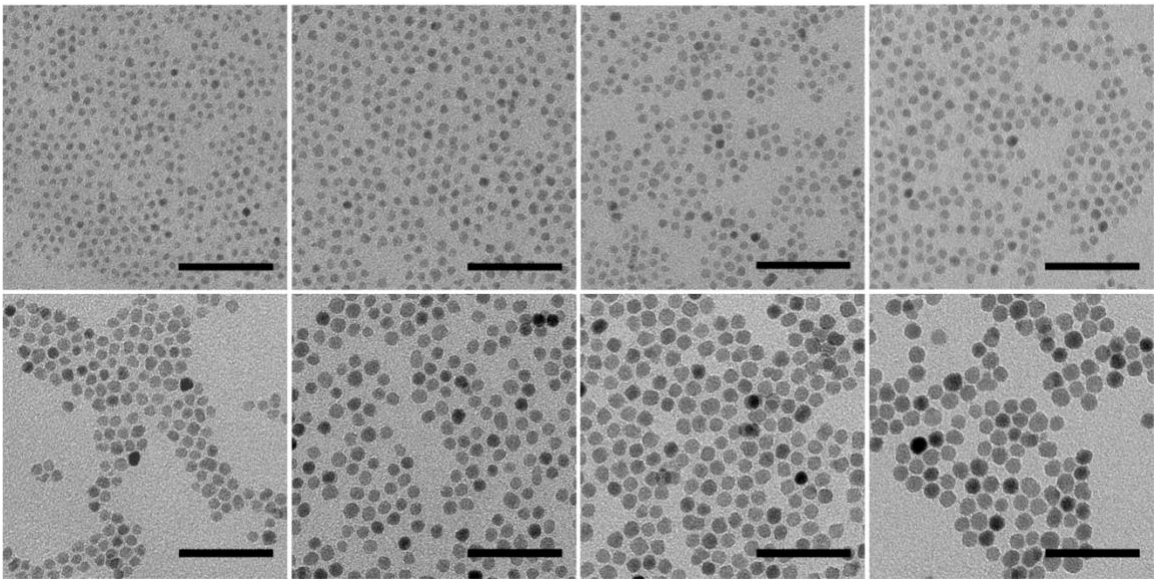

Figure A8. TEM images of all NC samples that were magnetically characterized. Scale bars are 50 nm.

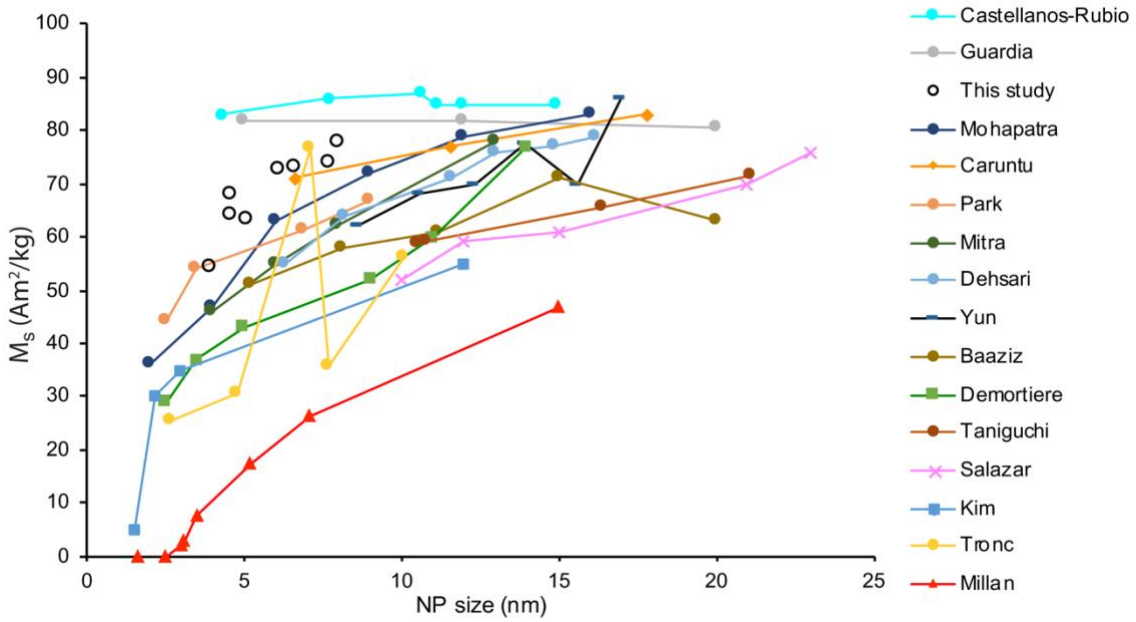

Figure A9. Collection of M_s values reported in the literature plotted versus nanoparticle size. Includes information from Castellanos-Rubio *et al.*,[5] Guardia *et al.*,[6] Mohapatra *et al.*,[7] Caruntu *et al.*,[8] Park *et al.*,[9] Mitra *et al.*,[10] Dehsari *et al.*,[11] Yun *et al.*,[12] Baaziz *et al.*,[13] Demortière *et al.*,[14] Taniguchi *et al.*,[15] Salazar *et al.*,[16] Kim *et al.*,[17] Tronc *et al.*,[18] Millan *et al.*,[19] and this study. Note that the values reported by Guardia *et al.*, Demortière *et al.*, and Baaziz *et al.* were measured at low temperature (5K), which has the effect of elevating the M_s compared to room temperature measurements.

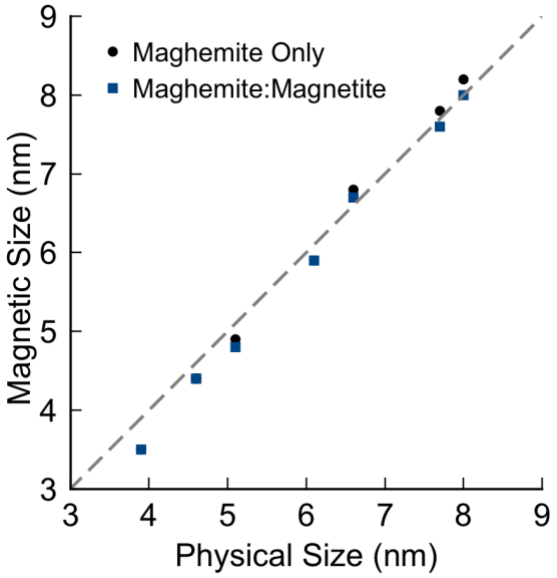

Figure A10. The effective magnetic size using two different values for M_D from Langevin function fit plotted as a function of physical size measured by SAXS. Black dots are calculated using M_D commonly used for maghemite of 76 Am^2/kg. Blue squares are calculated using M_D which reflects the ratio of maghemite:magnetite determined by Near-IR. For the blue squares M_D used for the maghemite percentage was 76 Am^2/kg and M_D used for the magnetite percentage was 92 Am^2/kg. The gray dashed line is y=x.

Discussion of Figure A10

We also calculated the magnetic size using an M_D equal to the variable percentage of maghemite:magnetite determined by near-IR in Table A5 in addition to using an M_D value for maghemite (Figure A10). We used M_D values of 76 Am^2/kg for maghemite and 92 Am^2/kg for magnetite to calculate the adjusted M_D of the NCs. We then used the M_D for each NC to calculate the magnetic size using $m = M_D * \frac{\pi}{6} D_C^3$ from Equation 1. Using a variable value of M_D lowers the magnetic size a bit for larger NCs, as would be expected due to larger magnetite content, so that the magnetic size is not larger than the physical size.

APPENDIX B

SUPPLEMENTARY INFORMATION FOR CHAPTER III: SIZE-DEPENDENT STRUCTURAL FEATURES AND ENHANCED REACTIVITY OF SUB-10 NM IRON OXIDE NANOCRYSTALS

Table B1. The nanocrystal (NC) size measured by three different methods: PDF, SAXS and TEM. Diameter was determined by PDF refinement using $P4_32_12$ space group. Size was determined by SAXS for 8 samples using a spherical form factor, a dilute structure function and a Gaussian distribution. Size analysis was used on TEMs to determine the size and dispersity of 4 samples across the size series to corroborate the other diameters.

PDF Crystallite Diameter (nm)	SAXS Diameter (nm)	TEM Diameter (nm)
2.9	--	--
3.7	--	--
3.8	4.4 ± 0.4	3.5 ± 0.9 (189 NCs)
3.9	--	--
3.7	5.0 ± 0.2	--
5.2	5.3 ± 0.3	--
4.8	--	4.8 ± 0.7 (1504 NCs)
4.8	--	--
4.8	--	--
5.2	--	--
6.1	5.9 ± 0.6	--
7.0	6.6 ± 0.6	7.3 ± 1.2 (180 NCs)
9.0	7.9 ± 0.9	--
7.1	--	--
8.2	8.0 ± 1.1	--
9.1	9.2 ± 0.9	9.2 ± 2.5 (125 NCs)
9.6	8.8 ± 1.1	--

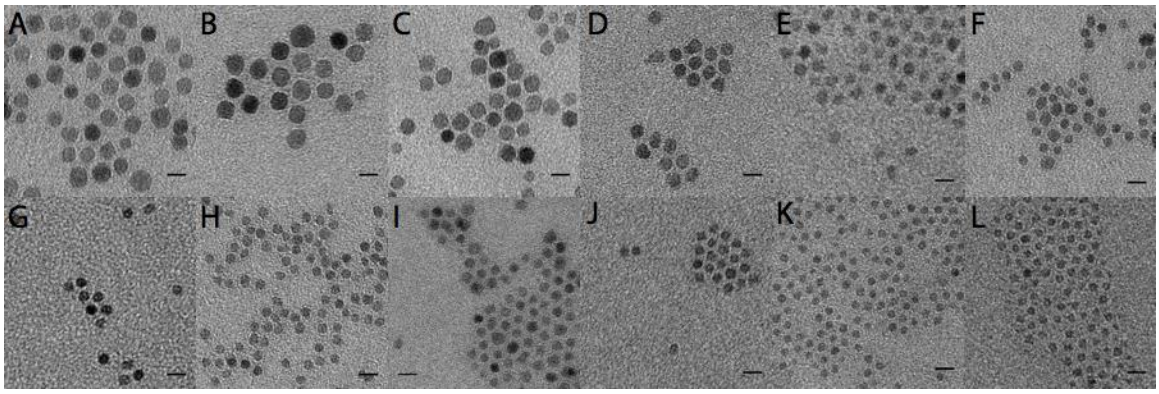

Figure B1. TEM for 12 samples with core diameters from 9.6-3.7 nm determined by PDF. A) 9.6 nm, B) 9.1 nm, C) 9.0 nm, D) 7.0 nm, E) 6.1 nm, F) 4.8 nm, G) 4.8 nm, H) 4.8 nm, I) 5.5 nm, J) 3.7 nm, K) 3.8 nm and L) 3.7 nm.

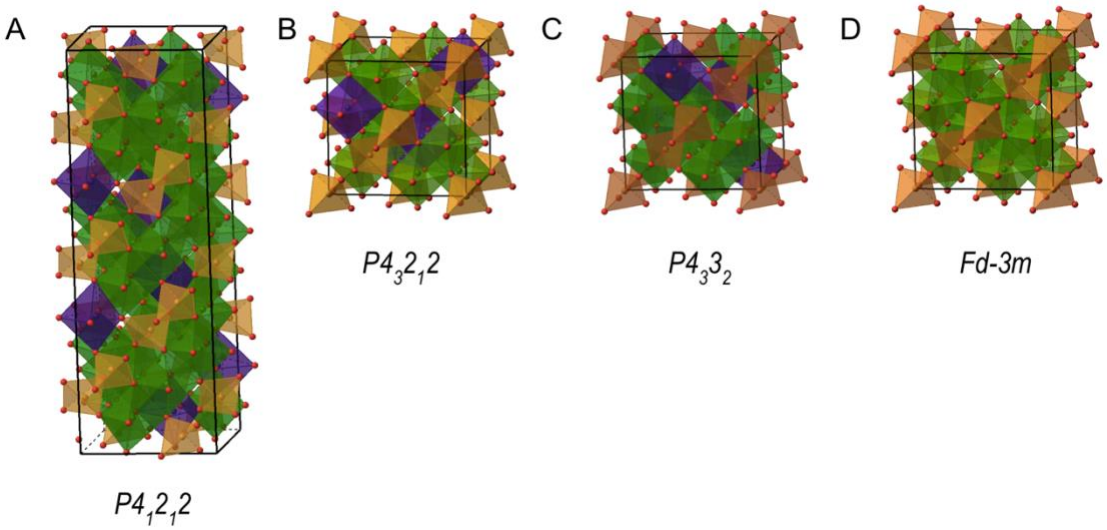

Figure B2. Polyhedral figures of 4 structures compared in this work: A)$P4_12_12$ B) $P4_32_12$ C) $P4_33_2$ and D) *Fd-3m*.

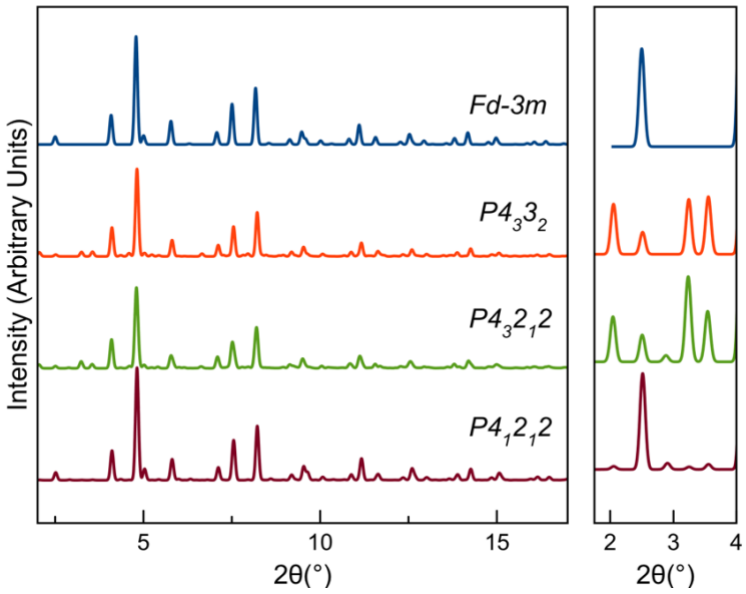

Figure B3. Reported XRD patterns of four crystallographic models. Using crystal diffract software we can display the superstructure in the various structural models that have been solved in the literature. Above plots from 2°-17° and from 1.7°-4° shows a zoom of the superstructure at low angles. From top to bottom crystallographic models are *Fd-3m*, $P4_33_2$, $P4_32_12$ and $P4_12_12$.

Rietveld Analysis of Synchrotron Powder Diffraction Data.

Rietveld refinement was performed on powder diffraction data collected at Argonne National Lab Advanced Photon Source at beamline 11-ID-B using the Fullprof[1] program. Instrumental broadening was determined by refining parameters for a CeO_2 standard. A linear interpolation of points was used to refine the background. The largest sample tested (9.6 nm by PDF) was refined with four different crystallographic models taking the space groups. *Fd-3m*,[2] $P4_33_2$,[3] $P4_32_12$,[4] $P4_12_12$[5]. Three samples were then analyzed by the structural model that takes the space group $P4_32_12$ which was used to analyze the PDF samples. The scale factor, cell parameters, Debye-Waller factor for iron and the Y and IG peak shape parameters were all refined for each refinement. The Debye-Waller factor for iron was constrained to be constant for all iron atoms in the structure except for in the

case of the structural model that takes the space group *Fd-3m*. Refinements and results are included in Figure B4- B6 and Table B2-B5.

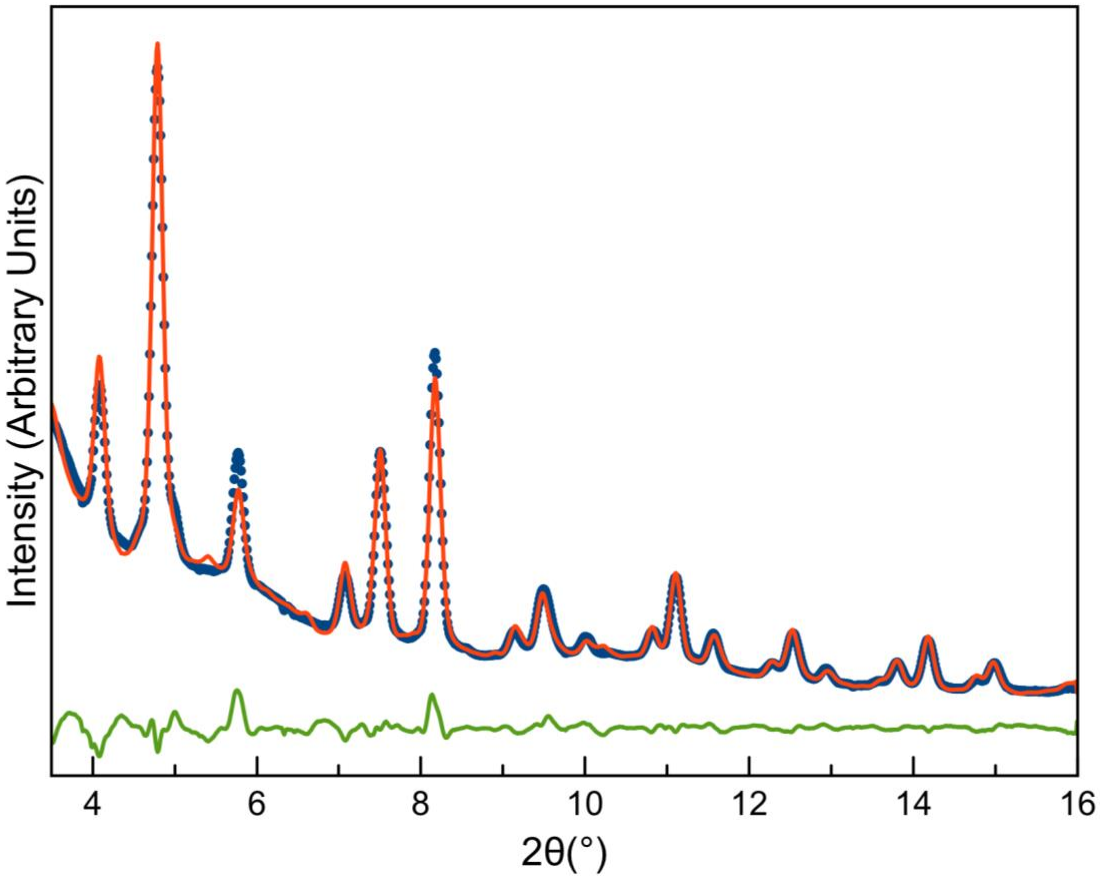

Figure B4. XRD pattern (blue dots) of a 9.6 nm NC (by PDF) fit using Rietveld refinement (red line) with the structural model in space group $P4_32_12$. The difference curve between the data and the model is shown in green. Space group $P4_32_12$.

Table B2. Refined parameters using Rietveld refinement of the 9.6 nm NC (measured by PDF). Space group $P4_32_12$.

Bragg R factor	5.2 %
Rf factor	4.5 %
a	8.381 Å
c	8.410 Å
Biso Fe	0.114 $Å^{-2}$
Instrument Displacement	-0.0006
Y	0.067
IG	0.013
Crystallite diameter (nm)	7.5 nm

Table B3. Refined parameters comparing Rietveld refinement of an 9.6 nm NC (measured by PDF) across the four different structural models: *Fd-3m, $P4_33_2$, $P4_32_12$, $P4_12_12$*.

Space Group	*Fd-3m*	*$P4_33_2$*	*$P4_32_12$*	*$P4_12_12$*
Bragg R factor	3.9 %	6.7 %	5.2 %	6.7 %
Rf factor	3.1 %	7.2 %	4.5 %	7.2 %
A	8.389 Å	8.391 Å	8.381 Å	8.386 Å
C	--	--	8.410 Å	25.204 Å
Biso Fe	0.598 $Å^{-2}$ (Fe1) 0.545 $Å^{-2}$ (Fe2)	0.090 $Å^{-2}$	0.114 $Å^{-2}$	0.542 $Å^{-2}$
Instrument Displacement	-0.0025	0.0002	-0.0006	-0.0010
Y	0.034	0.061	0.067	0.036
IG	0.018	0.014	0.013	0.017
Crystallite diameter (nm)	7.5 nm	7.4 nm	7.5 nm	7.5 nm

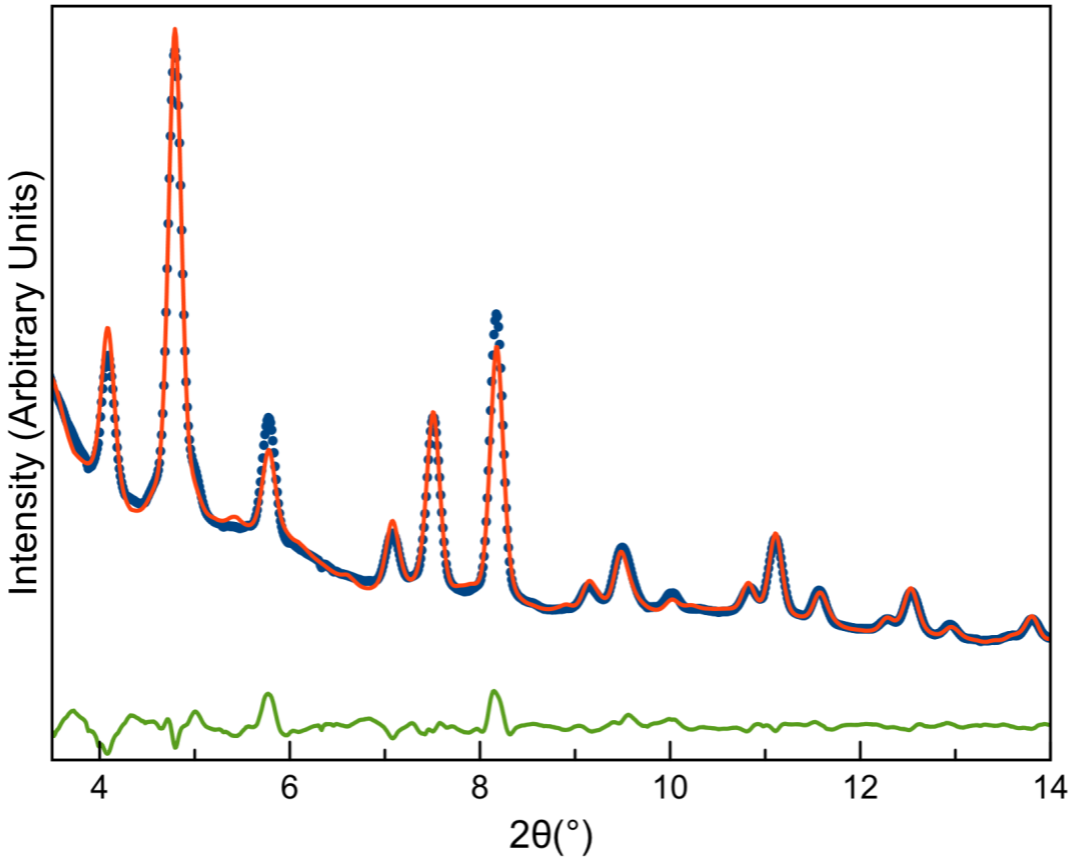

Figure B5. PXRD pattern (blue dots) of an 9.1 nm NC (by PDF) fit using Rietveld refinement (red line) with the structural model in space group $P4_32_12$. The difference curve between the data and the model is shown in green. Space group $P4_32_12$.

Table B4. Refined parameters using Rietveld refinement of the 9.1 nm NC (measured by PDF). Space group $P4_32_12$.

Bragg R factor	6.2 %
Rf factor	4.7 %
A	8.379 Å
C	8.398 Å
Biso Fe	0.162 $Å^{-2}$
Instrument Displacement	-0.0016
Y	0.061
IG	0.016
Crystallite diameter (nm)	7.1 nm

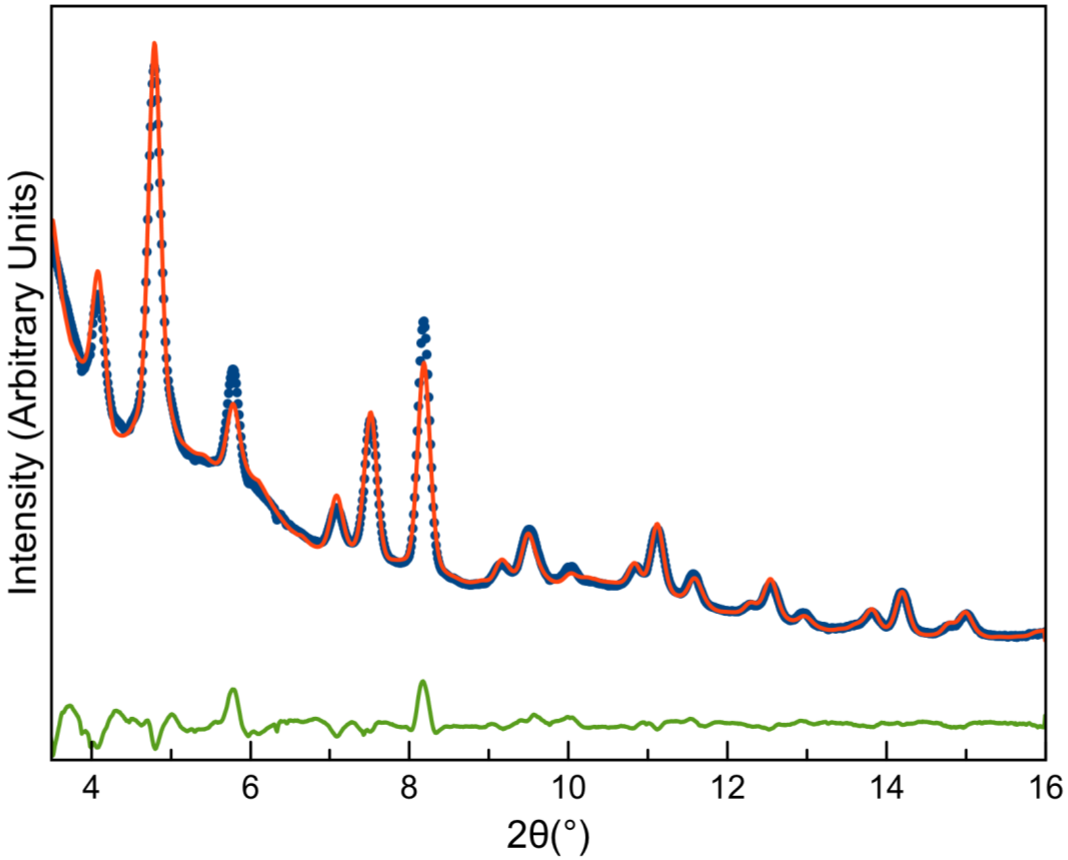

Figure B6. PXRD pattern (blue dots) of an 8.2 nm NC (by PDF) fit using Rietveld refinement (red line) with the structural model in space group $P4_32_12$. The difference curve between the data and the model is shown in green. Space group $P4_32_12$.

Table B5. Refined parameters using Rietveld refinement of the 8.2 nm NC (measured by PDF). Space group $P4_32_12$.

Bragg R factor	7.7 %
Rf factor	6.2 %
A	8.370 Å
C	8.401 Å
Biso Fe	0.0677 $Å^{-2}$
Instrument Displacement	-0.0019
Y	0.060
IG	0.022
Crystallite diameter (nm)	6.3 nm

Refinement of PDF Data

Data was refined with a spinel iron oxide model taking the space group $P4_32_12$[4] using Diffpy-CMI software. Instrumental resolution was refined using a CeO_2 standard with Q_{Broad} refined to a value of 0.01259 Å and Q_{Damp} refined to a value of 0.03321 Å. The value of Q_{Broad} was set to 0.01 and Q_{Damp} was set to 0.04. The scale, cell parameters, crystallite size, correlated atomic motion term (delta2), the occupancy of both Fe1 and Fe4, atomic positions and a dampened sine wave which used to describe the solvent were all refined. Fe1 is the tetrahedrally coordinated iron in the model that takes the space group $P4_32_12$. Fe4 is the octahedral iron which would have an occupancy of 0.33 if the NCs are 100% maghemite phase. The thermal parameters for both iron and oxygen were fixed at values that were refined for the 9.1 nm NC (Refined by PDF). Each iron thermal parameter was refined individually while all oxygen thermal parameters were refined together. Parameters for a dampened sine wave were also refined, which is discussed below along with Equation S1 and initial values used for refinement in Table B7.

Iron positions as well as O2 and O4 positions were also refined.The positions of O1 and O3 were held constant because the spread in the positions of O1 and O3 over all samples was very broad especially for the smallest NC sizes (Figure B11). There were also some shorter than physical Fe-O bond lengths refined for the samples with bond lengths shorter than 1.5 Å. The values of O1 and O3 were fixed at the average values determined by refining parameters, all positions and all thermal parameters (values from Figure B11). Fixing the O1 and O3 values at average positions gave shortest Fe-O bonds at 1.6 Å (Figure B11 and B12), closer to previously reported bond lengths for vacancy ordered maghemite[5] which refined shortest bond lengths of 1.64 Å. The bond lengths

were also more centered around 2 Å without a secondary population of short bonds. The refined bond lengths for the smallest and largest NC size are included in Figure B12 and S13 respectively.

The refinement was performed sequentially for all 17 samples commenced with a short range refinement (2.7-20 Å) with no wave parameters refined, a long range refinement (2.7-60 Å) with no wave parameters refined, long range refinement with only wave parameters refined and finally all parameters refined together. When wave parameters were refined initially with the first structral refinments it led to less consistent results.

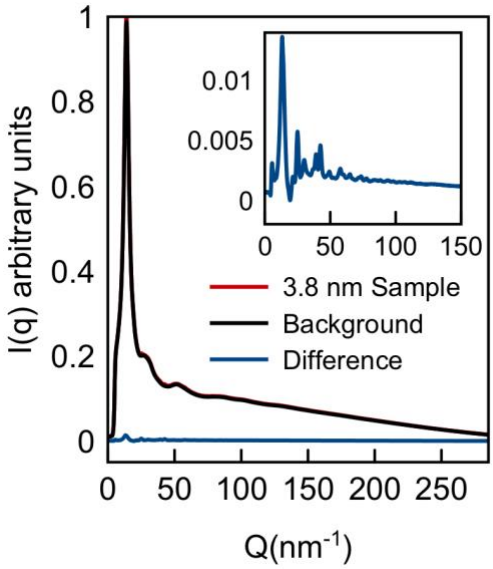

Figure B7. Total scattering (I(q)) for both the 3.8 nm sample measured by PDF (red), the background of oleic acid and oleyl alcohol (black) and the difference between the sample and the background (blue). The inset is a magnification of the difference curve (blue).

Table B6. Starting values for the PDF refinement. Space group $P4_32_12$

a,b	8.402 Å
c	8.305 Å
Delta 2	2 Å
Fe1 occupancy	0.7
Fe4 occupancy	0.33
Crystallite Diameter	40 Å
Biso Fe1	0.49 $Å^{-2}$
Biso Fe2	0.46 $Å^{-2}$
Biso Fe3	0.70 $Å^{-2}$
Biso Fe4	0.39 $Å^{-2}$
Biso O	0.9 $Å^{-2}$

Table B7. Starting values for the PDF refinement for positions. Space group $P4_32_12$

	x	y	z
Fe1	0.747	0.004	0.125
Fe2	0.630	0.630	0
Fe3	0.371	0.867	0.982
Fe4	0.132	0.132	0
O1	0.562	0.895	0.965
O2	0.119	0.377	-0.005
O3	0.109	0.828	0.041
O4	0.383	0.631	-0.003

Discussion of Equation B1

Initial fits showed a residual signal in the difference curve that appeared to be a dampened sine wave. This curve has been shown previously by Zobel *et al*. (Equation S1) and is due to solvent restructuring around the NPs for dilute NPs in solution.[6] In Equation S1, A is the amplitude, λ is the wavelength and φ is the phase shift. The value for the effective dampening (σ_{eff}) is $\sigma_{eff} = \sigma/a$ for $r < r_0$ and $\sigma_{eff} = \sigma * a$ for $r < r_0$ where a is the asymmetry parameter. The variable r_0 does not correspond to a physical parameter but is used to describe the different dampening behavior of the sine wave. The value of r_0 was fixed to have an upper bound of 2.7 Å so that the dampening behavior did not switch behavior in the middle of the range we are refining (2.7 – 60 Å). This switch led to sharp erroneous peaks in the sine wave. The starting values were set to approximate values that were refined for the data series. Data was fit using Diffpy-CMI to refine both the structural model and the damped sinusoidal wave (Equation B1).

$$w(r) = A\sin\left(2\pi\left(\frac{r}{\lambda} - \varphi\right)\right)e^{-\left(\frac{(r-r_0)}{2\sigma_{eff}}\right)^2} \quad \text{(Equation B1)}$$

Table B8. Starting values for the PDF refinement for the damped sine wave.

A	0.5 Å
λ	4 Å
φ	1°
r_0	1 Å
σ	4 Å
a	1

Table B9. Refined values for 4 select sizes using model. Space group $P4_32_12$

Crystallite Diameter	29 Å	53 Å	61 Å	92 Å
Rw	0.44	0.16	0.20	0.13
a,b	8.348 Å	8.389 Å	8.409 Å	8.376 Å
c	8.364 Å	8.332 Å	8.351 Å	8.376 Å
Delta 2	3.8 Å	3.8 Å	2.6 Å	3.6 Å
Fe1 occupancy	0.77	0.84	0.89	0.98
Fe4 occupancy	0.33	0.67	0.40	0.61
Fe1 x	0.748	0.748	0.744	0.747
Fe1 y	0.994	0.998	0.994	0.996
Fe1 z	0.120	0.122	0.117	0.118
Fe2 x=y	0.640	0.633	0.635	0.632
Fe3 x	0.376	0.374	0.375	0.374
Fe3 y	0.874	0.869	0.868	0.870
Fe3 z	0.983	0.992	0.991	0.989
Fe4 x=y	0.117	0.126	0.132	0.128
O2 x	0.108	0.120	0.121	0.122
O2 y	0.371	0.370	0.367	0.371
O2 z	0.999	0.993	1.000	0.995
O4 x	0.389	0.380	0.381	0.379
O4 y	0.637	0.622	0.624	0.629
O4 z	0.998	0.004	0.997	0.996
A	10400 Å	1420 Å	0.4 Å	281 Å
λ	4.8 Å	4.8 Å	4.9 Å	69.3 Å
φ	0.86 °	0.97 °	1.1 °	0.07 °
r_0	-56 Å	-77 Å	2.7 Å	-15 Å
σ	6.2 Å	7.4 Å	4.3 Å	4.0 Å
a	1.5	1.9	1.1	0.98

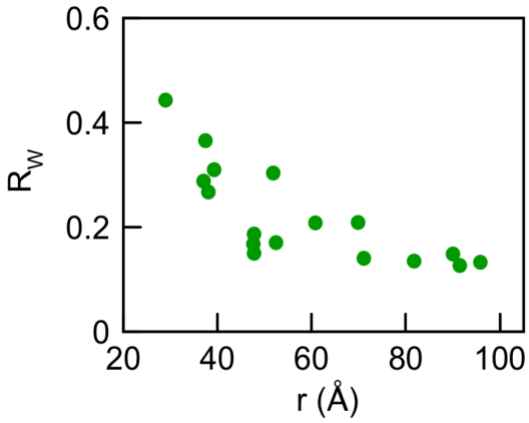

Figure B8. Refined values of R_W for the entire size series plotted against the refined crystallite size by PDF. Space group *P4₃2₁2*

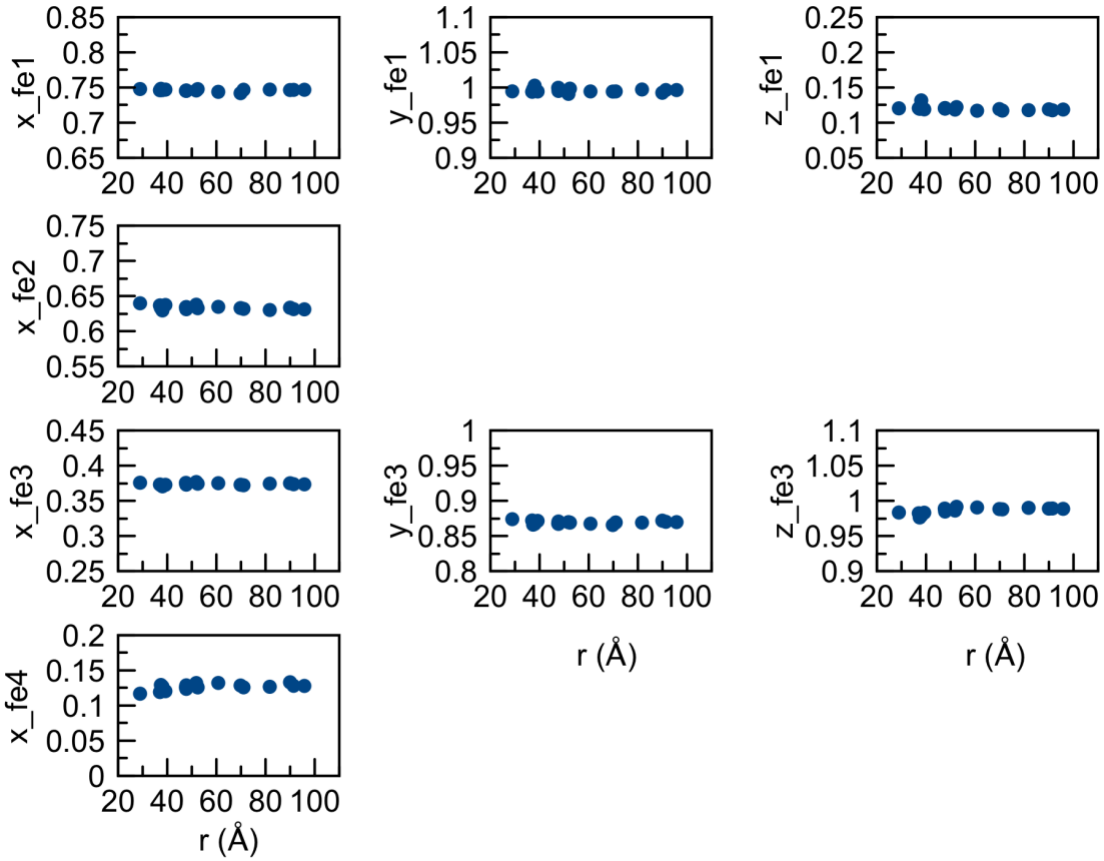

Figure B9. Refined atomic positions for all of the iron positions for the entire size series plotted against the refined crystallite size by PDF. Space group *P4₃2₁2*.

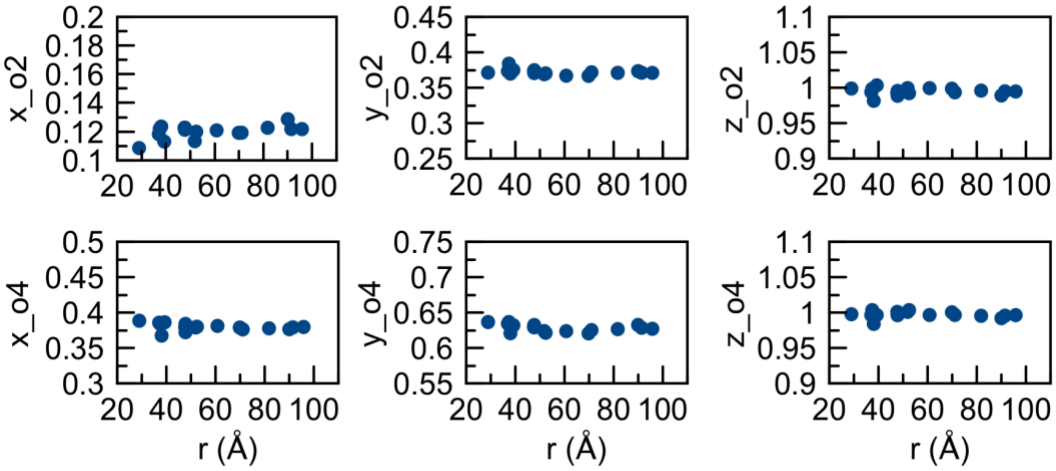

Figure B10. Refined atomic positions for all of the oxygen positions for the entire size series plotted against the refined crystallite size by PDF. Space group $P4_32_12$

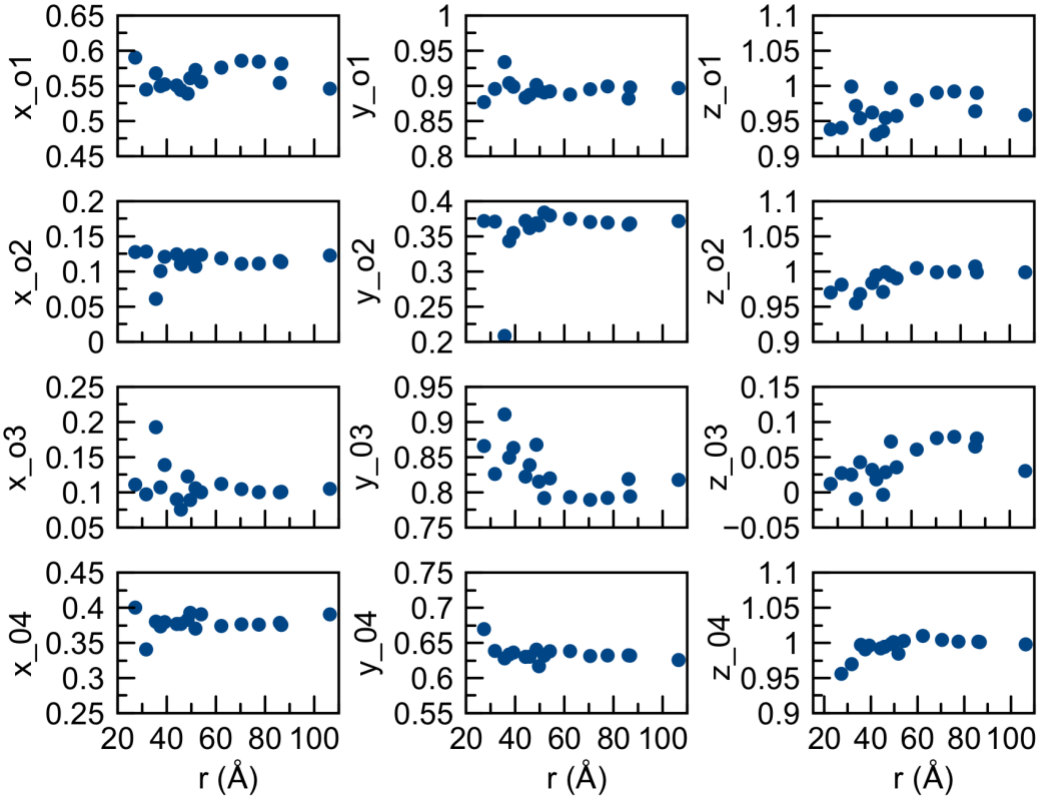

Figure B11. Refined atomic positions for all oxygen positions before fixing the positions of O1 and O3 at the average values. Space group $P4_32_12$

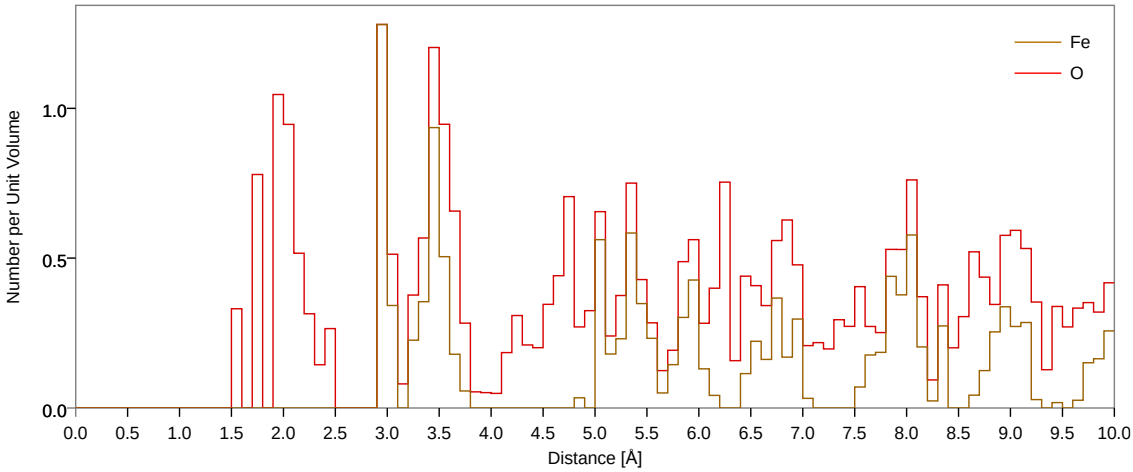

Figure B12. Bond distance histogram for the sample with a diameter of 2.9 nm NCs (PDF). Space group *P4₃2₁2*

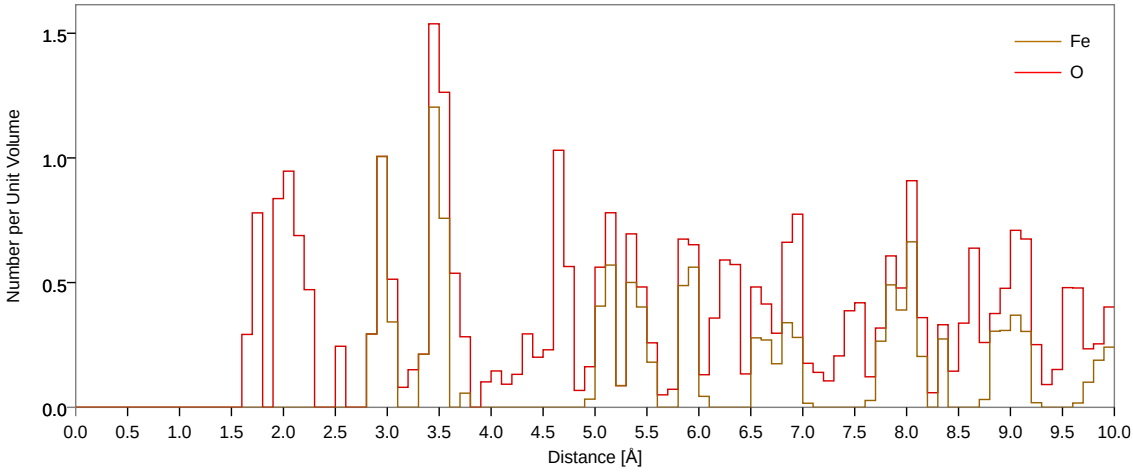

Figure B13. Bond distance histogram for the sample with a diameter of 9.1 nm NCs (PDF). Space group *P4₃2₁2*

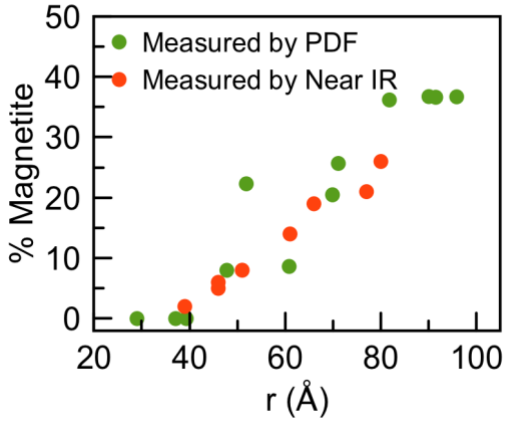

Figure B14. Percent magnetite of samples that were aged at least 3 weeks before analysis. The percent magnetite for the green dots was determined by refining PDF data and the orange dots were measured by Near IR in a previous publication of the same synthesis.

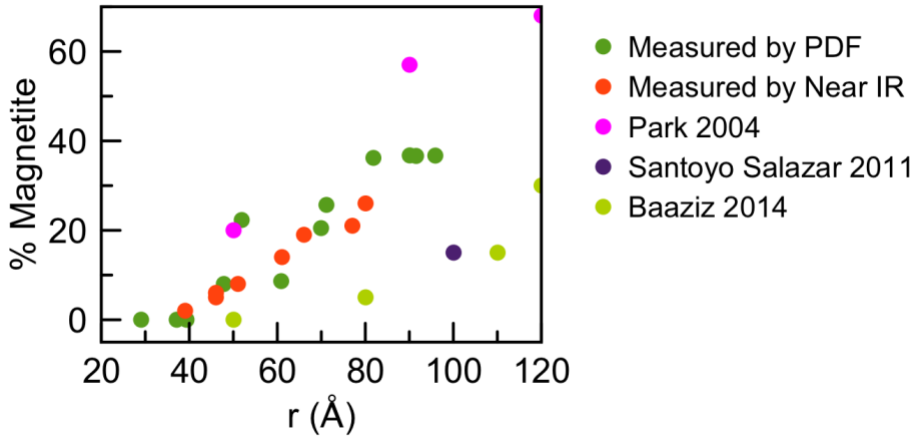

Figure B15. Shows the percent magnetite from other experiments that determined magnetite content by quantitative methods. Park measured the magnetite content by a combination of XMCD and XAS while Baaziz and Santoyo Salazar determined magnetite content with Mössbauer.

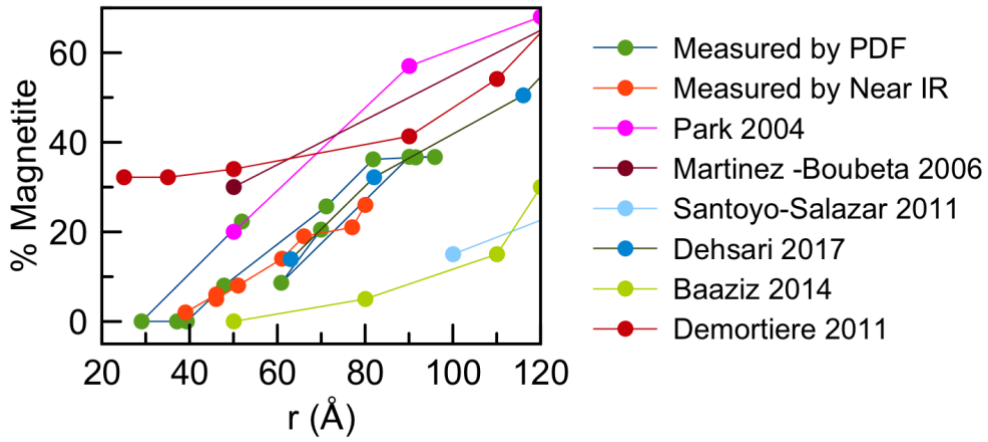

Figure B16. Shows our magnetite values compared to other values in literature over similar size ranges. This includes samples for which the percent magnetite was determined by the *a* parameter using the equation in Gorski *et al*[7].

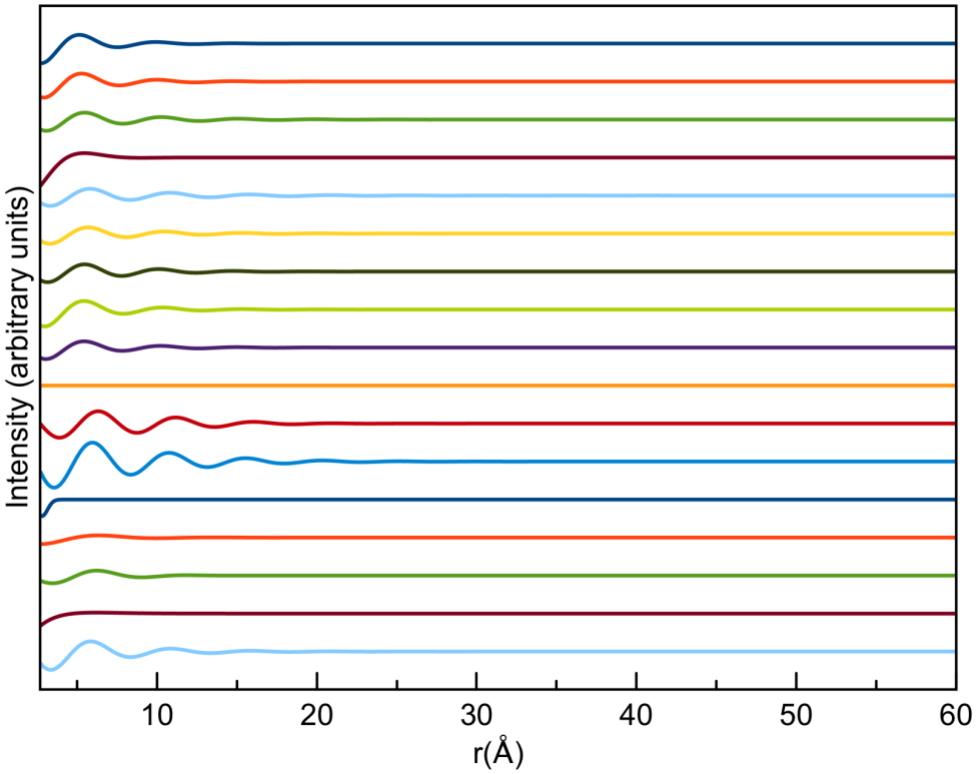

Figure B17. Waves refined for all samples. The smallest NC at the top and the largest NC on the bottom of the figure in the same order as Table B1. Space group $P4_32_12$.

PDF Refinement Using Other Crystallographic Models

Refinements with Fd-3m

Table B10. Starting parameters for refinement of PDF data. Space group *Fd-3m*

a	8.397 Å
Delta 2	2 Å
Fe1 occupancy	0.7
Fe2 occupancy	0.83
Crystallite Diameter	40 Å
Biso Fe1	0.39 $Å^{-2}$
Biso Fe2	0.55 $Å^{-2}$
Biso O	0.8 $Å^{-2}$
A	0.5 Å
λ	4 Å
φ	1º
r_0	1 Å
σ	4 Å
a	1

Table B11. Starting positions for refinement of PDF data. Space group *Fd-3m*

	x	y	z
Fe1	0.125	0.125	0.125
Fe2	0.5	0.5	0.5
O1	0.255	0.255	0.255

Table B12. Refined values for 4 select sizes using model. Space group *Fd-3m*

Crystallite Diameter	30 Å	48 Å	53 Å	80 Å
R_W	0.48	0.25	0.32	0.24
a	8.360 Å	8.371 Å	8.389 Å	8.377 Å
Delta 2	6.9 Å	1.6 Å	1.1E-05 Å	1.7 Å
Fe1 occupancy	1.00	1.00	1.00	1.00
Fe4 occupancy	0.89	1.00	0.86	0.95
O1 x=y=z	0.264	0.260	0.261	0.261
A	7955 Å	0.3 Å	0.4 Å	-0.01 Å
λ	4.4 Å	4.7 Å	4.9 Å	4.0 Å
φ	0.99 º	1.0 º	1.1 º	0.97 º
r_0	-71 Å	-4.4 Å	2.7 Å	0.4 Å
σ	6.8 Å	3.7 Å	4.2 Å	-2.1E+11 Å
a	1.7	1.6	1.0	1.9E+09

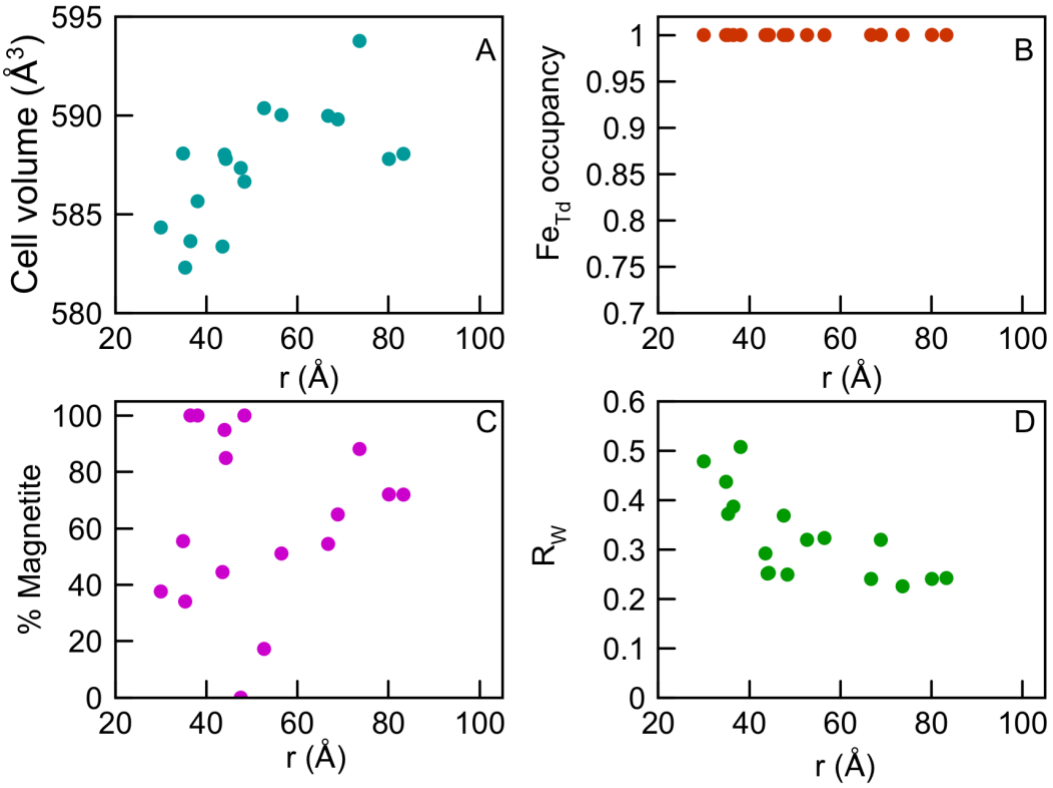

Figure B18. This figure shows refined parameters as a function of diameter for all 17 samples refined by PDF with A) Cell volume, B) vacancies on tetrahedrally coordinated iron sites, C) % magnetite and D) R_W factor expressing the goodness of fit at each size. Space group *Fd-3m*

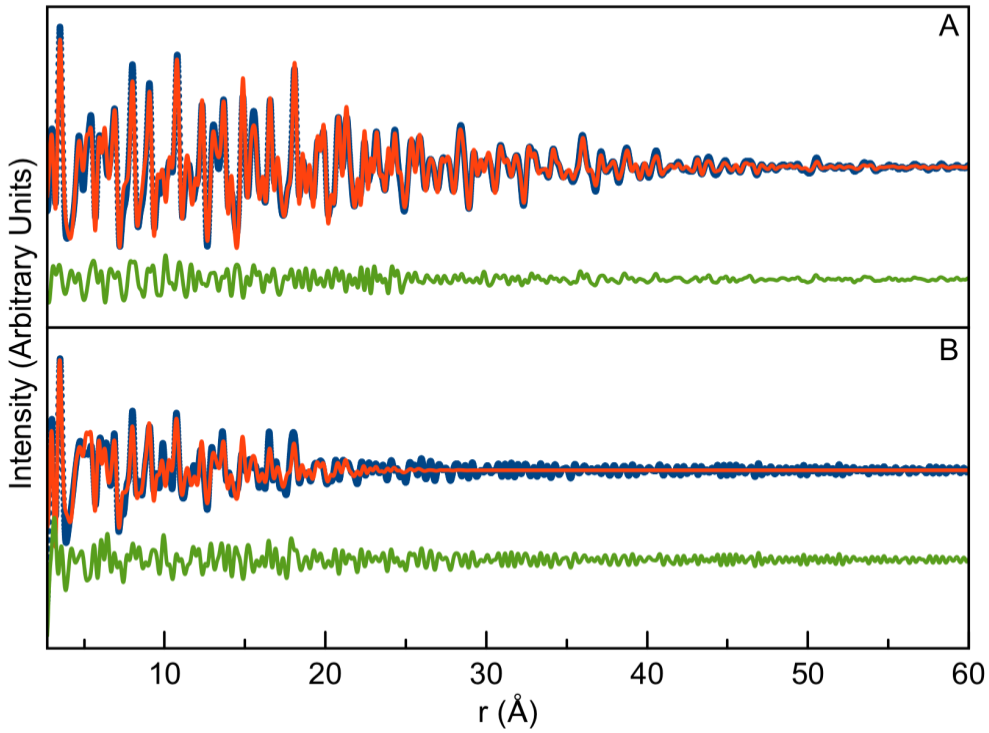

Figure B19. Data for a A) 9.6 nm NC B) 2.9 nm NC is shown in blue dots, red is the model and green is the difference between the model and the data. Space group *Fd-3m*

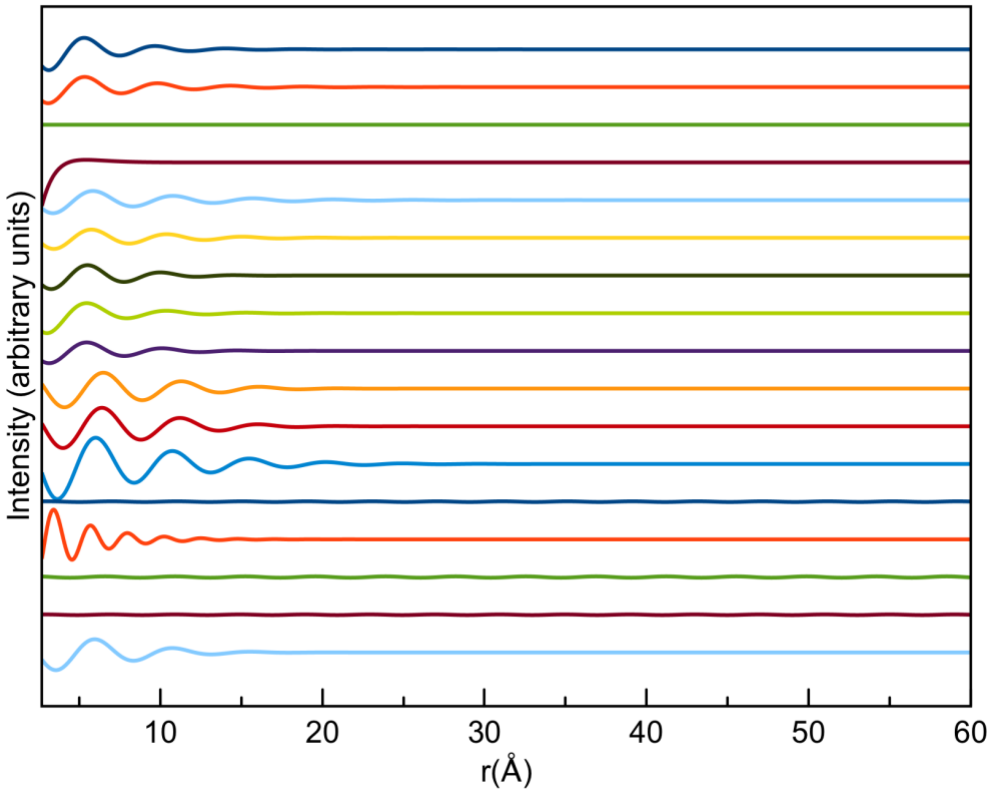

Figure B20. Waves refined for all samples with the smallest NC at the top and the largest NC on the bottom of the figure in the same order as Table B1. Space group *Fd-3m*

Refinements with $P4_33_2$

Table B13. Starting parameters for refinement of PDF data. Space group $P4_33_2$

a	8.347 Å
Delta 2	2 Å
Fe1 occupancy	0.8
Fe3 occupancy	0.8
Crystallite Diameter	40 Å
Biso Fe	0.54 $Å^{-2}$
Biso O	0.8 $Å^{-2}$
A	0.5 Å
λ	4 Å
φ	1º
r_0	1 Å
σ	4 Å
a	1

Table B14. Starting positions for refinement of PDF data. Space group $P4_32_2$

	x	y	z
Fe1	0.992	0.992	0.992
Fe2	0.865	0.615	0.875
Fe3	0.375	0.125	0.875
O1	0.861	0.861	0.861
O2	0.372	0.377	0.876

Table B15. Refined values for 4 select sizes using model taking the space group $P4_32_2$.

Crystallite Diameter	29 Å	50 Å	59 Å	88 Å
R_W	0.46	0.19	0.23	0.16
a	8.351	8.370	8.389	8.376
Delta 2	3.5 Å	3.4 Å	0.7 Å	2.9 Å
Fe1 occupancy	0.93	1.00	1.00	1.00
Fe3 occupancy	0.33	1.00	0.72	0.67
Fe1 x=y=z	1.000	0.000	0.995	0.998
Fe2 x (y+1/2, y+1/4, 7/8)	0.867	0.869	0.864	0.869
O1 x=y=z	0.837	0.835	0.831	0.833
O2 x	0.365	0.370	0.366	0.368
O2 y	0.360	0.364	0.371	0.362
O2 z	0.886	0.885	0.886	0.883
A	1363 Å	224 Å	0.4 Å	0.2 Å
λ	4.3 Å	4.6 Å	5.0 Å	3.4 Å
φ	0.98 º	1.0 º	1.0 º	1.5 º
r_0	-87 Å	-78 Å	2.7 Å	2.7 Å
σ	7.9 Å	14 Å	4.4 Å	2.7 Å
a	2.0	1.1	0.9	0.7

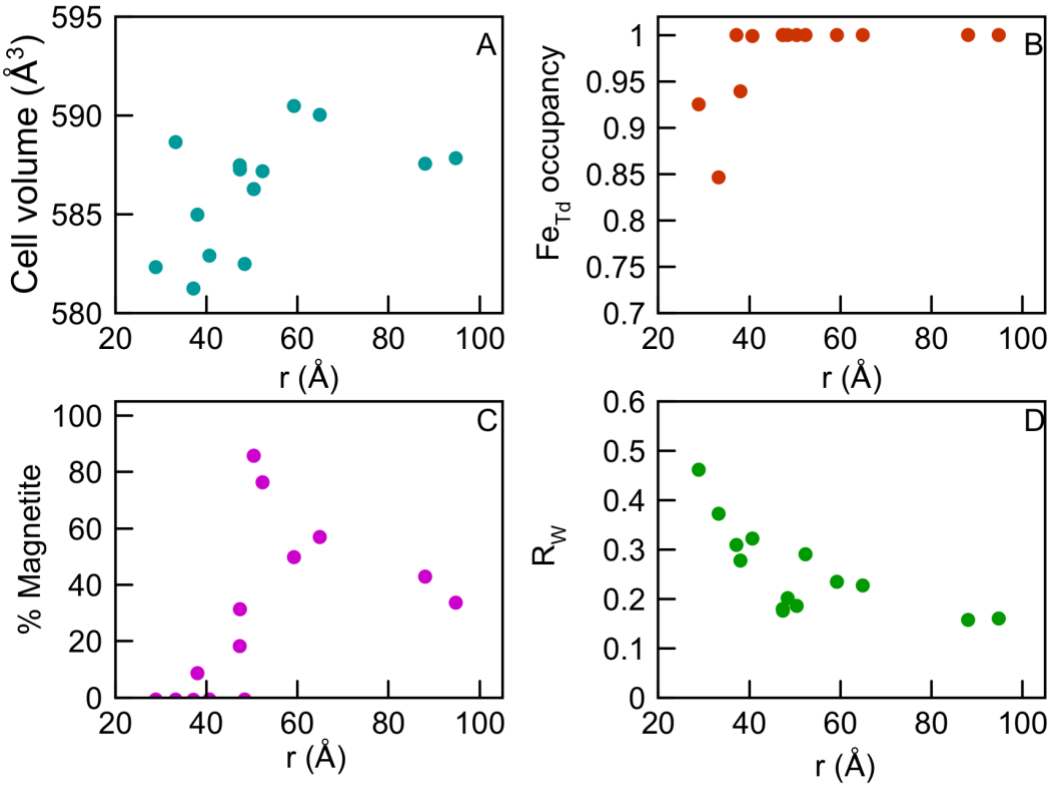

Figure B21. This figure shows refined parameters as a function of diameter for 14 samples refined by PDF with A) Cell volume, B) vacancies on tetrahedrally coordinated iron sites, C) % magnetite and D) R_W factor expressing the goodness of fit at each size. Space group $P4_32_2$

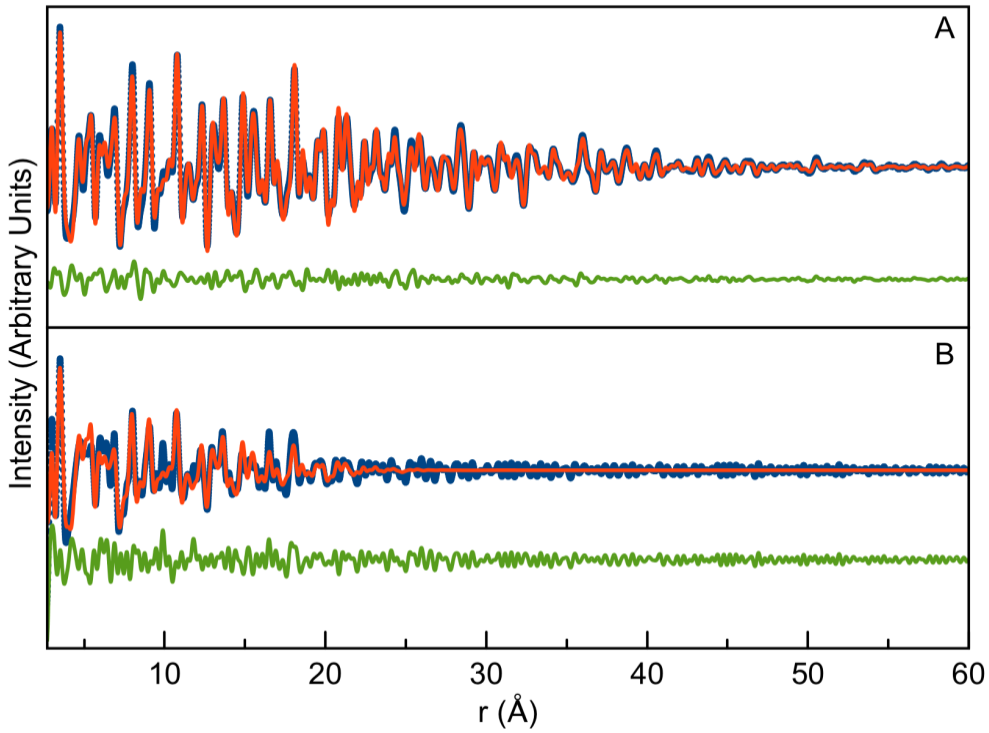

Figure B22. Data for a A) 9.6 nm NC B) 2.9 nm NC is shown in blue dots, red is the model and green is the difference between the model and the data. Space group $P4_32_2$

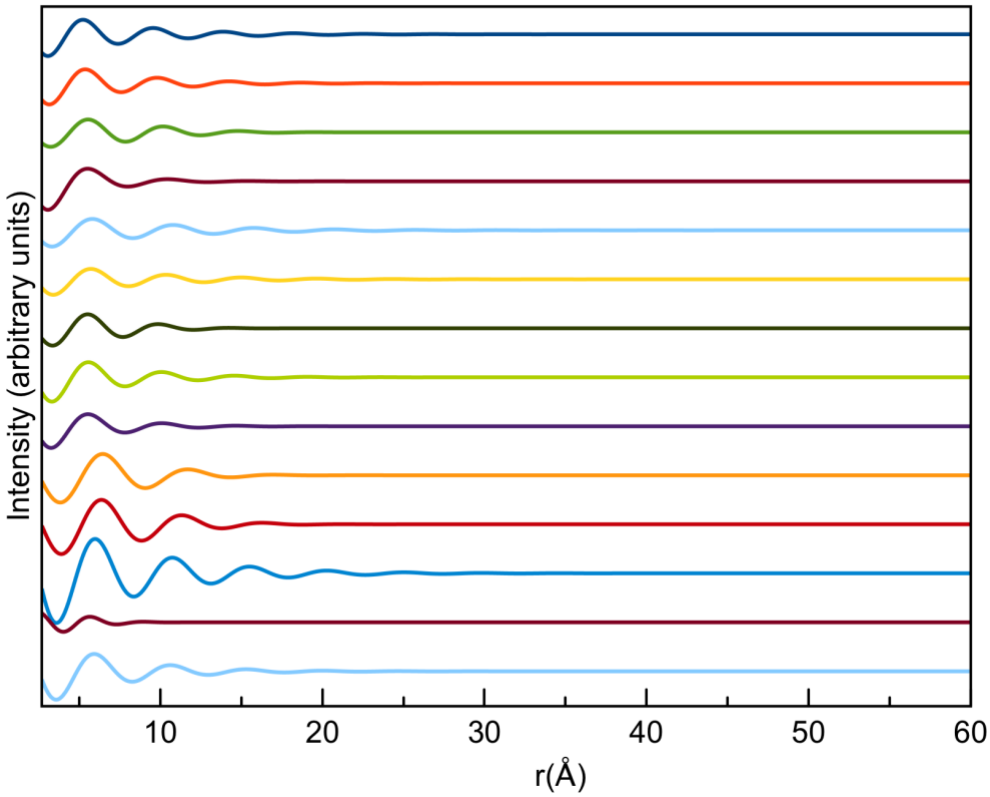

Figure B23. Waves refined for all samples with the smallest NC at the top and the largest NC on the bottom of the figure in the same order as Table B1. Space group $P4_32_2$

Refinements with $P4_12_12$

Table B16. Starting parameters for refinement of PDF data. Space group $P4_12_12$.

a, b	Å
c	Å
Delta 2	2 Å
Fe1 occupancy	0.8
Fe3 occupancy	0.8
Fe1 occupancy	40 Å
Fe3 occupancy	0.54 $Å^{-2}$
Crystallite Diameter	40 Å
Biso Fe	0.54 $Å^{-2}$
Biso O	0.8 $Å^{-2}$
A	0.5 Å
λ	4 Å
φ	1º
r_0	1 Å
σ	4 Å
a	1

Table B17. Starting positions for refinement of PDF data. Space group $P4_12_12$.

	x	y	z
Fe1	0.751	0.997	0.0417
Fe2	0.751	0.997	0.375
Fe3	0.751	0.997	0.7084
Fe4	0.621	0.621	0
Fe5	0.621	0.621	0.3333
Fe6	0.369	0.869	0.998
Fe7	0.369	0.869	0.3313
Fe8	0.369	0.869	0.6647
Fe9	0.128	0.128	0
Fe10	0.128	0.128	0.3333
O1	0.612	0.881	0
O2	0.612	0.881	0.333
O3	0.612	0.881	0.667
O4	0.11	0.317	0.003
O5	0.11	0.317	0.336
O6	0.11	0.317	0.67
O7	0.133	0.853	0
O8	0.133	0.853	0.333
O9	0.133	0.853	0.67
O10	0.385	0.626	0.006
O11	0.385	0.626	0.339
O12	0.385	0.626	0.673

Table B18. Refined values for 4 select sizes using model. Space group $P4_12_12$

Crystallite Diameter	32	46	61	92
R_W	0.32	0.13	0.15	0.08
a,b	8.327	8.368	8.369	8.389
c	25.376	25.133	25.288	25.039
Delta 2	2.0	3.4	2.0	3.3
Fe 1 occupancy	0.87	0.84	1.00	1.00
Fe 2 occupancy	0.71	1.00	0.69	0.88
Fe 3 occupancy	0.54	0.35	0.83	1.00
Fe10 occupancy	0.54	0.35	0.83	1.00
Fe1 x	0.751	0.755	0.756	0.749
Fe1 y	0.994	0.006	0.010	0.999
Fe1 z	0.050	0.043	0.041	0.038
Fe2 x	0.751	0.747	0.743	0.753
Fe2 y	0.001	0.002	0.997	0.996
Fe2 z	0.376	0.376	0.376	0.374
Fe3 x	0.753	0.760	0.749	0.747
Fe3 y	0.001	1.000	0.995	0.004
Fe3 z	0.711	0.709	0.706	0.709
Fe4 x=y=z	0.613	0.633	0.636	0.622
Fe5 x	0.632	0.619	0.620	0.613
Fe5 y	0.614	0.587	0.618	0.625
Fe5 z	0.329	0.325	0.328	0.334
Fe6 x	0.385	0.383	0.358	0.375
Fe6 y	0.868	0.879	0.865	0.854
Fe6 z	0.994	0.999	0.993	0.995
Fe7 x	0.374	0.350	0.375	0.387
Fe7 y	0.877	0.855	0.884	0.884
Fe7 z	0.328	0.332	0.330	0.335
Fe8 x	0.339	0.383	0.403	0.365
Fe8 y	0.834	0.873	0.846	0.865
Fe8 z	0.648	0.662	0.664	0.663
Fe9 x=y=z	0.119	0.117	0.129	0.126

Fe10 x	0.107	0.115	0.106	0.119
Fe10 y	0.133	0.128	0.128	0.139
Fe10 z	0.313	0.329	0.335	0.323
O1 x	0.633	0.619	0.578	0.624
O1 y	0.883	0.876	0.759	0.875
O1 z	0.003	0.998	0.972	0.996
O2	0.553	0.515	0.615	0.618
O2	0.831	0.759	0.874	0.873
O2	0.326	0.287	0.331	0.330
O3	0.627	0.534	0.561	0.621
O3	0.868	0.926	0.839	0.877
O3	0.673	0.646	0.681	0.663
O4	0.106	0.003	0.077	0.981
O4	0.291	0.292	0.284	0.284
O4	0.993	0.985	0.982	0.013
O5	0.065	0.995	0.995	0.989
O5	0.287	0.172	0.258	0.261
O5	0.295	0.279	0.294	0.301
O6	0.101	0.148	0.021	0.120
O6	0.313	0.281	0.234	0.322
O6	0.652	0.668	0.672	0.723
O7	0.142	0.244	0.131	0.144
O7	0.876	0.952	0.878	0.779
O7	0.023	0.006	0.001	0.978
O8	0.127	0.122	0.059	0.128
O8	0.886	0.876	0.899	0.878
O8	0.337	0.330	0.345	0.332
O9	0.121	0.137	0.125	0.157
O9	0.875	0.888	0.865	0.846
O9	0.669	0.664	0.666	0.666
O10	0.317	0.375	0.368	0.413
O10	0.641	0.628	0.629	0.556
O10	0.018	0.995	0.008	0.004
O11	0.347	0.380	0.364	0.377
O11	0.582	0.648	0.621	0.632
O11	0.348	0.325	0.337	0.334
O12	0.404	0.377	0.378	0.376
O12	0.628	0.619	0.641	0.621
O12	0.655	0.664	0.664	0.670

A	16388	1189	1	1778
λ	4.2	3.9	5.5	7.6
φ	1.0	1.1	0.9	0.7
r_0	-73	-25	-6	-49
σ	7.2	4.4	4.7	5.9
a	1.6	1.1	1.2	1.5

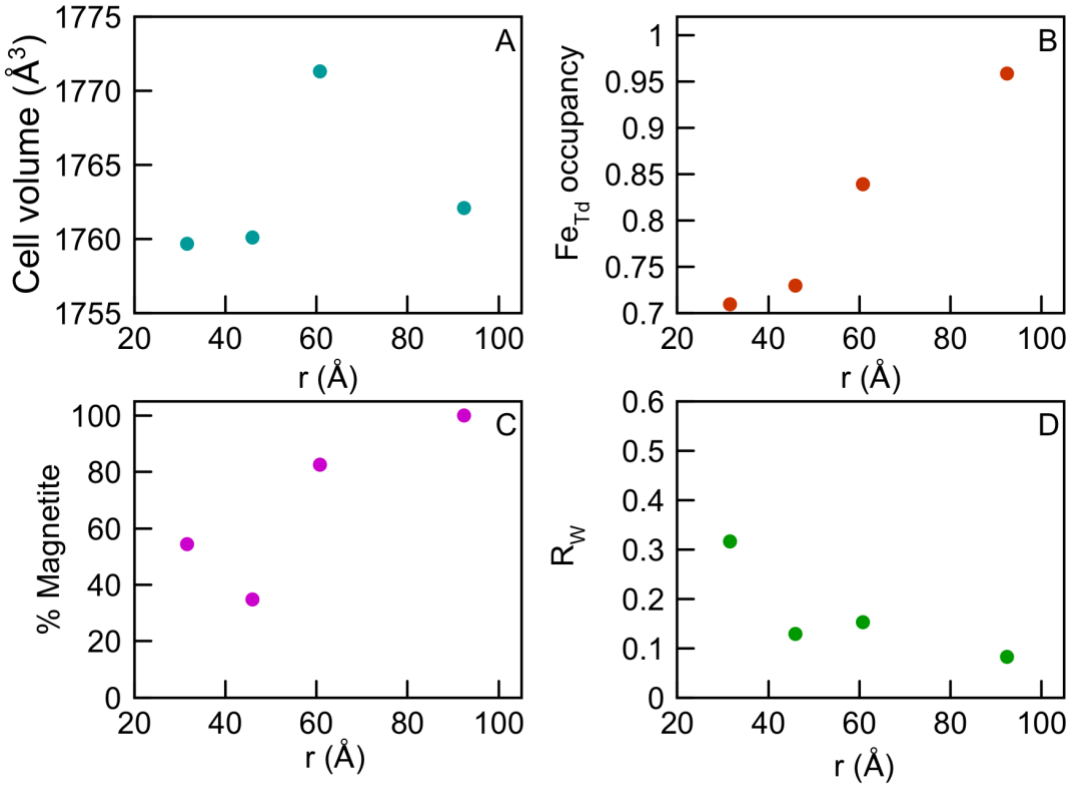

Figure B24. Refined parameters as a function of diameter for 14 samples refined by PDF with A) Cell volume, B) vacancies on tetrahedrally coordinated iron sites, C) % magnetite and D) R_W factor expressing the goodness of fit at each size. Space group $P4_12_12$

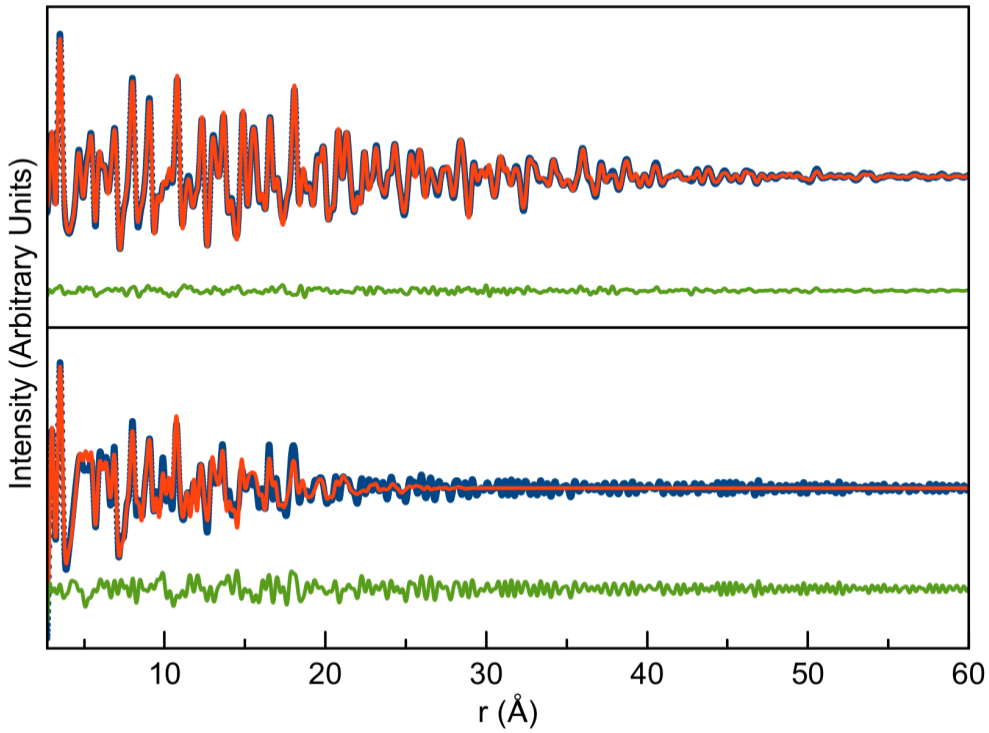

Figure B25. Data for a A) 9.6 nm NC B) 2.9 nm NC is shown in blue dots, red is the model and green is the difference between the model and the data. Space group $P4_12_12$

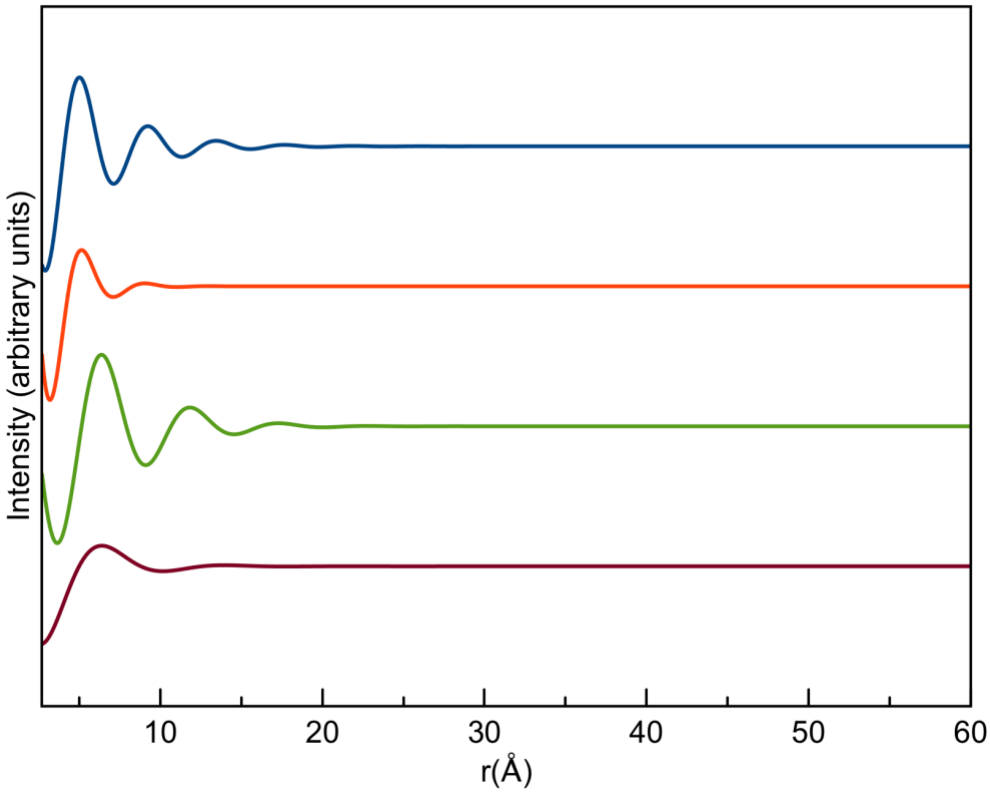

Figure B26. Waves refined for all samples with the smallest NC at the top and the largest NC on the bottom of the figure in the same order as Table B1. Space group $P4_12_12$

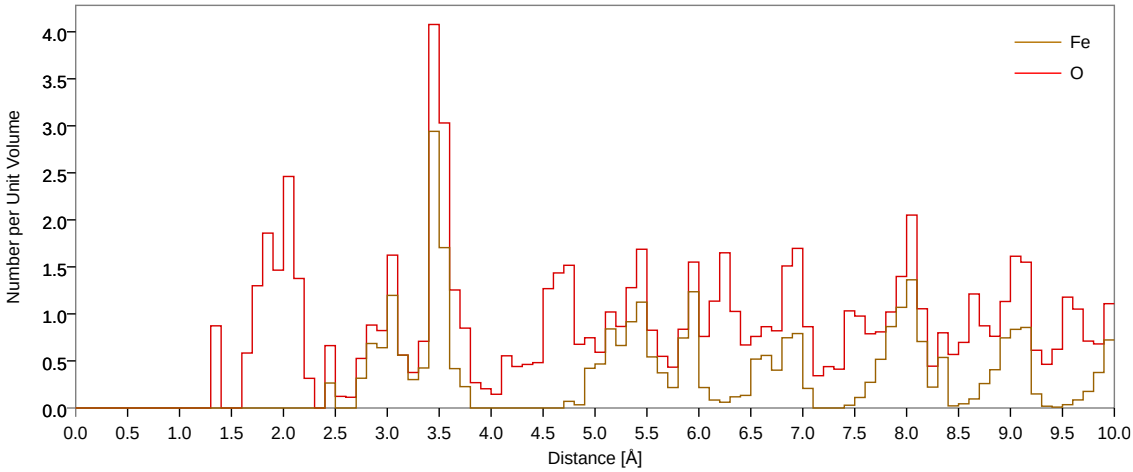

Figure B27. Bond distance histogram for the sample with a diameter of 9.1 nm NCs (PDF). Space group $P4_12_12$

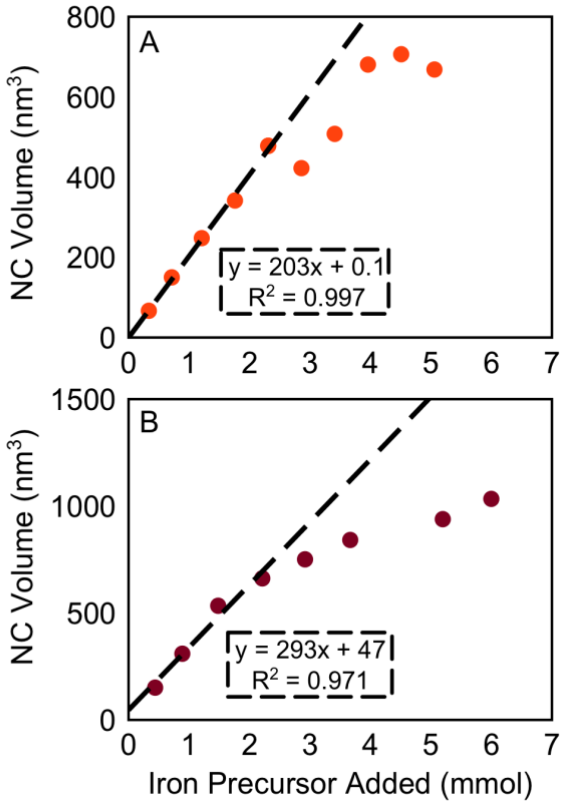

Figure B28. Shows growth of NCs in volume as increased precursor is added to the reaction flask for two syntheses. Linear equations for the growth behavior are shown.

Discussion of Figure B28

The size at which NCs change their reaction rate is different for the three different trials of this experiment (Figure B28). This is likely due to differences in the nucleation which is affected by many variables including drop size and moisture content of the solvents.

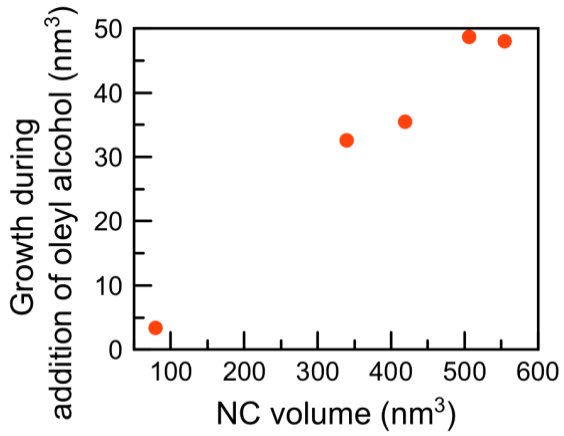

Figure B29. Shows the amount of volume that particles grow while oleyl alcohol is added to the reaction after 1 mmol, 4 mmol, 5, mmol, 6 mmol and 7 mmol of precursor has been added (from left to right).

Discussion of Figure B29

When we stop adding precursor and add oleyl alcohol to the reaction flask, we see a linear relationship of precursor added to volume of the NCs when adding up to 7 mmol of precursor and 500 nm^3 NC volume (Figure 11). While adding oleyl alcohol, we are able to measure if any growth happens during periods where there is no precursor being added to the flask. We took samples right after precursor addition stopped and then another aliquot after oleyl alcohol has been added (Figure B28 and B29). Growth during this period would indicate that precursor is not reacting as fast as it is being added. After the addition of 1 mmol of precursor there was very little growth during the addition of oleyl alcohol with only 3 nm^3 volume increase suggesting for these small NCs precursor is reacting as fast as it is being added. In all cases there was growth during the period where precursor was not added. This means that unlike in the smaller NCs (after 1 mmol of precursor had been added) the precursor is no longer reacting as fast as it is being added and excess precursor is remaining in the reaction.

APPENDIX C

SUPPLEMENTARY INFORMATION FOR CHAPTER IV: IN SITU TOTAL X-RAY SCATTERING STUDY OF THE FORMATION OF IRON OXIDE NANOPARTICLES

Table C1. Table of Contents organized by section for figures and tables in Appendix C.

Growth of Nanocrystals Made with Fe (III) Rich Oleate Analyzed *Ex Situ* by Small Angle X-ray Scattering

Figure C1 shows nanocrystal (NC) volume obtained by adding different amounts of Fe (III) rich oleate precursor at 230°C made by continuous growth. To analyze growth *ex situ*, samples were removed from the reaction flask during the reaction. Core diameter was determined by Small Angle X-ray Scattering (SAXS). The relationship between NC volume and the amount of precursor added, up to 25 mmol, to the reaction is linear when using Fe (III) rich oleate precursor.

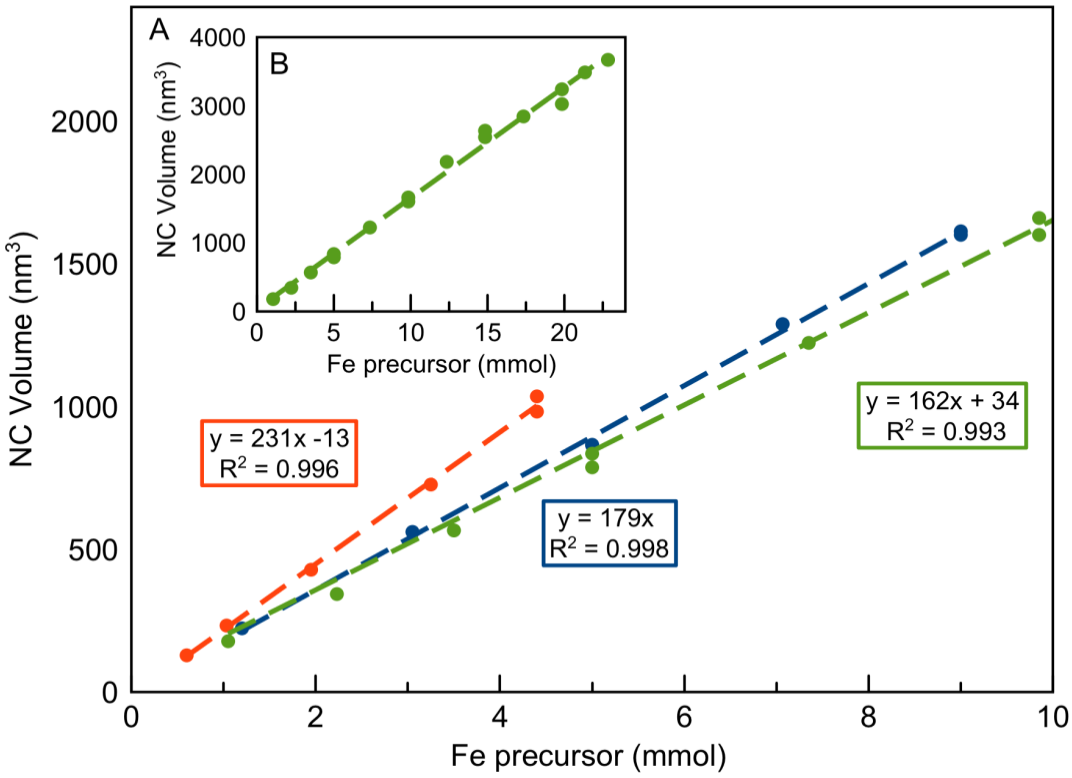

Figure C1. A) Comparison of three growth curves made from slow injection of Fe (III) rich oleate precursor with equations and R^2 for the volume of NCs vs the added iron precursor. The orange line had 4 mmol of precursor added to the reaction flask, the blue line had 9 mmol of precursor added and the green line had 25 mmol of precursor added. B) The inset is the full range of volume for all NCs made up to 25 mmol precursor added for the green curve.

Ex Situ Characterization of Nanoparticles Made with the *In Situ* Setup

NPs made by the continuous growth method with both Fe (II) rich oleate precursor and Fe (III) rich oleate precursor show the spinel structure as can be seen by the lab scale powder XRD in Figure C2.

The continuous growth method makes nanocrystals (NCs).[1] In order to verify that the continuous growth method still makes NCs when going through the *in situ* reaction setup High Resolution TEM was performed (HR-TEM). As can been seen in Figure C2, the NPs made with Fe (III) rich oleate at 230°C and Fe (II) rich oleate at 230°C, 200°C

and 180°C are all NCs. The NPs exhibiting lattice fringes that extend through the entire NP indicates the NPs are single crystals.

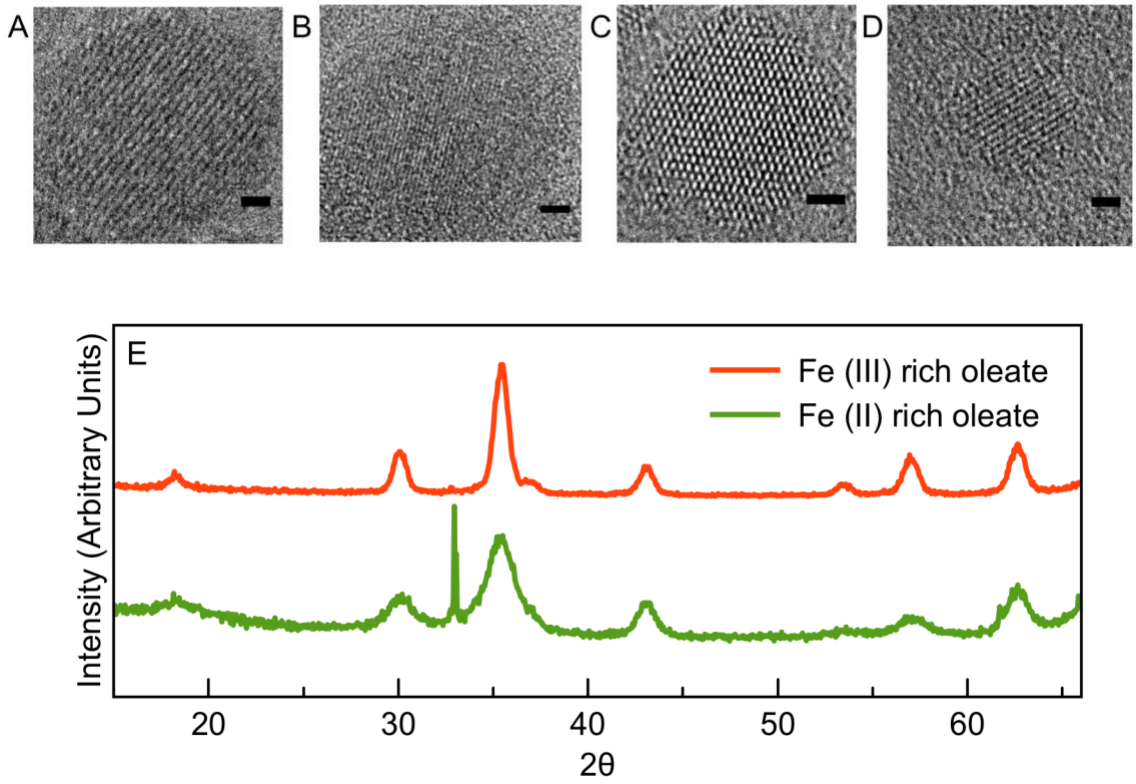

Figure C2. High Resolution TEM and XRD patterns for Fe (II) rich and Fe (III) rich oleate. High Resolution TEM of NPs from A) 230°C with Fe (III) rich oleate, B) 230°C with Fe (II) rich oleate, C) 200°C with Fe (II) rich oleate, D) 180°C with Fe (II) rich oleate. Scale bar is 1 nm. D) XRD of Fe (III) rich (red) and Fe (II) rich oleate (green).

Thermal Decomposition of Fe (II) rich oleate and Fe (III) rich oleate

The thermal decomposition temperature was determined by thermogravimetric analysis (TGA) of oleic acid alone, Fe (II) oleate and Fe (III) oleate. The sample mass loss events can be seen in the derivative curve (Figure C2-B). Free oleic acid is lost at around 230°C while Fe (II) oleate and Fe (III) oleate both lose mass just above 230°C. Neither Fe (II) oleate or Fe (III) oleate thermally decompose before 230°C and therefore thermal decomposition is not occurring in an appreciable amount in the formation of NCs by the continuous growth method.[1]

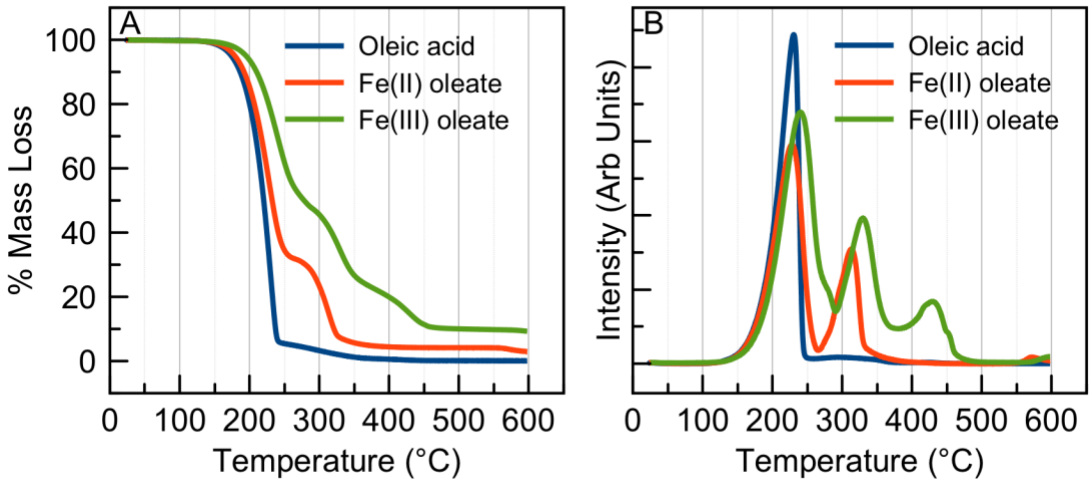

Figure C3. A) The thermal decomposition profile of oleic acid (blue), Fe (II) rich oleate with excess oleic acid (red) and Fe (III) rich oleate with excess oleic acid (green). B) The differential of the thermal decomposition profile of oleic acid (blue), Fe (II) rich oleate with excess oleic acid (red) and Fe (III) rich oleate with excess oleic acid (green).

Determination of Esterification Reaction Rates

In order to determine the metal catalyzed rate of esterification for Fe (II) rich oleate compared to Fe (III) rich oleate, NMR experiments were carried out using both precursors separately. One mmol of precursor (either Fe (II) oleate or Fe (III) oleate) was added to oleyl alcohol at our standard injection rate at 150 °C. This temperature was chosen because NCs are not formed, allowing determination of the rate of esterification of the precursor rather than the NCs. The NMR peak at 5.37 ppm is due to the alkene in the oleate carbon chain: Its intensity represents all organic oleate material in the sample. The NMR peak at 4.08 ppm is due to the carbon adjacent to the carbonyl in esterification product, oleyl oleate. Comparison oleyl oleate peak to the sum of the alkene peaks yields the relative amount of ester formed compared to all oleate in solution.

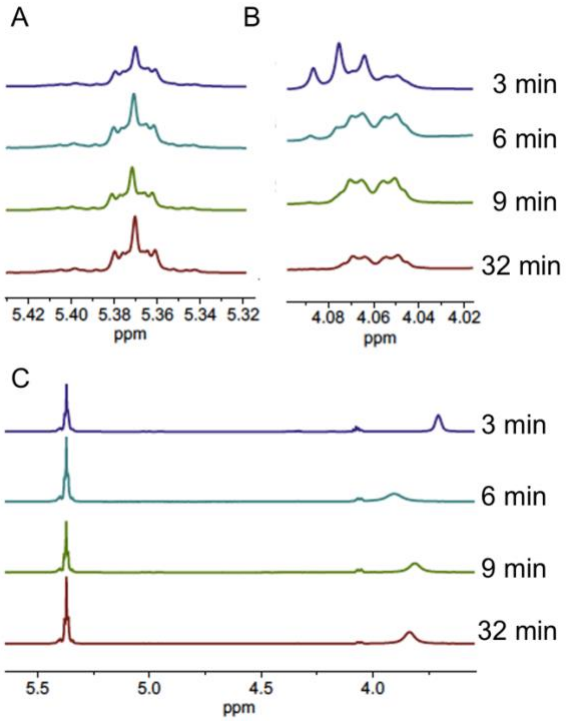

Figure C4. Fe (III) oleate esterification NMR of compared peaks that were used to determine ester content at different times in the reaction reported in Table C2. A) The peak at 5.37 ppm is due to the alkene functional group in the oleate carbon chain. B) The peak at 4.06 ppm is due to the carbon adjacent to the carbonyl in oleyl oleate. C) Shows the NMR from 5.5 to 3.0 ppm.

Table C2. The values for the normalized integrals of the oleate alkene peak, the carbonyl of the oleyl oleate, the time that the samples were taken for Fe rich (III) oleate.

Normalized integral of oleyl oleate peak (4.06 ppm) to alkene peak (5.37 ppm)	Time (min)	Percent ester of all oleate chains (%)
0.14	3	28
0.2	6	40
0.19	9	38
0.2	32	40

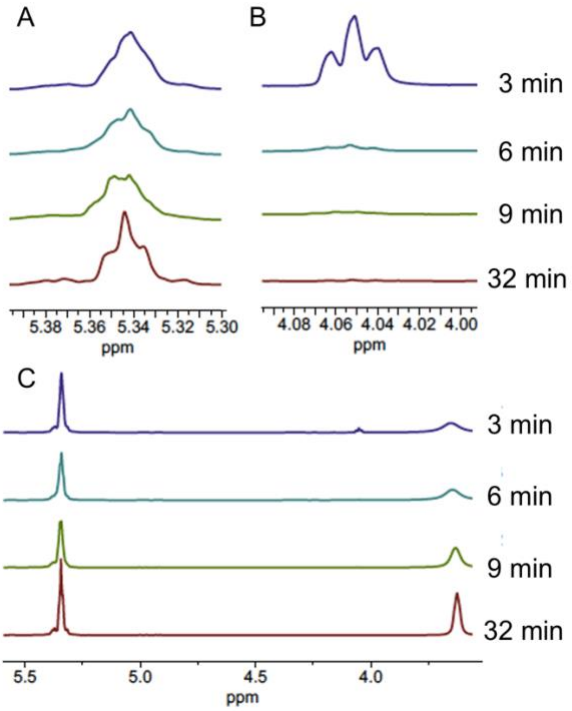

Figure C5. Fe (II) rich oleate esterification NMR of compared peaks that were used to determine ester content at different times in the reaction reported in Table C3. A) The peak at 5.37 ppm is due to the alkene functional group in the oleate carbon chain. B) The peak at 4.06 ppm is due to the carbon adjacent to the carbonyl in oleyl oleate. C) Shows the NMR from 5.5 to 3.0 ppm.

Table C3. The values for the normalized integrals of the oleate alkene peak, the carbonyl of the oleyl oleate, the time that the samples were taken for Fe (II) rich oleate.

Normalized integral of oleyl oleate peak (4.06 ppm) to alkene peak (5.37 ppm)	Time (min)	Percent ester of all oleate chains (%)
0	3	0
0.01	6	2
0.02	9	4
0.06	32	12

In Situ Setup for Total X-ray Scattering Data Acquisition

In order to collect scattering data as particles were forming we designed an *in situ* reaction setup. Reactions were carried out in a three neck round bottom flask. The left neck was closed with a septum through which precursor was slowly injected and also contained a needle to vent gas and vapor. The middle neck contained a septum supporting a thermocouple that was used in conjunction with a programmable temperature controller to keep the reaction temperature constant. Sampling occurred through a silicone septum rated for high temperature on the third neck. That septum was fitted with two needles; one for removing reaction liquid from the flask and one for returning reaction liquid after it had moved through the 3 mm glass detection cell.

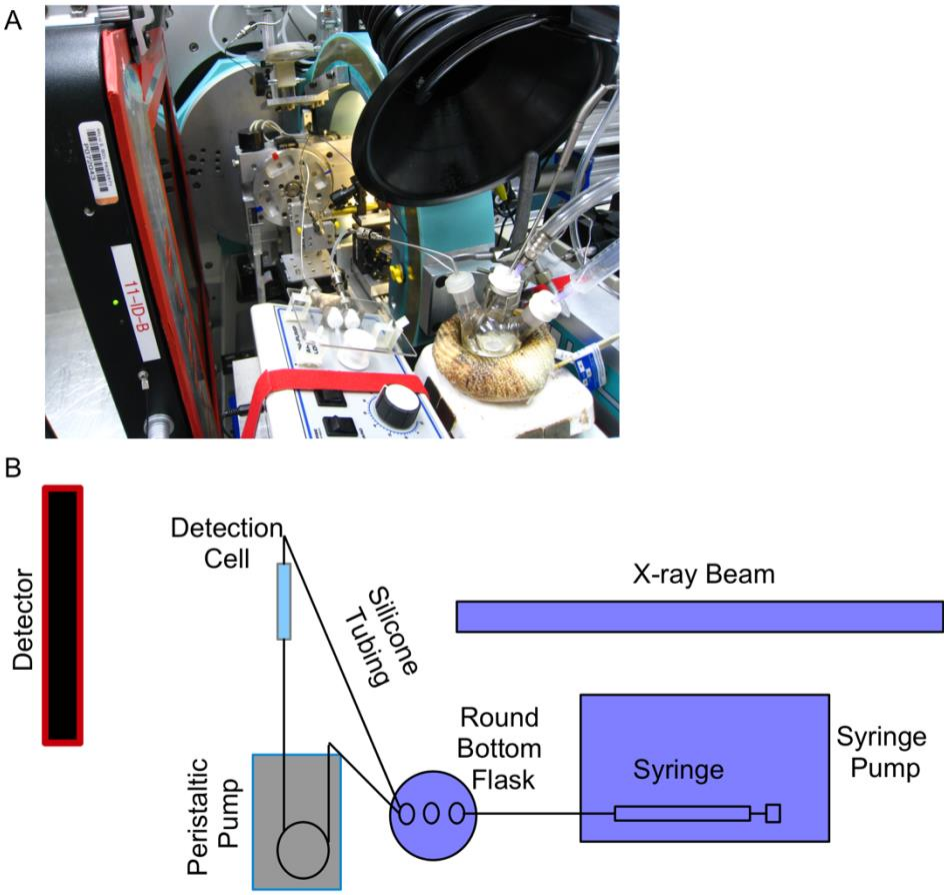

Figure C6. A) Photo of the *in situ* setup used to collect data for the continuous growth method[1]. The detector is in red on the left of the picture, In the forefront of the photograph, the peristaltic pump is next to the detector and the round bottom reaction flask is on the right of the photograph. To orient the photo a diagram is also included. B) A diagram of the *in situ* setup is shown in an aerial view. The detector is on the farthest left of the diagram and the X-ray beam is on the farthest right. Precursor is injected into the round bottom flask using a syringe pump. Reaction solution is being continuously pulled out of the round bottom flask using a peristaltic pump, through the detection cell, and returned to the round bottom flask.

In Situ PDF Data from Continuous Growth Synthesis with Fe (III) Rich Oleate Precursor at 230°C

Data was acquired at beamline 11-ID-B at Argonne National Lab's Advanced Photon Source. Instrumental resolution was refined using a CeO_2 standard. Q_{Broad} was set to 0.01 and Q_{Damp} was set to 0.04. PDFs from Total X-ray Scattering data acquired from

26 min to 176 min (0.8 mmol to 3 mmol of added iron precursor) were refined. PDFs of *in situ* Total X-ray Scattering data was refined with a spinel structural model taking the space group $P4_32_12$[2] as has been previously described in chapter two of this dissertation. Initial values are included in Table C4-C6. Debye-Waller factors were refined for the PDF of the last acquired time point and then the Debye-Waller factors were fixed for PDFs generated from data acquired at earlier time points. No positions were refined because there was more scatter in the refined NC diameter when refined. Delta 2 was also refined and maintained a physical value for all timepoints reported.

Equation C1 describes solvent ordering in dilute nanoparticle solutions.[3] In Equation S1, A is the amplitude, λ is the wavelength and φ is the phase shift. The value for the effective dampening (σ_{eff}) is $\sigma_{eff} = \sigma/a$ for $r < r_0$ and $\sigma_{eff} = \sigma * a$ for $r < r_0$ where a is the asymmetry parameter.

$$w(r) = A\sin\left(2\pi\left(\frac{r}{\lambda} - \varphi\right)\right)e^{-\left(\frac{(r-r_0)}{2\sigma_{eff}}\right)^2} \qquad \text{(Equation C1)}$$

Table C4. Starting values for the PDF refinement for the damped sine wave.

A	0.5 Å
λ	4 Å
φ	1°
r_0	1 Å
σ	4 Å
a	1

Table C5. The starting parameters used for the analysis of *in situ* data for NCs made by using Fe (III) rich mixed precursor. structural[2] model that takes space group $P4_32_12$ as was previously shown to be the best in *ex situ* samples made by the continuous growth method published previously.

a,b	8.406 Å
c	8.474 Å
Delta 2	2 Å
Fe1 occupancy	0.7
Fe4 occupancy	0.7
Crystallite Diameter	40 Å
Biso Fe1	0.49 $Å^{-2}$
Biso Fe2	0.46 $Å^{-2}$
Biso Fe3	0.70 $Å^{-2}$
Biso Fe4	0.39 $Å^{-2}$
Biso O	0.9 $Å^{-2}$

Table C6. Positions for spinel iron oxide using the structural[2] model that takes space group $P4_32_12$.

	x	y	z
Fe1	0.749	0.997	0.127
Fe2	0.629	0.629	0
Fe3	0.379	0.872	0.994
Fe4	0.125	0.125	0
O1	0.572	0.894	0.925
O2	0.121	0.369	0.997
O3	0.125	0.849	0.069
O4	0.382	0.628	0.996

Table C7. Refined values of Fe (III) rich oleate precursor continuous growth synthesis using 4 selected time points throughout the *in situ* reaction.

Time into reaction (min)	26	71	121	176
mmol added	0.63	1.77	3	3
Crystallite Diameter	51 Å	59 Å	65 Å	66 Å
R_W	0.22	0.15	0.12	0.12
a,b	8.410 Å	8.409 Å	8.406 Å	8.406 Å
c	8.477 Å	8.474 Å	8.471 Å	8.473 Å
Delta 2	2.4 Å	2.6 Å	2.6 Å	2.8 Å
Fe1 occupancy	0.84	0.87	0.93	0.93
Fe4 occupancy	0.99	0.84	0.77	0.82
A	2 Å	370000 Å	46000 Å	140000000 Å
λ	4 Å	5 Å	5 Å	5 Å
φ	1 º	1 º	1 º	1 º
r_0	-8 Å	-82 Å	-73 Å	-120 Å
σ	5 Å	7 Å	7 Å	8 Å
a	1	2	2	2

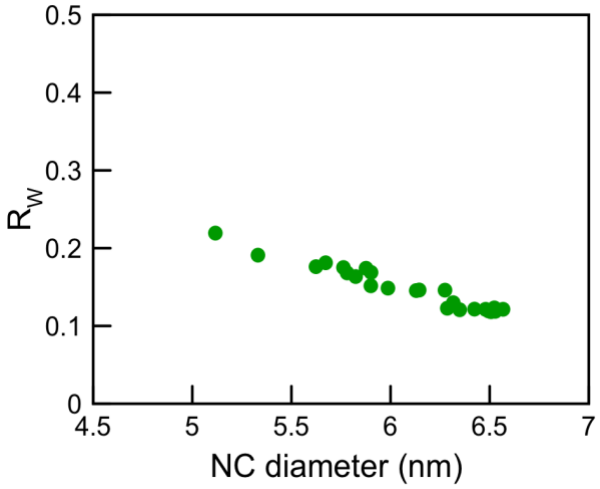

Figure C7. Rw from refinements of *in situ* PDF data made with Fe (III) oleate precursor at 230ºC through a continuous growth synthesis using the structural model for spinel iron oxide that takes the space group $P4_32_12$.

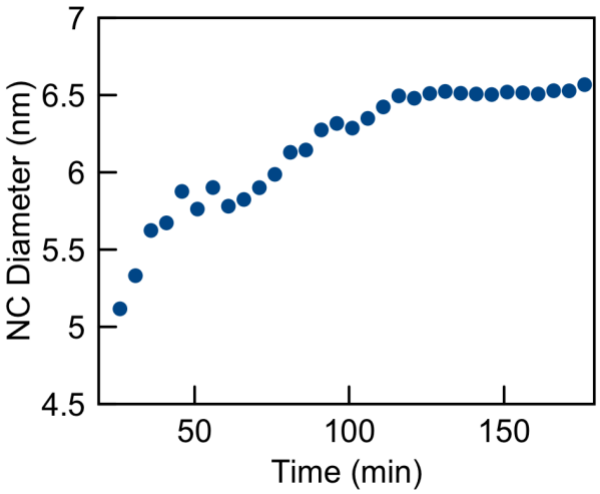

Figure C8. NC diameter from refinements of *in situ* PDF data made with Fe (III) oleate precursor at 230ºC through a continuous growth synthesis refined using the structural model for spinel iron oxide that takes the space group $P4_32_12$.

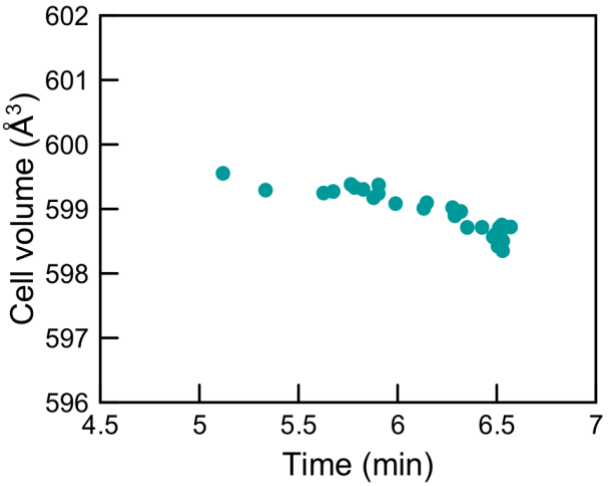

Figure C9. Cell volume from refinements of *in situ* PDF data made with Fe (III) oleate precursor at 230ºC through a continuous growth synthesis refined using the structural model for spinel iron oxide that takes the space group $P4_32_12$.

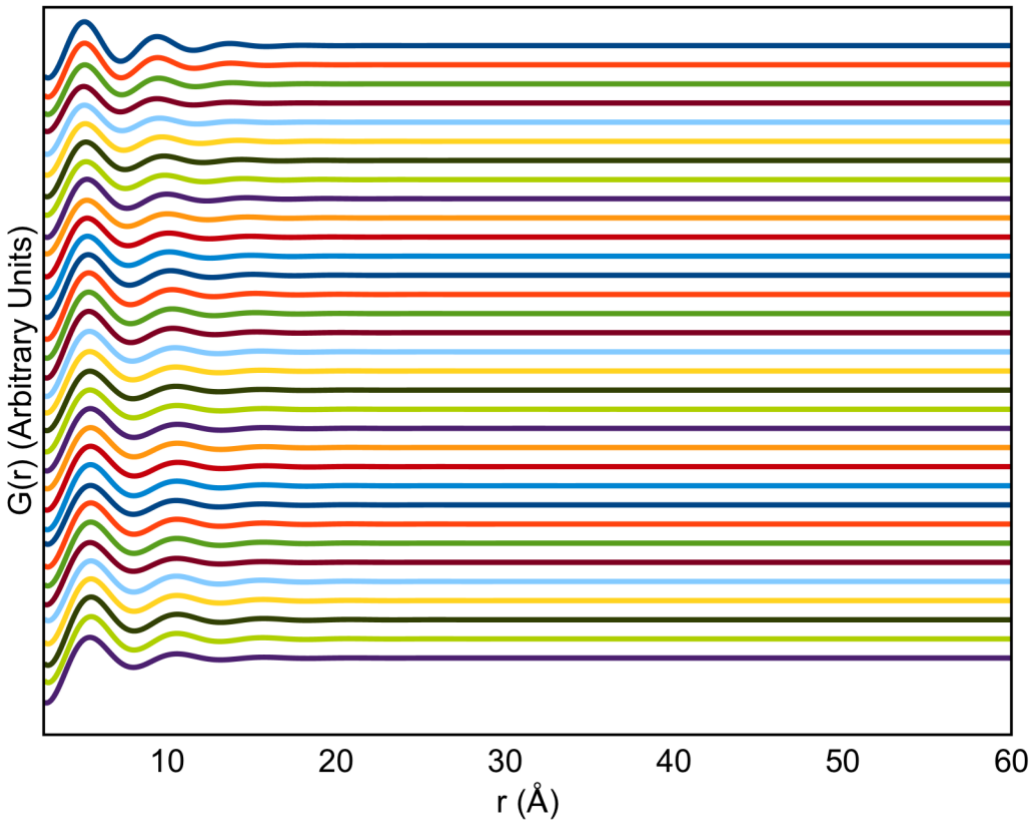

Figure C10. Waves described by equation one from refinements of *in situ* PDF data made with Fe (III) oleate precursor at 230ºC through a continuous growth synthesis refined using the structural model for spinel iron oxide that takes the space group $P4_32_12$. The order of the waves is from earliest time point to latest from top to bottom.

Duplicate in situ from continuous growth synthesis with Fe (III) rich oleate precursor at 230°C

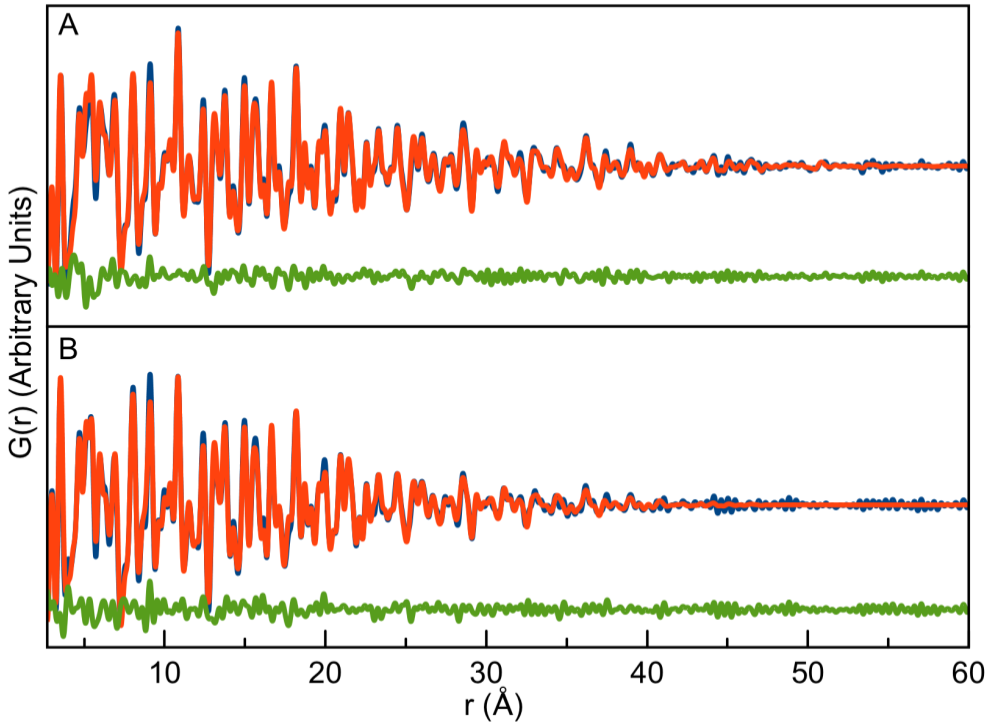

Figure C11. Fits from *in situ* PDF data made with Fe (III) rich oleate precursor at 230ºC through a continuous growth synthesis for A) 175 min and B) 22 min acquisition refined using the structural model for spinel iron oxide that takes the space group $P4_32_12$.

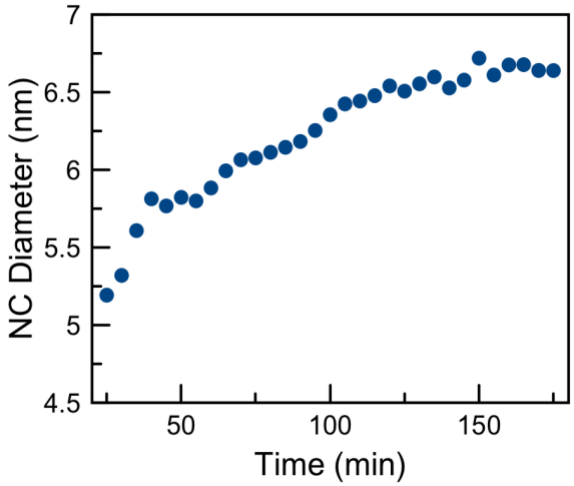

Figure C12. NC diameter from refinements of *in situ* PDF data made with Fe (III) oleate precursor at 230ºC through a continuous growth synthesis refined using the structural model for spinel iron oxide that takes the space group $P4_32_12$.

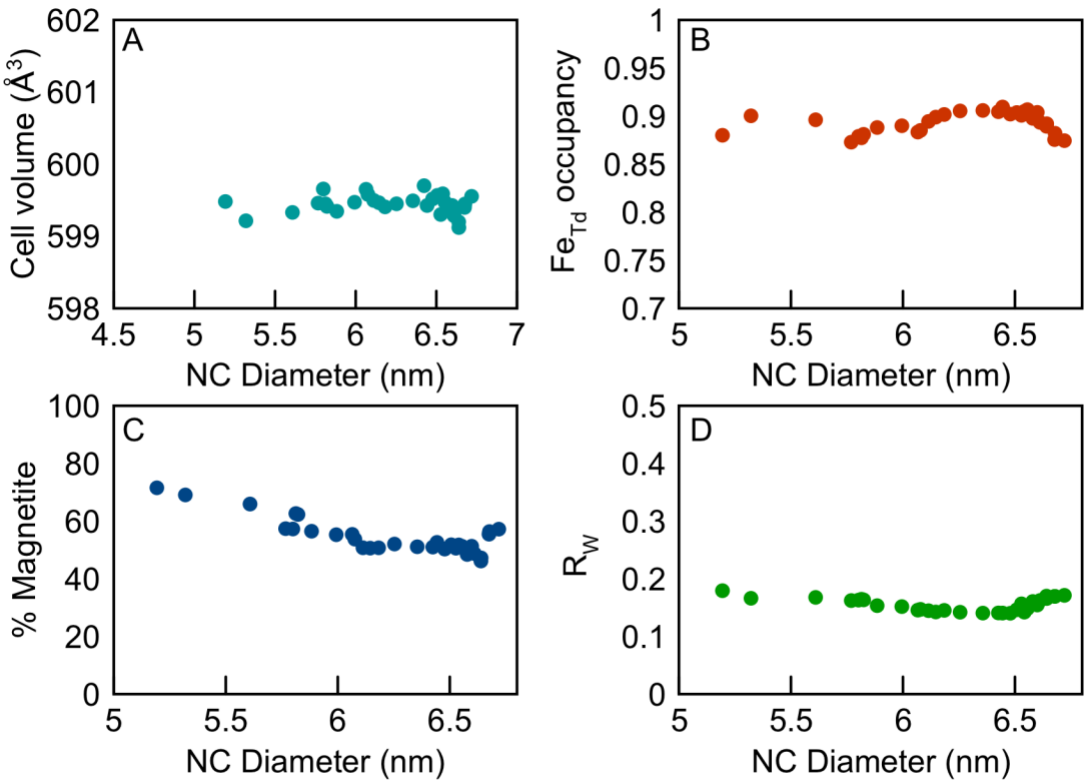

Figure C13. A) Cell volume, B) tetrahedrally coordinated cation occupancy, C) the percentage magnetite and D) the R_W are all plotted by the refined NC diameter from refinements of *in situ* PDF data made with Fe (III) oleate precursor at 230ºC through a continuous growth synthesis refined using the structural model for spinel iron oxide that takes the space group $P4_32_12$.

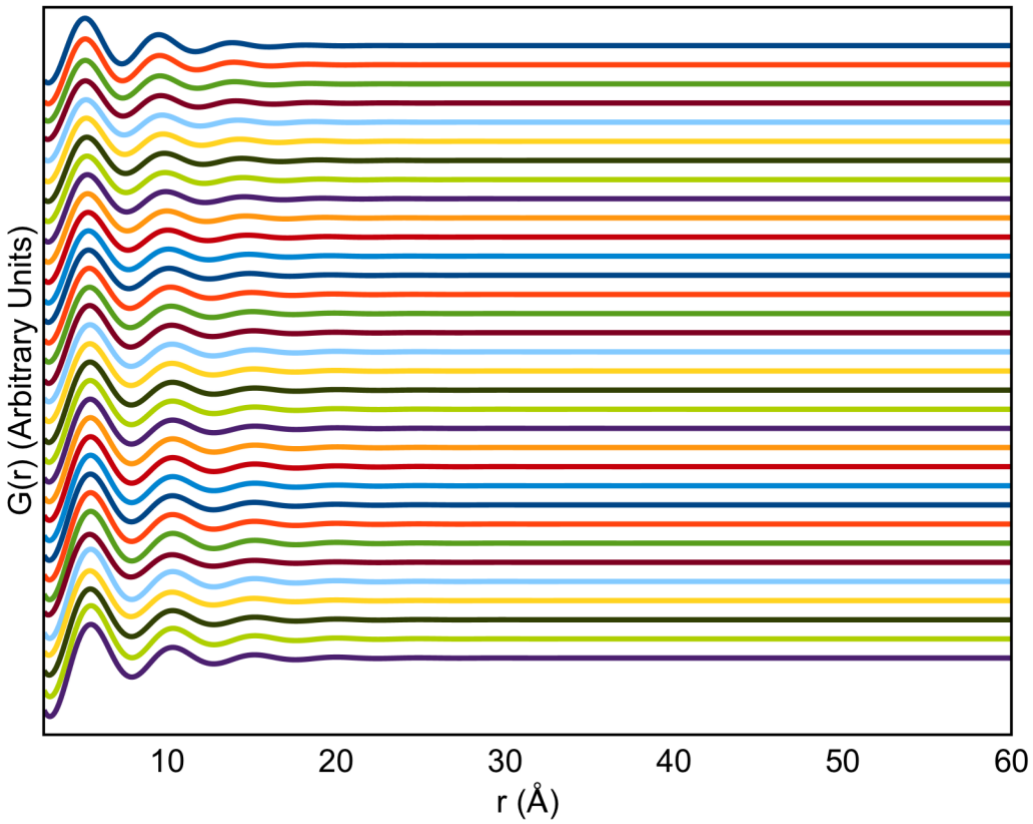

Figure C14. Waves described by equation one from refinements of *in situ* PDF data made with Fe (III) oleate precursor at 230ºC through a continuous growth synthesis refined using the structural model for spinel iron oxide that takes the space group $P4_32_12$. The order of the waves is from earliest time point to latest from top to bottom.

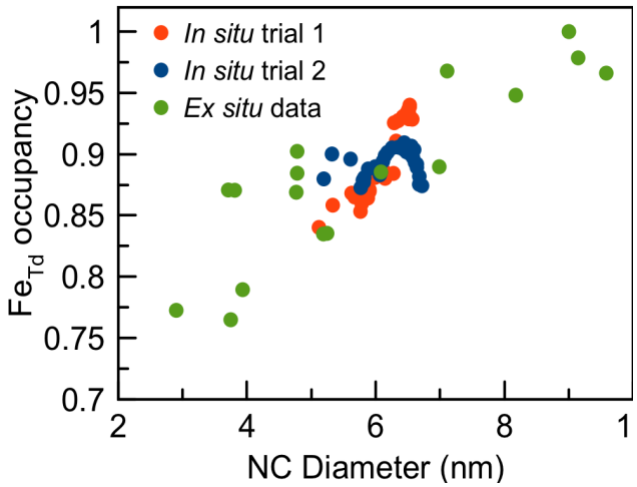

Figure C15. Tetrahedrally coordinated iron occupancy compared between duplicate *in situ* Total X-ray Scattering experiments and *ex situ* experiments reported in chapter three of this dissertation.

Analysis of In Situ PDF Products by Powder X-Ray Diffraction and PDF Made with Fe (III) Rich Oleate at 230°C

Table C8. Refined parameters for lab scale Powder X-Ray Diffraction **(**XRD) using spinel phase taking the space group *Fd-3m* of particles made with a Fe (III) rich precursor at the beamline measured a month after synthesis.

Bragg R factor	2.49
Rf factor	1.59
a	8.369
Biso Fe	0.598
Instrument Displacement	-0.0973
IG	1.42644
Crystallite diameter (nm)	6.9 nm

Table C9. Refined parameters for synchrotron PDF data using spinel phase taking the space group $P4_32_12$ of particles made with a Fe (III) rich precursor measured months after synthesis.

Crystallite Diameter	62 Å
R_W	0.21
a,b	8.326 Å
c	8.416 Å
Delta 2	0.3 Å
Fe1 occupancy	1
Fe4 occupancy	0.43
A	0.7Å
λ	4.5 Å
φ	1 º
r_0	-2 Å
σ	9 Å
a	-1

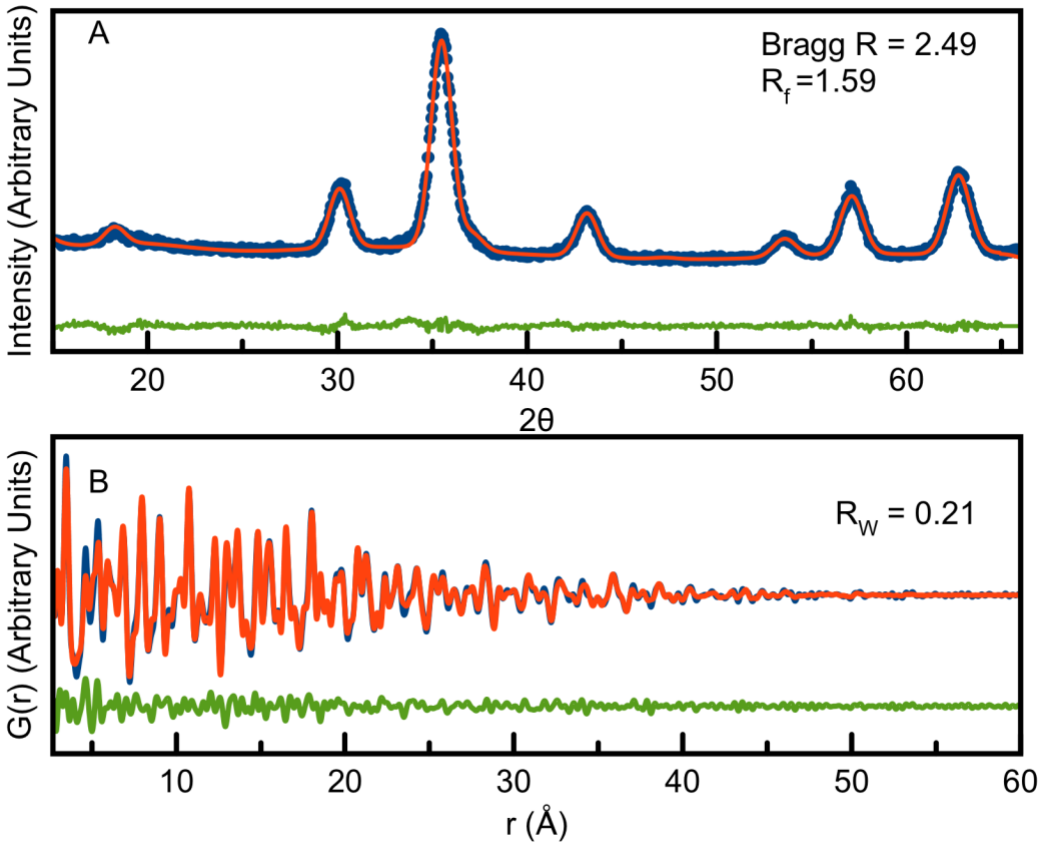

Figure C16. A) Fit of XRD pattern using the structural model of spinel iron oxide taking the space group *Fd-3m* and B) fit of PDF on samples using the structural model of spinel iron oxide taking the space group $P4_32_12$. Samples were obtained after an *in situ* beamline experiment that were made with Fe (III) rich oleate at 230ºC.

Possible Structural Models to use for Refinement of the *In Situ* PDF Data from Continuous Growth Synthesis Fe (II) Rich Oleate Precursor at 230°C

There are various wüstite and spinel models that could be used to describe the NPs that appear to be a mixture of the two phases. Wüstite is almost never stoichiometric and a variety of structures have been published describing the structure. Simple wüstite[4] with averaged cation vacancies, and wüstite with octahedral cation vacancies and tetrahedral cations.[5–7] Octahedral cation vacancies and emergence of tetrahedral cations are very similar to small bits of the spinel[2] structure in the wüstite phase. The different structural models have different percentages of tetrahedrally coordinated cations in the structure as

seen in Figure C17. Refinements were performed using structural models of spinel that take the spacegroup $P4_32_12$[2], and wüstite that takes the spacegroup $Fm\text{-}3m$[4], $P4\text{-}3m$[5] and $Fd\text{-}3m$[6] and fits are included in Figure C18 – C24.

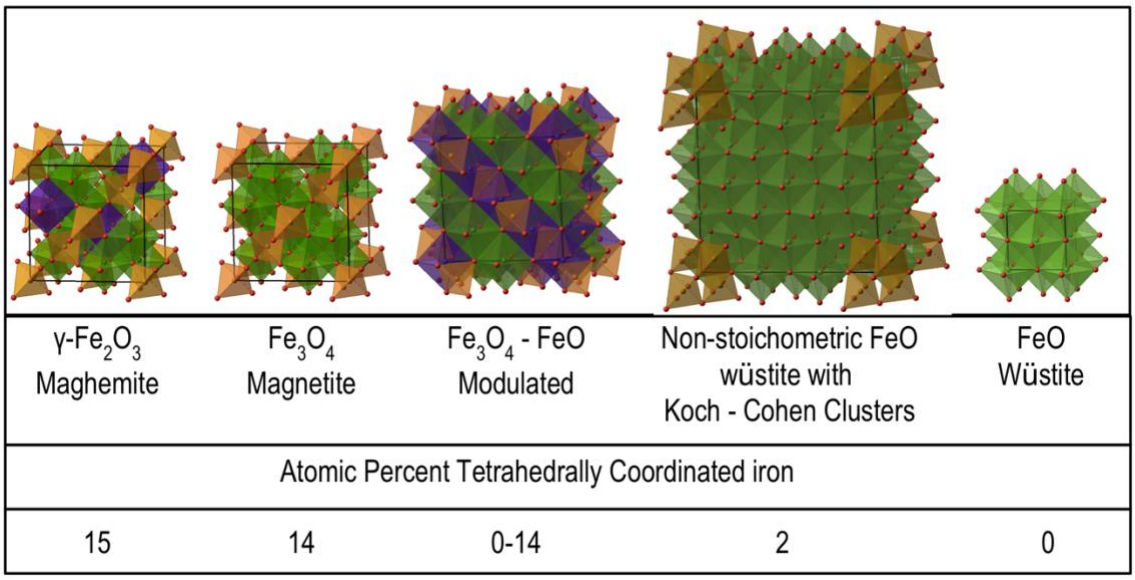

Figure C17. Shows the structural models from wüstite to spinel labeled with the atomic percent of tetrahedrally coordinated cations in each model.

Fits of in situ PDF data from continuous growth synthesis Fe (II) rich oleate precursor at 230°C with spinel structural models

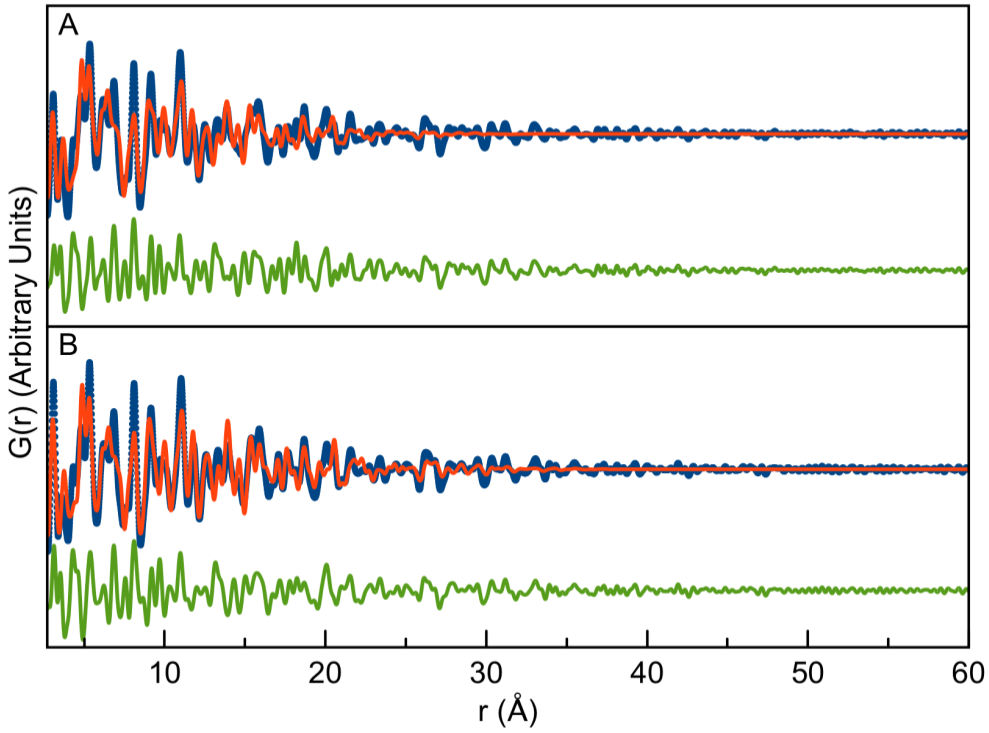

Figure C18. Fits from *in situ* PDF data made with Fe (II) rich oleate precursor at 230ºC through a continuous growth synthesis for A) 175 min and B) 30 min acquisitions refined using the structural model for spinel iron oxide that takes the space group $P4_32_12$.

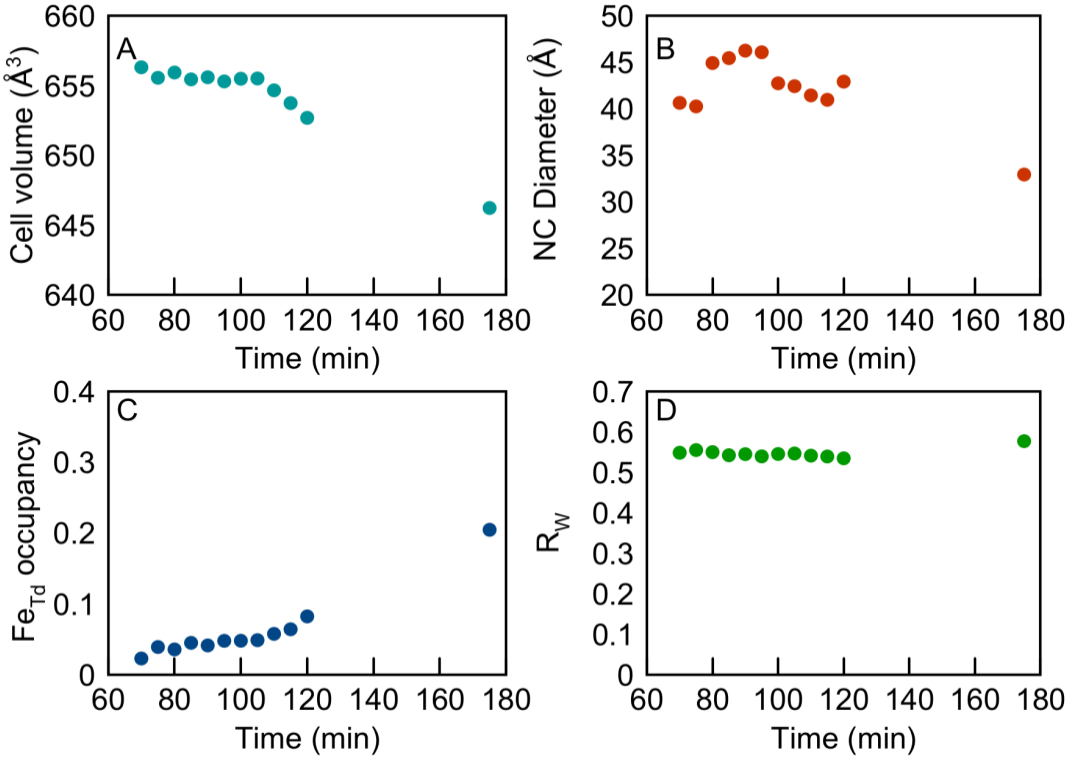

Figure C19. A) Cell volume, B) NC diameter, C) tetrahedrally coordinated cation occupancy and D) the Rw are all plotted by the refined NC diameter from refinements of *in situ* PDF data made with Fe (II) oleate precursor at 230ºC through a continuous growth synthesis refined using the structural model for spinel iron oxide that takes the space group $P4_32_12$.

Fits of in situ PDF data from continuous growth synthesis Fe (II) rich oleate precursor at 230°C with other wüstite structural models

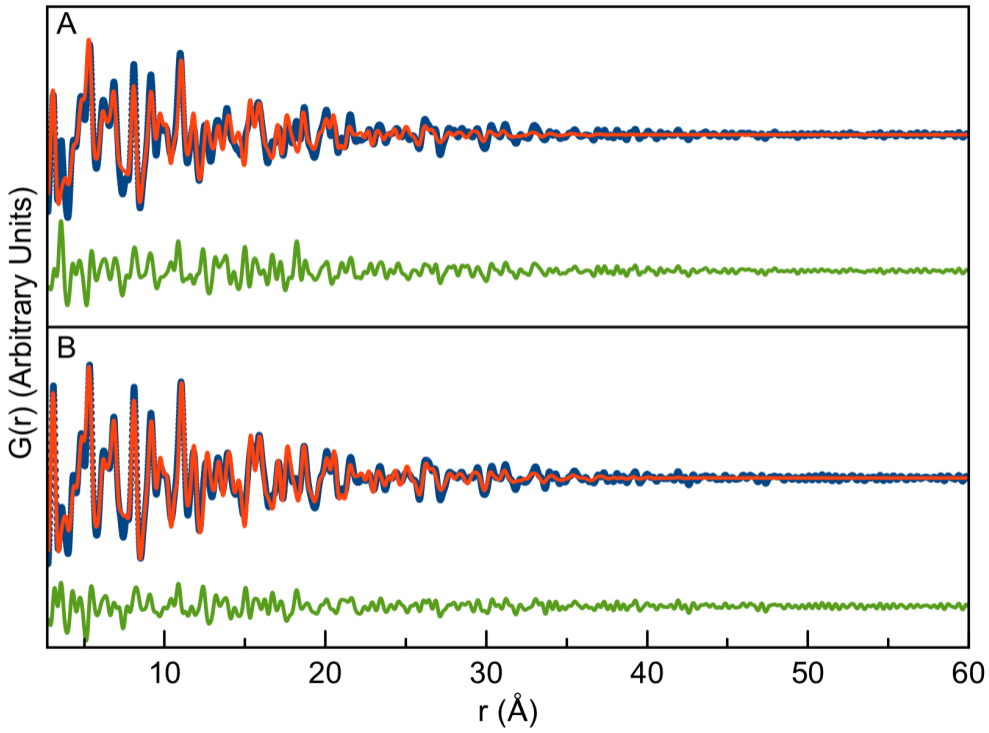

Figure C20. Fits from *in situ* PDF data made with Fe (II) rich oleate precursor at 230ºC through a continuous growth synthesis for A) 175 min and B) 30 min acquisitions refined using the structural model for wüstite taking the space group *Fm-3m*.

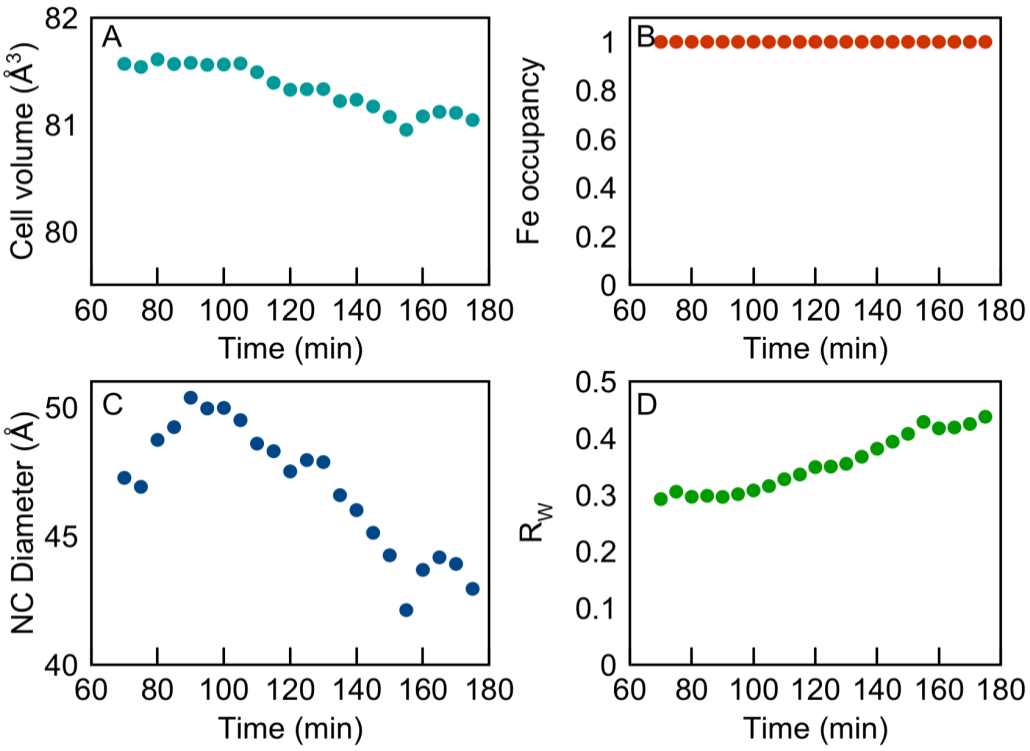

Figure C21. A) Cell volume, B) iron cation occupancy, C) NC diameter and D) the Rw are all plotted by time from refinements of *in situ* PDF data made with Fe (II) oleate precursor at 230ºC through a continuous growth synthesis refined using the structural model for wüstite taking the space group *Fm-3m*.

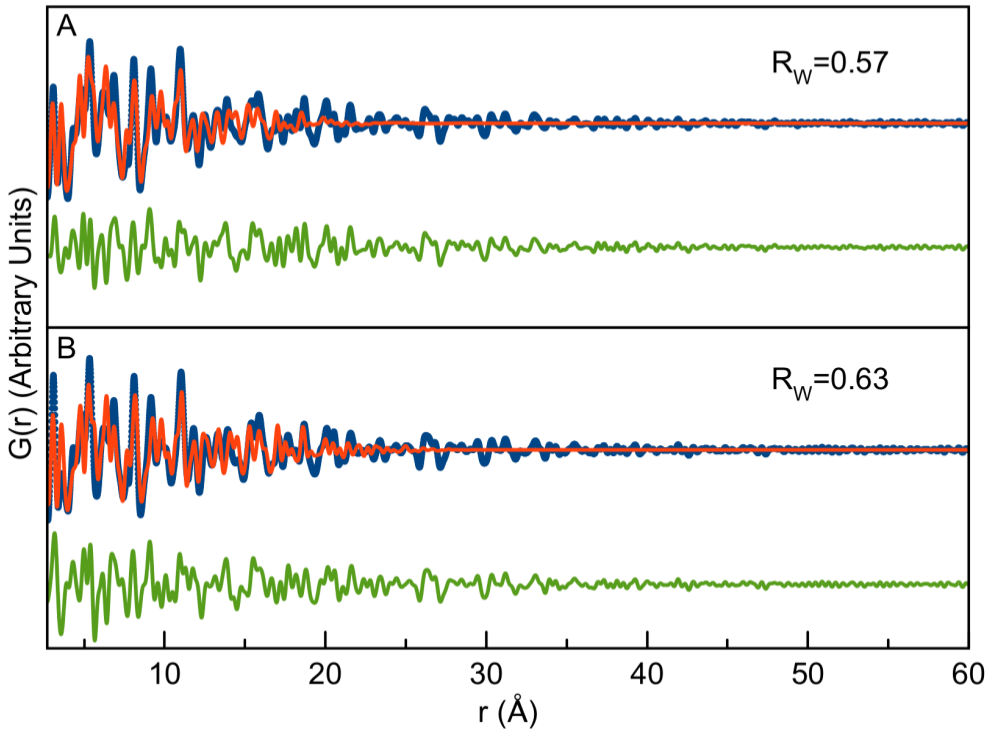

Figure C22. Fits from *in situ* PDF data made with Fe (II) rich oleate precursor at 230ºC through a continuous growth synthesis for A) 175 min and B) 30 min acquisitions refined using the structural model for wüstite with Koch-Cohen clusters taking the space group *P4-3m*.

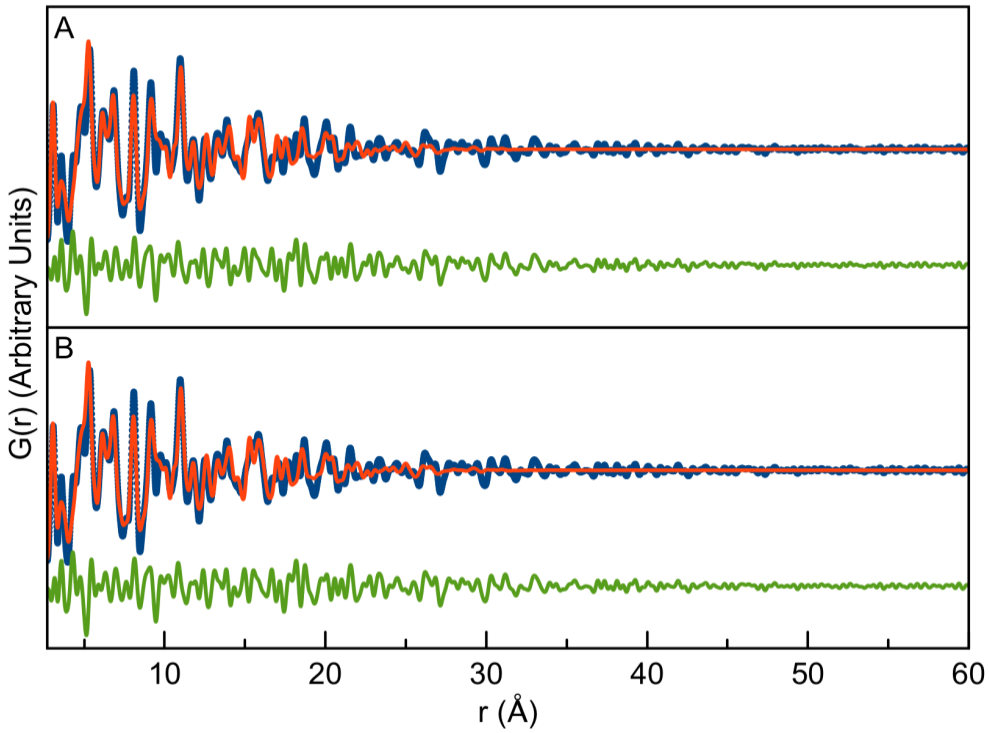

Figure C23. Fits from *in situ* PDF data made with Fe (II) rich oleate precursor at 230ºC through a continuous growth synthesis for A) 175 min and B) 30 min acquisitions refined using the structural model for modulated wüstite structure taking the space group *Fd-3m*.

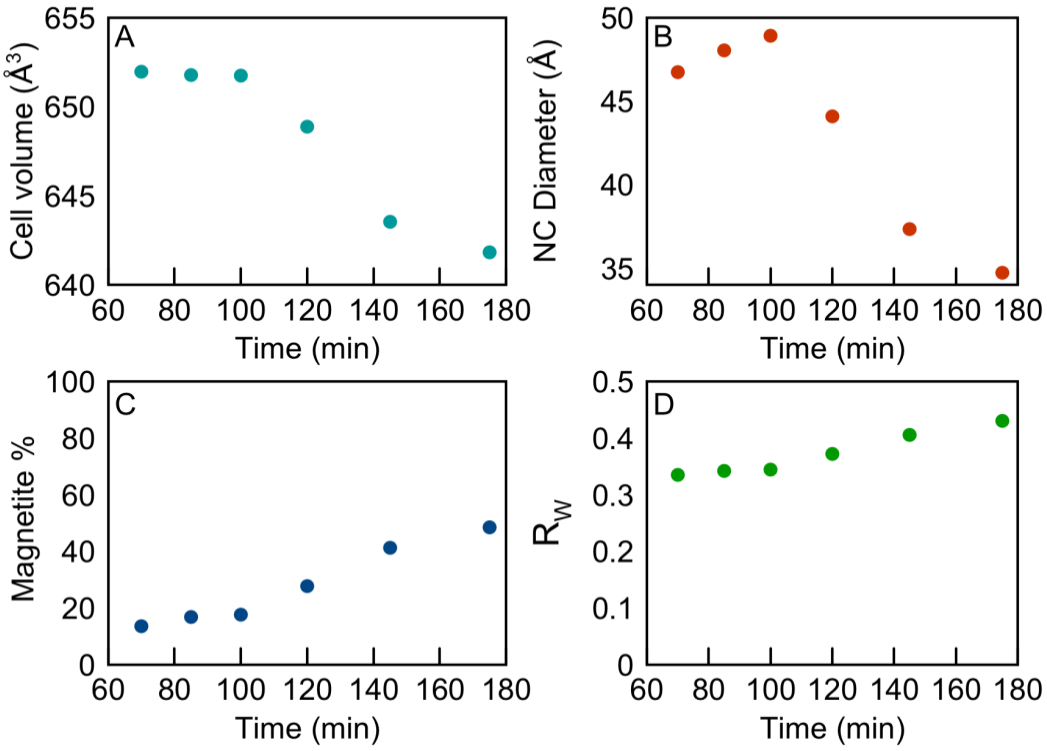

Figure C24. A) Cell volume, B) NC diameter, B) percent magnetite, and D) the Rw are all plotted by time from refinements of *in situ* PDF data made with Fe (II) oleate precursor at 230ºC through a continuous growth synthesis refined using the structural model for modulated wüstite structure taking the space group *Fd-3m*.

Bond Distances in Local r-Range for Spinel and Wüstite Structural Models

Table C10. Select bond distances in low r region for spinel iron oxide that takes the space group *Fd-3m*.[2,8]

Bond pair	Distance (Å)
Fe-O Td	1.87
Fe-O Oh	2.06
Fe-Fe Oh	2.97
FeOh - FeTd	3.48
FeTd - O	3.49
FeTd-FeTd	3.64
FeOh - O	3.67

Table C11. Select bond distances in low r region for and wüstite that takes the space group *Fm-3m*.[4]

Bond pair	Distance (Å)
Fe-O	2.15
Fe-Fe	3.04
Fe-O	3.72
Fe-Fe	4.30
Fe-O	4.81
Fe-Fe	5.27
Fe-O	2.15

In Situ PDF Data from Continuous Growth Synthesis with Fe (II) Rich Oleate Precursor at 230°C

This data fit a mixture of spinel[8] (*Fd-3m*) and wüsitite[4] (*Fm-3m*) phases. The wave describing solvent was also used in refinement of Fe (II) oleate values from 30 min to 175 min (0.4 – 3 mmol of added Fe (II) oleate precursor). In order to estimate diameter we assumed a core shell model used previously[9] with a wüstite core and a magnetite shell. The scales were used to determine the size of the particles using the wüstite size as the core particle.

Table C12. The parameters used for both the spinel[8] and wüstite[4] models used in refinements of data acquired in Fe (II) oleate *in situ* synthesis.

a spinel	8.44 Å
Delta 2 spinel	2 Å
Crystallite Diameter spinel	50 Å
Occupancy Fe1, Fe2 spinel	1
Biso Fe spinel	0.7 $Å^{-2}$
Biso O spinel	2.0 $Å^{-2}$
Scale spinel	0.4
a wüstite	4.35 Å
Delta 2 wüstite	2 Å
Crystallite Diameter wüstite	50 Å
Occupancy Fe1 wüstite	1
Biso Fe wüstite	0.86 $Å^{-2}$
Biso O wüstite	3.0 $Å^{-2}$
Scale wüstite	0.4
A	12959 Å
λ	5.2 Å
φ	-0.17 º
r_0	-62 Å
σ	9.3 Å
a	1.1

Table C13. Positions for spinel model taking the spacegroup *Fd-3m* used in refinements of data acquired in Fe (II) oleate *in situ* synthesis.

	x	y	z
Fe1	0.125	0.125	0.125
Fe2	0.5	0.5	0.5
O1	0.255	0.255	0.255

Table C14. Positions for wüstite model taking the spacegroup *Fm-3m* used in refinements of data acquired in Fe (II) oleate *in situ* synthesis.

	x	y	z
Fe1	0	0	0
O1	0.5	0.5	0.5

Table C15. Results refined for Fe (II) oleate synthesis at 230ºC using mixed phase fit using spinel model that takes the structural group *Fd-3m* and a wüstite model taking the space group *Fm-3m*.

Time into reaction (min)	30	70	125	175
mmol added	0.8	1.9	3	3
a spinel	8.51 Å	8.49 Å	8.48 Å	8.47 Å
Crystallite Diameter spinel	44.9 Å	41.4 Å	43.0 Å	44.2 Å
Scale spinel	0.33	0.39	0.49	0.60
a wüstite	4.34 Å	4.34 Å	4.34 Å	4.34 Å
Crystallite Diameter wüstite	40.0 Å	42.6 Å	48.0 Å	48.3 Å
Scale wüstite	0.67	0.61	0.51	0.40
A	1.0 Å	2.0E+09 Å	5.0E+08 Å	1.5E+08 Å
λ	4.4 Å	4.9 Å	4.8 Å	4.7 Å
φ	-0.03 º	-0.10 º	-0.08 º	-0.06 º
r_0	0.3 Å	-1.9E+02 Å	-1.9E+02 Å	-2.0E+02 Å
σ	7 Å	13 Å	13 Å	14 Å
a	0.5	1.6	1.6	1.7

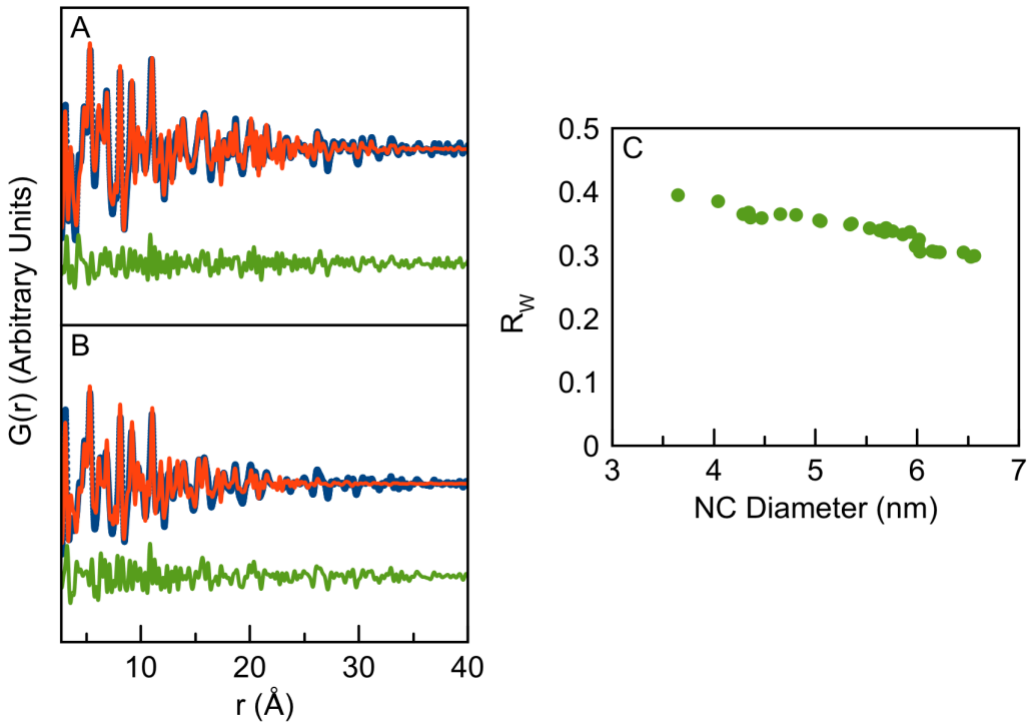

Figure C25. Fits of at A) 175 min and B) 30 min as well as R_W (C) refined for the *in situ* data collected during a continuous growth synthesis using Fe (II) oleate synthesis at 230ºC. Data was refined with a mixed phase model using a spinel model that takes the structural group *Fd-3m* and a wüstite model taking the space group *Fm-3m*.

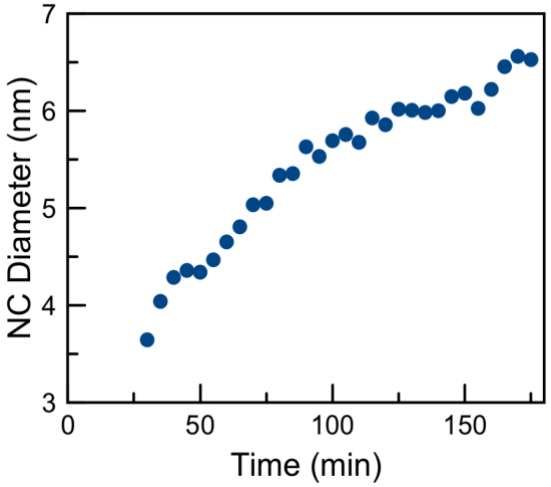

Figure C26. NC diameter determined by refined values of wüstite diameter and wüstite fraction for the *in situ* data collected during a continuous growth synthesis using Fe (II) oleate synthesis at 230ºC. Data was refined with a mixed phase model using a spinel model that takes the structural group *Fd-3m* and a wüstite model taking the space group *Fm-3m*.

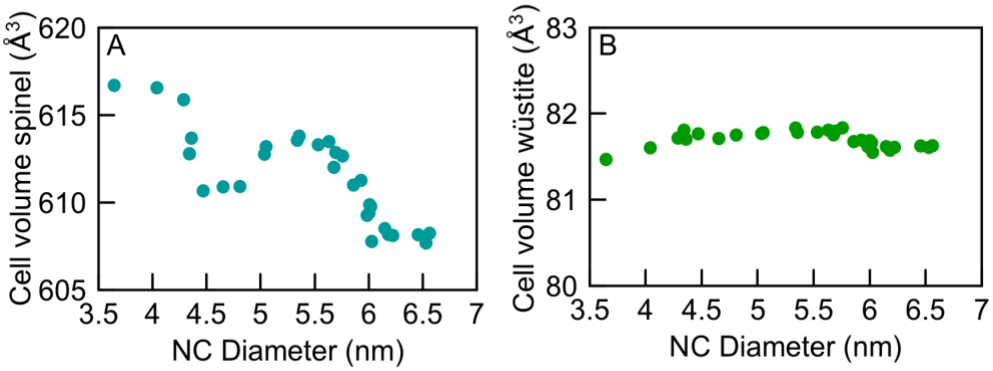

Figure C27. Refined values of cell volume of spinel and wüstite versus NC diameter determined by refined values of wüstite diameter and wüstite fraction for the *in situ* data collected during a continuous growth synthesis using Fe (II) oleate synthesis at 230ºC. Data was refined with a mixed phase model using a spinel model that takes the structural group *Fd-3m* and a wüstite model taking the space group *Fm-3m*.

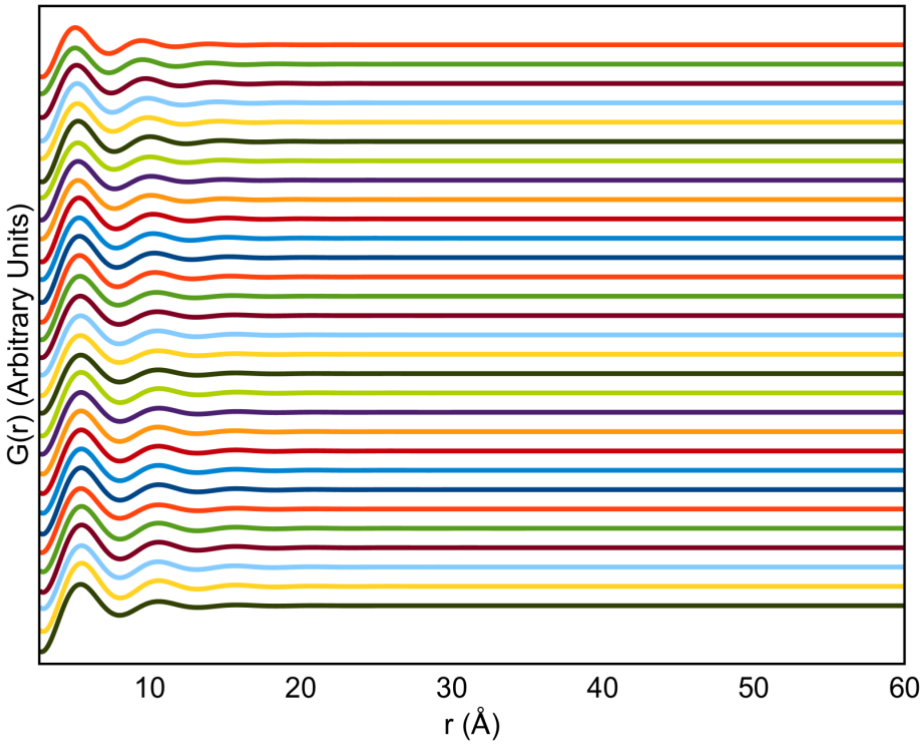

Figure C28. Waves described by equation one from refinements of *in situ* PDF data made with Fe (II) oleate precursor at 230ºC through a continuous growth synthesis refined using a mixed phase model using a spinel model that takes the structural group *Fd-3m* and a wüstite model taking the space group *Fm-3m*. The order of the waves is from earliest time point to latest from top to bottom.

Analysis of *In Situ* PDF Products by Powder X-Ray Diffraction and PDF Made with Fe (II) Rich Oleate at 230°C

Table C16. Refined parameters for lab scale Powder X-Ray Diffraction **(**XRD) using spinel phase taking the space group *Fd-3m* and wüstite taking the space group *Fm-3m* of particles made with a Fe (II) rich precursor at the beamline measured a month after synthesis.

	Spinel	Wüstite
Bragg R factor	9.41	10.2
Rf factor	4.13	5.32
a	8.364	4.182
Biso Fe	2.459	-
Instrument Displacement	-0.230	-0.230
IG	2.166	0.447
Crystallite diameter (nm)	5.6	12.4
scale	4.1E-5	1.9E-4
Weight percent (%)	92%	8%
Atom percent (%)	78%	22%

Table C17. Refined parameters for lab scale Powder X-Ray Diffraction **(**XRD) of particles made with a Fe (II) rich precursor at the beamline measured a month after synthesis using a spinel phase taking the space group *Fd-3m*.

Bragg R factor	10.1
Rf factor	5.19
a	8.369
Biso Fe	2.63
Instrument Displacement	-0.18
IG	2.156
Crystallite diameter (nm)	5.7

Table C18. Refined parameters for synchrotron PDF data of particles made with a Fe (II) rich precursor at the beamline measured six months after synthesis using a spinel phase taking the space group *Fd-3m* and a wüstite phase taking the space group *Fm-3m*.

	Spinel	Wüstite
Crystallite Diameter	59 Å	21 Å
R_W	0.24	0.24
a = b = c	8.36	4.32
Atom percent (%)	93 %	7 %
A	2 Å	2 Å
λ	4 Å	4 Å
φ	0.4 º	0.4 º
r_0	5.2 Å	5.2 Å
σ	0.2 Å	0.2 Å
a	1.4 Å	1.4 Å

Table C19. Refined parameters for synchrotron PDF data of particles made with a Fe (II) rich precursor at the beamline measured six months after synthesis using a spinel phase taking the space group $P4_32_12$.

Crystallite Diameter	57 Å
R_W	0.28
a,b	8.333 Å
c	8.426 Å
Delta 2	0.3 Å
Fe1 occupancy	0.83
Fe4 occupancy	0.47
A	0.6 Å
λ	0.7 Å
φ	4.3 º
r_0	3 Å
σ	0 Å
a	2

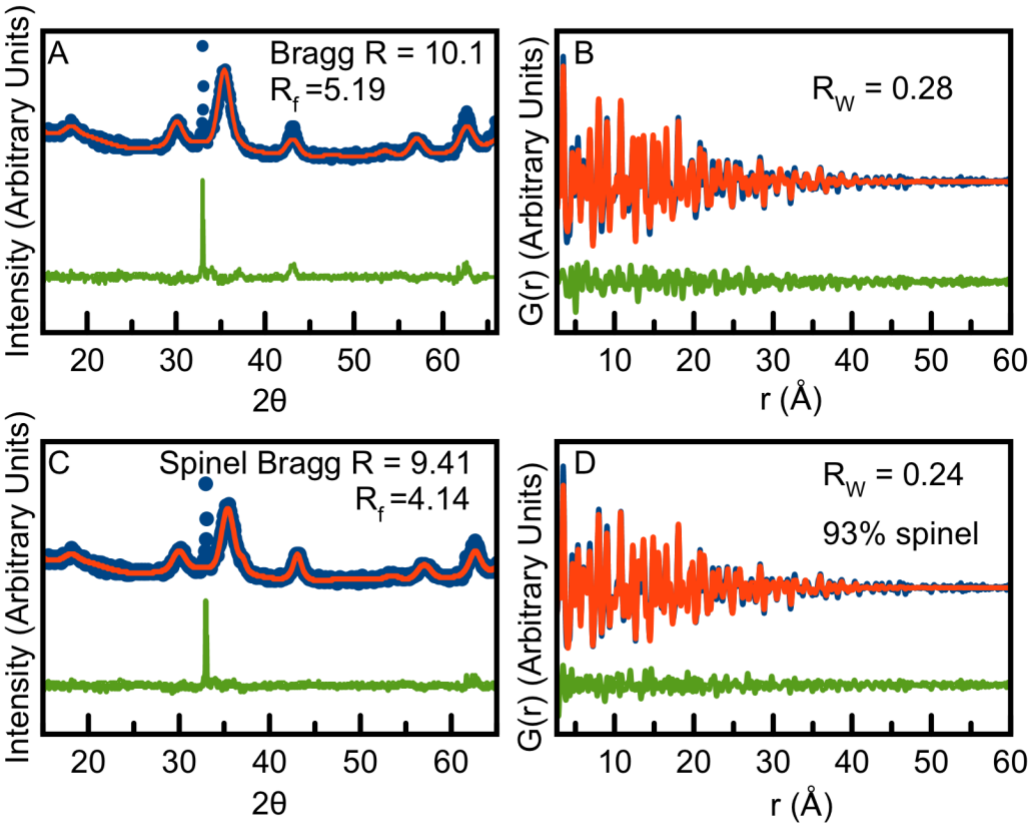

Figure C29. Products from an *in situ* beamline experiment that were made with Fe (II) rich oleate at 230ºC analyzed by both XRD and PDF weeks after synthesis. The data was refined, and fits are included above. A) Fit of XRD pattern with spinel iron oxide with spacegroup *Fd-3m* and B) fit of PDF with spinel iron oxide with spacegroup $P4_32_12$, C) fit of XRD pattern with spinel iron oxide with spacegroup *Fd-3m* and wüstite taking the space group *Fm-3m and D)* fit of PDF with spinel iron oxide with spacegroup *Fd-3m* and wüstite taking the space group *Fm-3m*.

Precursor Structure for Fe (II) Rich Oleate and Fe (III) Rich Oleate

Possible structural models are shown in Figure C30. Structural models used to refine PDFs of Fe (II) rich and Fe (III) rich oleate precursor include Fe (II) acetate[10], Fe (III) acetylacetonate [11,12] previously published iron oxide clusters [13–16] or a structural motif contained in spinel iron oxide crystal structures[8].

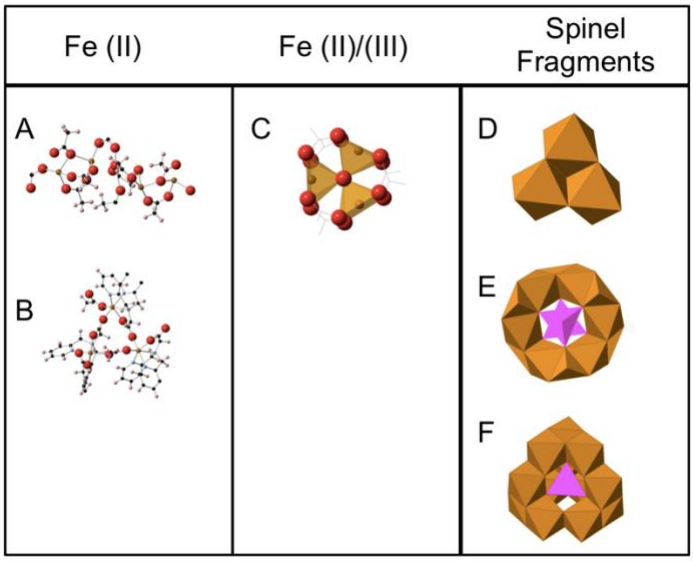

Figure C30. Structures most likely to be comparable to structural features in the precursors of each oxidation state. In the case of iron two there are two likely options: A) The structure of iron (II) acetate[10] and B) an iron (II) trimer[17]. For mixed valence structures there is a published mixed valence acetate trimer[11] which is the same structure as Fe(III) acetylacetonate[12]. Small fragments of a spinel structure. D) A trimer that forms in spinel[8], E) A cluster that is structurally contained in spinel and has also been published previously[18] and D) an iron Keggin cluster which is contained in spinel and a iron Keggin cluster has been recently reported[16] in literature.

Refinements of Fe (II) rich oleate and Fe (III) rich oleate

Precursor was refined using Diffpy-CMI. Each structural model was converted to an XYZ coordinate file using Crystal Maker to refine data. Total X-ray Scattering data was fit only refining the zoom scale, scale and delta 2 values. Positions were not refined. PDFs of Fe (II) rich oleate fit best with a mixed valence trimer structural model as opposed to a Fe (II) acetate structural model.

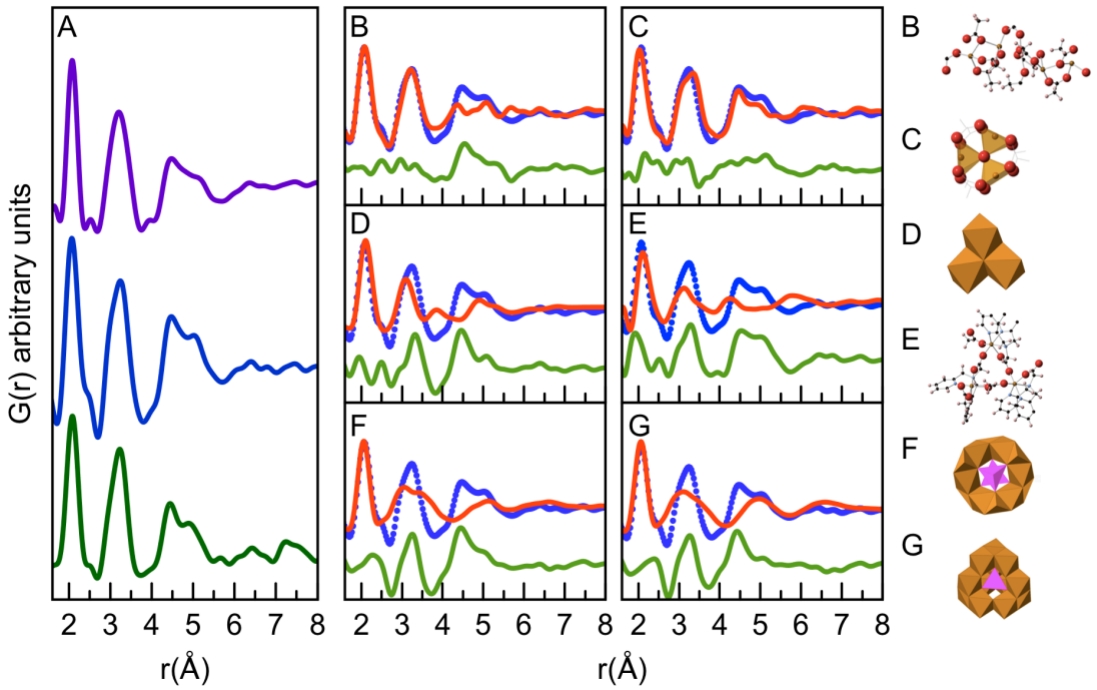

Figure C31. PDF of Fe (II) rich oleate precursor fit with possible cluster structural models. A) Three PDFs of Fe (II) rich oleate precursor. B-G) Shows fits of possible clusters A-F with data

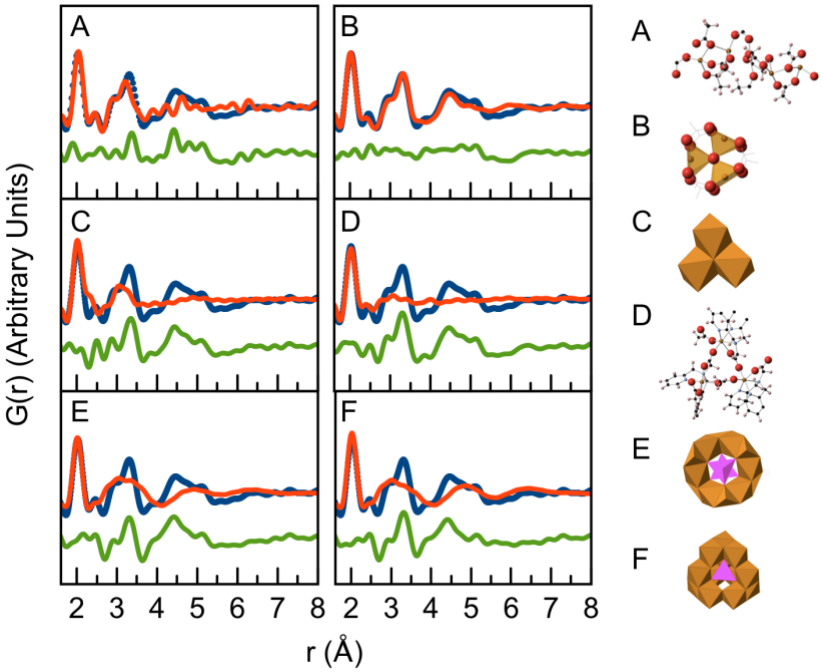

Figure C32. Shows fits of possible clusters A-F with Total X-ray Scattering data from a mixed valence oleate cluster that was synthesized using an established protocol.[11]

Ex Situ PDF Data from Continuous Growth Synthesis with Fe (II) Rich Oleate Precursor at 180°C

Samples removed from a continuous growth synthesis performed at 180°C with Fe (II) rich oleate precursor were analyzed by Total X-ray Scattering data. Generated PDFs are included in Figure C33-A from before during and after the 20 min annealing period of the synthesis where no excess precursor is added to the reaction flask. As can be seen there is no long-range structural order seen in PDFs until after the annealing has begun. This is in contrast to samples removed from a continuous growth synthesis made with Fe (II) rich oleate at 230°C where long range structural order is seen well before the annealing period (Figure C33-B).

The PDF of the sample taken during annealing (Figure C33-A) appears to have both Fe (II) oleate and some very small spinel species. In Figure C34, fits to the local-range order are fit to a mixed valence trimer structure (Figure C34-A) and fits from 7.2-20 Å fit well to a spinel structural model taking the space group *Fd-3m* (Figure C34-B). The PDF from 7.2-20 Å was fit with the spinel structural model using PDFGui.

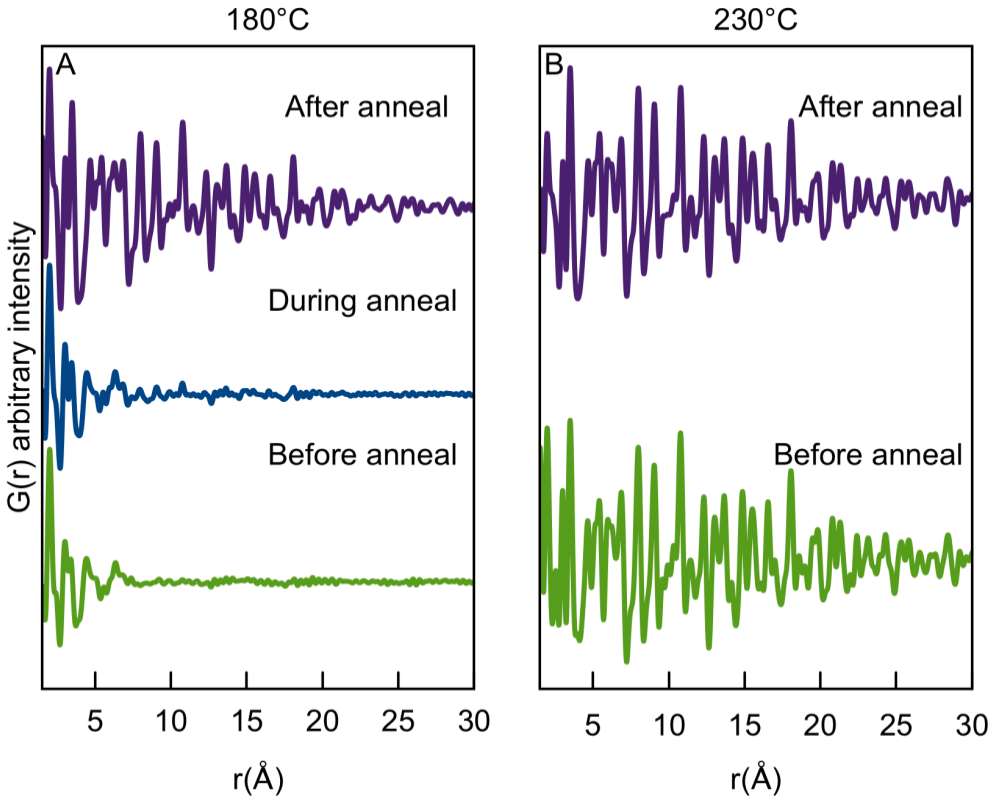

Figure C33. Shows PDFs from continuous growth using Fe (II) rich oleate precursor at A) 180°C before, during and after the annealing period and B) at 230°C before and after the annealing period.

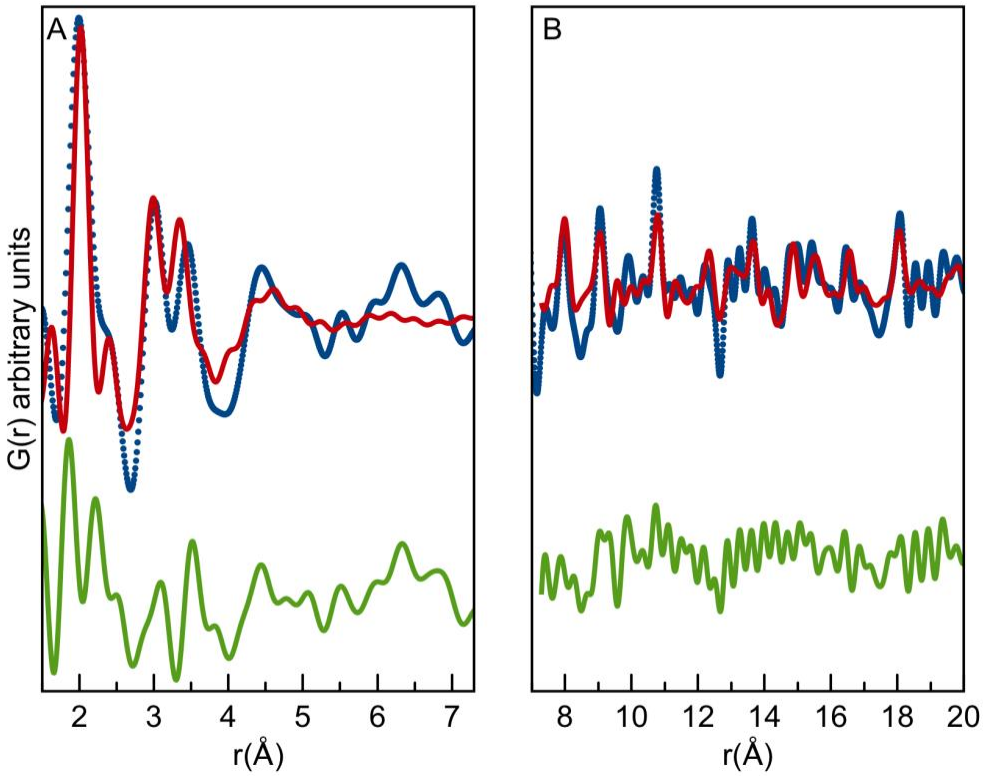

Figure C34. Fits of ex situ PDF samples taken during the annealing period of the continuous growth synthesis with Fe (II) oleate precursor at 180°C. Fits are of A) r-range from 1.5-7.2 Å and B) r-range 7.2-20 Å.

***In Situ* PDF Data from Continuous Growth Synthesis with Fe (II) Rich Oleate at 180°C**

Data fit the same way with the same fit parameters as Fe (II) oleate at 230°C Table S8 – Table S10. One difference in refinement of data collected at 180°C is that PDFs were refined from 4.2 Å instead of 2.7 Å to avoid precursor peaks in the PDF. Excess precursor was seen in the PDFs of 180°C data that increased the refined wüstite component of the fit but only described local r-range features in the PDF.

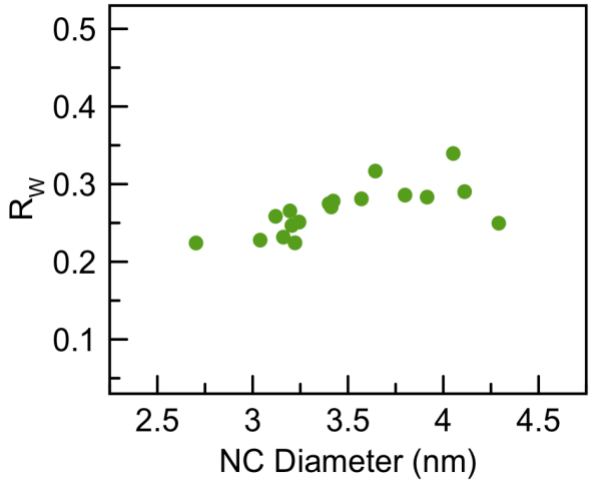

Figure C35. Rw refined for the Fe (II) oleate synthesis at 180°C using mixed phase fit using spinel model that takes the structural group *Fd-3m* and a wüstite model taking the space group *Fm-3m*.

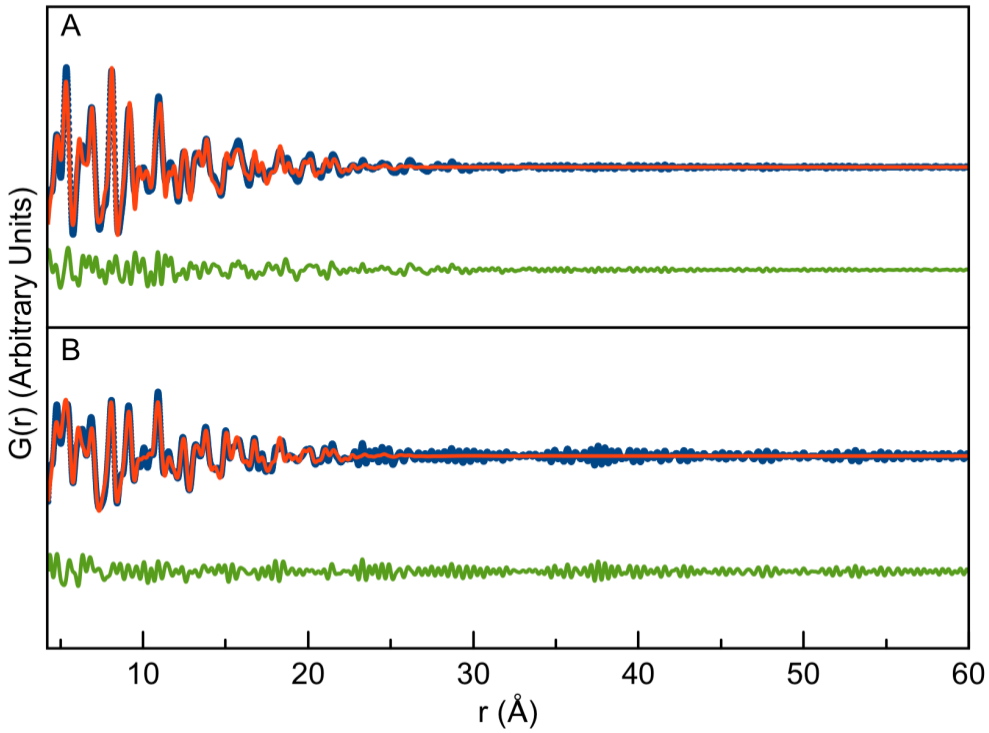

Figure C36. Fits of the samples at 175 min (top) and 70 min (bottom) into the *in situ* reaction using a mixed phase structural model with simple spinel and wüstite phases for a synthesis at 180°C using Fe (II) oleate precursor.

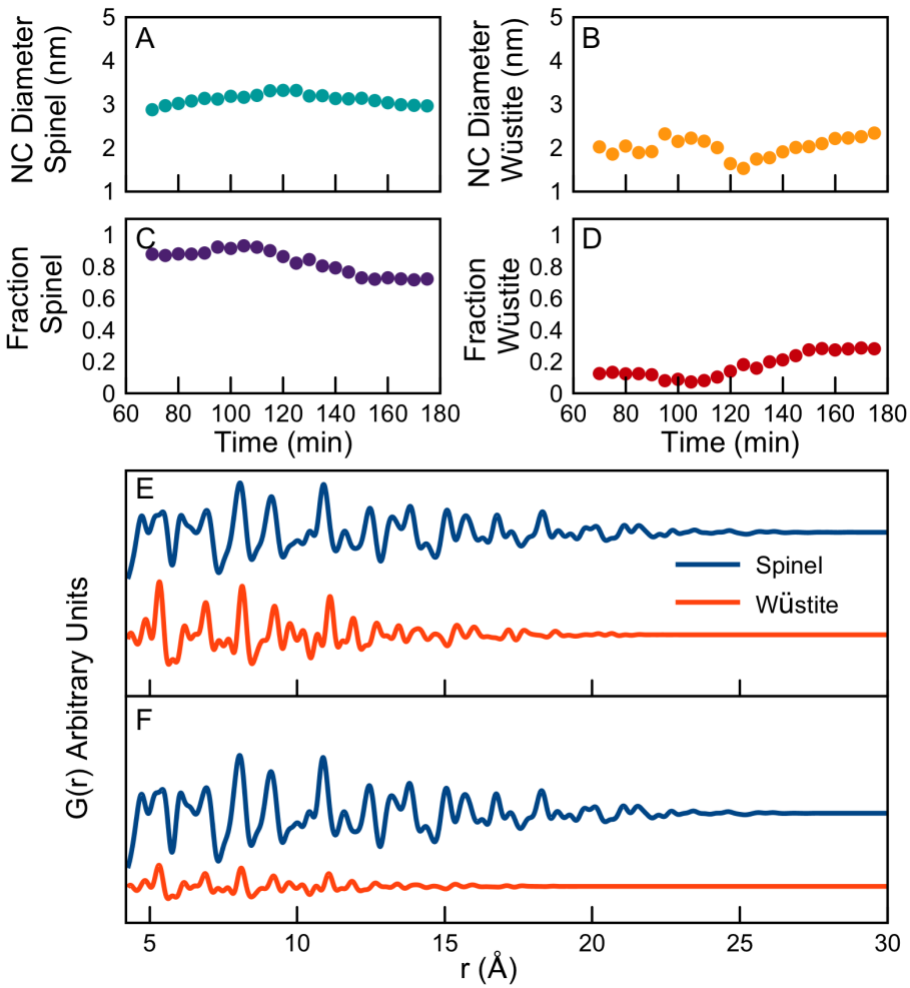

Figure C37. Refinement results for the amount of the two phases wüstite and spinel in particles over the course of the reaction at 180°C using Fe (II) oleate. Diameter refined for the A) spinel and B) wüstite portions of the NPs, the fraction of C) spinel and D) wüstite phases in the NPs and the fit contribution for the sample at E) 175 min and F) 70 min in the reaction.

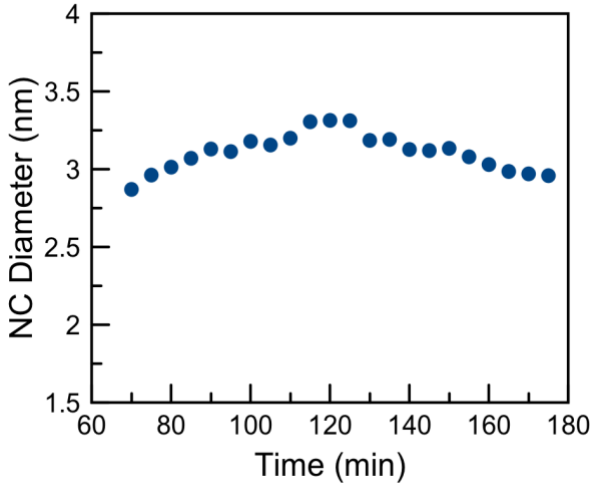

Figure C38. Diameter estimated from refined values of scale for both spinel and wüstite phases and the diameter refined for the wüstite core for the Fe (II) oleate synthesis at 180°C with a mixed phase fit using a spinel model that takes the structural group *Fd-3m* and a wüstite model taking the space group *Fm-3m*.

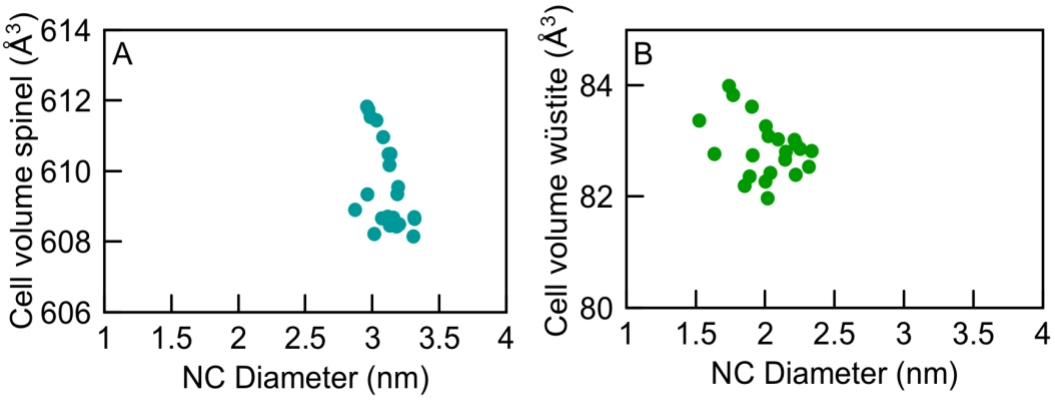

Figure C39. Cell volume of A) spinel and B) wüstite refined for the Fe (II) oleate synthesis at 180°C with a mixed phase fit using spinel model that takes the structural group *Fd-3m* and a wüstite model taking the space group *Fm-3m*.

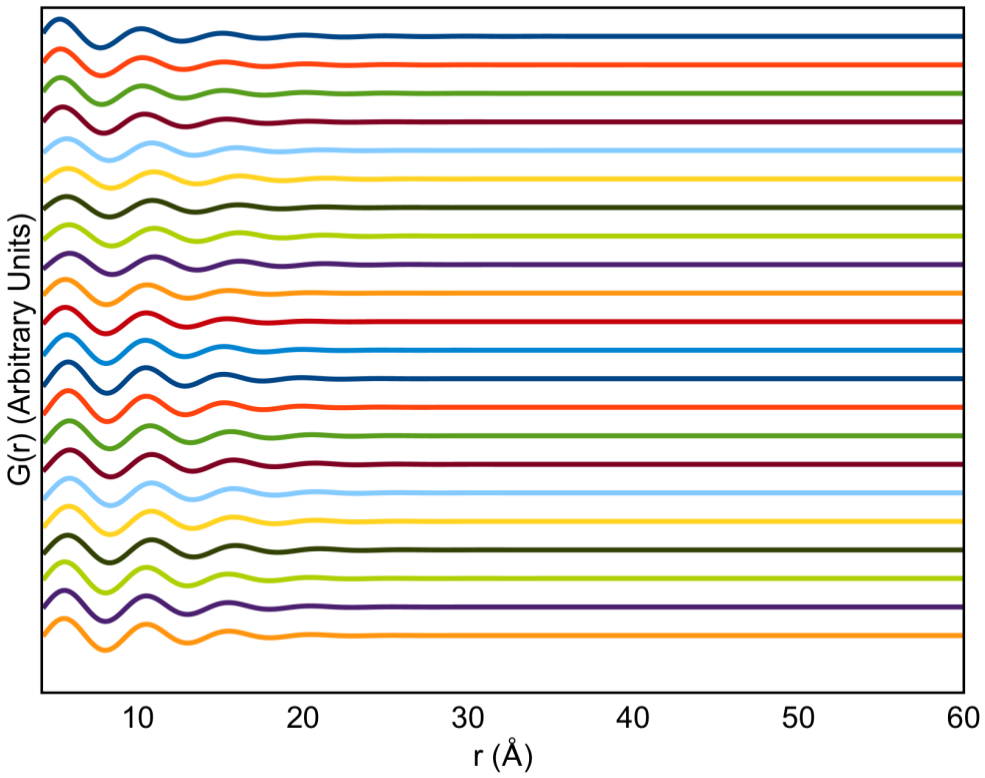

Figure C40. Shows the waves that describe the solvent in these dilutes samples that were refined for the Fe (II) oleate synthesis at 180°C using mixed phase fit using spinel model that takes the structural group *Fd-3m* and a wüstite model taking the space group *Fm-3m*. The order of the waves is from earliest time point to latest from top to bottom.

Analysis of *In Situ* PDF Products by Powder X-Ray Diffraction and PDF Made with Fe (II) Rich Oleate at 180°C

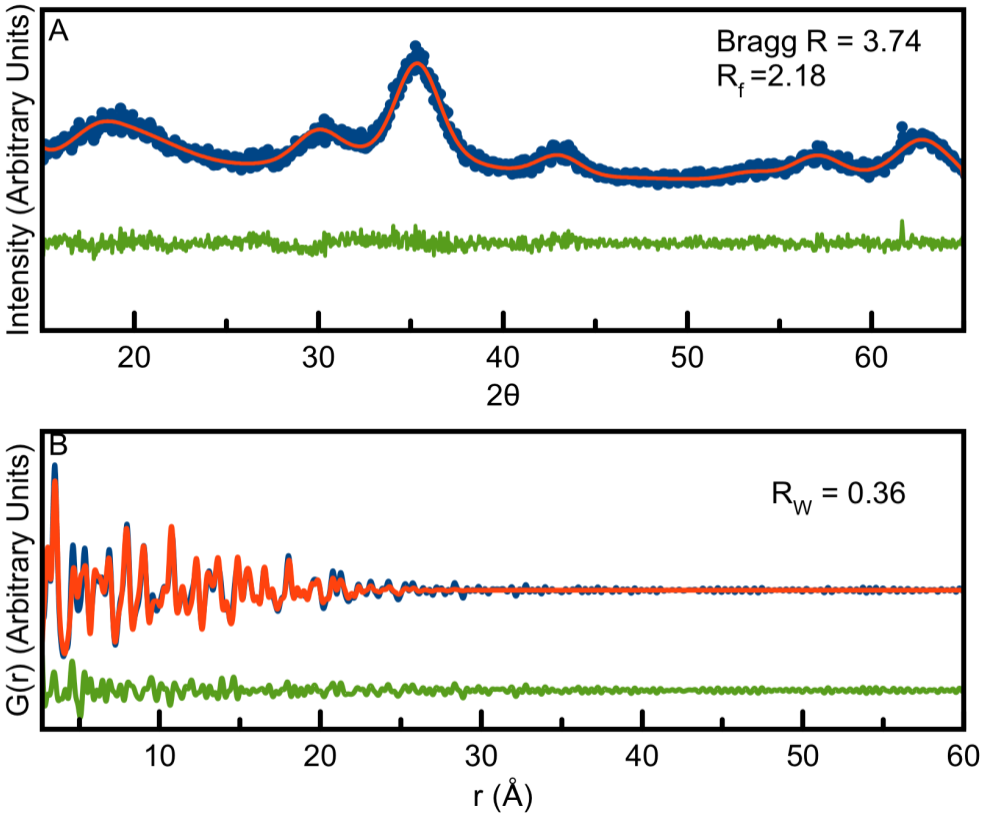

Figure C41. A) Fit of XRD pattern using the structural model of spinel iron oxide taking the space group *Fd-3m* and B) fit of PDF on samples using the structural model of spinel iron oxide taking the space group $P4_32_12$. obtained after an *in situ* beamline experiment that were made with Fe (III) rich oleate at 180ºC.

Analysis of *In Situ* PDF Data from Continuous Growth Synthesis Fe (II) Rich Oleate Precursor at 180°C with Pure Wüstite and Spinel Structural Models

Due to the small wüstite content in samples made by continuous growth with Fe (II) rich oleate at 180ºC, samples were also fit with pure phases of wüstite and spinel to verify that the mixed phase structural model was still appropriate at this lower temperature.

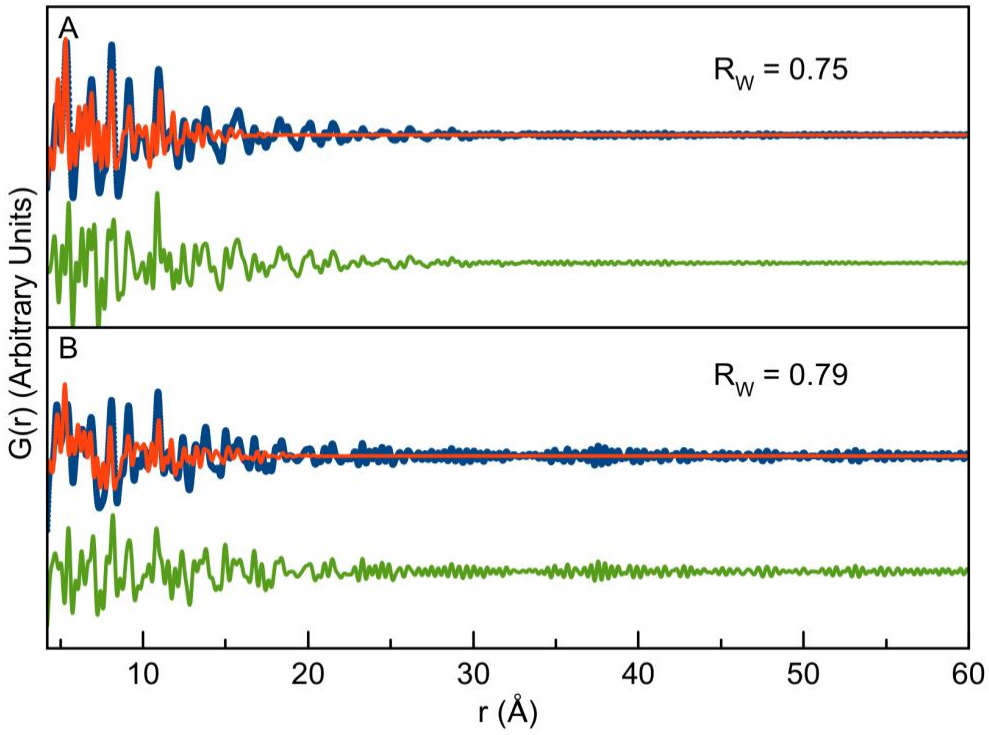

Figure C42. Fits of the samples at 175 min (top) and 70 min (bottom) into the *in situ* reaction using a structural model of wüstite taking the spacegroup *Fm-3m* for a synthesis at 180°C using Fe (II) oleate precursor.

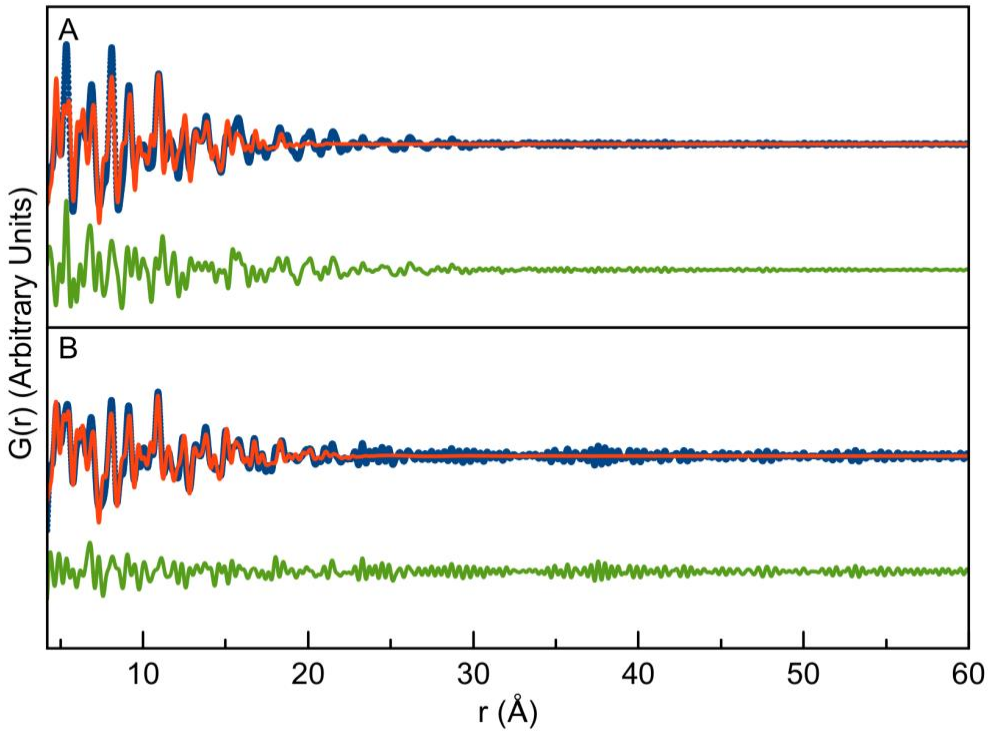

Figure C43. Fits of the samples at 175 min (top) and 70 min (bottom) into the *in situ* reaction using a structural model of spinel taking the spacegroup $P4_32_12$ for a synthesis at 180°C using Fe (II) oleate precursor.

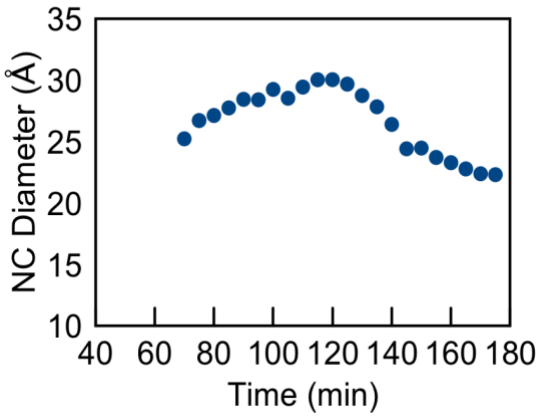

Figure C44. NC diameter from refinements of *in situ* PDF data made with Fe (II) oleate precursor at 180ºC through a continuous growth synthesis refined using the structural model for spinel iron oxide that takes the space group $P4_32_12$.

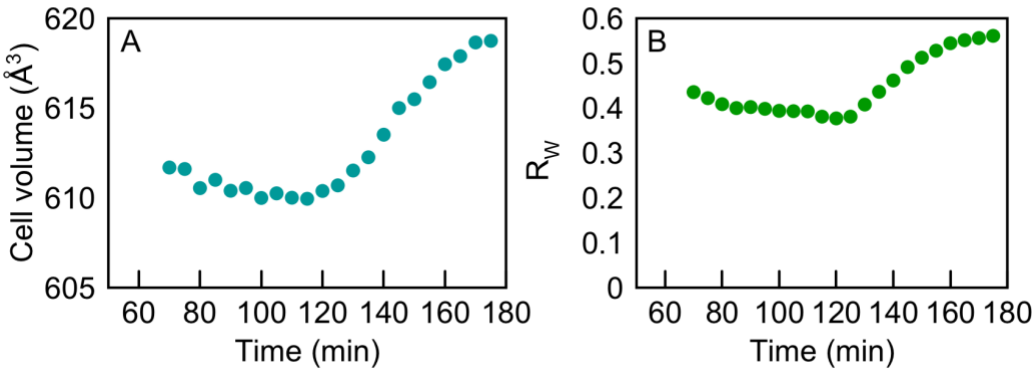

Figure C45. A) Cell volume and B) Rw from refinements of *in situ* PDF data made with Fe (II) oleate precursor at 180ºC through a continuous growth synthesis refined using the structural model for spinel iron oxide that takes the space group $P4_32_12$.

In Situ PDF Data from Continuous Growth Synthesis with Fe (II) Rich Oleate Precursor at 200°C

PDFs generated from Total X-ray Scattering Data was refined in the same way as PDFs generated from *in situ* data of Fe (II) oleate at 230ºC (Table C12 – Table C15). One particularly interesting feature is the refined parameters from data collected at 200°C with Fe (II) rich oleate precursor is the increase in diameter of NPs after addition of precursor to the reaction stops (Figure C48). The diameter for the NPs made at 200°C could increase either because of a second nucleation event or an increase in growth after injection of precursor stops. Samples analyzed at 180°C shows similar behavior of growth after addition of precursor ceases.

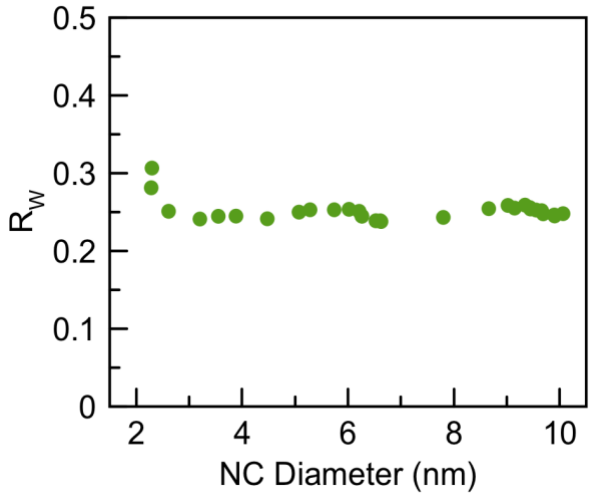

Figure C46. Rw refined for the *in situ* data collected during a continuous growth synthesis using Fe (II) rich oleate synthesis at 200ºC. Data was refined with a mixed phase fit using a spinel model that takes the spacegroup *Fd-3m* and a wüstite model taking the space group *Fm-3m*.

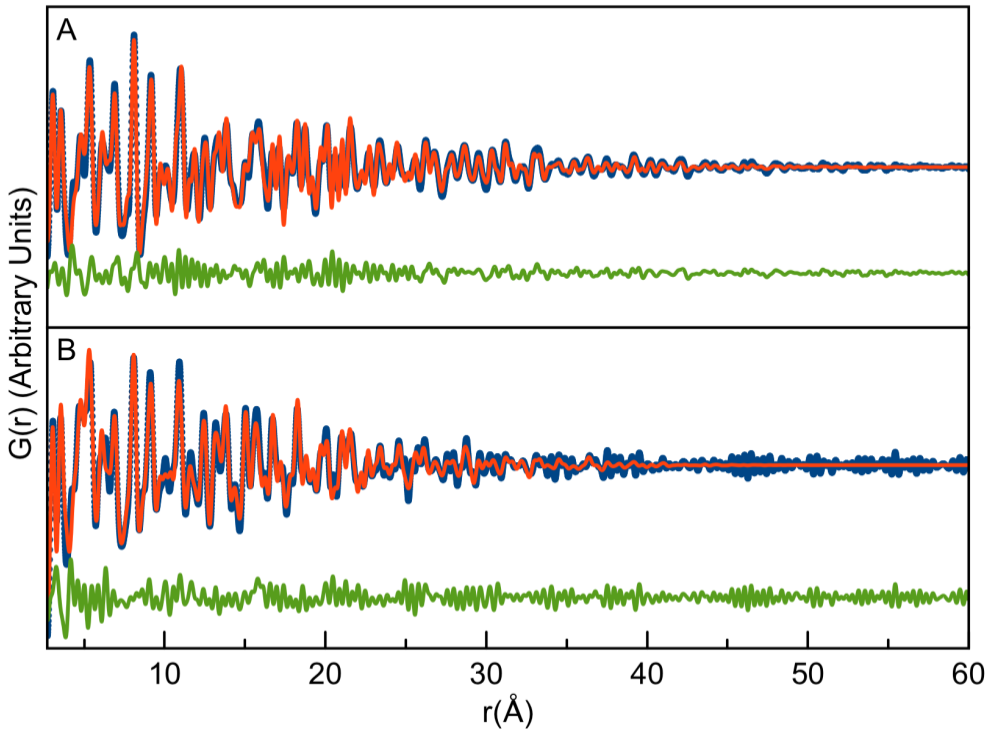

Figure C47. Fits of the sample acquired at 175 minutes (A) and at 30 min (B) samples using a mixed model with simple spinel and wüstite phases for a synthesis at 200°C using Fe (II) rich oleate precursor.

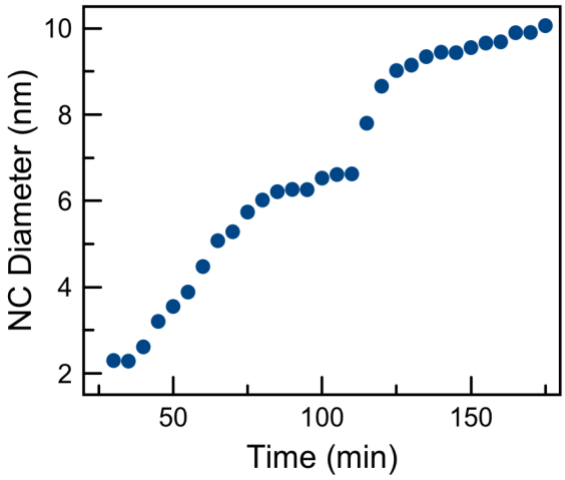

Figure C48. Diameter estimated from refined values of scale for both spinel and wüstite phases and the diameter refined for the wüstite core for the Fe (II) oleate synthesis at 200°C using mixed phase fit using spinel model that takes the structural group *Fd-3m* and a wüstite model taking the space group *Fm-3m*.

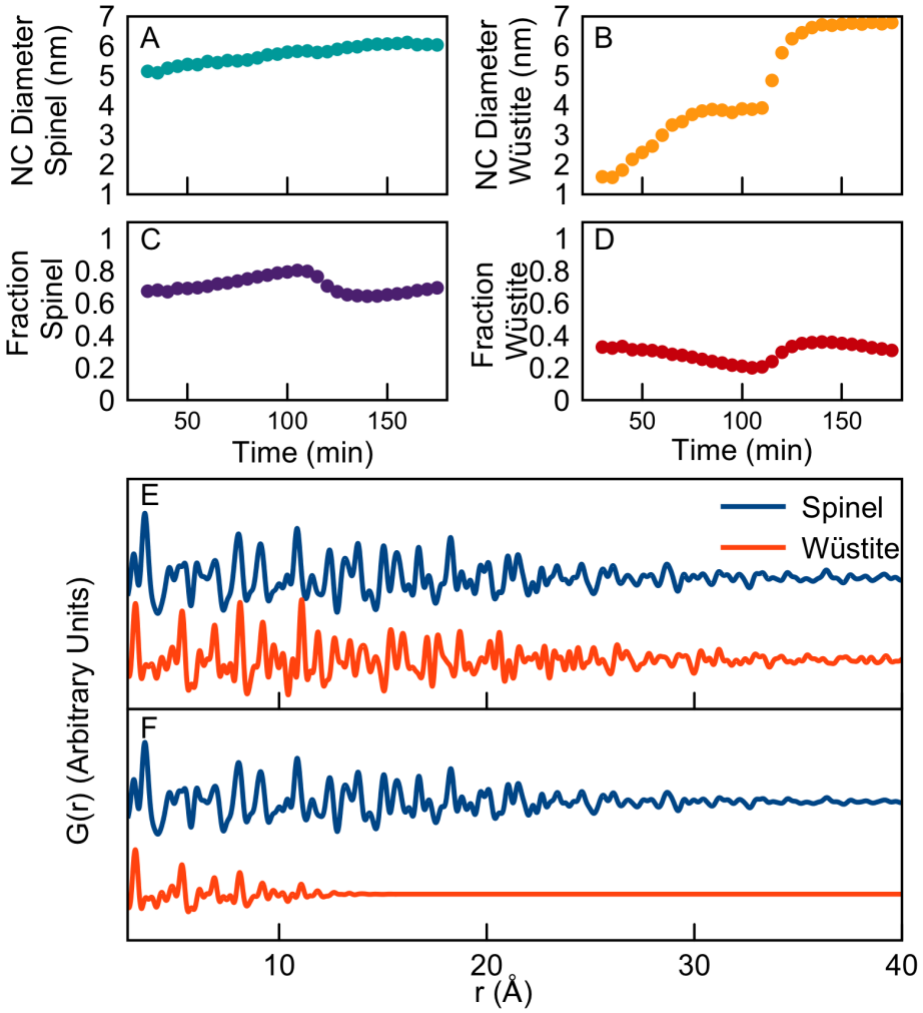

Figure C49. Refinement parameters for the amount of the two phases wüstite and spinel in NPs over the course of the reaction at 200°C using Fe (II) oleate. Diameter refined for A) spinel and B) wüstite, the fraction of each phase of C) spinel and D) wüstite and the fit contribution for the sample at E) 175 min and F) 30 min in the reaction.

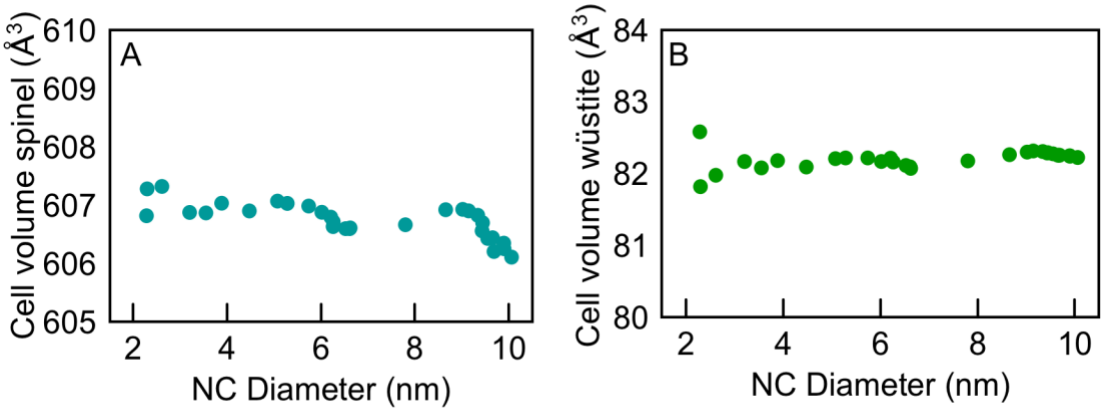

Figure C50. Cell volume wüstite and spinel refined for the Fe (II) oleate synthesis at 200°C using mixed phase fit using spinel model that takes the structural group *Fd-3m* and a wüstite model taking the space group *Fm-3m*.

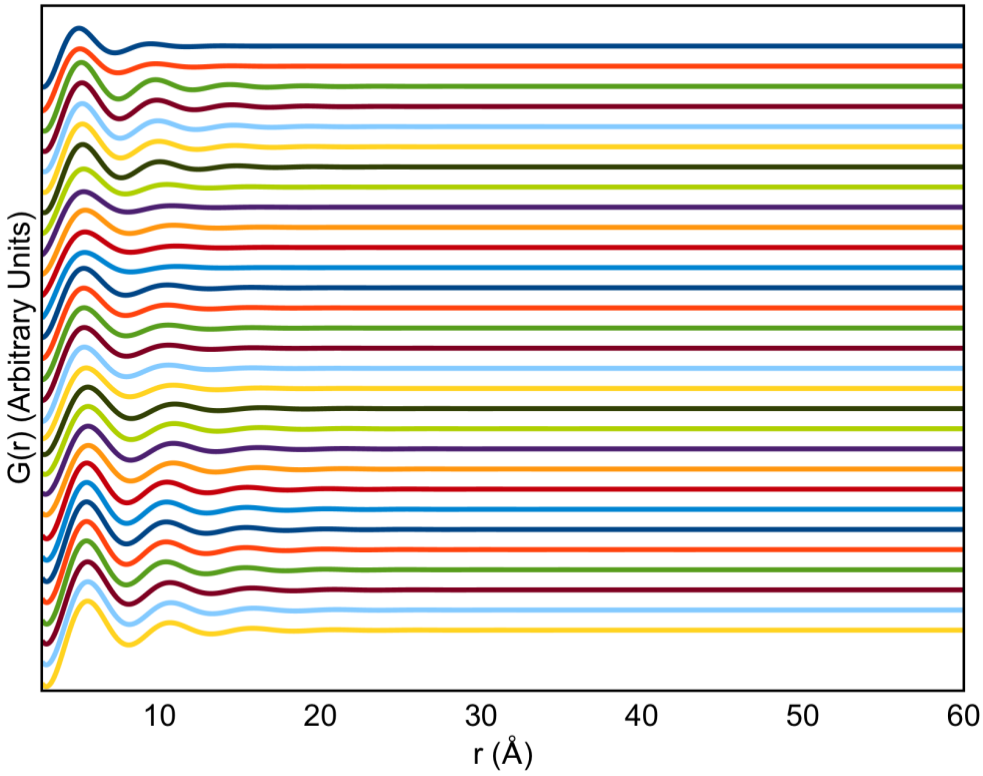

Figure C51. Shows the waves that describe the solvent in these dilutes samples that were refined for the Fe (II) oleate synthesis at 200°C using mixed phase fit using spinel model that takes the structural group *Fd-3m* and a wüstite model taking the space group *Fm-3m*.

Analysis of *In Situ* PDF Products by Powder X-Ray Diffraction and PDF Made with Fe (II) Rich Oleate at 200°C

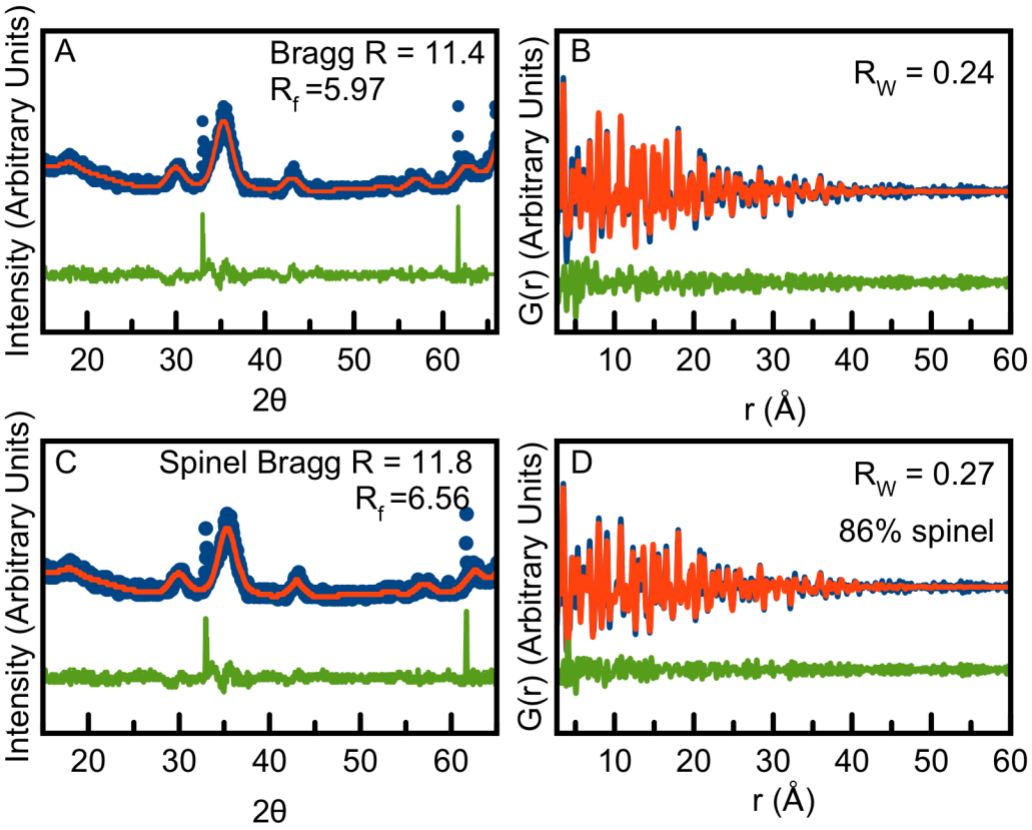

Figure C52. Products from an *in situ* beamline experiment that were made with Fe (II) rich oleate at 200ºC, analyzed by both XRD and PDF, weeks after synthesis. Data was refined, and fits are included above. A) Fit of XRD pattern with spinel iron oxide taking the spacegroup *Fd-3m* and B) fit of PDF with spinel iron oxide taking the spacegroup $P4_32_12$, C) fit of XRD pattern with spinel iron oxide taking the spacegroup *Fd-3m* and wüstite taking the space group *Fm-3m and D)* fit of PDF with spinel iron oxide taking the spacegroup *Fd-3m* and wüstite taking the space group *Fm-3m*.

In Situ PDF Data from Capillary Heat-Up Synthesis with Fe (II) Rich Oleate Precursor at 200°C

In situ Total X-ray Scattering data was also collected using a capillary heat-up synthesis at 200°C. We collected heat-up synthesis data in a capillary as well because of the complexity of the *in situ* setup used for acquiring Total X-ray Scattering data for the continuous growth method. Iron (II) rich oleate was used in the heat-up synthesis, however, the precursor turned from brown to red, indicating oxidation, upon mixing with oleyl alcohol at room temperature. Because of this color change we believe that the precursor was not Fe (II) rich oleate, which is why these particles grew as spinel.

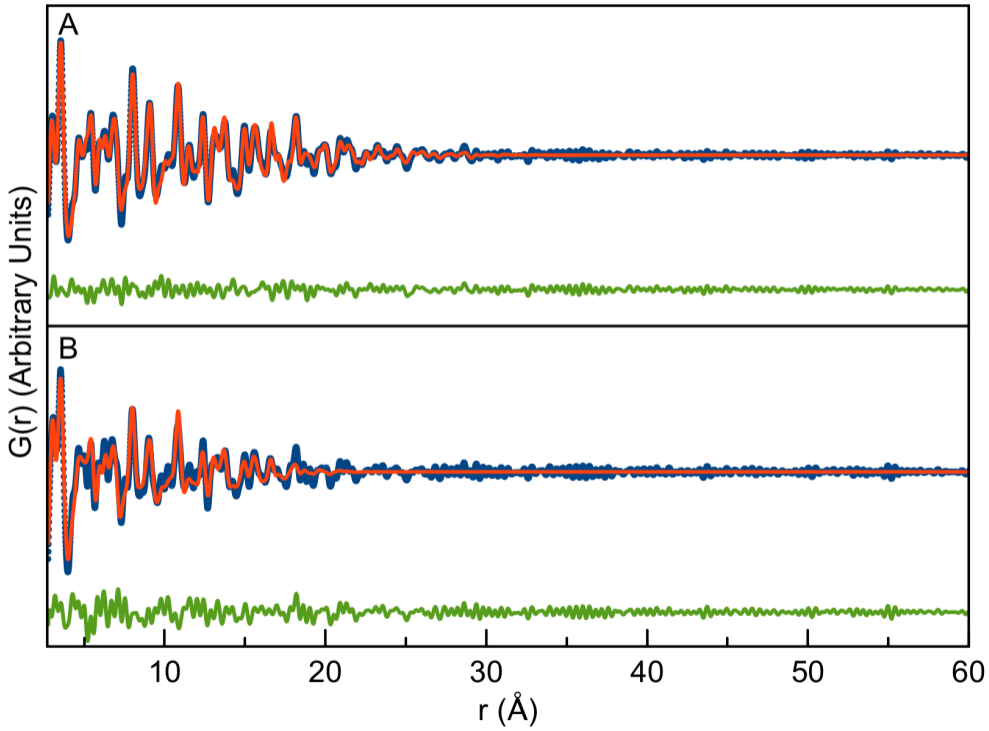

Figure C53. Fits of the samples at 114 min (top) and 40 min (bottom) into the *in situ* capillary heat-up reaction using a structural model of spinel taking the spacegroup $P4_32_12$. Synthesis was performed at 200°C using Fe (II) rich oleate precursor and oleyl alcohol by heating up a cap.

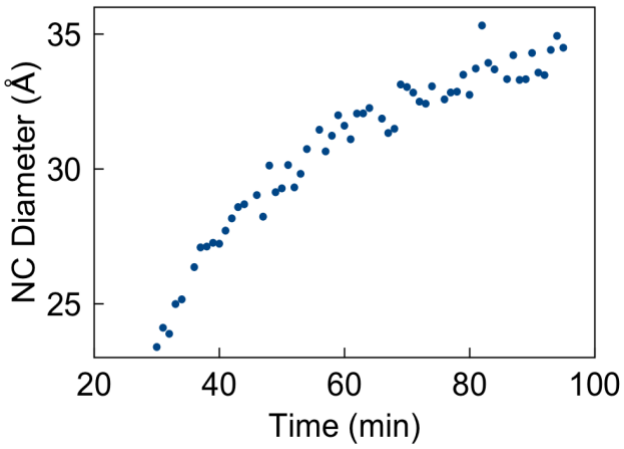

Figure C54. NC diameter from refinements of *in situ* PDF data made with Fe (II) oleate precursor at 200ºC through a capillary heat-up synthesis refined using the structural model for spinel iron oxide that takes the space group $P4_32_12$.

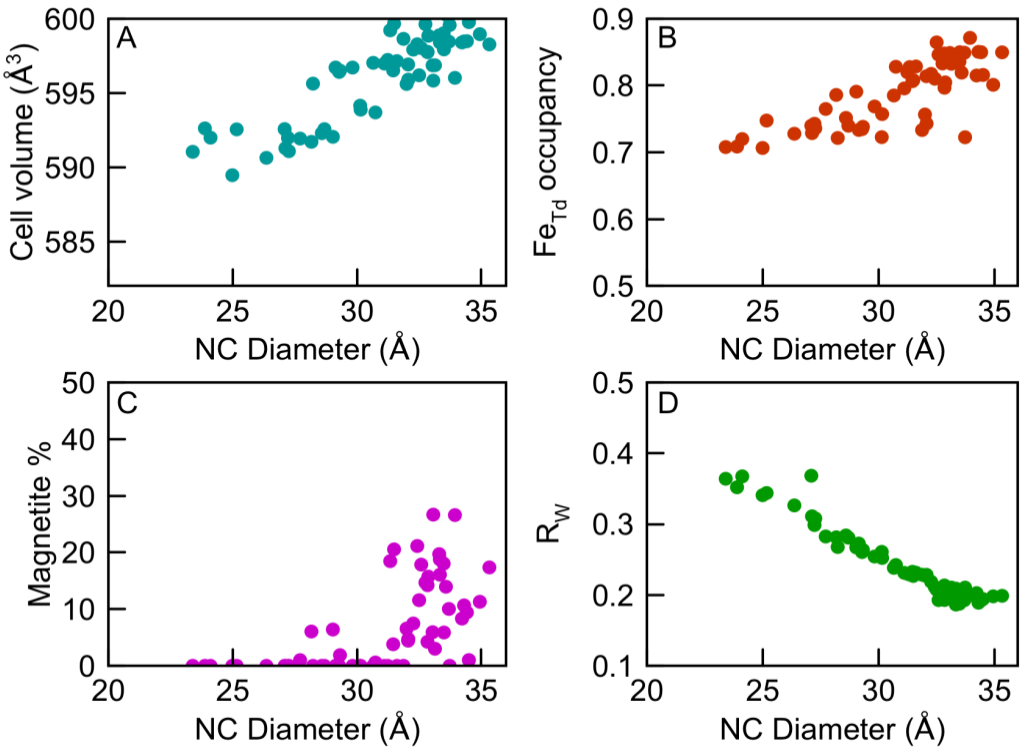

Figure C55. A) Cell volume, B) tetrahedrally coordinated cation occupancy, C) percent magnetite and D) the Rw are all plotted by time from refinements of *in situ* PDF data made with Fe (II) oleate precursor at 200ºC through a capillary heat-up synthesis refined using the structural model for spinel iron oxide that takes the space group $P4_32_12$.

REFERENCES SITED

Chapter 1

(1) Grassian, V. H. When Size Really Matters: Size-Dependent Properties and Surface Chemistry of Metal and Metal Oxide Nanoparticles in Gas and Liquid Phase Environments. *J. Phys. Chem. C* **2008**, *112*, 18303–18313.

(2) Auffan, M.; Rose, J. J.; Bottero, J. Y.; Lowry, G. V.; Jolivet, J. P.; Wiesner, M. R. Towards a Definition of Inorganic Nanoparticles from an Environmental, Health and Safety Perspective. *Nat. Nanotechnol.* **2009**, *4*, 634–641.

(3) Roduner, E. Size Matters : Why Nanomaterials Are Different. *Chem. Soc. Rev.* **2006**, *35*, 583–592.

(4) Kovalenko, M. V; Manna, L.; Cabot, A.; Hens, Z.; Talapin, D. V; Kagan, C. R.; Klimov, V. I.; Rogach, A. L.; Reiss, P.; Milliron, D. J.; *et al.* Prospects of Nanoscience with Nanocrystals. *ACS Nano* **2015**, *9*, 1012–1057.

(5) Auffan, M.; Rose, J.; Proux, O.; Borschneck, D.; Masion, A.; Chaurand, P.; Hazemann, J.-L.; Chaneac, C.; Jolivet, J.-P.; Wiesner, M. R.; *et al.* Enhanced Adsorption of Arsenic onto Maghemites Nanoparticles : As(III) as a Probe of the Surface Structure and Heterogeneity. *Langmuir* **2008**, *24*, 3215–3222.

(6) Kumar, M.; Dubey, A.; Adhikari, N.; Venkatesan, S.; Qiao, Q. Strategic Review of Secondary Phases, Defects and Defect-Complexes in Kesterite CZTS-Se Solar Cells. *Energy Environ. Sci.* **2015**, *8*, 3134–3159.

(7) Cooper, S. R.; Plummer, L. K.; Cosby, A. G.; Lenox, P.; Jander, A.; Dhagat, P.; Hutchison, J. E. Insights into the Magnetic Properties of Sub-10 Nm Iron Oxide Nanocrystals through the Use of a Continuous Growth Synthesis. *Chem. Mater.* **2018**, *30*, 6053–6062.

(8) Unni, M.; Uhl, A. M.; Savliwala, S.; Savitzky, B. H.; Dhavalikar, R.; Garraud, N.; Arnold, D. P.; Kourkoutis, L. F.; Andrew, J. S.; Rinaldi, C. Thermal Decomposition Synthesis of Iron Oxide Nanoparticles with Diminished Magnetic Dead Layer by Controlled Addition of Oxygen. *ACS Nano* **2017**, *11*, 2284–2303.

(9) Gilbert, B.; Huang, F.; Zhang, H.; Waychunas, G. A.; Banfield, J. F. Nanoparticles: Strained and Stiff. *Science* **2004**, *305*, 651–654.

(10) Frison, R.; Cernuto, G.; Cervellino, A.; Zaharko, O.; Colonna, G. M.; Guagliardi, A.; Masciocchi, N. Magnetite − Maghemite Nanoparticles in the 5 − 15 Nm Range : Correlating the Core − Shell Composition and the Surface Structure to the Magnetic Properties . A Total Scattering Study. *Chem. Mater.* **2013**, *25*, 4820–4827.

(11) Coughlan, C.; Ibáñez, M.; Dobrozhan, O.; Singh, A.; Cabot, A.; Ryan, K. M. Compound Copper Chalcogenide Nanocrystals. *Chem. Rev.* **2017**, *117*, 5865–6109.

(12) Gilbert, B.; Huang, F.; Lin, Z.; Goodell, C.; Zhang, H.; Banfield, J. F. Surface Chemistry Controls Crystallinity of ZnS Nanoparticles. *Nano Lett.* **2006**, *6*, 605–610.

(13) Kolhatkar, A. G.; Jamison, A. C.; Litvinov, D.; Willson, R. C.; Lee, T. R. Tuning the Magnetic Properties of Nanoparticles. *Int. J. Mol. Sci.* **2013**, *14*, 15977–16009.

(14) Lim, E.-K.; Kim, T.; Paik, S.; Haam, S.; Huh, Y.-M.; Lee, K. Nanomaterials for Theranostics: Recent Advances and Future Challenges. *Chem. Rev.* **2015**, *115*, 327–394.

(15) Ling, D.; Lee, N.; Hyeon, T. Chemical Synthesis and Assembly of Uniformly Sized Iron Oxide Nanoparticles for Medical Applications. *Acc. Chem. Res.* **2015**, *48*, 1276–1285.

(16) Lee, N.; Yoo, D.; Ling, D.; Cho, M. H.; Hyeon, T.; Cheon, J. Iron Oxide Based Nanoparticles for Multimodal Imaging and Magnetoresponsive Therapy. *Chem. Rev.* **2015**, *115*, 10637–10689.

(17) Wallace, S. K.; Mitzi, D. B.; Walsh, A. The Steady Rise of Kesterite Solar Cells. *ACS Energy Lett.* **2017**, *2*, 776–779.

(18) Chen, X.; Li, C.; Gratzel, M.; Kostecki, R.; Mao, S. S. Nanomaterials for Renewable Energy Production and Storage. *Chem. Soc. Rev.* **2012**, *41*, 7909–7937.

(19) Shannon, M. A; Bohn, P. W.; Elimelech, M.; Georgiadis, J. G.; Mariñas, B. J.; Mayes, A. M. Science and Technology for Water Purification in the Coming Decades. *Nature* **2008**, *452*, 301–310.

(20) Hua, M.; Zhang, S.; Pan, B.; Zhang, W.; Lv, L.; Zhang, Q. Heavy Metal Removal from Water/Wastewater by Nanosized Metal Oxides: A Review. *J. Hazard. Mater.* **2012**, *211–212*, 317–331.

(21) Khare, A.; Wills, A. W.; Ammerman, L. M.; Norris, D. J.; Aydil, E. S. Size Control and Quantum Confinement in Cu_2ZnSnS_4 Nanocrystals. *Chem. Commun.* **2011**, *47*, 11721.

(22) Gao, M.-R.; Xu, Y.-F.; Jiang, J.; Yu, S.-H. Nanostructured Metal Chalcogenides: Synthesis, Modification, and Applications in Energy Conversion and Storage Devices. *Chem. Soc. Rev.* **2013**, *42*, 2986-3017.

(23) Zhou, H.; Hsu, W. C.; Duan, H. S.; Bob, B.; Yang, W.; Song, T. Bin; Hsu, C. J.; Yang, Y. CZTS Nanocrystals: A Promising Approach for next Generation Thin Film Photovoltaics. *Energy Environ. Sci.* **2013**, *6*, 2822–2838.

(24) Batzill, M.; Diebold, U. The Surface and Materials Science of Tin Oxide. *Prog. Surf. Sci.* **2005**, *79*, 47–154.

(25) Yavuz, C. T.; Mayo, J. T.; Yu, W. W.; Prakash, A.; Falkner, J. C.; Yean, S.; Cong, L.; Shipley, H. J.; Kan, A.; Tomson, M.; *et al.* Low-Field Magnetic Separation of Monodisperse Fe_3O_4 Nanocrystals. *Science* **2006**, *314*, 964–967.

(26) Park, J.; An, K.; Hwang, Y.; Park, J.-G.; Noh, H.-J.; Kim, J.-Y.; Park, J.-H.; Hwang, N.-M.; Hyeon, T. Ultra-Large-Scale Syntheses of Monodisperse Nanocrystals. *Nat. Mater.* **2004**, *3*, 891–895.

(27) Roca, A. G.; Niznansky, D.; Poltierova-Vejpravova, J.; Bittova, B.; González-Fernández, M. A.; Serna, C. J.; Morales, M. P. Magnetite Nanoparticles with No Surface Spin Canting. *J. Appl. Phys.* **2009**, *105*, 114309.

(28) Mitra, A.; Mohapatra, J.; Meena, S. S.; Tomy, C. V.; Aslam, M. Verwey Transition in Ultrasmall-Sized Octahedral Fe_3O_4 Nanoparticles. *J. Phys. Chem. C* **2014**, *118*, 19356–19362.

(29) Nguyen, T.-D. From Formation Mechanisms to Synthetic Methods toward Shape-Controlled Oxide Nanoparticles. *Nanoscale* **2013**, *5*, 9455–9482.

(30) Qiao, L.; Fu, Z.; Li, J.; Ghosen, J.; Zeng, M.; Stebbins, J.; Prasad, P. N.; Swihart, M. T. Standardizing Size- and Shape-Controlled Synthesis of Monodisperse Magnetite (Fe_3O_4) Nanocrystals by Identifying and Exploiting Effects of Organic Impurities. *ACS Nano* **2017**, *11*, 6370–6381.

(31) Zhou, Z.; Zhu, X.; Wu, D.; Chen, Q.; Huang, D.; Sun, C.; Xin, J.; Ni, K.; Gao, J. Anisotropic Shaped Iron Oxide Nanostructures: Controlled Synthesis and Proton Relaxation Shortening Effects. *Chem. Mater.* **2015**, *27*, 3505–3515.

(32) Demortière, A.; Panissod, P.; Pichon, B. P.; Pourroy, G.; Guillon, D.; Donnio, B.; Bégin-Colin, S. Size-Dependent Properties of Magnetic Iron Oxide Nanocrystals. *Nanoscale* **2011**, *3*, 225–232.

(33) Kim, B. H.; Lee, N.; Kim, H.; An, K.; Park, Y. I.; Choi, Y.; Shin, K.; Lee, Y.; Kwon, S. G.; Na, H. B.; *et al.* Large-Scale Synthesis of Uniform and Extremely Small-Sized Iron Oxide Nanoparticles for High-Resolution T1 Magnetic Resonance Imaging Contrast Agents. *J. Am. Chem. Soc.* **2011**, *133*, 12624–12631.

(34) Choi, B. S.; An, K.; Kim, E.; Yu, J. H.; Kim, H.; Hyeon, T. Simple and Generalized Synthesis of Semiconducting Metal Sulfide Nanocrystals. *Adv. Funct. Mater.* **2009**, *19*, 1645–1649.

(35) Liu, L.; Zhong, H.; Bai, Z.; Zhang, T.; Fu, W.; Shi, L.; Xie, H.; Deng, L.; Zou, B. Controllable Transformation from Rhombohedral $Cu_{1.8}S$ Nanocrystals to Hexagonal CuS Clusters: Phase- and Composition- Dependent Plasmonic Properties. *Chem. Mater.* **2013**, *25*, 6–12.

(36) Liu, X.; Wang, X.; Zhou, B.; Law, W.; Cartwright, A. N.; Swihart, M. T. Size-Controlled Synthesis of $Cu_{2-x}E$ (E = S , Se) Nanocrystals with Strong Tunable Near-Infrared Localized Surface Plasmon Resonance and High Conductivity in Thin Films. *Adv. Funct. Mater.* **2013**, *23*, 1256–1264.

(37) Caruntu, D.; Caruntu, G.; O'Connor, C. J. Magnetic Properties of Variable-Sized Fe_3O_4 Nanoparticles Synthesized from Non-Aqueous Homogeneous Solutions of Polyols. *J. Phys. D. Appl. Phys.* **2007**, *40*, 5801–5809.

(38) Yun, H.; Liu, X.; Paik, T.; Palanisamy, D.; Kim, J.; Vogel, W. D.; Viescas, A. J.; Chen, J.; Papaefthymiou, G. C.; Kikkawa, J. M.; *et al.* Size- and Composition-Dependent Radio Frequency Magnetic Permeability of Iron Oxide Nanocrystals. *ACS Nano* **2014**, *8*, 12323–12337.

(39) Taniguchi, T.; Nakagawa, K.; Watanabe, T.; Matsushita, N.; Yoshimura, M. Hydrothermal Growth of Fatty Acid Stabilized Iron Oxide Nanocrystals. *J. Phys. Chem. C* **2009**, *113*, 839–843.

(40) Baaziz, W.; Pichon, B. P.; Fleutot, S.; Liu, Y.; Lefevre, C.; Greneche, J.-M. M.; Toumi, M.; Mhiri, T.; Bégin-Colin, S. Magnetic Iron Oxide Nanoparticles: Reproducible Tuning of the Size and Nanosized-Dependent Composition, Defects, and Spin Canting. *J. Phys. Chem. C* **2014**, *118*, 3795–3810.

(41) Mohapatra, J.; Mitra, A.; Bahadur, D.; Aslam, M. Surface Controlled Synthesis of MFe_2O_4 (M = Mn, Fe, Co, Ni and Zn) Nanoparticles and Their Magnetic Characteristics. *CrystEngComm* **2013**, *15*, 524–532.

(42) Park, B.; Kim, B. H.; Yu, T. Synthesis of Spherical and Cubic Magnetic Iron Oxide Nanocrystals at Low Temperature in Air. *J. Colloid Interface Sci.* **2018**, *518*, 27–33.

(43) Yu, W. W.; Falkner, J. C.; Yavuz, C. T.; Colvin, V. L. Synthesis of Monodisperse Iron Oxide Nanocrystals by Thermal Decomposition of Iron Carboxylate Salts. *Chem. Commun.* **2004**, 2306–2307.

(44) Santoyo Salazar, J.; Perez, L.; De Abril, O.; Truong Phuoc, L.; Ihiawakrim, D.; Vazquez, M.; Greneche, J. M.; Begin-Colin, S.; Pourroy, G. Magnetic Iron Oxide Nanoparticles in 10-40 Nm Range: Composition in Terms of Magnetite/Maghemite Ratio and Effect on the Magnetic Properties. *Chem. Mater.* **2011**, *23*, 1379–1386.

(45) Sharifi Dehsari, H.; Heidari, M.; Halda Ribeiro, A.; Tremel, W.; Jakob, G.; Donadio, D.; Potestio, R.; Asadi, K. Combined Experimental and Theoretical Investigation of Heating Rate on Growth of Iron Oxide Nanoparticles. *Chem. Mater.* **2017**, *29*, 9648–9656.

(46) Vreeland, E. C.; Watt, J.; Schober, G. B.; Hance, B. G.; Austin, M. J.; Price, A. D.; Fellows, B. D.; Monson, T. C.; Hudak, N. S.; Maldonado-Camargo, L.; *et al.* Enhanced Nanoparticle Size Control by Extending LaMer's Mechanism. *Chem. Mater.* **2015**, *27*, 6059–6066.

(47) Jansons, A. W.; Hutchison, J. E. Continuous Growth of Metal Oxide Nanocrystals: Enhanced Control of Nanocrystal Size and Radial Dopant Distribution. *ACS Nano* **2016**, *10*, 6942–6951.

(48) Han, W.; Yi, L.; Zhao, N.; Tang, A.; Gao, M.; Tang, Z. Synthesis and Shape-Tailoring of Copper Sulfide/Indium Sulfide-Based Nanocrystals. *J. Am. Chem. Soc.* **2008**, *130*, 13152–13161.

(49) Luther, J. M.; Jain, P. K.; Ewers, T.; Alivisatos, A. P. Localized Surface Plasmon Resonances Arising from Free Carriers in Doped Quantum Dots. *Nat. Mater.* **2011**, *10*, 361–366.

(50) Ho, C.; Tsai, C.; Chung, C.; Tsai, C.; Chen, F.; Lin, H.; Lai, C. Shape-Controlled Growth and Shape-Dependent Cation Site Occupancy of Monodisperse Fe_3O_4 Nanoparticles. *Chem. Mater.* **2011**, *23*, 1753–1760.

(51) Li, S.; Wang, H.; Xu, W.; Si, H.; Tao, X.; Lou, S.; Du, Z.; Li, L. S. Synthesis and Assembly of Monodisperse Spherical Cu_2S Nanocrystals. *J. Colloid Interface Sci.* **2009**, *330*, 483–487.

(52) Pacakova, B.; Kubickova, S.; Salas, G.; Mantlikova, A. R.; Marciello, M.; Morales, M. P.; Niznansky, D.; Vejpravova, J. The Internal Structure of Magnetic Nanoparticles Determines the Magnetic Response. *Nanoscale* **2017**, *9*, 5129–5140.

(53) Wetterskog, E.; Tai, C.-W.; Grins, J.; Bergstrom, L.; Salazar-Alvarez, G. Anomalous Magnetic Properties of Nanoparticles Arising from Defect Structures : Topotaxial Oxidation of FeO|Fe_3O_4 Core|Shell. *ACS Nano* **2013**, *7*, 7132–7144.

(54) Levy, M.; Quarta, A.; Espinosa, A.; Figuerola, A.; Wilhelm, C.; García-hern, M.; Genovese, A.; Falqui, A.; Alloyeau, D.; Cozzoli, P. D.; *et al.* Correlating Magneto-Structural Properties to Hyperthermia Performance of Highly Monodisperse Iron Oxide Nanoparticles Prepared by a Seeded-Growth Route. *Chem. Mater.* **2011**, *23*, 4170–4180.

(55) Chen, R.; Christiansen, M. G.; Sourakov, A.; Mohr, A.; Matsumoto, Y.; Okada, S.; Jasanoff, A.; Anikeeva, P. High-Performance Ferrite Nanoparticles through Nonaqueous Redox Phase Tuning. *Nano Lett.* **2016**, *16*, 1345–1351.

(56) Polman, A.; Knight, M.; Garnett, E. C.; Ehrler, B.; Sinke, W. C. Photovoltaic Materials: Present Efficiencies and Future Challenges. *Science* **2016**, *352*, aad4424.

(57) Wang, F.; Richards, V. N.; Shields, S. P.; Buhro, W. E. Kinetics and Mechanisms of Aggregative Nanocrystal Growth. *Chem. Mater.* **2014**, *26*, 5–21.

(58) Thanh, N. T. K.; Maclean, N.; Mahiddine, S. Mechanisms of Nucleation and Growth of Nanoparticles in Solution. *Chem. Rev.* **2014**, *114*, 7610–7630.

(59) Kwon, S. G.; Hyeon, T. Formation Mechanisms of Uniform Nanocrystals via Hot-Injection and Heat-Up Methods. *Small* **2011**, *19*, 2685–2702.

(60) Zhou, X.; Xu, W.; Liu, G.; Panda, D.; Chen, P. Size Dependent Catalytic Activity and Dynamics of Gold Nanoparticles at the Single-Molecule Level. *J. Am. Chem. Soc.* **2010**, *132*, 138–146.

(61) Watzky, M. A.; Finke, R. G. Nanocluster Size-Control and " Magic Number " Investigations . Experimental Tests of the " Living-Metal Polymer " Concept and of Mechanism-Based Size-Control Predictions Leading to the Syntheses of Iridium (0) Nanoclusters Centering about Four Sequentia. *Chem. Mater.* **1997**, *9*, 3083–3095.

(62) Lee, J.; Yang, J.; Kwon, S. G.; Hyeon, T. Nonclassical Nucleation and Growth of Inorganic Nanoparticles. *Nat. Rev. Mater.* **2016**, *1*, 1–18.

(63) Harrell, S. M.; Mcbride, J. R.; Rosenthal, S. J. Synthesis of Ultrasmall and Magic-Sized CdSe Nanocrystals. *Chem. Mater.* **2013**, *25*, 1199–1210.

(64) Lee, J.; Yang, J.; Kwon, S. G.; Hyeon, T. Nonclassical Nucleation and Growth of Inorganic Nanoparticles. *Nat. Rev.* **2016**, *1*, 1–16.

(65) Billinge, S. J. L.; Levin, I. The Problem with Determining Atomic Structure at the Nanoscale. *Science* **2007**, *316*, 561–565.

(66) Wood, S. R.; Woods, K. N.; Plassmeyer, P. N.; Marsh, D. A.; Johnson, D. W.; Page, C. J.; Jensen, K. M. Ø.; Johnson, D. C. Same Precursor, Two Different Products: Comparing the Structural Evolution of In-Ga-O "Gel-Derived" Powders and Solution-Cast Films Using Pair Distribution Function Analysis. *J. Am. Chem. Soc.* **2017**, *139*, 5607–5613.

(67) Jensen, K. M. Ø.; Christensen, M.; Juhas, P.; Bøjesen, E. D.; Lock, N.; Billinge, S. J. L.; Iversen, B. B. Revealing the Mechanisms behind SnO_2 Nanoparticle Formation and Growth during Hydrothermal Synthesis: An In Situ Total Scattering Study. *J. Am. Chem. Soc.* **2012**, *134*, 6785–6792.

(68) Jensen, K. K. M. Ø.; Andersen, H. L. H.; Tyrsted, C.; Bøjesen, E. D.; Dippel, A.-C.; Lock, N.; Billinge, S. J. L.; Iversen, B. B.; Christensen, M. Mechanisms for Iron Oxide Formation under Hydrothermal Conditions: An In Situ Total Scattering Study. *ACS Nano* **2014**, *8*, 10704–10714.

(69) Bøjesen, E. D.; Iversen, B. B. The Chemistry of Nucleation. *CrystEngComm* **2016**, *18*, 8332–8353.

(70) Billinge, S. J. L.; Kanatzidis, M. G. Beyond Crystallography : The Study of Disorder, Nanocrystallinity and Crystallographically Challenged Materials with Pair Distribution Functions. *Chem. Commun.* **2004**, 749–760.

(71) Gary, D. C.; Terban, M. W.; Billinge, S. J. L.; Cossairt, B. M. Two-Step Nucleation and Growth of InP Quantum Dots via Magic-Sized Cluster Intermediates. *Chem. Mater.* **2015**, *27*, 1432–1441.

(72) Friedfeld, M. R.; Stein, J. L.; Cossairt, B. M. Main-Group-Semiconductor Cluster Molecules as Synthetic Intermediates to Nanostructures. *Inorg. Chem.* **2017**, *56*, 8689–8697.

(73) Niederberger, M. Nonaqueous Sol – Gel Routes to Metal Oxide Nanoparticles. *Acc. Chem. Res.* **2007**, *40*, 793–800.

(74) Tronc, E.; Ezzir, A.; Cherkaoui, R.; Chaneac, C.; Nogues, M.; Kachkachi, H.; Fiorani, D.; Testa, A. M.; Greneche, J. M.; Jolivet, J. P. Surface-Related Properties of Fe_2O_3 Nanoparticles. *J. Magn. Magn. Mater.* **2000**, *221*, 63–79.

(75) Ito, D.; Yokoyama, S.; Zaikova, T.; Masuko, K.; Hutchison, J. E. Synthesis of Ligand-Stabilized Metal Oxide Nanocrystals and Epitaxial Core/Shell Nanocrystals via a Lower- Temperature Esterification Process. *ACS Nano* **2014**, *8*, 64–75.

(76) Jansons, A. W.; Plummer, L. K.; Hutchison, J. E. Living Nanocrystals. *Chem. Mater.* **2017**, *29*, 5415–5425.

(77) Garnweitner, G.; Niederberger, M. Organic Chemistry in Inorganic Nanomaterials Synthesis. *J. Mater. Chem.* **2008**, *18*, 1171–1182.

(78) Sun, S.; Zeng, H. Size-Controlled Synthesis of Magnetite Nanoparticles. *J. Am. Chem. Soc.* **2002**, *124*, 8204–8205.

(79) Soon, G. K.; Piao, Y.; Park, J.; Angappane, S.; Jo, Y.; Hwang, N.-M.; Park, J.-G.; Hyeon, T. Kinetics of Monodisperse Iron Oxide Nanocrystal Formation by "Heating-up" Process. *J. Am. Chem. Soc.* **2007**, *129*, 12571–12584.

(80) Buck, M. R.; Biacchi, A. J.; Schaak, R. E. Insights into the Thermal Decomposition of Co (II) Oleate for the Shape-Controlled Synthesis of Wurtzite-Type CoO Nanocrystals. *Chem. Mater.* **2014**, *26*, 1492–1499.

(81) Crockett, B. M.; Jansons, A. W.; Koskela, K. M.; Johnson, D. W.; Hutchison, J. E. Radial Dopant Placement for Tuning Plasmonic Properties in Metal Oxide Nanocrystals. *ACS Nano* **2017**, *11*, 7719–7728.

(82) Millan, A.; Urtizberea, A.; Silva, N. J. O.; Palacio, F.; Amaral, V. S.; Snoeck, E.; Serin, V. Surface Effects in Maghemite Nanoparticles. *J. Magn. Magn. Mater.* **2007**, *312*, L5–L9.

(83) Guardia, P.; Batlle-Brugal, B.; Roca, A. G.; Iglesias, O.; Morales, M. P.; Serna, C. J.; Labarta, A.; Batlle, X. Surfactant Effects in Magnetite Nanoparticles of Controlled Size. *J. Magn. Magn. Mater.* **2007**, *316*, 756–759.

(84) Dutta, P.; Pal, S.; Seehra, M. S.; Shah, N.; Huffman, G. P. Size Dependence of Magnetic Parameters and Surface Disorder in Magnetite Nanoparticles. *J. Appl. Phys.* **2009**, *105*, 10–13.

(85) Chantrell, R. W.; Popplewell, J.; Charles, S. W. Measurement of Particle Size Distribution Parameters in Ferrofluids. *IEEE Trans. Magn.* **1978**, *MAG-14*, 975–977.

(86) Grau-Crespo, R.; Al-Baitai, A. Y.; Saadoune, I.; De Leeuw, N. H. Vacancy Ordering and Electronic Structure of γ-Fe_2O_3 (Maghemite): A Theoretical Investigation. *J. Phys. Condens. Matter* **2010**, *22*, 255401.

(87) Morales, M. P.; de Julian, C.; Gonzalez, J. M.; Serna, C. J. The Effect of the Distribution of Vacancies on the Magnetic Properties of γ-Fe_2O_3 Particles. *J. Mater. Res.* **1994**, *9*, 135–141.

(88) Ouyang, G.; Zhu, W. G.; Sun, C. Q.; Zhu, Z. M.; Liao, S. Z. Atomistic Origin of Lattice Strain on Stiffness of Nanoparticles. *Phys. Chem. Chem. Phys.* **2010**, *12*, 1543–1549.

(89) Zhang, S.; Zhang, X.; Jiang, G.; Zhu, H.; Guo, S.; Su, D.; Lu, G.; Sun, S. Tuning Nanoparticle Structure and Surface Strain for Catalysis Optimization. *J. Am. Chem. Soc.* **2014**, *136*, 7734–7739.

(90) Reddy, D. H. K.; Yun, Y. S. Spinel Ferrite Magnetic Adsorbents: Alternative Future Materials for Water Purification. *Coord. Chem. Rev.* **2016**, *315*, 90–111.

(91) Parkinson, G. S. Iron Oxide Surfaces. *Surf. Sci. Rep.* **2016**, *71*, 272–365.

(92) Zhu, M.; Northrup, P.; Shi, C.; Billinge, S. J. L.; Sparks, D. L.; Waychunas, G. A. Structure of Sulfate Adsorption Complexes on Ferrihydrite. *Environ. Sci. Technol. Lett.* **2013**, *1*, 97–101.

(93) Kumari, M.; Pittman, C. U.; Mohan, D. Heavy Metals [Chromium (VI) and Lead (II)] Removal from Water Using Mesoporous Magnetite (Fe_3O_4) Nanospheres. *J. Colloid Interface Sci.* **2015**, *442*, 120–132.

(94) Chowdhury, S.; Yanful, E. Arsenic and Chromium Removal by Mixed Magnetite–Maghemite Nanoparticles and the Effect of Phosphate on Removal. *J. Environ. Manage.* **2010**, *91*, 2238–2247.

(95) van Embden, J.; Chesman, A. S. R.; Jasieniak, J. J. The Heat-Up Synthesis of Colloidal Nanocrystals. *Chem. Mater.* **2015**, *27*, 2246–2285.

(96) Hendricks, M. P.; Campos, M. P.; Cleveland, G. T.; Plante, I. J; Owen, J. S. A Tunable Library of Substituted Thiourea Precursors to Metal Sulfide Nanocrystals. *Science* **2015**, *348*, 1226–1230.

(97) Li, M.; Zhou, W. H.; Guo, J.; Zhou, Y. L.; Hou, Z. L.; Jiao, J.; Zhou, Z. J.; Du, Z. L.; Wu, S. X. Synthesis of Pure Metastable Wurtzite CZTS Nanocrystals by Facile One-Pot Method. *J. Phys. Chem. C* **2012**, *116*, 26507–26516.

Chapter II

(1) Kolhatkar, A.; Jamison, A.; Litvinov, D.; Willson, R.; Lee, T. Tuning the Magnetic Properties of Nanoparticles. *Int. J. Mol. Sci.* **2013**, *14*, 15977–16009.

(2) Speliotis, D. E. Magnetic Recording beyond the First 100 Years. *J. Magn. Magn. Mater.* **1999**, *193*, 29–35.

(3) Lim, E.-K.; Kim, T.; Paik, S.; Haam, S.; Huh, Y.-M.; Lee, K. Nanomaterials for Theranostics: Recent Advances and Future Challenges. *Chem. Rev.* **2015**, *115*, 327–394.

(4) Lee, N.; Yoo, D.; Ling, D.; Cho, M. H.; Hyeon, T.; Cheon, J. Iron Oxide Based Nanoparticles for Multimodal Imaging and Magnetoresponsive Therapy. *Chem. Rev.*, **2015**, *115*, 10637–10689.

(5) Laurent, S.; Dutz, S.; Häfeli, U. O.; Mahmoudi, M. Magnetic Fluid Hyperthermia: Focus on Superparamagnetic Iron Oxide Nanoparticles. *Adv. Colloid Interface Sci.*, **2011**, *166*, 8–23.

(6) Krishnan, K. M.; Pakhomov, A. B.; Bao, Y.; Blomqvist, P.; Chun, Y.; Gonzales, M.; Griffin, K.; Ji, X.; Roberts, B. K. Nanomagnetism and Spin Electronics: Materials, Microstructure and Novel Properties. *J. Mater. Sci.* **2006**, *41*, 793–815.

(7) Auffan, M.; Rose, J.; Bottero, J.-Y.; Lowry, G. V.; Jolivet, J.-P.; Wiesner, M. R. Towards a Definition of Inorganic Nanoparticles from an Environmental, Health and Safety Perspective. *Nat. Nanotechnol.* **2009**, *4*, 634–641.

(8) Roduner, E. Size Matters : Why Nanomaterials Are Different. *Chem. Soc. Rev.* **2006**, *35*, 583–592.

(9) Auffan, M.; Rose, J.; Proux, O.; Borschneck, D.; Masion, A.; Chaurand, P.; Hazemann, J.-L.; Chaneac, C.; Jolivet, J.-P.; Wiesner, M. R.; *et al.* Enhanced Adsorption of Arsenic onto Maghemites Nanoparticles: As(III) as a Probe of the Surface Structure and Heterogeneity. *Langmuir* **2008**, *24*, 3215–3222.

(10) Park, J.; An, K.; Hwang, Y.; Park, J.-G.; Noh, H.-J.; Kim, J.-Y.; Park, J.-H.; Hwang, N.-M.; Hyeon, T. Ultra-Large-Scale Syntheses of Monodisperse Nanocrystals. *Nat. Mater.* **2004**, *3*, 891–895.

(11) Lak, A.; Kraken, M.; Ludwig, F.; Kornowski, A.; Eberbeck, D.; Sievers, S.; Litterst, F. J.; Weller, H.; Schilling, M. Size Dependent Structural and Magnetic Properties of FeO–Fe_3O_4 Nanoparticles. *Nanoscale* **2013**, *5*, 12286-12295.

(12) Wetterskog, E.; Tai, C. W.; Grins, J.; Bergström, L.; Salazar-Alvarez, G. Anomalous Magnetic Properties of Nanoparticles Arising from Defect Structures: Topotaxial Oxidation of $Fe_{1-x}O|Fe_{3-\delta}O_4$ Core|shell Nanocubes to Single-Phase Particles. *ACS Nano* **2013**, *7*, 7132–7144.

(13) Pichon, B. P.; Gerber, O.; Lefevre, C.; Florea, I.; Fleutot, S.; Baaziz, W.; Pauly, M.; Ohlmann, M.; Ulhaq, C.; Ersen, O.; *et al.* Microstructural and Magnetic Investigations of Wüstite-Spinel Core-Shell Cubic-Shaped Nanoparticles. *Chem. Mater.* **2011**, *23*, 2886–2900.

(14) Estrader, M.; López-Ortega, A.; Golosovsky, I. V.; Estradé, S.; Roca, A. G.; Salazar-Alvarez, G.; López-Conesa, L.; Tobia, D.; Winkler, E.; Ardisson, J. D.; *et al.* Origin of the Large Dispersion of Magnetic Properties in Nanostructured Oxides: Fe_xO/Fe_3O_4 Nanoparticles as a Case Study. *Nanoscale* **2015**, *7*, 3002–3015.

(15) Millan, A.; Urtizberea, A.; Silva, N. J. O.; Palacio, F.; Amaral, V. S.; Snoeck, E.; Serin, V. Surface Effects in Maghemte Nanoparticles. *J. Magn. Magn. Mater.* **2007**, *312*, L5–L9.

(16) Mohapatra, J.; Mitra, A.; Bahadur, D.; Aslam, M. Surface Controlled Synthesis of MFe_2O_4 (M = Mn, Fe, Co, Ni and Zn) Nanoparticles and Their Magnetic Characteristics. *CrystEngComm* **2013**, *15*, 524-532.

(17) Roca, A. G.; Niznansky, D.; Poltierova-Vejpravova, J.; Bittova, B.; González-Fernández, M. A.; Serna, C. J.; Morales, M. P. Magnetite Nanoparticles with No Surface Spin Canting. *J. Appl. Phys.* **2009**, *105*, 114309.

(18) Tronc, E.; Ezzir, A.; Cherkaoui, R.; Chanéac, C.; Noguès, M.; Kachkachi, H.; Fiorani, D.; Testa, A. M.; Grenèche, J. M.; Jolivet, J. P. Surface-Related Properties of ɣ-Fe_2O_3 Nanoparticles. *J. Magn. Magn. Mater.* **2000**, *221*, 63–79.

(19) Vestal, C. R.; Zhang, Z. J. Effects of Surface Coordination Chemistry on the Magnetic Properties of $MnFe_2O_4$ Spinel Ferrite Nanoparticles. *J. Am. Chem. Soc.* **2003**, *125*, 9828–9833.

(20) Daou, T. J.; Grenèche, J. M.; Pourroy, G.; Buathong, S.; Derory, A.; Ulhaq-Bouillet, C.; Donnio, B.; Guillon, D.; Begin-Colin, S. Coupling Agent Effect on Magnetic Properties of Functionalized Magnetite-Based Nanoparticles. *Chem. Mater.* **2008**, *20*, 5869–5875.

(21) Demortière, A.; Panissod, P.; Pichon, B. P.; Pourroy, G.; Guillon, D.; Donnio, B.; Bégin-Colin, S. Size-Dependent Properties of Magnetic Iron Oxidenanocrystals. *Nanoscale* **2011**, *3*, 225–232.

(22) Lee, J.; Kwon, S. G.; Park, J.-G.; Hyeon, T. Size Dependence of Metal–Insulator Transition in Stoichiometric Fe_3O_4 Nanocrystals. *Nano Lett.* **2015**, *15*, 4337–4342.

(23) Kim, B. H.; Lee, N.; Kim, H.; An, K.; Park, Y. I.; Choi, Y.; Shin, K.; Lee, Y.; Kwon, S. G.; Na, H. B.; *et al.* Large-Scale Synthesis of Uniform and Extremely Small-Sized Iron Oxide Nanoparticles for High-Resolution T_1 Magnetic Resonance Imaging Contrast Agents. *J. Am. Chem. Soc.* **2011**, *133*, 12624–12631.

(24) Martínez-Boubeta, C.; Simeonidis, K.; Angelakeris, M.; Pazos-Pérez, N.; Giersig, M.; Delimitis, A.; Nalbandian, L.; Alexandrakis, V.; Niarchos, D. Critical Radius for Exchange Bias in Naturally Oxidized Fe Nanoparticles. *Phys. Rev. B* **2006**, *74*, 054430.

(25) Salazar-Alvarez, G.; Qin, J.; Šepelák, V.; Bergmann, I.; Vasilakaki, M.; Trohidou, K. N.; Ardisson, J. D.; Macedo, W. A. A.; Mikhaylova, M.; Muhammed, M.; *et al.* Cubic versus Spherical Magnetic Nanoparticles: The Role of Surface Anisotropy. *J. Am. Chem. Soc.* **2008**, *130*, 13234–13239.

(26) Mitra, A.; Mohapatra, J.; Meena, S. S.; Tomy, C. V.; Aslam, M. Verwey Transition in Ultrasmall-Sized Octahedral Fe_3O_4 Nanoparticles. *J. Phys. Chem. C* **2014**, *118*, 19356–19362.

(27) Zhou, Z.; Zhu, X.; Wu, D.; Chen, Q.; Huang, D.; Sun, C.; Xin, J.; Ni, K.; Gao, J. Anisotropic Shaped Iron Oxide Nanostructures: Controlled Synthesis and Proton Relaxation Shortening Effects. *Chem. Mater.* **2015**, *27*, 3505–3515.

(28) Ge, W.; Sato, R.; Wu, H.-L.; Teranishi, T. Simple Surfactant Concentration-Dependent Shape Control of Polyhedral Fe_3O_4 Nanoparticles and Their Magnetic Properties. *ChemPhysChem* **2015**, *16*, 3200–3205.

(29) Fortin, J. P.; Wilhelm, C.; Servais, J.; Ménager, C.; Bacri, J. C.; Gazeau, F. Size-Sorted Anionic Iron Oxide Nanomagnets as Colloidal Mediators for Magnetic Hyperthermia. *J. Am. Chem. Soc.* **2007**, *129*, 2628–2635.

(30) Deatsch, A. E.; Evans, B. A. Heating Efficiency in Magnetic Nanoparticle Hyperthermia. *J. Magn. Magn. Mater.* **2014**, *354*, 163–172.

(31) Yavuz, C. T.; Mayo, J. T.; Yu, W. W.; Prakash, A.; Falkner, J. C.; Yean, S.; Cong, L.; Shipley, H. J.; Kan, A.; Tomson, M.; *et al.* Low-Field Magnetic Separation of Monodisperse Fe_3O_4 Nanocrystals. *Science* **2006**, *314*, 964–968.

(32) Guardia, P.; Pérez, N.; Labarta, A.; Batlle, X. Controlled Synthesis of Iron Oxide Nanoparticles over a Wide Size Range. *Langmuir* **2010**, *26*, 5843–5847.

(33) Unni, M.; Uhl, A. M.; Savliwala, S.; Savitzky, B. H.; Dhavalikar, R.; Garraud, N.; Arnold, D. P.; Kourkoutis, L. F.; Andrew, J. S.; Rinaldi, C. Thermal Decomposition Synthesis of Iron Oxide Nanoparticles with Diminished Magnetic Dead Layer by Controlled Addition of Oxygen. *ACS Nano* **2017**, *11*, 2284–2303.

(34) Santoyo Salazar, J.; Perez, L.; de Abril, O.; Truong Phuoc, L.; Ihiawakrim, D.; Vazquez, M.; Greneche, J.-M.; Begin-Colin, S.; Pourroy, G. Magnetic Iron Oxide Nanoparticles in 10−40 Nm Range: Composition in Terms of Magnetite/Maghemite Ratio and Effect on the Magnetic Properties. *Chem. Mater.* **2011**, *23*, 1379–1386.

(35) Signorini, L.; Pasquini, L.; Savini, L.; Carboni, R.; Boscherini, F.; Bonetti, E.; Giglia, A.; Pedio, M.; Mahne, N..; *et al.* Size-Dependent Oxidation in Iron/iron Oxide Core-Shell Nanoparticles. *Phys. Rev. B* **2003**, *68*, 195423.

(36) Luigjes, B.; Woudenberg, S. M. C.; de Groot, R.; Meeldijk, J. D.; Torres Galvis, H. M.; de Jong, K. P.; Philipse, A. P.; Erné, B. H. Diverging Geometric and Magnetic Size Distributions of Iron Oxide Nanocrystals. *J. Phys. Chem. C* **2011**, *115*, 14598–14605.

(37) Chen, R.; Christiansen, M. G.; Sourakov, A.; Mohr, A.; Matsumoto, Y.; Okada, S.; Jasanoff, A.; Anikeeva, P. High-Performance Ferrite Nanoparticles through Nonaqueous Redox Phase Tuning. *Nano Lett.* **2016**, *16*, 1345–1351.

(38) Vreeland, E. C.; Watt, J.; Schober, G. B.; Hance, B. G.; Austin, M. J.; Price, A. D.; Fellows, B. D.; Monson, T. C.; Hudak, N. S.; Maldonado-Camargo, L.; *et al.* Enhanced Nanoparticle Size Control by Extending LaMer's Mechanism. *Chem. Mater.* **2015**, *27*, 6059–6066.

(39) Caruntu, D.; Caruntu, G.; O'Connor, C. J. Magnetic Properties of Variable-Sized Fe_3O_4 Nanoparticles Synthesized from Non-Aqueous Homogeneous Solutions of Polyols. *J. Phys. D. Appl. Phys.* **2007**, *40*, 5801–5809.

(40) Park, B.; Kim, B. H.; Yu, T. Synthesis of Spherical and Cubic Magnetic Iron Oxide Nanocrystals at Low Temperature in Air. *J. Colloid Interface Sci.* **2018**, *518*, 27–33.

(41) Dehsari, H. S.; Heidari, M.; Ribeiro, A. H.; Tremel, W.; Jakob, G.; Donadio, D.; Potestio, R.; Asadi, K. Combined Experimental and Theoretical Investigation of Heating Rate on Growth of Iron Oxide Nanoparticles. *Chem. Mater.* **2017**, *29*, 9648-9656.

(42) Yun, H.; Liu, X.; Paik, T.; Palanisamy, D.; Kim, J.; Vogel, W. D.; Viescas, A. J.; Chen, J.; Papaefthymiou, G. C.; Kikkawa, J. M.; *et al.* Size- and Composition-Dependent Radio Frequency Magnetic Permeability of Iron Oxide Nanocrystals. *ACS Nano* **2014**, *8*, 12323–12337.

(43) Baaziz, W.; Pichon, B. P.; Fleutot, S.; Liu, Y.; Lefevre, C.; Greneche, J.-M.; Toumi, M.; Mhiri, T.; Begin-Colin, S. Magnetic Iron Oxide Nanoparticles: Reproducible Tuning of the Size and Nanosized-Dependent Composition, Defects, and Spin Canting. *J. Phys. Chem. C* **2014**, *118*, 3795–3810.

(44) Taniguchi, T.; Nakagawa, K.; Watanabe, T.; Matsushita, N.; Yoshimura, M. Hydrothermal Growth of Fatty Acid Stabilized Iron Oxide Nanocrystals. *J. Phys. Chem. C* **2009**, *113*, 839–843.

(45) Castellanos-Rubio, I.; Insausti, M.; Garaio, E.; Gil de Muro, I.; Plazaola, F.; Rojo, T.; Lezama, L. Fe_3O_4 Nanoparticles Prepared by the Seeded-Growth Route for Hyperthermia: Electron Magnetic Resonance as a Key Tool to Evaluate Size Distribution in Magnetic Nanoparticles. *Nanoscale* **2014**, *6*, 7542-7552.

(46) Coey, J. M. D. Noncollinear Spin Arrangement in Ultrafine Ferrimagnetic Crystallites. *Phys. Rev. Lett.* **1971**, *27*, 1140-1142.

(47) Dutta, P.; Pal, S.; Seehra, M. S.; Shah, N.; Huffman, G. P. Size Dependence of Magnetic Parameters and Surface Disorder in Magnetite Nanoparticles. *J. Appl. Phys.* **2009**, *105*, 07B501.

(48) Bronstein, L. M.; Huang, X.; Retrum, J.; Schmucker, A.; Pink, M.; Stein, B. D.; Dragnea, B. Influence of Iron Oleate Complex Structure on Iron Oxide Nanoparticle Formation. *Chem. Mater.* **2007**, *19*, 3624–3632.

(49) Kemp, S. J.; Ferguson, R. M.; Khandhar, A. P.; Krishnan, K. M. Monodisperse Magnetite Nanoparticles with Nearly Ideal Saturation Magnetization. *RSC Adv.* **2016**, *6*, 77452–77464.

(50) Pérez, N.; López-Calahorra, F.; Labarta, A.; Batlle, X. Reduction of Iron by Decarboxylation in the Formation of Magnetite Nanoparticles. *Phys. Chem. Chem. Phys.* **2011**, *13*, 19485-19489.

(51) Kwon, S. G.; Piao, Y.; Park, J.; Angappane, S.; Jo, Y.; Hwang, N.-M.; Park, J.-G.; Hyeon, T. Kinetics of Monodisperse Iron Oxide Nanocrystal Formation by "Heating-Up" Process. *J. Am. Chem. Soc.* **2007**, *129*, 12571–12584.

(52) Hai, H. T.; Kura, H.; Takahashi, M.; Ogawa, T. Facile Synthesis of Fe3O4 Nanoparticles by Reduction Phase Transformation from ?-Fe2O3 Nanoparticles in Organic Solvent. *J. Colloid Interface Sci.* **2010**, *341*, 194–199.

(53) Ito, D.; Yokoyama, S.; Zaikova, T.; Masuko, K.; Hutchison, J. E. Synthesis of Ligand-Stabilized Metal Oxide Nanocrystals and Epitaxial Core/Shell Nanocrystals via a Lower- Temperature Esterification Process. *ACS Nano* **2014**, *8*, 64–75.

(54) Jansons, A. W.; Hutchison, J. E. Continuous Growth of Metal Oxide Nanocrystals: Enhanced Control of Nanocrystal Size and Radial Dopant Distribution. *ACS Nano* **2016**, *10*, 6942–6951.

(55) Crockett, B. M.; Jansons, A. W.; Koskela, K. M.; Johnson, D. W.; Hutchison, J. E. Radial Dopant Placement for Tuning Plasmonic Properties in Metal Oxide Nanocrystals. *ACS Nano* **2017**, *11*, 7719–7728.

(56) Tang, J.; Myers, M.; Bosnick, K. A.; Brus, L. E. Magnetite Fe_3O_4 Nanocrystals: Spectroscopic Observation of Aqueous Oxidation Kinetics. *J. Phys. Chem. B* **2003**, *107*, 7501–7506.

(57) Jansons, A. W.; Plummer, L. K.; Hutchison, J. E. Living Nanocrystals. *Chem. Mater.* **2017**, *29*, 5415–5425.

(58) Fleet, M. E. The Structure of Magnetite. *Acta Cryst.* **1981**, *B37*, 917–920.

(59) Annersten, H.; Hafner, S. S. Vacancy Distribution in Synthetic Spinels of the Series Fe_3O_4—γ-Fe_2O_3. *Zeitschrift für Krist.* **1973**, *137*, 321–340.

(60) Grau-Crespo, R.; Al-Baitai, A. Y.; Saadoune, I.; De Leeuw, N. H. Vacancy Ordering and Electronic Structure of γ-Fe_2O_3 (Maghemite): A Theoretical Investigation. *J. Phys. Condens. Matter* **2010**, *22*, 255401.

(61) Chantrell, R. W.; Popplewell, J.; Charles, S. W. Measurement of Particle Size Distribution Parameters in Ferrofluids. *IEEE Trans. Magn.* **1978**, *MAG-14*, 975–977.

(62) Cornell, R. M.; Schwertmann, U. *The Iron Oxides: Structure, Properties, Reactions, Occurrences, and Uses*; 2nd ed.; Wiley-VCH: Weinheim, 2003.

(63) Huber, D. L. Synthesis, Properties, and Applications of Iron Nanoparticles. *Small* **2005**, *1*, 482–501.

(64) Hyeon, T. Chemical Synthesis of Magnetic Nanoparticles. *Chem. Commun.* **2003**, 927–934.

(65) Levy, M.; Quarta, A.; Espinosa, A.; Figuerola, A.; Wilhelm, C.; García-Hernández, M.; Genovese, A.; Falqui, A.; Alloyeau, D.; Buonsanti, R.; *et al.* Correlating Magneto-Structural Properties to Hyperthermia Performance of Highly Monodisperse Iron Oxide Nanoparticles Prepared by a Seeded-Growth Route. *Chem. Mater.* **2011**, *23*, 4170–4180.

(66) Pacakova, B.; Kubickova, S.; Salas, G.; Mantlikova, A. R.; Marciello, M.; Morales, M. P.; Niznansky, D.; Vejpravova, J. The Internal Structure of Magnetic Nanoparticles Determines the Magnetic Response. *Nanoscale* **2017**, *9*, 5129–5140.

(67) Gordon, T. R.; Cargnello, M.; Paik, T.; Mangolini, F.; Weber, R. T.; Fornasiero, P.; Murray, C. B. Nonaqueous Synthesis of TiO_2 Nanocrystals Using TiF_4 to Engineer Morphology, Oxygen Vacancy Concentration, and Photocatalytic Activity. *J. Am. Chem. Soc.* **2012**, *134*, 6751–6761.

(68) Vioux, A. Nonhydrolytic Sol-Gel Routes to Oxides. *Chem. Mater.* **1997**, *9*, 2292–2299.

(69) Niederberger, M. Nonaqueous Sol–Gel Routes to Metal Oxide Nanoparticles. *Acc. Chem. Res.* **2007**, *40*, 793–800.

(70) Chen, Y.; Kim, M.; Lian, G.; Johnson, M. B.; Peng, X. Side Reactions in Controlling the Quality, Yield, and Stability of High Quality Colloidal Nanocrystals. *J. Am. Chem. Soc.* **2005**, *127*, 13331–13337.

(71) Linderoth, S.; Hendriksen, P. V.; Bødker, F.; Wells, S.; Davies, K.; Charles, S. W.; Mørup, S. On Spin-Canting in Maghemite Particles. *J. Appl. Phys.* **1994**, *75*, 6583-6585.

(72) Nguyen, T.-D. From Formation Mechanisms to Synthetic Methods toward Shape-Controlled Oxide Nanoparticles. *Nanoscale* **2013**, *5*, 9455-9482.

(73) Schindelin, J.; Arganda-Carreras, I.; Frise, E.; Kaynig, V.; Longair, M.; Pietzsch, T.; Preibisch, S.; Rueden, C.; Saalfeld, S.; Schmid, B.; *et al.* Fiji: An Open-Source Platform for Biological-Image Analysis. *Nat. Methods* **2012**, *9*, 676–682.

(74) Ilavsky, J.; Jemian, P. R. *Irena*: Tool Suite for Modeling and Analysis of Small-Angle Scattering. *J. Appl. Crystallogr.* **2009**, *42*, 347–353.

Chapter III

(1) Auffan, M.; Rose, J. J.; Bottero, J. Y.; Lowry, G. V.; Jolivet, J. P.; Wiesner, M. R. Towards a Definition of Inorganic Nanoparticles from an Environmental, Health and Safety Perspective. *Nat. Nanotechnol.* **2009**, *4*, 634–641.

(2) Grassian, V. H. When Size Really Matters: Size-Dependent Properties and Surface Chemistry of Metal and Metal Oxide Nanoparticles in Gas and Liquid Phase Environments. *J. Phys. Chem. C* **2008**, *112*, 18303–18313.

(3) Roduner, E. Size Matters : Why Nanomaterials Are Different. *Chem. Soc. Rev.* **2006**, *35*, 583–592.

(4) Kolhatkar, A. G.; Jamison, A. C.; Litvinov, D.; Willson, R. C.; Lee, T. R. Tuning the Magnetic Properties of Nanoparticles. *Int. J. Mol. Sci.* **2013**, *14*, 15977–16009.

(5) Auffan, M.; Rose, J.; Proux, O.; Borschneck, D.; Masion, A.; Chaurand, P.; Hazemann, J.-L.; Chaneac, C.; Jolivet, J.-P.; Wiesner, M. R.; *et al.* Enhanced Adsorption of Arsenic onto Maghemites Nanoparticles : As (III) as a Probe of the Surface Structure and Heterogeneity. *Langmuir* **2008**, *24*, 3215–3222.

(6) Cooper, S. R.; Plummer, L. K.; Cosby, A. G.; Lenox, P.; Jander, A.; Dhagat, P.; Hutchison, J. E. Insights into the Magnetic Properties of Sub-10 nm Iron Oxide Nanocrystals through the Use of a Continuous Growth Synthesis. *Chem. Mater.* **2018**, *30*, 6053–6062.

(7) Fleet, M. E. The Structure of Magnetite. *Acta Crystallogr.* **1981**, *2549*, 917–920.

(8) Greaves, C. A Powder Neutron Diffraction Investigation of Vacancy Ordering and Covalence in γ-Fe_2O_3. *J. Solid State Chem.* **1983**, *49*, 325–333.

(9) Annersten, H.; Hafner, S. S. Vacancy Distribution in Synthetic Spinels of the Series Fe_3O_4—γ-Fe_2O_3. *Zeitschrift fur Krist. - New Cryst. Struct.* **1973**, *137*, 321–340.

(10) Park, J.; An, K.; Hwang, Y.; Park, J.-G.; Noh, H.-J.; Kim, J.-Y.; Park, J.-H.; Hwang, N.-M.; Hyeon, T. Ultra-Large-Scale Syntheses of Monodisperse Nanocrystals. *Nat. Mater.* **2004**, *3*, 891–895.

(11) Martínez-Boubeta, C.; Simeonidis, K.; Angelakeris, M.; Pazos-Pérez, N.; Giersig, M.; Delimitis, A.; Nalbandian, L.; Alexandrakis, V.; Niarchos, D. Critical Radius for Exchange Bias in Naturally Oxidized Fe Nanoparticles. *Phys. Rev. B* **2006**, *74*, 053340.

(12) Santoyo Salazar, J.; Perez, L.; De Abril, O.; Truong Phuoc, L.; Ihiawakrim, D.; Vazquez, M.; Greneche, J. M.; Bégin-Colin, S.; Pourroy, G. Magnetic Iron Oxide Nanoparticles in 10-40 nm Range: Composition in Terms of Magnetite/Maghemite Ratio and Effect on the Magnetic Properties. *Chem. Mater.* **2011**, *23*, 1379–1386.

(13) Daou, T. J.; Pourroy, G.; Bégin-Colin, S.; Grenèche, J. M.; Ulhaq-Bouillet, C.; Legaré, P.; Bernhardt, P.; Leuvrey, C.; Rogez, G. Hydrothermal Synthesis of Monodisperse Magnetite Nanoparticles. *Chem. Mater.* **2006**, *18*, 4399–4404.

(14) Topsoe, H.; Dumesic, J. A.; Boudart, M. Mössbauer Spectra of Stoichiometric and Nonstoichiometric Fe_3O_4 Microcrystals. *J. Phys. Colloq.* **1974**, *35*, 411–413.

(15) Signorini, L.; Pasquini, L.; Savini, L.; Carboni, R.; Boscherini, F.; Bonetti, E.; Giglia, A.; Pedio, M.; Mahne, N.; Nannarone, S. Size-Dependent Oxidation in Iron/Iron Oxide Core-Shell Nanoparticles. *Phys. Rev. B* **2003**, *68*, 195423.

(16) Baaziz, W.; Pichon, B. P.; Fleutot, S.; Liu, Y.; Lefevre, C.; Greneche, J.-M.; Toumi, M.; Mhiri, T.; Begin-Colin, S. Magnetic Iron Oxide Nanoparticles: Reproducible Tuning of the Size and Nanosized-Dependent Composition, Defects, and Spin Canting. *J. Phys. Chem. C* **2014**, *118*, 3795–3810.

(17) Kim, B. H.; Lee, N.; Kim, H.; An, K.; Park, Y. I; Choi, Y.; Shin, K.; Lee, Y.; Kwon, S. G.; Na, H. B.; *et al.* Large-Scale Synthesis of Uniform and Extremely Small-Sized Iron Oxide Nanoparticles for High-Resolution T1 Magnetic Resonance Imaging Contrast Agents. *J. Am. Chem. Soc.* **2011**, *133*, 12624–12631.

(18) Demortière, A.; Panissod, P.; Pichon, B. P.; Pourroy, G.; Guillon, D.; Donnio, B.; Bégin-Colin, S. Size-Dependent Properties of Magnetic Iron Oxide Nanocrystals. *Nanoscale* **2011**, *3*, 225–232.

(19) Mohapatra, J.; Mitra, A.; Bahadur, D.; Aslam, M. Surface Controlled Synthesis of MFe_2O_4 (M = Mn, Fe, Co, Ni and Zn) Nanoparticles and Their Magnetic Characteristics. *CrystEngComm* **2013**, *15*, 524-532.

(20) Sharifi Dehsari, H.; Heidari, M.; Halda Ribeiro, A.; Tremel, W.; Jakob, G.; Donadio, D.; Potestio, R.; Asadi, K. Combined Experimental and Theoretical Investigation of Heating Rate on Growth of Iron Oxide Nanoparticles. *Chem. Mater.* **2017**, *29*, 9648–9656.

(21) Park, B.; Kim, B. H.; Yu, T. Synthesis of Spherical and Cubic Magnetic Iron Oxide Nanocrystals at Low Temperature in Air. *J. Colloid Interface Sci.* **2018**, *518*, 27–33.

(22) Mitra, A.; Mohapatra, J.; Meena, S. S.; Tomy, C. V.; Aslam, M. Verwey Transition in Ultrasmall-Sized Octahedral Fe_3O_4 Nanoparticles. *J. Phys. Chem. C* **2014**, *118*, 19356–19362.

(23) Yang, J. B.; Zhou, X. D.; Yelon, W. B.; James, W. J.; Cai, Q.; Gopalakrishnan, K. V.; Malik, S. K.; Sun, X. C.; Nikles, D. E. Magnetic and Structural Studies of the Verwey Transition in Fe_3O_4 Nanoparticles. *J. Appl. Phys.* **2004**, *95*, 7540–7542.

(24) Itai, R.; Shibuya, M.; Matsumura, T.; Ishi, G. Electrical Resistivity of Magnetite Anodes. *J. Electrochem. Soc.* **1970**, *118*, 1709–1711.

(25) Gorski, C. A.; Nurmi, J. T.; Tratnyek, P. G.; Hofstetter, T. B.; Scherer, M. M. Redox Behavior of Magnetite : Reduction. *Environ. Sci. Technol.* **2010**, *44*, 55–60.

(26) Tang, J.; Myers, M.; Bosnick, K. A.; Brus, L. E. Magnetite Fe_3O_4 Nanocrystals: Spectroscopic Observation of Aqueous Oxidation Kinetics. *J. Phys. Chem. B* **2003**, *107*, 7501–7506.

(27) Bourgeois, F.; Gergaud, P.; Renevier, H.; Leclere, C.; Feuillet, G. Low Temperature Oxidation Mechanisms of Nanocrystalline Magnetite Thin Film. *J. Appl. Phys.* **2013**, *113*, 013510.

(28) Jensen, K. K. M. Ø.; Andersen, H. L. H.; Tyrsted, C.; Bøjesen, E. D.; Dippel, A.-C.; Lock, N.; Billinge, S. J. L.; Iversen, B. B.; Christensen, M. Mechanisms for Iron Oxide Formation under Hydrothermal Conditions: An *In Situ* Total Scattering Study. *ACS Nano* **2014**, *8*, 10704–10714.

(29) Frison, R.; Cernuto, G.; Cervellino, A.; Zaharko, O.; Colonna, G. M.; Guagliardi, A.; Masciocchi, N. Magnetite − Maghemite Nanoparticles in the 5 − 15 nm Range : Correlating the Core − Shell Composition and the Surface Structure to the Magnetic Properties . A Total Scattering Study. *Chem. Mater.* **2013**, *25*, 4820–4827.

(30) Dutta, P.; Pal, S.; Seehra, M. S.; Shah, N.; Huffman, G. P. Size Dependence of Magnetic Parameters and Surface Disorder in Magnetite Nanoparticles. *J. Appl. Phys.* **2009**, *105*, 10–13.

(31) Tronc, E.; Ezzir, A.; Cherkaoui, R.; Chaneac, C.; Nogues, M.; Kachkachi, H.; Fiorani, D.; Testa, A. M.; Greneche, J. M.; Jolivet, J. P. Surface-Related Properties of Fe_2O_3 Nanoparticles. *J. Magn. Magn. Mater.* **2000**, *221*, 63–79.

(32) Zhou, X.; Xu, W.; Liu, G.; Panda, D.; Chen, P. Size Dependent Catalytic Activity and Dynamics of Gold Nanoparticles at the Single-Molecule Level. *J. Am. Chem. Soc.* **2010**, *132*, 138–146.

(33) Tyo, E. C.; Vajda, S. Catalysis by Clusters with Precise Numbers of Atoms. *Nat. Nanotechnol.* **2015**, *10*, 577–588.

(34) Billinge, S. J. L.; Levin, I. The Problem with Determining Atomic Structure at the Nanoscale. *Science* **2007**, *316*, 561–565.

(35) Billinge, S. J. L.; Kanatzidis, M. G. Beyond Crystallography: The Study of Disorder, Nanocrystallinity and Crystallographically Challenged Materials with Pair Distribution Functions. *Chem. Commun.* **2004**, 749–760.

(36) Wang, F.; Richards, V. N.; Shields, S. P.; Buhro, W. E. Kinetics and Mechanisms of Aggregative Nanocrystal Growth. *Chem. Mater.* **2014**, *26*, 5–21.

(37) Caruntu, D.; Caruntu, G.; O'Connor, C. J. Magnetic Properties of Variable-Sized Fe_3O_4 Nanoparticles Synthesized from Non-Aqueous Homogeneous Solutions of Polyols. *J. Phys. D. Appl. Phys.* **2007**, *40*, 5801–5809.

(38) Yun, H.; Liu, X.; Paik, T.; Palanisamy, D.; Kim, J.; Vogel, W. D.; Viescas, A. J.; Chen, J.; Papaefthymiou, G. C.; Kikkawa, J. M.; *et al.* Size- and Composition-Dependent Radio Frequency Magnetic Permeability of Iron Oxide Nanocrystals. *ACS Nano* **2014**, *8*, 12323–12337.

(39) Taniguchi, T.; Nakagawa, K.; Watanabe, T.; Matsushita, N.; Yoshimura, M. Hydrothermal Growth of Fatty Acid Stabilized Iron Oxide Nanocrystals. *J. Phys. Chem. C* **2009**, *113*, 839–843.

(40) Yu, W. W.; Falkner, J. C.; Yavuz, C. T.; Colvin, V. L. Synthesis of Monodisperse Iron Oxide Nanocrystals by Thermal Decomposition of Iron Carboxylate Salts. *Chem. Commun.* **2004**, 2306–2307.

(41) Soon, G. K.; Piao, Y.; Park, J.; Angappane, S.; Jo, Y.; Hwang, N.-M.; Park, J.-G.; Hyeon, T. Kinetics of Monodisperse Iron Oxide Nanocrystal Formation by "Heating-up" Process. *J. Am. Chem. Soc.* **2007**, *129*, 12571–12584.

(42) Chen, R.; Christiansen, M. G.; Sourakov, A.; Mohr, A.; Matsumoto, Y.; Okada, S.; Jasanoff, A.; Anikeeva, P. High-Performance Ferrite Nanoparticles through Nonaqueous Redox Phase Tuning. *Nano Lett.* **2016**, *16*, 1345–1351.

(43) Jansons, A. W.; Hutchison, J. E. Continuous Growth of Metal Oxide Nanocrystals: Enhanced Control of Nanocrystal Size and Radial Dopant Distribution. *ACS Nano* **2016**, *10*, 6942–6951.

(44) Unni, M.; Uhl, A. M.; Savliwala, S.; Savitzky, B. H.; Dhavalikar, R.; Garraud, N.; Arnold, D. P.; Kourkoutis, L. F.; Andrew, J. S.; Rinaldi, C. Thermal Decomposition Synthesis of Iron Oxide Nanoparticles with Diminished Magnetic Dead Layer by Controlled Addition of Oxygen. *ACS Nano* **2017**, *11*, 2284–2303.

(45) Pacakova, B.; Kubickova, S.; Salas, G.; Mantlikova, A. R.; Marciello, M.; Morales, M. P.; Niznansky, D.; Vejpravova, J. The Internal Structure of Magnetic Nanoparticles Determines the Magnetic Response. *Nanoscale* **2017**, *9*, 5129–5140.

(46) Levy, M.; Quarta, A.; Espinosa, A.; Figuerola, A.; Wilhelm, C.; García-hern, M.; Genovese, A.; Falqui, A.; Alloyeau, D.; Cozzoli, P. D.; *et al.* Correlating Magneto-Structural Properties to Hyperthermia Performance of Highly Monodisperse Iron Oxide Nanoparticles Prepared by a Seeded-Growth Route. *Chem. Mater.* **2011**, *23*, 4170–4180.

(47) Zhou, Z.; Zhu, X.; Wu, D.; Chen, Q.; Huang, D.; Sun, C.; Xin, J.; Ni, K.; Gao, J. Anisotropic Shaped Iron Oxide Nanostructures: Controlled Synthesis and Proton Relaxation Shortening Effects. *Chem. Mater.* **2015**, *27*, 3505–3515.

(48) De Montferrand, C.; Hu, L.; Milosevic, I.; Russier, V.; Bonnin, D.; Motte, L.; Brioude, A.; Lalatonne, Y. Iron Oxide Nanoparticles with Sizes, Shapes and Compositions Resulting in Different Magnetization Signatures as Potential Labels for Multiparametric Detection. *Acta Biomater.* **2013**, *9*, 6150–6157.

(49) Redl, F. X.; Black, C. T.; Papaefthymiou, G. C.; Sandstrom, R. L.; Yin, M.; Zeng, H.; Murray, C. B.; Brien, S. P. O. Magnetic, Electronic, and Structural Characterization of Nonstoichiometric Iron Oxides at the Nanoscale. *J. Am. Chem. Soc.* **2004**, *126*, 14583–14599.

(50) Bøjesen, E. D.; Iversen, B. B. The Chemistry of Nucleation. *CrystEngComm* **2016**, *18*, 8332–8353.

(51) Friedfeld, M. R.; Stein, J. L.; Cossairt, B. M. Main-Group-Semiconductor Cluster Molecules as Synthetic Intermediates to Nanostructures. *Inorg. Chem.* **2017**, *56*, 8689–8697.

(52) Harrell, S. M.; Mcbride, J. R.; Rosenthal, S. J. Synthesis of Ultrasmall and Magic-Sized CdSe Nanocrystals. *Chem. Mater.* **2013**, *25*, 1199–1210.

(53) Hendricks, M. P.; Campos, M. P.; Cleveland, G. T.; Plante, I. J. L; Owen, J. S. A Tunable Library of Substituted Thiourea Precursors to Metal Sulfide Nanocrystals. *Science* **2015**, *348*, 1226–1230.

(54) Scheck, J.; Wu, B.; Drechsler, M.; Rosenberg, R.; Van Driessche, A. E. S.; Stawski, T. M.; Gebauer, D. The Molecular Mechanism of Iron(III) Oxide Nucleation. *J. Phys. Chem. Lett.* **2016**, *7*, 3123–3130.

(55) Zhen, G.; Muir, B. W.; Moffat, B. A.; Harbour, P.; Murray, K. S.; Moubaraki, B.; Suzuki, K.; Madsen, I.; Agron-Olshina, N.; Waddington, L.; *et al.* Comparative Study of the Magnetic Behavior of Spherical and Cubic Superparamagnetic Iron Oxide Nanoparticles. *J. Phys. Chem. C* **2011**, *115*, 327–334.

(56) Salazar-Alvarez, G.; Qin, J.; Šepelák, V.; Bergmann, I.; Vasilakaki, M.; Trohidou, K. N.; Ardisson, J. D.; Macedo, W. A. A.; Mikhaylova, M.; Muhammed, M.; *et al.* Cubic versus Spherical Magnetic Nanoparticles : The Role of Surface Anisotropy. *J. Am. Chem. Soc.* **2008**, *130*, 13234–13239.

(57) Ito, D.; Yokoyama, S.; Zaikova, T.; Masuko, K.; Hutchison, J. E. Synthesis of Ligand-Stabilized Metal Oxide Nanocrystals and Epitaxial Core/Shell Nanocrystals via a Lower-Temperature Esterification Process. *ACS Nano* **2014**, *8*, 64–75.

(58) Ilavsky, J.; Jemian, P. R. Irena : Tool Suite for Modeling and Analysis of Small-Angle Scattering. *J. Appl. Crystallogr.* **2009**, *42*, 347–353.

(59) Grau-Crespo, R.; Al-Baitai, A. Y.; Saadoune, I.; De Leeuw, N. H. Vacancy Ordering and Electronic Structure of γ-Fe_2O_3 (Maghemite): A Theoretical Investigation. *J. Phys. Condens. Matter* **2010**, *22*, 255401.

(60) Jørgensen, J.; Mosegaard, L.; Thomsen, L. E.; Jensen, T. R.; Hanson, J. C. Formation of γ-Fe_2O_3 Nanoparticles and Vacancy Ordering : An *In Situ* X-Ray Powder Diffraction Study. *J. Solid State Chem.* **2007**, *180*, 180–185.

(61) Shmakov, A. N.; Krvukova, G. N.; Tsvbulya, S. V; Chuvilin, A. L.; Solovyeva, L. P. Vacancy Ordering in γ-Fe_2O_3: Synchrotron X-Ray Powder Diffraction and High-Resolution Electron Microscopy Studies. *J. Appl. Crystallogr.* **1995**, *28*, 141–145.

(62) Perriat, P.; Domenichini, B.; Gillot, B. A Model for Oxidation in Finely Divided Ferrites Taking into Account the Stresses Generated During Reaction. *J. Phys. Chem. Solids* **1996**, *57*, 1641–1652.

(63) Guigue-Millot, N.; Champion, Y.; Hÿtch, M. J.; Bernard, F.; Bégin-Colin, S.; Perriat, P. Chemical Heterogeneities in Nanometric Titanomagnetites Prepared by Soft Chemistry and Studied *Ex Situ*: Evidence for Fe-Segregation and Oxidation Kinetics. *J. Phys. Chem. B* **2001**, *105*, 7125–7132.

(64) Kwon, S. G.; Hyeon, T. Formation Mechanisms of Uniform Nanocrystals via Hot-Injection and Heat-Up Methods. *Small* **2011**, *19*, 2685–2702.

(65) Chowdhury, S.; Yanful, E. Arsenic and Chromium Removal by Mixed Magnetite–Maghemite Nanoparticles and the Effect of Phosphate on Removal. *J. Environ. Manage.* **2010**, *91*, 2238–2247.

(66) Kumari, M.; Pittman, C. U.; Mohan, D. Heavy Metals [Chromium (VI) and Lead (II)] Removal from Water Using Mesoporous Magnetite (Fe_3O_4) Nanospheres. *J. Colloid Interface Sci.* **2015**, *442*, 120–132.

(67) Jordan, N.; Ritter, A.; Scheinost, A. C.; Weiss, S.; Schild, D.; Hübner, R. Selenium(IV) Uptake by Maghemite (γ-Fe_2O_3). *Environ. Sci. Technol.* **2014**, *48*, 1665–1674.

(68) Hammersley, A. P.; Svenson, S. O.; Hanfland, M.; D. Hauserman. Two-Dimensional Detector Software: From Real Detector to Idealised Image or Two-Theta Scan. *High Press. Res.* **1996**, *14*, 235–248.

(69) Juhás, P.; Farrow, C. L.; Yang, X.; Knox, K. R.; Billinge, S. J. L. Complex Modeling: A Strategy and Software Program for Combining Multiple Information Sources to Solve Ill Posed Structure and Nanostructure Inverse Problems. *Acta Crystallogr. Sect. A Found. Adv.* **2015**, *A71*, 562–568.

(70) Zobel, M.; Neder, R. B.; Kimber, S. A. J. Universal Solvent Restructuring Induced by Colloidal Nanoparticles. *Science* **2015**, *347*, 201–204.

71) Schindelin, J.; Arganda-Carreras, I.; Frise, E.; Kaynig, V.; Longair, M.; Pietzsch, T.; Preibisch, S.; Rueden, C.; Saalfeld, S.; Schmid, B.; *et al.* Fiji: An Open-Source Platform for Biological-Image Analysis. *Nat. Methods* **2012**, *9*, 676–682.

Chapter IV

(1) Roduner, E. Size Matters : Why Nanomaterials Are Different. *Chem. Soc. Rev.* **2006**, *35*, 583–592.

(2) Auffan, M.; Rose, J. J.; Bottero, J. Y.; Lowry, G. V.; Jolivet, J. P.; Wiesner, M. R. Towards a Definition of Inorganic Nanoparticles from an Environmental, Health and Safety Perspective. *Nat. Nanotechnol.* **2009**, *4*, 634–641.

(3) Grassian, V. H. When Size Really Matters: Size-Dependent Properties and Surface Chemistry of Metal and Metal Oxide Nanoparticles in Gas and Liquid Phase Environments. *J. Phys. Chem. C* **2008**, *112*, 18303–18313.

(4) Auffan, M.; Rose, J.; Proux, O.; Borschneck, D.; Masion, A.; Chaurand, P.; Hazemann, J.-L.; Chaneac, C.; Jolivet, J.-P.; Wiesner, M. R.; *et al.* Enhanced Adsorption of Arsenic onto Maghemites Nanoparticles : As (III) as a Probe of the Surface Structure and Heterogeneity. *Langmuir* **2008**, *24*, 3215–3222.

(5) Yavuz, C. T.; Mayo, J. T.; Yu, W. W.; Prakash, A.; Falkner, J. C.; Yean, S.; Cong, L.; Shipley, H. J.; Kan, A.; Tomson, M.; *et al.* Low-Field Magnetic Separation of Monodisperse Fe3O4 Nanocrystals. *Science* **2006**, *314*, 964–967.

(6) Niederberger, M. Nonaqueous Sol – Gel Routes to Metal Oxide Nanoparticles. *Acc. Chem. Res.* **2007**, *40*, 793–800.

(7) Wang, F.; Richards, V. N.; Shields, S. P.; Buhro, W. E. Kinetics and Mechanisms of Aggregative Nanocrystal Growth. *Chem. Mater.* **2014**, *26*, 5–21.

(8) Cooper, S. R.; Plummer, L. K.; Cosby, A. G.; Lenox, P.; Jander, A.; Dhagat, P.; Hutchison, J. E. Insights into the Magnetic Properties of Sub-10 nm Iron Oxide Nanocrystals through the Use of a Continuous Growth Synthesis. *Chem. Mater.* **2018**, *30*, 6053–6062.

(9) Frison, R.; Cernuto, G.; Cervellino, A.; Zaharko, O.; Colonna, G. M.; Guagliardi, A.; Masciocchi, N. Magnetite−Maghemite Nanoparticles in the 5 − 15 nm Range : Correlating the Core−Shell Composition and the Surface Structure to the Magnetic Properties. A Total Scattering Study. *Chem. Mater.* **2013**, *25*, 4820–4827.

(10) Demortière, A.; Panissod, P.; Pichon, B. P.; Pourroy, G.; Guillon, D.; Donnio, B.; Bégin-Colin, S. Size-Dependent Properties of Magnetic Iron Oxide Nanocrystals. *Nanoscale* **2011**, *3*, 225–232.

(11) Unni, M.; Uhl, A. M.; Savliwala, S.; Savitzky, B. H.; Dhavalikar, R.; Garraud, N.; Arnold, D. P.; Kourkoutis, L. F.; Andrew, J. S.; Rinaldi, C. Thermal Decomposition Synthesis of Iron Oxide Nanoparticles with Diminished Magnetic Dead Layer by Controlled Addition of Oxygen. *ACS Nano* **2017**, *11*, 2284–2303.

(12) Chen, R.; Christiansen, M. G.; Sourakov, A.; Mohr, A.; Matsumoto, Y.; Okada, S.; Jasanoff, A.; Anikeeva, P. High-Performance Ferrite Nanoparticles through Nonaqueous Redox Phase Tuning. *Nano Lett.* **2016**, *16*, 1345–1351.

(13) Pacakova, B.; Kubickova, S.; Salas, G.; Mantlikova, A. R.; Marciello, M.; Morales, M. P.; Niznansky, D.; Vejpravova, J. The Internal Structure of Magnetic Nanoparticles Determines the Magnetic Response. *Nanoscale* **2017**, *9*, 5129–5140.

(14) Levy, M.; Quarta, A.; Espinosa, A.; Figuerola, A.; Wilhelm, C.; García-hern, M.; Genovese, A.; Falqui, A.; Alloyeau, D.; Cozzoli, P. D.; *et al.* Correlating Magneto-Structural Properties to Hyperthermia Performance of Highly Monodisperse Iron Oxide Nanoparticles Prepared by a Seeded-Growth Route. *Chem. Mater.* **2011**, *23*, 4170–4180.

(15) Park, J.; An, K.; Hwang, Y.; Park, J.-G.; Noh, H.-J.; Kim, J.-Y.; Park, J.-H.; Hwang, N.-M.; Hyeon, T. Ultra-Large-Scale Syntheses of Monodisperse Nanocrystals. *Nat. Mater.* **2004**, *3*, 891–895.

(16) Baaziz, W.; Pichon, B. P.; Fleutot, S.; Liu, Y.; Lefevre, C.; Greneche, J.-M.; Toumi, M.; Mhiri, T.; Begin-Colin, S. Magnetic Iron Oxide Nanoparticles: Reproducible Tuning of the Size and Nanosized-Dependent Composition, Defects, and Spin Canting. *J. Phys. Chem. C* **2014**, *118*, 3795–3810.

(17) Mohapatra, J.; Mitra, A.; Bahadur, D.; Aslam, M. Surface Controlled Synthesis of MFe_2O_4 (M = Mn, Fe, Co, Ni and Zn) Nanoparticles and Their Magnetic Characteristics. *CrystEngComm* **2013**, *15*, 524.

(18) Park, B.; Kim, B. H.; Yu, T. Synthesis of Spherical and Cubic Magnetic Iron Oxide Nanocrystals at Low Temperature in Air. *J. Colloid Interface Sci.* **2018**, *518*, 27–33.

(19) Caruntu, D.; Caruntu, G.; O'Connor, C. J. Magnetic Properties of Variable-Sized Fe_3O_4 Nanoparticles Synthesized from Non-Aqueous Homogeneous Solutions of Polyols. *J. Phys. D. Appl. Phys.* **2007**, *40*, 5801–5809.

(20) Yun, H.; Liu, X.; Paik, T.; Palanisamy, D.; Kim, J.; Vogel, W. D.; Viescas, A. J.; Chen, J.; Papaefthymiou, G. C.; Kikkawa, J. M.; *et al.* Size- and Composition-Dependent Radio Frequency Magnetic Permeability of Iron Oxide Nanocrystals. *ACS Nano* **2014**, *8*, 12323–12337.

(21) Taniguchi, T.; Nakagawa, K.; Watanabe, T.; Matsushita, N.; Yoshimura, M. Hydrothermal Growth of Fatty Acid Stabilized Iron Oxide Nanocrystals. *J. Phys. Chem. C* **2009**, *113*, 839–843.

(22) Yu, W. W.; Falkner, J. C.; Yavuz, C. T.; Colvin, V. L. Synthesis of Monodisperse Iron Oxide Nanocrystals by Thermal Decomposition of Iron Carboxylate Salts. *Chem. Commun.* **2004**, 2306–2307.

(23) Sharifi Dehsari, H.; Heidari, M.; Halda Ribeiro, A.; Tremel, W.; Jakob, G.; Donadio, D.; Potestio, R.; Asadi, K. Combined Experimental and Theoretical Investigation of Heating Rate on Growth of Iron Oxide Nanoparticles. *Chem. Mater.* **2017**, *29*, 9648–9656.

(24) Vreeland, E. C.; Watt, J.; Schober, G. B.; Hance, B. G.; Austin, M. J.; Price, A. D.; Fellows, B. D.; Monson, T. C.; Hudak, N. S.; Maldonado-Camargo, L.; *et al.* Enhanced Nanoparticle Size Control by Extending LaMer's Mechanism. *Chem. Mater.* **2015**, *27*, 6059–6066.

(25) Jansons, A. W.; Hutchison, J. E. Continuous Growth of Metal Oxide Nanocrystals: Enhanced Control of Nanocrystal Size and Radial Dopant Distribution. *ACS Nano* **2016**, *10*, 6942–6951.

(26) Han, W.; Yi, L.; Zhao, N.; Tang, A.; Gao, M.; Tang, Z. Synthesis and Shape-Tailoring of Copper Sulfide/Indium Sulfide-Based Nanocrystals. *J. Am. Chem. Soc.* **2008**, *130*, 13152–13161.

(27) Choi, B. S.; An, K.; Kim, E.; Yu, J. H.; Kim, H.; Hyeon, T. Simple and Generalized Synthesis of Semiconducting Metal Sulfide Nanocrystals. *Adv. Funct. Mater.* **2009**, *19*, 1645–1649.

(28) Luther, J. M.; Jain, P. K.; Ewers, T.; Alivisatos, A. P. Localized Surface Plasmon Resonances Arising from Free Carriers in Doped Quantum Dots. *Nat. Mater.* **2011**, *10*, 361–366.

(29) Ho, C.; Tsai, C.; Chung, C.; Tsai, C.; Chen, F.; Lin, H.; Lai, C. Shape-Controlled Growth and Shape-Dependent Cation Site Occupancy of Monodisperse Fe_3O_4 Nanoparticles. *Chem. Mater.* **2011**, *23*, 1753–1760.

(30) Soon, G. K.; Piao, Y.; Park, J.; Angappane, S.; Jo, Y.; Hwang, N.-M.; Park, J.-G.; Hyeon, T.; Kwon, S. G.; Piao, Y.; *et al.* Kinetics of Monodisperse Iron Oxide Nanocrystal Formation by "Heating-up" Process. *J. Am. Chem. Soc.* **2007**, *129*, 12571–12584.

(31) Li, S.; Wang, H.; Xu, W.; Si, H.; Tao, X.; Lou, S.; Du, Z.; Li, L. S. Synthesis and Assembly of Monodisperse Spherical Cu_2S Nanocrystals. *J. Colloid Interface Sci.* **2009**, *330*, 483–487.

(32) Liu, X.; Wang, X.; Zhou, B.; Law, W.; Cartwright, A. N.; Swihart, M. T. Size-Controlled Synthesis of $Cu_{2-x}E$ (E = S , Se) Nanocrystals with Strong Tunable Near-Infrared Localized Surface Plasmon Resonance and High Conductivity in Thin Films. *Adv. Funct. Mater.* **2013**, *23*, 1256–1264.

(33) Zhou, Z.; Zhu, X.; Wu, D.; Chen, Q.; Huang, D.; Sun, C.; Xin, J.; Ni, K.; Gao, J. Anisotropic Shaped Iron Oxide Nanostructures: Controlled Synthesis and Proton Relaxation Shortening Effects. *Chem. Mater.* **2015**, *27*, 3505–3515.

(34) De Montferrand, C.; Hu, L.; Milosevic, I.; Russier, V.; Bonnin, D.; Motte, L.; Brioude, A.; Lalatonne, Y. Iron Oxide Nanoparticles with Sizes, Shapes and Compositions Resulting in Different Magnetization Signatures as Potential Labels for Multiparametric Detection. *Acta Biomater.* **2013**, *9*, 6150–6157.

(35) Redl, F. X.; Black, C. T.; Papaefthymiou, G. C.; Sandstrom, R. L.; Yin, M.; Zeng, H.; Murray, C. B.; Brien, S. P. O. Magnetic, Electronic, and Structural Characterization of Nonstoichiometric Iron Oxides at the Nanoscale. *J. Am. Chem. Soc.* **2004**, *126*, 14583–14599.

(36) Bøjesen, E. D.; Iversen, B. B. The Chemistry of Nucleation. *CrystEngComm* **2016**, *18*, 8332–8353.

(37) Friedfeld, M. R.; Stein, J. L.; Cossairt, B. M. Main-Group-Semiconductor Cluster Molecules as Synthetic Intermediates to Nanostructures. *Inorg. Chem.* **2017**, *56*, 8689–8697.

(38) Harrell, S. M.; Mcbride, J. R.; Rosenthal, S. J. Synthesis of Ultrasmall and Magic-Sized CdSe Nanocrystals. *Chem. Mater.* **2013**, *25*, 1199–1210.

(39) Hendricks, M. P.; Campos, M. P.; Cleveland, G. T.; Plante, I. J. L; Owen, J. S. A Tunable Library of Substituted Thiourea Precursors to Metal Sulfide Nanocrystals. *Science* **2015**, *348*, 1226–1230.

(40) Scheck, J.; Wu, B.; Drechsler, M.; Rosenberg, R.; Van Driessche, A. E. S.; Stawski, T. M.; Gebauer, D. The Molecular Mechanism of Iron (III) Oxide Nucleation. *J. Phys. Chem. Lett.* **2016**, *7*, 3123–3130.

(41) Zhen, G.; Muir, B. W.; Moffat, B. A.; Harbour, P.; Murray, K. S.; Moubaraki, B.; Suzuki, K.; Madsen, I.; Agron-Olshina, N.; Waddington, L.; *et al.* Comparative Study of the Magnetic Behavior of Spherical and Cubic Superparamagnetic Iron Oxide Nanoparticles. *J. Phys. Chem. C* **2011**, *115*, 327–334.

(42) Salazar-Alvarez, G.; Qin, J.; Šepelák, V.; Bergmann, I.; Vasilakaki, M.; Trohidou, K. N.; Ardisson, J. D.; Macedo, W. A. A.; Mikhaylova, M.; Muhammed, M.; *et al.* Cubic versus Spherical Magnetic Nanoparticles : The Role of Surface Anisotropy *J. Am. Chem. Soc.* **2008**, *130*, 13234–13239.

(43) Castellanos-Rubio, I.; Insausti, M.; Garaio, E.; Gil De Muro, I.; Plazaola, F.; Rojo, T. T.; Lezama, L. Fe_3O_4 Nanoparticles Prepared by the Seeded-Growth Route for Hyperthermia: Electron Magnetic Resonance as a Key Tool to Evaluate Size Distribution in Magnetic Nanoparticles. *Nanoscale* **2014**, *6*, 7542–7552.

(44) Mitra, A.; Mohapatra, J.; Meena, S. S.; Tomy, C. V.; Aslam, M. Verwey Transition in Ultrasmall-Sized Octahedral Fe_3O_4 Nanoparticles. *J. Phys. Chem. C* **2014**, *118*, 19356–19362.

(45) Guardia, P.; Pérez, N.; Labarta, A.; Batlle, X. Controlled Synthesis of Iron Oxide Nanoparticles over a Wide Size Range. *Langmuir* **2010**, *26*, 5843–5847.

(46) Kim, B. H.; Lee, N.; Kim, H.; An, K.; Park, Y. I.; Choi, Y.; Shin, K.; Lee, Y.; Kwon, S. G.; Na, H. B.; *et al.* Large-Scale Synthesis of Uniform and Extremely Small-Sized Iron Oxide Nanoparticles for High-Resolution T1 Magnetic Resonance Imaging Contrast Agents. *J. Am. Chem. Soc.* **2011**, *133*, 12624–12631.

(47) Garnaud, G.; Rapp, R. A. Thickness of the Oxide Layers Formed during the Oxidation of Iron. *Oxid. Met.* **1977**, *11*, 193–198.

(48) Signorini, L.; Pasquini, L.; Savini, L.; Carboni, R.; Boscherini, F.; Bonetti, E.; Giglia, A.; Pedio, M.; Mahne, N.; Nannarone, S. Size-Dependent Oxidation in Iron/Iron Oxide Core-Shell Nanoparticles. *Phys. Rev. B* **2003**, *68*, 195423.

(49) Sidhu, P. S.; Gilkes, R. J.; Posner, A. M. Mechanism of the Low Temperature Oxidation of Synthetic Magnetites. *J. Inorg. Nucl. Chem.* **1977**, *39*, 1953–1958.

(50) Navrotsky, A.; Ma, C.; Lilova, K.; Birkner, N. Nanophase Transition Metal Oxides Show Large Thermodynamically Driven Shifts in Oxidation-Reduction Equilibria. *Science* **2010**, *330*, 199–201.

(51) Hai, H. T.; Kura, H.; Takahashi, M.; Ogawa, T. Facile Synthesis of Fe_3O_4 Nanoparticles by Reduction Phase Transformation from γ-Fe_2O_3 Nanoparticles in Organic Solvent. *J. Colloid Interface Sci.* **2010**, *341*, 194–199.

(52) Huber, D. L. Synthesis, Properties, and Applications of Iron Nanoparticles. *Small* **2005**, *1*, 482–501.

(53) Navrotsky, A.; Mazeina, L.; Majzlan, J. Size-Driven Structural and Thermodynamic Complexity in Iron Oxides. *Science* **2007**, *319*, 1635–1638.

(54) Roth, W. L. Defects in the Crystal and Magnetic Structures of Ferrous Oxide. *Acta Crystallogr.* **1960**, *13*, 140–149.

(55) van Rijssel, J.; Kuipers, B. W. M.; Erné, B. H. Bimodal Distribution of the Magnetic Dipole Moment in Nanoparticles with a Monomodal Distribution of the Physical Size. *J. Magn. Magn. Mater.* **2015**, *380*, 325–329.

(56) Estrader, M.; López-Ortega, A.; Golosovsky, I. V.; Estradé, S.; Roca, A. G.; Salazar-Alvarez, G.; López-Conesa, L.; Tobia, D.; Winkler, E.; Ardisson, J. D.; *et al.* Origin of the Large Dispersion of Magnetic Properties in Nanostructured Oxides: Fe_xO/Fe_3O_4 Nanoparticles as a Case Study. *Nanoscale* **2015**, *7*, 3002–3015.

(57) Khurshid, H.; Li, W.; Chandra, S.; Phan, M.-H. H.; Hadjipanayis, G. C.; Mukherjee, P.; Srikanth, H. Mechanism and Controlled Growth of Shape and Size Variant Core/Shell FeO/Fe_3O_4 Nanoparticles. *Nanoscale* **2013**, *5*, 7942–7952.

(58) Sharma, S. K.; Vargas, J. M.; Pirota, K. R.; Kumar, S.; Lee, C. G.; Knobel, M. Synthesis and Ageing Effect in FeO Nanoparticles: Transformation to Core-Shell FeO/Fe_3O_4 and Their Magnetic Characterization. *J. Alloys Compd.* **2011**, *509*, 6414–6417.

(59) Chen, C.-J.; Lai, H.-Y.; Lin, C.-C.; Wang, J.-S.; Chiang, R.-K. Preparation of Monodisperse Iron Oxide Nanoparticles via the Synthesis and Decomposition of Iron Fatty Acid Complexes. *Nanoscale Res. Lett.* **2009**, *4*, 1343–1350.

(60) Pichon, B. P.; Gerber, O.; Lefevre, C.; Florea, I.; Fleutot, S.; Baaziz, W.; Pauly, M.; Ohlmann, M.; Ulhaq, C.; Ersen, O.; *et al.* Microstructural and Magnetic Investigations of Wüstite-Spinel Core-Shell Cubic-Shaped Nanoparticles. *Chem. Mater.* **2011**, *23*, 2886–2900.

(61) Chen, C.-J.; Chiang, R.-K.; Lai, H.-Y.; Lin, C.-R. Characterization of Monodisperse Wüstite Nanoparticles Following Partial Oxidation. *J. Phys. Chem. C* **2010**, *114*, 4258–4263.

(62) Cornell, R. M. M.; Schwertmann, U. *The Iron Oxides*; Wiley-VCH GmbH & Co. KGaA, 2003.

(63) Anderson, A. B.; Grimes, W.; Heuer, A. Defect Clusters in Wüstite, $Fe_{1-x}O$. *J. Solid State Chem.* **1984**, *55*, 353–361.

(64) Radler, M. J.; Cohen, J. B.; Faber, J. Point Defect Clusters in Wüstite. *J. Phys. Chem. Solids* **1990**, *51*, 217–228.

(65) Koch, F.; Cohen, J. B. The Defect Structure of $Fe_{1-x}O$. *Acta Crystallogr. Sect. B* **1969**, *25*, 275–287.

(66) Greaves, C. A Powder Neutron Diffraction Investigation of Vacancy Ordering and Covalence in γ-Fe_2O_3. *J. Solid State Chem.* **1983**, *49*, 325–333.

(67) Fleet, M. E. The Structure of Magnetite. *Acta Crystallogr.* **1981**, *2549*, 917–920.

(68) Lassenberger, A.; Grünewald, T. A.; van Oostrum, P. D. J.; Rennhofer, H.; Amenitsch, H.; Zirbs, R.; Lichtenegger, H. C.; Reimhult, E. Monodisperse Iron Oxide Nanoparticles by Thermal Decomposition: Elucidating Particle Formation by Second-Resolved *in Situ* Small-Angle X-Ray Scattering. *Chem. Mater.* **2017**, *29*, 4511–4522.

(69) Andersen, H. L.; Jensen, K. M. Ø.; Tyrsted, C.; Bøjesen, E. D.; Christensen, M. Size and Size Distribution Control of γ-Fe_2O_3 Nanocrystallites: An in Situ Study. *Cryst. Growth Des.* **2014**, *14*, 1307–1313.

(70) Ingham, B. X-Ray Scattering Characterisation of Nanoparticles. *Crystallogr. Rev.* **2015**, *21*, 229–303.

(71) Billinge, S. J. L. Nanoscale Structural Order from the Atomic Pair Distribution Function (PDF): There's Plenty of Room in the Middle. *J. Solid State Chem.* **2008**, *181*, 1695–1700.

(72) Billinge, S. J. L.; Levin, I. The Problem with Determining Atomic Structure at the Nanoscale. *Science* **2007**, *316*, 561–565.

(73) Jensen, K. M. Ø.; Juhas, P.; Tofanelli, M. A.; Heinecke, C. L.; Vaughan, G.; Ackerson, C. J.; Billinge, S. J. L. Polymorphism in Magic-Sized $Au_{144}(SR)_{60}$ Clusters. *Nat. Commun.* **2016**, *7*, 11859.

(74) Jensen, K. M. Ø.; Andersen, H. L. H.; Tyrsted, C.; Bøjesen, E. D.; Dippel, A.-C.; Lock, N.; Billinge, S. J. L.; Iversen, B. B.; Christensen, M. Mechanisms for Iron Oxide Formation under Hydrothermal Conditions: An *In Situ* Total Scattering Study. *ACS Nano* **2014**, *8*, 10704–10714.

(75) Jensen, K. M. Ø.; Christensen, M.; Juhas, P.; Bøjesen, E. D.; Lock, N.; Billinge, S. J. L.; Iversen, B. B. Revealing the Mechanisms behind SnO_2 Nanoparticle Formation and Growth during Hydrothermal Synthesis: An *In Situ* Total Scattering Study. *J. Am. Chem. Soc.* **2012**, *134*, 6785–6792.

(76) Saha, D.; Jensen, K. M. Ø.; Tyrsted, C.; Bøjesen, E. D.; Mamakhel, A. H.; Dippel, A.-C.; Christensen, M.; Iversen, B. B. *In Situ* Total X-Ray Scattering Study of WO_3 Nanoparticle Formation under Hydrothermal Conditions. *Angew. Chemie* **2014**, *126*, 3741–3744.

(77) Tyrsted, C.; Lock, N.; Jensen, K. M. Ø.; Christensen, M.; Bøjesen, E. D.; Emerich, H.; Vaughan, G.; Billinge, S. J. L.; Iversen, B. B. Evolution of Atomic Structure During Nanoparticle Formation. *IUCrJ* **2014**, *1*, 165–171.

(78) Roca, A. G.; Niznansky, D.; Poltierova-Vejpravova, J.; Bittova, B.; González-Fernández, M. A.; Serna, C. J.; Morales, M. P. Magnetite Nanoparticles with No Surface Spin Canting. *J. Appl. Phys.* **2009**, *105*, 114309.

(79) Ito, D.; Yokoyama, S.; Zaikova, T.; Masuko, K.; Hutchison, J. E. Synthesis of Ligand-Stabilized Metal Oxide Nanocrystals and Epitaxial Core/Shell Nanocrystals via a Lower- Temperature Esterification Process. *ACS Nano* **2014**, *8*, 64–75.

(80) Juhás, P.; Farrow, C. L.; Yang, X.; Knox, K. R.; Billinge, S. J. L. Complex Modeling: A Strategy and Software Program for Combining Multiple Information Sources to Solve Ill Posed Structure and Nanostructure Inverse Problems. *Acta Crystallogr. Sect. A Found. Adv.* **2015**, *A71*, 562–568.

(81) Yamamoto, A. Modulated Structure of Wüstite ($Fe_{1-x}O$) (Three-Dimensional Modulation). *Acta Crystallogr. Sect. B Struct. Crystallogr. Cryst. Chem.* **1982**, *38*, 1451–1456.

(82) Weber, B.; Betz, R.; Bauer, W.; Schlamp, S. Crystal Structure of Iron (II) Acetate. *J. Inorg. Gen. Chem.* **2011**, *637*, 102–107.

(83) Wilson, C.; Iversen, B. B.; Overgaard, J.; Larsen, F. K.; Wu, G.; Palii, S. P.; Timco, G. A.; Gerbeleu, N. V. Multi-Temperature Crystallographic Studies of Mixed-Valence Polynuclear Complexes ; Valence Trapping Process in the Trinuclear Oxo-Bridged Iron Compound, $[Fe_3O(O_2CC(CH_3)_3)_6(C_5H_5N)_3]$. *J. Am. Chem. Soc.* 2000, *122*, 11370–11379.

(84) Zheng, Y.; Tong, M.; Xue, W.; Zhang, W.; Chen, X.; Grandjean, F.; Long, G. J. A " Star " Antiferromagnet : A Polymeric Iron (III) Acetate That Exhibits Both Spin Frustration and Long-Range Magnetic Ordering. *Angew. Chemie Int. Ed.* **2007**, *46*, 6076–6080.

(85) Mandal, S. K.; Young, V. G.; Que, L. Polynuclear Carboxylato-Bridged Iron (II) Clusters : Synthesis, Structure, and Host-Guest Chemistry. *Inorg. Chem.* **2000**, *39*, 1831–1833.

(86) Yao, H.; Wang, J.; Ma, Y.; Waldmann, O.; Du, W.; Song, Y. An Iron (III) Phosphonate Cluster Containing a Nonanuclear Ring *Chem Commun.* **2006**, *1*, 1745–1747.

(87) Gorun, S. M.; Lippard, S. J. Synthesis, Structure, and Characterization of the Tetranuclear Iron(III)Oxo Complex $[Fe_4O_2(BICOH)_2(BICO)_2(O_2CPh)_4]Cl_2$. *Inorg. Chem.* 1988, *27*, 149–156.

(88) Gorun, S. M.; Lippard, S. J. A New Synthetic Approach to the Ferritin Core Uncovers the Soluble Iron (III) Oxo-Hydroxo Aggregate $[Fe_{11}O_6(OH)_6(O_2CPh)_{15}]$. *Nature* **1986**, *319*, 666–668.

(89) Sadeghi, O.; Zakharov, L. N.; Nyman, M. Aqueous Formation and Manipulation of the Iron-Oxo Keggin Ion. *Science* **2015**, *347*, 1359–1362.

(90) Low, D. M.; Jones, L. F.; Bell, A.; Brechin, E. K.; Mallah, T.; Rivière, E.; Teat, S. J.; Mcinnes, E. J. L. Solvothermal Synthesis of a Tetradecametallic FeIII Cluster. *Angew. Chemie* **2003**, *115*, 3911–3914.

(91) Hammersley, A. P.; Svenson, S. O.; Hanfland, M.; D. Hauserman. Two-Dimensional Detector Software: From Real Detector to Idealised Image or Two-Theta Scan. *High Press. Res.* **1996**, *14*, 235–248.

(92) Ilavsky, J.; Jemian, P. R. Irena : Tool Suite for Modeling and Analysis of Small-Angle Scattering. *J. Appl. Crystallogr.* **2009**, *42*, 347–353.

(93) Schindelin, J.; Arganda-Carreras, I.; Frise, E.; Kaynig, V.; Longair, M.; Pietzsch, T.; Preibisch, S.; Rueden, C.; Saalfeld, S.; Schmid, B.; *et al.* Fiji: An Open-Source Platform for Biological-Image Analysis. *Nat. Methods* **2012**, *9*, 676–682.

(94) Rodríguez-Carvajal, J. Recent Advances in Magnetic Structure Determination by Neutron Powder Diffraction. *Phys. B Condens. Matter* **1993**, *192*, 55–69.

Chapter V

(1) Chen, X.; Li, C.; Grätzel, M.; Kostecki, R.; Mao, S. S. Nanomaterials for Renewable Energy Production and Storage. *Chem. Soc. Rev.* **2012**, *41*, 7909–7937.

(2) Shannon, M. A; Bohn, P. W.; Elimelech, M.; Georgiadis, J. G.; Mariñas, B. J.; Mayes, A. M. Science and Technology for Water Purification in the Coming Decades. *Nature* **2008**, *452*, 301–310.

(3) Shi, J.; Kantoff, P. W.; Wooster, R.; Farokhzad, O. C. Cancer Nanomedicine: Progress, Challenges and Opportunities. *Nat. Rev. Cancer* **2016**, *17*, 20–37.

(4) Cooper, S. R.; Plummer, L. K.; Cosby, A. G.; Lenox, P.; Jander, A.; Dhagat, P.; Hutchison, J. E. Insights into the Magnetic Properties of Sub-10 nm Iron Oxide Nanocrystals Through the Use of a Continuous Growth Synthesis. *Chem. Mater.* **2018**, *30*, 6053–6062.

(5) Wang, F.; Richards, V. N.; Shields, S. P.; Buhro, W. E. Kinetics and Mechanisms of Aggregative Nanocrystal Growth. *Chem. Mater.* **2014**, *26*, 5–21.

(6) Auffan, M.; Rose, J. J.; Bottero, J. Y.; Lowry, G. V.; Jolivet, J. P.; Wiesner, M. R. Towards a Definition of Inorganic Nanoparticles from an Environmental, Health and Safety Perspective. *Nat. Nanotechnol.* **2009**, *4*, 634–641.

(7) Grassian, V. H. When Size Really Matters: Size-Dependent Properties and Surface Chemistry of Metal and Metal Oxide Nanoparticles in Gas and Liquid Phase Environments. *J. Phys. Chem. C* **2008**, *112*, 18303–18313.

(8) Roduner, E. Size Matters : Why Nanomaterials Are Different. *Chem. Soc. Rev.* **2006**, *35*, 583–592.

(9) Billinge, S. J. L.; Levin, I. The Problem with Determining Atomic Structure at the Nanoscale. *Science* **2007**, *316*, 561–565.

(10) Ito, D.; Yokoyama, S.; Zaikova, T.; Masuko, K.; Hutchison, J. E. Synthesis of Ligand-Stabilized Metal Oxide Nanocrystals and Epitaxial Core/Shell Nanocrystals via a Lower-Temperature Esterification Process. *ACS Nano* **2014**, *8*, 64–75.

(11) Buck, M. R.; Biacchi, A. J.; Schaak, R. E. Insights into the Thermal Decomposition of Co (II) Oleate for the Shape-Controlled Synthesis of Wurtzite-Type CoO Nanocrystals. *Chem. Mater.* **2014**, *26*, 1492–1499.

(12) Unni, M.; Uhl, A. M.; Savliwala, S.; Savitzky, B. H.; Dhavalikar, R.; Garraud, N.; Arnold, D. P.; Kourkoutis, L. F.; Andrew, J. S.; Rinaldi, C. Thermal Decomposition Synthesis of Iron Oxide Nanoparticles with Diminished Magnetic Dead Layer by Controlled Addition of Oxygen. *ACS Nano* **2017**, *11*, 2284–2303.

(13) Millan, A.; Urtizberea, A.; Silva, N. J. O.; Palacio, F.; Amaral, V. S.; Snoeck, E.; Serin, V. Surface Effects in Maghemite Nanoparticles. *J. Magn. Magn. Mater.* **2007**, *312*, L5–L9.

(14) Dutta, P.; Pal, S.; Seehra, M. S.; Shah, N.; Huffman, G. P. Size Dependence of Magnetic Parameters and Surface Disorder in Magnetite Nanoparticles. *J. Appl. Phys.* **2009**, *105*, 10–13.

(15) Frison, R.; Cernuto, G.; Cervellino, A.; Zaharko, O.; Colonna, G. M.; Guagliardi, A.; Masciocchi, N. Magnetite−Maghemite Nanoparticles in the 5−15 nm Range : Correlating the Core−Shell Composition and the Surface Structure to the Magnetic Properties. A Total Scattering Study. *Chem. Mater.* **2013**, *25*, 4820–4827.

(16) Chen, R.; Christiansen, M. G.; Sourakov, A.; Mohr, A.; Matsumoto, Y.; Okada, S.; Jasanoff, A.; Anikeeva, P. High-Performance Ferrite Nanoparticles Through Nonaqueous Redox Phase Tuning. *Nano Lett.* **2016**, *16*, 1345–1351.

(17) Pacakova, B.; Kubickova, S.; Salas, G.; Mantlikova, A. R.; Marciello, M.; Morales, M. P.; Niznansky, D.; Vejpravova, J. The Internal Structure of Magnetic Nanoparticles Determines the Magnetic Response. *Nanoscale* **2017**, *9*, 5129–5140.

(18) Levy, M.; Quarta, A.; Espinosa, A.; Figuerola, A.; Wilhelm, C.; García-hern, M.; Genovese, A.; Falqui, A.; Alloyeau, D.; Cozzoli, P. D.; *et al.* Correlating Magneto-Structural Properties to Hyperthermia Performance of Highly Monodisperse Iron Oxide Nanoparticles Prepared by a Seeded-Growth Route. *Chem. Mater.* **2011**, *23*, 4170–4180.

(19) Mohapatra, J.; Mitra, A.; Bahadur, D.; Aslam, M. Surface Controlled Synthesis of MFe_2O_4 (M = Mn, Fe, Co, Ni and Zn) Nanoparticles and Their Magnetic Characteristics. *CrystEngComm* **2013**, *15*, 524.

(20) Roca, A. G.; Niznansky, D.; Poltierova-Vejpravova, J.; Bittova, B.; González-Fernández, M. A.; Serna, C. J.; Morales, M. P. Magnetite Nanoparticles with No Surface Spin Canting. *J. Appl. Phys.* **2009**, *105*, 114309.

(21) Salazar-Alvarez, G.; Qin, J.; Šepelák, V.; Bergmann, I.; Vasilakaki, M.; Trohidou, K. N.; Ardisson, J. D.; Macedo, W. A. A.; Mikhaylova, M.; Muhammed, M.; *et al.* Cubic versus Spherical Magnetic Nanoparticles : The Role of Surface Anisotropy. *J. Am. Chem. Soc.* **2008**, *130*, 13234–13239.

(22) Kolhatkar, A. G.; Jamison, A. C.; Litvinov, D.; Willson, R. C.; Lee, T. R. Tuning the Magnetic Properties of Nanoparticles. *Int. J. Mol. Sci.* **2013**, *14*, 15977–16009.

(23) Jansons, A. W.; Hutchison, J. E. Continuous Growth of Metal Oxide Nanocrystals: Enhanced Control of Nanocrystal Size and Radial Dopant Distribution. *ACS Nano* **2016**, *10*, 6942–6951.

(24) Jansons, A. W.; Plummer, L. K.; Hutchison, J. E. Living Nanocrystals. *Chem. Mater.* **2017**, *29*, 5415–5425.

(25) Crockett, B. M.; Jansons, A. W.; Koskela, K. M.; Johnson, D. W.; Hutchison, J. E. Radial Dopant Placement for Tuning Plasmonic Properties in Metal Oxide Nanocrystals. *ACS Nano* **2017**, *11*, 7719–7728.

(26) Polman, A.; Knight, M.; Garnett, E. C.; Ehrler, B.; Sinke, W. C. Photovoltaic Materials: Present Efficiencies and Future Challenges. *Science* **2016**, *352*, aad4424.

(27) Wallace, S. K.; Mitzi, D. B.; Walsh, A. The Steady Rise of Kesterite Solar Cells. *ACS Energy Lett.* **2017**, *2*, 776–779.

(28) Coughlan, C.; Ibáñez, M.; Dobrozhan, O.; Singh, A.; Cabot, A.; Ryan, K. M. Compound Copper Chalcogenide Nanocrystals. *Chem. Rev.* **2017**, *117*, 5865–6109.

(29) Fenton, J. L.; Steimle, B. C.; Schaak, R. E. Tunable Intraparticle Frameworks for Creating Complex Heterostructured Nanoparticle Libraries. *Science* **2018**, *360*, 513–517.

Appendix A

(1) Thanh, N. T. K.; Maclean, N.; Mahiddine, S. Mechanisms of Nucleation and Growth of Nanoparticles in Solution. *Chem. Rev.* **2014**, *114*, 7610–7630.

(2) Rodríguez-Carvajal, J. Recent Advances in Magnetic Structure Determination by Neutron Powder Diffraction. *Phys. B Condens. Matter* **1993**, *192*, 55–69.

(3) Fleet, M. E. The Structure of Magnetite. *Int. Union Crystallogr.* **1981**, *2549*, 917–920.

(4) Andersen, H. L.; Jensen, K. M. Ø.; Tyrsted, C.; Bøjesen, E. D.; Christensen, M. Size and Size Distribution Control of γ-Fe_2O_3 Nanocrystallites: An *in Situ* Study. *Cryst. Growth Des.* **2014**, *14*, 1307–1313.

(5) Castellanos-Rubio, I.; Insausti, M.; Garaio, E.; Gil de Muro, I.; Plazaola, F.; Rojo, T.; Lezama, L. Fe_3O_4 Nanoparticles Prepared by the Seeded-Growth Route for Hyperthermia: Electron Magnetic Resonance as a Key Tool to Evaluate Size Distribution in Magnetic Nanoparticles. *Nanoscale* **2014**, *6*, 7542-7552.

(6) Guardia, P.; Pérez, N.; Labarta, A.; Batlle, X. Controlled Synthesis of Iron Oxide Nanoparticles over a Wide Size Range. *Langmuir* **2010**, *26*, 5843–5847.

(7) Mohapatra, J.; Mitra, A.; Bahadur, D.; Aslam, M. Surface Controlled Synthesis of MFe_2O_4 (M = Mn, Fe, Co, Ni and Zn) Nanoparticles and Their Magnetic Characteristics. *CrystEngComm* **2013**, *15*, 524-532.

(8) Caruntu, D.; Caruntu, G.; O'Connor, C. J. Magnetic Properties of Variable-Sized Fe_3O_4 Nanoparticles Synthesized from Non-Aqueous Homogeneous Solutions of Polyols. *J. Phys. D. Appl. Phys.* **2007**, *40*, 5801–5809.

(9) Park, B.; Kim, B. H.; Yu, T. Synthesis of Spherical and Cubic Magnetic Iron Oxide Nanocrystals at Low Temperature in Air. *J. Colloid Interface Sci.* **2018**, *518*, 27–33.

(10) Mitra, A.; Mohapatra, J.; Meena, S. S.; Tomy, C. V.; Aslam, M. Verwey Transition in Ultrasmall-Sized Octahedral Fe_3O_4 Nanoparticles. *J. Phys. Chem. C* **2014**, *118*, 19356–19362.

(11) Dehsari, H. S.; Heidari, M.; Ribeiro, A. H.; Tremel, W.; Jakob, G.; Donadio, D.; Potestio, R.; Asadi, K. Combined Experimental and Theoretical Investigation of Heating Rate on Growth of Iron Oxide Nanoparticles. *Chem. Mater.* **2017**, *29*, 9648-9656.

(12) Yun, H.; Liu, X.; Paik, T.; Palanisamy, D.; Kim, J.; Vogel, W. D.; Viescas, A. J.; Chen, J.; Papaefthymiou, G. C.; Kikkawa, J. M.; *et al.* Size- and Composition-Dependent Radio Frequency Magnetic Permeability of Iron Oxide Nanocrystals. *ACS Nano* **2014**, *8*, 12323–12337.

(13) Baaziz, W.; Pichon, B. P.; Fleutot, S.; Liu, Y.; Lefevre, C.; Greneche, J.-M.; Toumi, M.; Mhiri, T.; Bégin-Colin, S. Magnetic Iron Oxide Nanoparticles: Reproducible Tuning of the Size and Nanosized-Dependent Composition, Defects, and Spin Canting. *J. Phys. Chem. C* **2014**, *118*, 3795–3810.

(14) Demortière, A.; Panissod, P.; Pichon, B. P.; Pourroy, G.; Guillon, D.; Donnio, B.; Bégin-Colin, S. Size-Dependent Properties of Magnetic Iron Oxidenanocrystals. *Nanoscale* **2011**, *3*, 225–232.

(15) Taniguchi, T.; Nakagawa, K.; Watanabe, T.; Matsushita, N.; Yoshimura, M. Hydrothermal Growth of Fatty Acid Stabilized Iron Oxide Nanocrystals. *J. Phys. Chem. C* **2009**, *113*, 839–843.

(16) Santoyo Salazar, J.; Perez, L.; de Abril, O.; Truong Phuoc, L.; Ihiawakrim, D.; Vazquez, M.; Greneche, J.-M.; Begin-Colin, S.; Pourroy, G. Magnetic Iron Oxide Nanoparticles in 10−40 Nm Range: Composition in Terms of Magnetite/Maghemite Ratio and Effect on the Magnetic Properties. *Chem. Mater.* **2011**, *23*, 1379–1386.

(17) Kim, B. H.; Lee, N.; Kim, H.; An, K.; Park, Y. I.; Choi, Y.; Shin, K.; Lee, Y.; Kwon, S. G.; Na, H. B.; *et al.* Large-Scale Synthesis of Uniform and Extremely Small-Sized Iron Oxide Nanoparticles for High-Resolution T1 Magnetic Resonance Imaging Contrast Agents. *J. Am. Chem. Soc.* **2011**, *133*, 12624–12631.

(18) Tronc, E.; Ezzir, A.; Cherkaoui, R.; Chanéac, C.; Noguès, M.; Kachkachi, H.; Fiorani, D.; Testa, A. M.; Grenèche, J. M.; Jolivet, J. P. Surface-Related Properties of γ-Fe_2O_3 Nanoparticles. *J. Magn. Magn. Mater.* **2000**, *221*, 63–79.

(19) Millan, A.; Urtizberea, A.; Silva, N. J. O.; Palacio, F.; Amaral, V. S.; Snoeck, E.; Serin, V. Surface Effects in Maghemite Nanoparticles. *J. Magn. Magn. Mater.* **2007**, *312*, L5–L9.

Appendix B

(1) Rodríguez-Carvajal, J. Recent Advances in Magnetic Structure Determination by Neutron Powder Diffraction. *Phys. B Condens. Matter* **1993**, *192*, 55–69.

(2) Fleet, M. E. The Structure of Magnetite. *Acta Crystallogr.* **1981**, *2549*, 917–920.

(3) Shmakov, A. N.; Krvukova, G. N.; Tsvbulva, S. V; Chuvilin, A. L.; Solovveva, L. P. Vacancy Ordering in γ-Fe_2O_3: Synchrotron X-Ray Powder Diffraction and High-Resolution Electron Microscopy Studies. *J. Appl. Crystallogr.* **1995**, *28*, 141–145.

(4) Greaves, C. A Powder Neutron Diffraction Investigation of Vacancy Ordering and Covalence in γ-Fe_2O_3. *J. Solid State Chem.* **1983**, *49*, 325–333.

(5) Jørgensen, J.; Mosegaard, L.; Thomsen, L. E.; Jensen, T. R.; Hanson, J. C. Formation of γ-Fe_2O_3 Nanoparticles and Vacancy Ordering : An *in Situ* X-Ray Powder Diffraction Study. *J. Solid State Chem.* **2007**, *180*, 180–185.

(6) Zobel, M.; Neder, R. B.; Kimber, S. A. J. Universal Solvent Restructuring Induced by Colloidal Nanoparticles. *Science* **2015**, *347*, 201–204.

(7) Gorski, C.; Scherer, M. Determination of Nanoparticulate Magnetite Stoichiometry by Mössbauer Spectroscopy, Acidic Dissolution, and Powder X-Ray Diffraction : A Critical Review. *Am. Mineral.* **2010**, *95*, 1017–1026.

Appendix C

(1) Cooper, S. R.; Plummer, L. K.; Cosby, A. G.; Lenox, P.; Jander, A.; Dhagat, P.; Hutchison, J. E. Insights into the Magnetic Properties of Sub-10 nm Iron Oxide Nanocrystals through the Use of a Continuous Growth Synthesis. *Chem. Mater.* **2018**, *30*, 6053–6062.

(2) Greaves, C. A Powder Neutron Diffraction Investigation of Vacancy Ordering and Covalence in γ-Fe_2O_3. *J. Solid State Chem.* **1983**, *49*, 325–333.

(3) Zobel, M.; Neder, R. B.; Kimber, S. A. J. Universal Solvent Restructuring Induced by Colloidal Nanoparticles. *Science* **2015**, *347*, 201–204.

(4) Yamamoto, A. Modulated Structure of Wüstite ($Fe_{1-x}O$) (Three-Dimensional Modulation). *Acta Crystallogr. Sect. B* **1982**, *38*, 1451–1456.

(5) Koch, F.; Cohen, J. B. The Defect Structure of $Fe_{1-x}O$. *Acta Crystallogr. Sect. B* **1969**, *25*, 275–287.

(6) Roth, W. L. Defects in the Crystal and Magnetic Structures of Ferrous Oxide. *Acta Crystallogr.* **1960**, *13*, 140–149.

(7) Andersen, B.; Sletnes, J. O. Decomposition and Ordering in $Fe_{1-X}O$. *Acta Crystallogr.* **1977**, *33*, 268–276.

(8) Fleet, M. E. The Structure of Magnetite. *Acta Crystallogr.* **1981**, *2549*, 917–920.

(9) Frison, R.; Cernuto, G.; Cervellino, A.; Zaharko, O.; Colonna, G. M.; Guagliardi, A.; Masciocchi, N. Magnetite−Maghemite Nanoparticles in the 5−15 nm Range : Correlating the Core−Shell Composition and the Surface Structure to the Magnetic Properties. A Total Scattering Study. *Chem. Mater.* **2013**, *25*, 4820–4827.

(10) Weber, B.; Betz, R.; Bauer, W.; Schlamp, S. Crystal Structure of Iron (II) Acetate. *J. Inorg. Gen. Chem.* **2011**, *637*, 102–107.

(11) Wilson, C.; Iversen, B. B.; Overgaard, J.; Larsen, F. K.; Wu, G.; Palii, S. P.; Timco, G. A.; Gerbeleu, N. V. Multi-Temperature Crystallographic Studies of Mixed-Valence Polynuclear Complexes ; Valence Trapping Process in the Trinuclear Oxo-Bridged Iron Compound, $[Fe_3O(O_2CC(CH_3)_3)_6(C_5H_5N)_3]$. *J. Am. Chem. Soc.* 2000, *122*, 11370–11379.

(12) Zheng, Y.; Tong, M.; Xue, W.; Zhang, W.; Chen, X.; Grandjean, F.; Long, G. J. A " Star " Antiferromagnet : A Polymeric Iron (III) Acetate That Exhibits Both Spin Frustration and Long-Range Magnetic Ordering. *Angew. Chemie Int. Ed.* **2007**, *46*, 6076–6080.

(13) Yao, H.; Wang, J.; Ma, Y.; Waldmann, O.; Du, W.; Song, Y. An Iron (III) Phosphonate Cluster Containing a Nonanuclear Ring *Chem Commun.* **2006**, *1*, 1745–1747.

(14) Gorun, S. M.; Lippard, S. J. Synthesis, Structure, and Characterization of the Tetranuclear Iron(III)Oxo Complex $[Fe_4O_2(BICOH)_2(BICO)_2(O_2CPh)_4]Cl_2$. *Inorg. Chem.* **1988**, *27*, 149–156.

(15) Gorun, S. M.; Lippard, S. J. A New Synthetic Approach to the Ferritin Core Uncovers the Soluble Iron (III) Oxo-Hydroxo Aggregate $[Fe_{11}O_6(OH)_6(O_2CPh)_{15}]$. *Nature* **1986**, *319*, 666–668.

(16) Sadeghi, O.; Zakharov, L. N.; Nyman, M. Aqueous Formation and Manipulation of the Iron-Oxo Keggin Ion. *Science* **2015**, *347*, 1359–1362.

(17) Mandal, S. K.; Young, V. G.; Que, L. Polynuclear Carboxylato-Bridged Iron (II) Clusters : Synthesis, Structure, and Host-Guest Chemistry. *Inorg. Chem.* **2000**, *39*, 1831–1833.

(18) Low, D. M.; Jones, L. F.; Bell, A.; Brechin, E. K.; Mallah, T.; Rivière, E.; Teat, S. J.; Mcinnes, E. J. Solvothermal Synthesis of a Tetradecametallic Fe (III) Cluster. *Angew. Chemie* **2003**, *115*, 3911–3914.